UNIVERSITA' DEGLI STUDI DI PADOVA
Dipartimento di Ingegneria Elettrica

UNIVERSITÀ
DEGLI STUDI
DI PADOVA

DIE

SCUOLA DI DOTTORATO DI RICERCA
IN INGEGNERIA INDUSTRIALE
INDIRIZZO IN INGEGNERIA ELETTROTECNICA
CICLO XXIII

Algorithms and Rotor Designs for the Position Estimation of PM Synchronous motors at Zero and Nonzero Speed

Direttore della Scuola:
Ch.mo Prof. Paolo Bariani ....

Coordinatore d'indirizzo:
Ch.mo Prof. Giovanni Martinelli ....

Supervisore:
Ch.mo Prof. Silverio Bolognani ....

Dottorando:
Adriano Faggion ....

31 Gennaio 2011

To my family and Enrica

Contents

Sommario

I convenzionali azionamenti elettrici per il controllo dei motori a Magneti Permanenti (PM) richiedo la conoscenza della posizione rotorica per poter applicare le trasformazioni dal sistema di riferimento stazionario a quello rotorico e viceversa. La posizione viene di norma determinata con un trasduttore di posizione che può essere un resolver, sonde ad effetto Hall o encoder. La presenza di questo trasduttore aumenta i costi, la grandezza e la complessitá circuitale degli azionamenti e dei motori. Inoltre la loro manutenzione o sostituzione diventa difficoltosa in particolari applicazione, per es. pompe sommerse, macchine per l'eolico, ecc.

L'eliminazione di questi trasduttori, quindi, risulta essere un gran vantaggio in termini di costi, affidabilitá e riduzione della grandezza fisica del motore o anche dello stesso azionamento. E' chiaro che questa eliminazione comporta che l'azionamento includa una tecnica alternativa in grado di stimare la posizione e la velocità rotoriche: questi azionamenti vengono definiti azionamenti sensorless.

Negli ultimi anni la ricerca ha proposto diverse soluzioni di tipo sensorless che permettono la stima della posizione, diversificando però le tecniche per la regione di funzionamento in alta velocità da quelle in bassa velocità o a rotore fermo. Al giorno d'oggi, stimatori basati sulla ricostruzione del vettore di flusso o della fem (stimatori MRAS) vengono utilizzati per il primo caso, mentre nel secondo caso vengono utilizzati stimatori basati sulla iniezione di tensione ad alta frequenza.

Mentre nel primo caso la tipologia di stimatore può essere applicata sia ai motori di tipo isotropi che con quelli anisotropi, la seconda tipologia di stimatore può essere applicata solo a motori anisotropi, visto che sfrutta la salienza magnetica per estrarre la posizione elettrica.

Questa tesi verte appunto su queste due tipologie di stimatori, riassumendo in dettaglio i principali algoritmi utilizzati oggigiorno e implementandoli sia a livello simulativo che a livello sperimentale. Per una trattazione completa di questo argomento, vengono anche studiate le tre piú comuni configurazioni rotoriche (a PM Interni, a PM a montaggio Superficiale ed Inset (incassati)) con una particolare attenzione verso quello che è il comportamento anisotropo o isotropo della macchina stessa e la possibilità di applicare uno o l'altro degli algoritmi sensorless descritti.

Entrando in maggior dettaglio, per quanto riguarda lo stimatore MRAS, dopo una sua descrizione, viene presentato in una particolare applicazione che si riferisce ad un catamarano ibrido. Vengono quindi affrontate e discusse le problematiche legate alla strategia di partenza del motore tramite rampa di velocità, dell'aggancio sulla posizione stimata, dell'inversione di marcia. Inoltre viene studiata la sensitivitá dello stimatore che si dimostra dipendere dall'induttanza di statore e non dalla resistenza.

Invece per quanto riguarda lo stimatore basato sull'iniezione di segnali ad alta frequenza è stato per prima cosa descritto sia nel caso con iniezione nel sistema di riferimento statorico sia in quello rotorico. Lo studio è stato effettuato con una formulazione di tipo generale, adattata poi per il tipo di iniezione di segnale effettuata. La trattazione tiene conto anche della induttanza differenziale mutua e questo ha permesso di ricavare un legame tra l'errore di stima la induttanza mutua stessa. Vengono presentati inoltre tre diversi schemi per l'estrazione della posizione elettrica: mediante regolatore PI, osservatore a due stati ed osservatore a tre stati.

Dopo di che, lo stimatore con iniezione nel sistema di riferimento rotorico é stato testato sia in simulazione che su banco prova. La bontà dell'algoritmo di stima é stata provata su motori con due diverse configurazioni rotoriche: a PM Interni e di tipo Inset. L'induttanze diretta, in quadratura e mutua sono state studiate in dettaglio con il supporto di simulazioni agli elementi finiti (FEM). Grazie a questo studio è possibile prevedere l'errore di stima che verrá poi confrontato con quello ottenuto dalle prove sperimentali. Come detto in precedenza lo stimatore ad iniezione di segnale può essere utilizzato solo con quei motori che presentano una salienza magnetica. Da questa categoria quindi sono esclusi i motori SPM che, salvo alcune eccezioni come l'Inset, sono isotropi. Si è quindi pensato a come indurre in questi motori un comportamento anisotropo solo alle alte frequenze, cioè alle frequenze del segnale iniettato per la stima. In questa tesi viene presentata questa nuova configurazione rotorica definita "Ringed–pole". Questa consiste nella realizzazione di una gabbia di rotore inserendo degli anelli di rame cortocircuitato attorno a ciascun magnete permanente. La soluzione permette di andare a modificare alle alte frequenze il comportamento magnetico dell'asse diretto, mantenendo invariato quello di quadratura. In questo modo si viene a creare un comportamento anisotropo appunto alle alte frequenze, mantenendo però il comportamento isotropo della macchina per le basse frequenze. Questa caratteristica permette quindi di sfruttare lo stimatore basato sull'iniezione di tensioni alle alte frequenze, per la stima di posizione anche nel caso di motori SPM isotropi. Sono state eseguite simulazioni FEM e prove sperimentali per validare l'idea di base e provare l'effettiva possibilità della stima di posizione.

Un secondo contributo riguarda la presentazione di un nuovo stimatore basato sulle armoniche di corrente causate dalla modulazione PWM. L'idea di base consiste nel pensare che la modulazione PWM effettui una intrinseca iniezione di tensione ad alta frequenza, più precisamente alla frequenza di switching. Queste tensioni inducono delle armoniche di corrente alla stessa frequenza che contiene l'informazione sulla posizione elettrica. L'informazione può essere estratta mediante uno schema di stima simile a quello che viene utilizzato nella normale iniezione di tensione. É stata quindi effettuata una trattazione matematica per ricavare le espressioni delle componenti di tensione e di correnti alla frequenza di switching. Sono state eseguite delle simulazioni preliminari per confermare la correttezza dell'idea di base.

Introduction

Background

Conventional vector controlled permanent magnet motor drives require the knowledge of the rotor flux position to apply the transformations from the stator reference frame $\alpha\beta$ to the rotor reference dq and viceversa. The instantaneous angular position of the rotor flux is usually determined by position transducers that include resolvers, flux or Hall effect sensors and optical encoders. The presence of them increases cost, size and circuit complexity of motor drives. In addition, their maintenance or substitutions in some applications are very difficult, e.g. submersed pumps, windpower machines.

Elimination of any mechanical equipment for speed or angle detection represents a practical manufacturing advantage in terms of cost, reliability and size reduction of the electric drive. Then it is clear that position and speed sensors had to be eliminated in favor of alternative techniques, that should be included in any controlled drive, able to estimate the electrical rotor position and speed.

In the past years, several research efforts have focused on proposing techniques for sensorless speed and position control, useful for operations at any speed and also at very low speed including zero speed. However, a robust solution generally accepted for all different applications still does not exist. There are theoretical issues to be solved and implementation is hard, according to a specific application and to the level of the performance one wants to achieve. And yet, there is a noticeable interest from industry, transport and civil applications to make available on the market low cost, precise sensorless systems able to effectively drive different kinds of PM motors at low and zero speed.

Nowadays, *MRAS estimator* is used in the high speed region and the estimation exploiting the anisotropy of the rotor is applied in the low speed region. The first can be applied to both isotropic and anisotropic machine, instead the latter can be used also with the anisotropic motor.

Main contributions of the thesis

This thesis deals with the estimation algorithms, reassuming in detail the principles commons techniques and testing them in simulation and by experimentation. The following estimator typologies are discussed: MRAS estimator in the high speed region, estimator based on the high frequency injection signals in the low and zero speed region.

As regards the MRAS estimator, after its description, a particular application that exploits this estimation solution is presented. Then, a sensorless control of a Permanent Magnet synchronous motor drive for a hybrid electric catamaran is reported. A Surface–mounted Permanent Magnet motor has been chosen and a distinctive sensorless control of this machine is deeply described. Control performance is validated by simulation and experimental results. Start–up mode, reversal of speed and synchronization lost occurrence will be specifically treated. Moreover the estimator sensitivity is studied. The dependence on the stator inductance and the independence of the resistance of the estimation error is demonstrated and verified by means of experimental tests.

After that, a high frequency injected voltage for estimating the electrical angular position of the rotor is used for the sensorless control of salient–pole Permanent Magnet (PM) synchronous motor drives. A high frequency speed–dependent ellipse rotating voltage vector is injected to the motor. It generates a high frequency current vector in the estimated synchronous reference frame, that contains information on actual rotor position. This type of estimation technique exploits the anisotropy of the rotor and gives an estimation that is not affected by rotor speed. A recent aspect of the topic intensively investigated is the behaviour of different rotor geometries when subjected to high frequency rotor position estimations and, consequently, the design of sensorless oriented configurations. The reasons of these studies arise from the iron saturation which occurs in the rotor and that modifies and can even cancel rotor saliency and introduces a cross coupling (cross–saturation) between d– and q–axis. This paper experiments the behaviour of two of the principal sensorless oriented rotor configurations (IPM and Inset) and compare the experimental results with those predicted by the finite element simulations carried out during the motor design, in order to validate prediction tools and find out new design hints. In addition, the estimation error dependence on the mutual inductance is demonstrated. Estimation error quantities calculated by means of FEM simulations and measured with experimental tests are compared for both the machines.

Main contribution of this thesis consists in introducing a new configuration of SPM motor, in which a turn has been wound around each pole in order to modify the direct axes flux linkage dynamics while preserving the quadrature axis one, thus creating a rotor dynamic anisotropy (ringed–pole rotor). Consequently, the motor can be used in a position sensorless control which exploits the anisotropic rotor features by high frequency injected signals. The model of the machine is described in the paper, and the main equations describing the motor dynamics are reported. Simulations, design hints and experimental results are reported so as to validate the proposed new rotor structure.

With this solution, the novel machine can be used in a position sensorless control drive which exploits the anisotropic rotor features by high frequency injected signals. A Ringed–pole motor has been tested with two different estimator: a two states observer and a three states observer. Expected drive performance is validated by simulation and experimental results.

Finally the thesis investigates successfully the possibility of extract rotor position information of Interior Permanent Magnet Motors from PWM current harmonic contents. To this aim, a general description of PWM voltage harmonics is at first given. Current harmonics are then derived assuming an anisotropic rotor. It is proved that rotor position information can be derived if single edge PWM is adopted. A speed and position estimation scheme is illustrated and the new rotor position estimation technique is then validated by simulations.

Outline of the thesis

Chapter 1 reassumes the main equations that describe a motor. In particular the voltage balance equations are derived in the three–phase, stator and rotor reference frames. Moreover, the mutual and auto inductances are described in detail. Finally the real behaviour of the machine is approached including the iron and cross saturation effects.

Chapter 2 studies, by means of Finite Elements Method (FEM) simulations, three machines with different rotor geometry: Interior Permanent Magnet (IPM), Surface–mounted Permanent Magnet (SPM) and Inset machine. For each of them the voltage balance equations in the dq reference and the respective motor scheme are reported. In addition, the d– and q–axis flux–linkage behaviour are plotted. Flux lines are plotted both with currents only in the only d–axis and in the q–axis. Descriptions are completed including the main geometry and electric parameters of the three different machines.

Chapter 3 presents an overview of the most common estimators used nowadays. More precisely, MRAS estimator are presented in high–speed region and the estimator based on high frequency injection signals in the low speed region. As regard the former, a scheme that reconstructs the flux vector is presented. The discussion is accompanied by the main system of equations and the principle diagrams of the estimators. As regards the second type of estimator, both injection signal in the stator and in the rotor reference frame are examined. For the latter are also reported three different schemes for the position estimation: with a standard PI regulator, a two–state observer and a three–state observer.

Chapter 4 shows a particular application in which a MRAS estimator is used. This application is a hybrid catamaran, which uses two SPM motors for propulsion. The use of a sensorless control is required for space and reliability reasons. Simulation and experimental test results are plotted and discussed here with particular attention regard to the start–up of the machine, the speed reversal and estimator sensitivity.

Chapter 5 considers two machines with anisotropic behavior of the rotor: the IPM and the Inset. These have been tested using the estimation algorithm based on the injection of high frequency voltage in the rotor reference frame. Tests and simulation results are reported for both the motors. Finally, effect of cross and iron saturation in the estimation error is investigated. Estimation errors derive with FEM simulations and measures are compared.

Chapter 6 presents a new rotor configuration defined Ringed–pole. A cage rotor is created by giving each pole of a short–circuit copper ring. This feature allows to create an anisotropic behaviour at high frequencies, modifying the electromagnetic behaviour of the d–axis without changing that of the q–axis. The idea is confirmed from the FEM simulations and experimental tests reported. Particular attention is paid to the measure of the d– and q–axis inductances at both low and high frequencies and on the anisotropic behaviour at different frequencies. In addition, the motor equations are obtained taking into account the presence of the ring.

Chapter 7 verifies the effective possibility to estimate the electrical position applying the technique of high frequency injection signal on the proposed Ringed–pole machine. Simulation and experimental tests are reported, using both two– and three–state estimation scheme.

Chapter 8 gives a new estimator that exploits the high–frequency current harmonics due to the single edge PWM modulation. For this purpose, the modulated voltage harmonics, at switching frequency of the inverter, are derived in the stator reference system. Current harmonics expressions are given, which confirm that they contain the electrical position information. The demodulation and extraction scheme for the position is presented and commented with simulation results. Mathematical treatment is addressed in **Appendix A**.

List of publications

Several parts of the thesis have been presented by the author during the course of the doctoral study in international conferences and journals. Hereafter the publications are listed. Conference papers are marked as $C*$, while the journal papers are marked as $J*$.

J1 M. Barcaro, A. Faggion, L. Sgarbossa, N. Bianchi, and S. Bolognani. "Performance evaluation of an integrated starter alternator using an interior permanent magnet machine". In *Proceedings of IET Electric Power Applications*, Vol.4, Issue 7, pages 539–546, August 2010. DOI 10.1049/iet–epa.2009.0216.

J2 L. Alberti, M. Barcaro, M.D. Pré and, A. Faggion, L. Sgarbossa, N. Bianchi, and S. Bolognani. "Ipm machine drive design and tests for an integrated starter alternator application". In *IEEE Transactions on Industry Applications*, vol. 46, no. 3, pp. 993–1001, May–June 2010. DOI 10.1109/TIA.2010.2045323

J3 L. Alberti, N. Bianchi,M. Barcaro,D. Bon, S. Bolognani, M. Castiello, A. Faggion, E. Fornasiero and L. Sgarbossa. "Interior Permanent Magnet Integrated Starter Alternator". In *The International Journal for Computation and Mathematics in Electronic Engineering COMPEL*, ISSN: 0332–1649.

C1 N. Bianchi, S. Bolognani, A. Faggion. "Rotor design arrangement of spm motors for the sensorless control at low speed and standstill". In 14th *International Power Electronics and Motion Control Conference EPE/PEMC*, Ohrid (MK), 6-8 Sept. 2010, p.S1-S23, ISBN/ISSN: 978-1-4244-7856-9, doi: 10.1109/EPEPEMC.2010.5606533.

C2 N. Bianchi, S. Bolognani, A. Faggion. "A Ringed–Pole SPM Motor for Sensorless Drives – Electromagnetic analysis, prototyping and tests". In *IEEE International Symposium on Industrial Electronics ISIE*. Bari (IT), 4–7 July 2010.

C3 A. Faggion, S. Bolognani. "A new proposal of rotor position estimation in ipm motor drives based on pwm current harmonics". In *First Symposium on Sensorless Control for Electrical Drives SLED*, Padova (IT), 9-10 July 2010, p. 86, ISBN/ISSN: 978–1–4244–7034–1, doi: 10.1109/SLED.2010.5542797

C4 N. Bianchi, S. Bolognani, A. Faggion. "Ringed-pole permanent magnet synchronous motor for position sensorless drives". In *IEEE Energy Conversion Congress and Exposition ECCE*, San Josè (US), 20–24 September 2009, p. 3837, ISBN/ISSN: 978–1–4244–2893–9, doi: 10.1109/ECCE.2009.5316112

C5 S. Bolognani, A. Faggion, L. Sgarbossa. ”Model-based sensorless control of an SPM synchronous motor drive for a hybrid catamaran”. In *13th European Conference on Power Electronics and Applications EPE*. Barcelona, Spain. 8–10 September 2009. pages 1–10, ISBN/ISSN: 978-1-4244-4432-8

C6 N. Bianchi, S. Bolognani, A. Faggion. ”Predicted and measured errors in estimating rotor position by signal injection for salient-pole PM synchronous motors”. In *IEEE International Electric Machines and Drives Conference IEMDC*. Miami, Florida (US), 3–6 May 2009, p. 1565, ISBN/ISSN: 978–1–4244–4251–5, doi: 10.1109/IEMDC.2009.5075412

C7 L. Alberti, M. Barcaro, N. Bianchi, S. Bolognani, D. Bon, M. Castiello, A. Faggion, E. Fornasiero, L. Sgarbossa. ”Interior Permanent Magnet Integrated Starter–Alternator”. In *International Conference on Ecologic Vehicles* & *Renewable Energies EVER*. Principato di Monaco, 25–28 March 2009.

C8 S. Bolognani, A. Faggion , L. Sgarbossa. ”Model-based Sensorless Control of an SPM Synchronous Motor Drive for a Hybrid Catamaran”. In *13th International European Power Electronics Conference and Exhibition EPE*. Spain, Barcellona, 8–10 September 2009, p. 1, ISBN/ISSN: 978–1–4244–4432–8

C9 L. Alberti, M. Barcaro, N. Bianchi, S. Bolognani, A. Faggion, M Dai Prè, L. Sgarbossa. ”Effective control of an Integrated Starter–Alternator with an IPM Synchronous Machine”. In *IEEE Power Electronics Specialists Conference PESC*. Rhodes (GR), 16–19 June 2008, p. 43, ISBN/ISSN: 978–1–4244–1667–7, doi: 10.1109/PESC.2008.4591894

C10 L. Alberti, M. Barcaro, N. Bianchi, S. Bolognani, A. Faggion, M Dai Prè, L. Sgarbossa. ”Experimental Tests on a 12–Slot 8–Pole integrated Starter-Alternator”. In *18th International Conference on Electrical Machines ICEM*. Vilamoura, Portugal, 6–9 September 2008, p. 1, ISBN/ISSN.978–1–4244–1735–3, doi: 10.1109/ICELMACH.2008.4799841

C11 L. Alberti, M. Barcaro, N. Bianchi, S. Bolognani, A. Faggion, M Dai Prè, L. Sgarbossa. ”IPM Machine Drive Design and Tests for an Integrated Starter-Alternator Application”. In *IEEE Industry Applications Society Annual Meeting IAS*. Edmonton, Alberta, Canada, 5–9 Oct. 2008, p. 1, ISBN/ISSN: 978–1–4244–2278–4, doi: 10.1109/08IAS.2008.217

C12 S. Bolognani, A. Faggion, L. Perretti, L. Sgarbossa. ”Sensorless V-type Vector-controlled IM Drive with Inherent Flux-Weakening Capability”. *In 4th IET Conference on Power Electronics, Machines and Drives PEMD*. York St John University College, YORK UK, 2–4 Aprile 2008, p. 465, ISBN/ISSN: 978–0–86341–900–3

C13 S. Bolognani, A. Faggion, L. Sgarbossa. ”High efficiency multi-drive system for a hybrid electric catamaran with submersed PM synchronous motors”. *In 18th International Conference on Electrical Machines ICEM*. Vilamoura Portugal, 6–9 Sept.2008, p. 1, ISBN/ISSN: 978–1–4244–1735–3, doi: 10.1109/ICELMACH.2008.4800105

C14 S. Bolognani, A. Faggion, L. Sgarbossa. ”Design of a flux weakening control scheme for DC motor drives featuring full voltage operation”. In *43rd International Universities Power Engineering Conference UPEC*. Padova, Italy, 1–4 settembre 2008, p. 1, ISBN/ISSN: 978–1–4244–3294–3,
doi: 10.1109/UPEC.2008.4651658

1

Permanent Magnet Synchronous Motors

1.1 Structure and operating principle

The Permanent Magnet (PM) synchronous motors are diffused in the industrial field, especially in the small and medium power drives. The PM motors are widely adopted in the high performance drives, where the particular performances justify the costs, higher than other motors with the same torque but realized with a different technology. The cost increment is due to the presence of precious permanent magnets in the inductor system.

The stator and the rotor present both a cylindric form of laminated iron material and they are separated from an air gap. The magnets are mounted in the rotor and their differential magnetic permeability is very similar to that of the air. Therefore, according to their placement in the rotor and to the design of the latter, it is possible to obtain rotor structures isotropic and anisotropic from the magnetic point of the view. The first can be obtained placing the magnets on the external surface of the rotor; the latter is obtained with the magnets buried inside the rotor. Generally the PM synchronous machines can be classified as follow:

SPM – Surface–mounted Permanent Magnet (Fig.1.1), with an isotropic rotor behaviour;

IPM – Interior Permanent Magnet (Fig.1.2), with an anisotropic rotor behaviour.

In machine with an isotropic rotor *electromechanical conversion* is actuated according to principle of electrodynamic systems, as for the DC motor. Conversion is based on interaction between the conductors and the magnetic fields create by other conductors or permanent magnets. In SPM motors the conductors subjected to the forces are placed in the stator, while the magnets are on the rotor. In anisotropic machine the electromechanical conversion follows double principle of the electrodynamic and reluctance systems. The torque generated by this motor is given by the sum of the contributions of these two mechanisms.

The stator winding of a PM synchronous machine (independently from the rotor configuration) is of three–phase type; the phases have the same number and distribution of conductors (identified with aa', bb' and cc' in Fig.1.3) but they have each other a phase displacement of $\frac{2\pi}{3}$. The winding can be fed by an external three-phase source through the terminals of each phase. In Fig.1.3 each phase is presented schematically with only one couple of conductors and the phase axis is the straight line normal to the plane that contains the conductors .

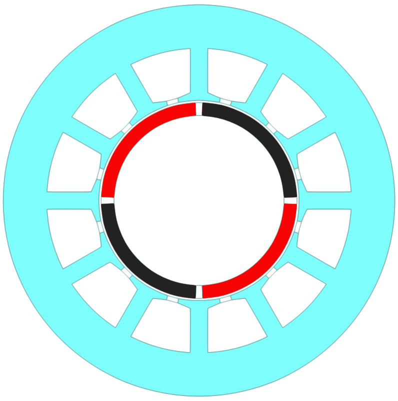

Figure 1.1: Sketch of four-pole SPM motor (isotropic motor)

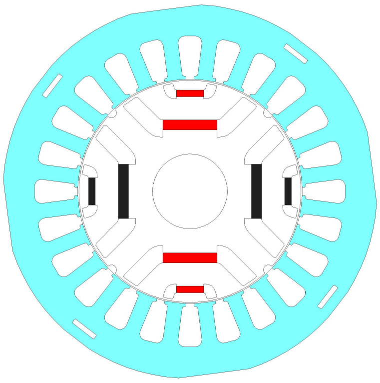

Figure 1.2: Sketch of four-pole IPM motor (anisotropic motor)

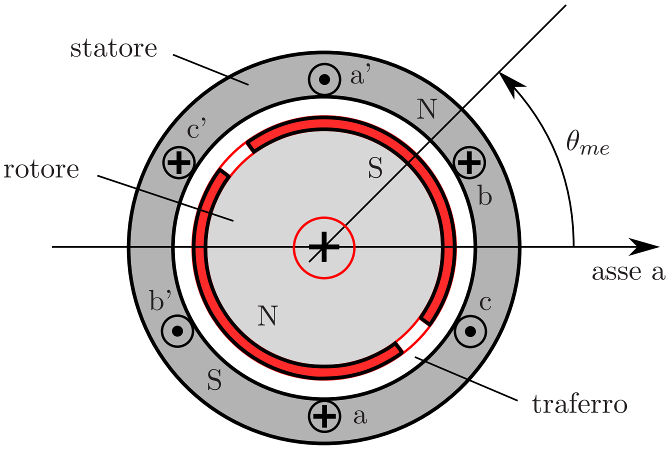

Figure 1.3: Schematic representation of the stator windings

1.2 Electric equations in the stator reference frame

In order to describe the operation of the PM synchronous motor, one can start from the general equations of the three–phase voltage balance:

$$\begin{aligned} u_a(t) &= R_s i_a(t) + \frac{d\lambda_a(t,\theta_{me})}{dt} \\ u_b(t) &= R_s i_b(t) + \frac{d\lambda_b(t,\theta_{me})}{dt} \\ u_c(t) &= R_s i_c(t) + \frac{d\lambda_c(t,\theta_{me})}{dt} \end{aligned} \tag{1.1}$$

where θ_{me} is the *electrical rotor position* given by the product from the number of pole–pair p and the mechanical position θ_m, and:

- u_a, u_b, u_c are the phase voltages;
- i_a, i_b, i_c are the phase currents;

- λ_a, λ_b, λ_c are the magnetic flux linkage of each phase;
- R_s is the phase resistance that is supposed to be equal for all the three phases, defined also as stator resistance.

This equations are valid in absence of hysteresis and eddy currents in the iron core.

Assuming that no saturation affects the magnetic circuits, the flux linkage of each phase is the sum of the flux linkage given by the permanent magnet and the flux due to the phase currents:

$$\begin{aligned}\lambda_a(t) &= \lambda_{a,mg}(t)+\lambda_{a,i}(t)\\ \lambda_b(t) &= \lambda_{b,mg}(t)+\lambda_{b,i}(t)\\ \lambda_c(t) &= \lambda_{c,mg}(t)+\lambda_{c,i}(t)\end{aligned}\tag{1.2}$$

For the sake of simplicity, the time dependency is not explicitly written in the following. The distribution of stator windings (and secondary the magnet forms) allows to assume sinusoidal the flux linkages $\lambda_{a,mg}$, $\lambda_{b,mg}$ and $\lambda_{c,mg}$:

$$\begin{aligned}\lambda_{a,mg} &= \Lambda_{mg}\cos(\theta_{me})\\ \lambda_{b,mg} &= \Lambda_{mg}\cos\left(\theta_{me}-\frac{2\pi}{3}\right)\\ \lambda_{c,mg} &= \Lambda_{mg}\cos\left(\theta_{me}+\frac{2\pi}{3}\right)\end{aligned}\tag{1.3}$$

where Λ_{mg} represents the maximum flux linkage of each phase due to the permanent magnet. The three equations in (1.3) can be associated to the spatial vector[1]:

$$\bar{\lambda}^s_{mg}=\Lambda_{mg}e^{j\theta_{me}}\tag{1.4}$$

where the apex ^{s} indicates the *stationary reference frame* with the axes α–β shown in Fig.1.4.

The second terms of the (1.2) are the fluxes due to the phase inductances and the currents. They can be expressed as follows:

$$\begin{aligned}\lambda_{a,i} &= L_{aa}i_a+L_{ab}i_b+L_{ac}i_c\\ \lambda_{b,i} &= L_{bb}i_b+L_{bc}i_c+L_{ab}i_a\\ \lambda_{c,i} &= L_{cc}i_c+L_{ac}i_a+L_{ab}i_b\end{aligned}\tag{1.5}$$

$$\tag{1.6}$$

where the L_{aa}, L_{bb} and L_{cc} are the self–inductances of the three phases, L_{ab}, L_{bc} and L_{ac} are the mutual–inductances between one phase to the another ones. The auto and mutual inductances can be considered dependent on the rotor position and then also on the time. The self–inductances can be expressed as follow

$$\begin{aligned}L_{aa} &= L_\sigma+L_0-L_2\cos(2\theta_{me})\\ L_{bb} &= L_\sigma+L_0-L_2\cos\left(2\theta_{me}+\frac{2\pi}{3}\right)\\ L_{cc} &= L_\sigma+L_0-L_2\cos\left(2\theta_{me}-\frac{2\pi}{3}\right)\end{aligned}\tag{1.7}$$

---

[1] Spatial vector quantities will be indicated with the subscript $-$ as $\bar{\lambda}$

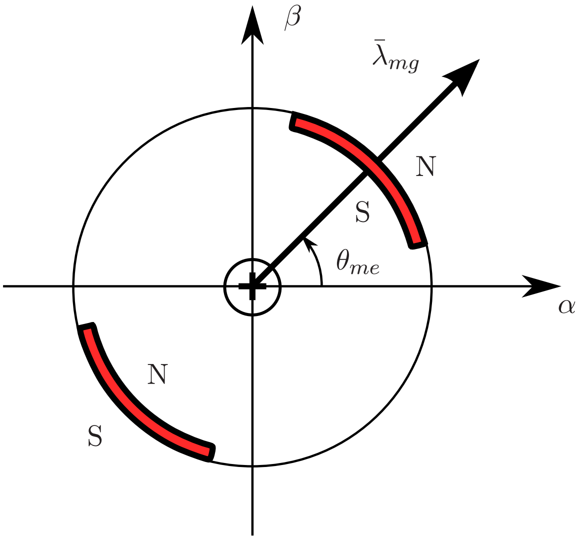

Figure 1.4: Spatial vector of the flux due to the magnet

that is given by the sum of a sinusoidal term with a double electrical frequency (of amplitude L_2) and a constant term $(L_\sigma + L_0)$. The constant L_σ represents the *leakege inductance* and it is relative to the stator flux which encloses in the air without interesting the rotor. As regard the other two terms, indicating with $\Re_d$ and $\Re_q$ respectively, the reluctance along the d– and q–axis and with N the effective number of each phase coils[2], they result as follow:

$$L_0 = \frac{N^2}{2}\left(\frac{1}{\Re_d} + \frac{1}{\Re_q}\right) \tag{1.8}$$

$$L_2 = \frac{N^2}{2}\left(\frac{1}{\Re_d} - \frac{1}{\Re_q}\right) \tag{1.9}$$

One can note that the term L_2 is related to the anisotropy of the structure. In similar manner, it is possible to express the mutual inductances among the windings of the stator phases as follow:

$$\begin{aligned} L_{ab} &= -\frac{L_0}{2} - L_2\cos\left(2\theta_{me} - \frac{2\pi}{3}\right) \\ L_{bc} &= -\frac{L_0}{2} - L_2\cos\left(2\theta_{me}\right) \\ L_{ac} &= -\frac{L_0}{2} - L_2\cos\left(2\theta_{me} + \frac{2\pi}{3}\right) \end{aligned} \tag{1.10}$$

---

[2] The number includes the factors necessary to correlate the coils number of a distribuite windings with the coils of an equivalent concentrated windings along each axis.

Substituting Eqs.(1.2)–(1.10) in (1.1), the three–phase voltages result in:

$$\begin{aligned}
u_a &= R_s i_a + L_{aa}\frac{di_a}{dt} + L_{ab}\frac{di_b}{dt} + L_{ac}\frac{di_c}{dt} + \frac{dL_{aa}}{dt}i_a + \frac{dL_{ab}}{dt}i_b + \frac{dL_{ac}}{dt}i_c + e_a \\
u_b &= R_s i_b + L_{bb}\frac{di_b}{dt} + L_{ba}\frac{di_a}{dt} + L_{bc}\frac{di_c}{dt} + \frac{dL_{bb}}{dt}i_b + \frac{dL_{ab}}{dt}i_a + \frac{dL_{bc}}{dt}i_c + e_b \\
u_c &= R_s i_c + L_{cc}\frac{di_c}{dt} + L_{ac}\frac{di_a}{dt} + L_{bc}\frac{di_b}{dt} + \frac{dL_{cc}}{dt}i_c + \frac{dL_{ac}}{dt}i_a + \frac{dL_{bc}}{dt}i_b + e_c
\end{aligned} \tag{1.11}$$

where e_a, e_b and e_c are the back electromotive forces defined by:

$$\begin{aligned}
e_a &= \frac{d\lambda_{a,mg}}{dt} = -\Lambda_{mg}\omega_{me}\sin(\theta_{me}) = \Lambda_{mg}\omega_{me}\cos\left(\theta_{me} + \frac{\pi}{2}\right) \\
e_b &= \frac{d\lambda_{b,mg}}{dt} = \Lambda_{mg}\omega_{me}\cos\left(\theta_{me} + \frac{\pi}{2} - \frac{2\pi}{3}\right) \\
e_c &= \frac{d\lambda_{c,mg}}{dt} = \Lambda_{mg}\omega_{me}\cos\left(\theta_{me} + \frac{\pi}{2} + \frac{2\pi}{3}\right)
\end{aligned} \tag{1.12}$$

where $\omega_{me} = d\theta_{me}/dt$ is the electromechanical speed, expressed in $el.rad./s$.

From (1.4), it is possible to write the back–electromotive force in the spatial vector form:

$$\bar{e} = \frac{d\bar{\lambda}_{mg}}{dt} = \frac{d(\Lambda_{mg}e^{j\theta_{me}})}{dt} = j\Lambda_{mg}\omega_{me}e^{j\theta_{me}} = j\omega_{me}\bar{\lambda}_{mg} \tag{1.13}$$

in order to derive a compact form for the voltage balance equations (1.11), a matrix notation can be used[3]:

$$\underline{u} = R\underline{i} + \underline{L}\frac{d\underline{i}}{dt} + \underline{i}\frac{d\underline{L}}{dt} + \underline{e} \tag{1.14}$$

where $\underline{L}$ is the inductance matrix

$$\underline{L} = \begin{bmatrix} L_{aa} & L_{ab} & L_{ac} \\ L_{ab} & L_{bb} & L_{bc} \\ L_{ac} & L_{bc} & L_{cc} \end{bmatrix} \tag{1.15}$$

whose elements are in (1.7) and (1.10). From (1.14) the two components of the voltage, current, flux linkage, back emf spatial vectors meet the equation:

$$\underline{u}^s = R_s\underline{i}^s + \frac{d\underline{\lambda}^s}{dt} = R_s\underline{i}^s + \underline{L}^s\frac{d\underline{i}^s}{dt} + \underline{i}^s\frac{d\underline{L}^s}{dt} + \underline{e}^s \tag{1.16}$$

---

[3] matrix quantities will be indicates by underscript characters as $\underline{u}$ or square brackets as $[u]$.

where

$$\underline{u}^s = \begin{bmatrix} u_\alpha \\ u_\beta \end{bmatrix} \tag{1.17}$$

$$\underline{i}^s = \begin{bmatrix} i_\alpha \\ i_\beta \end{bmatrix} \tag{1.18}$$

$$\underline{e}^s = \begin{bmatrix} e_\alpha \\ e_\beta \end{bmatrix} = \begin{bmatrix} -\omega_{me}\Lambda_{mg}\sin(\theta_{me}) \\ \omega_{me}\Lambda_{mg}\cos(\theta_{me}) \end{bmatrix} \tag{1.19}$$

$$\underline{L}^s = \begin{bmatrix} L_{\alpha\alpha} & L_{\alpha\beta} \\ L_{\alpha\beta} & L_{\beta\beta} \end{bmatrix} = \underline{T}_{abc/\alpha\beta}\underline{L}\underline{T}_{\alpha\beta/abc} \tag{1.20}$$

$$= \begin{bmatrix} L_\sigma + \frac{3}{2}(L_0 - L_2\cos(2\theta_{me})) & -\frac{3}{2}\sin(2\theta_{me}) \\ -\frac{3}{2}\sin(2\theta_{me}) & L_\sigma + \frac{3}{2}(L_0 + L_2\cos(2\theta_{me})) \end{bmatrix} \tag{1.21}$$

$$\tag{1.22}$$

being

$$\underline{T}_{abc/\alpha\beta} = \frac{2}{3}\begin{bmatrix} 1 & -\frac{1}{2} & -\frac{1}{2} \\ 0 & \frac{\sqrt{3}}{2} & -\frac{\sqrt{3}}{2} \end{bmatrix} \tag{1.23}$$

$$\underline{T}_{\alpha\beta/abc} = \begin{bmatrix} 1 & 0 \\ -\frac{1}{2} & \frac{\sqrt{3}}{2} \\ -\frac{1}{2} & -\frac{\sqrt{3}}{2} \end{bmatrix} \tag{1.24}$$

$$\tag{1.25}$$

The apex ^{s} represents the stator reference frame. The power balance can be applied at the (1.1). Multiplying the voltage phase for the respectively current and summing term to term, one can obtain:

$$u_a i_a + u_b i_b + u_c i_c = R_s(i_a^2 + i_b^2 + i_c^2) + \left(\frac{d\lambda_{a,i}}{dt}i_a + \frac{d\lambda_{b,i}}{dt}i_b + \frac{d\lambda_{c,i}}{dt}i_c\right) + (e_a i_a + e_b i_b + e_c i_c) \tag{1.26}$$

The first term represents the dissipated power due to Joule effect on the resistance phase. The second term is the absorbed power used to produce the magnetic energy variation connected with the magnetic field due to the phase current.The latter term is the electromechanical power equal to the product between the torque developed m and the speed ω_{me}:

$$e_a i_a + e_b i_b + e_c i_c = m\omega_m = \frac{m\omega_{me}}{p} \tag{1.27}$$

In the α–β reference frame, instead, results:

$$\frac{2}{3}(e_\alpha i_\alpha + e_\beta i_\beta) = \frac{m\omega_{me}}{p} \tag{1.28}$$

From the (1.28), the expression of the torque can be derived in:

$$\begin{aligned} m &= \frac{3}{2}p[\lambda_\alpha i_\beta - \lambda_\beta i_\alpha] \\ &= \frac{3}{2}p[\lambda_{\alpha,mg} i_\beta - \lambda_{\beta,mg} i_\alpha] \end{aligned} \tag{1.29}$$

This expression can be rearranged in this manner:

$$m = \frac{3}{2}pIm[\bar{i}_s^s \breve{\bar{\lambda}}_s^s] = \frac{3}{2}p|\bar{i}_s^s||\bar{\lambda}_s^s|\sin(\theta_i^s - \theta_\lambda^s) = \frac{3}{2}p|\bar{i}_s^s||\bar{\lambda}_s^s|\sin(\theta_i^\lambda) \tag{1.30}$$

where $Im[\bullet]$ is the "Imaginary" operator, θ_i^λ is the displacement between the spatial vectors of the current and the stator flux, and it is taken the follow notation:

$$\begin{aligned} \bar{i}_s^s &= |\bar{i}_s^s|e^{j\theta_i^s} \\ \bar{\lambda}_s^s &= |\bar{\lambda}_s^s|e^{j\theta_\lambda^s} \\ \breve{\bar{\lambda}}_s^s &= |\bar{\lambda}_s^s|e^{-j\theta_\lambda^s} \qquad \text{(complex conjugated)} \end{aligned}$$

The (1.30) demonstrates that the torque is independently from the reference frame being all the size (module and displacement) independently from it. Therefore, the torque can be expressed in this way:

$$m = \frac{3}{2}p[\lambda_{\alpha,mg}^x i_\beta^x - \lambda_{\beta,mg}^x i_\alpha^x] \tag{1.31}$$

where the apex ^{x} indicates a general reference frame and the subscripts $_\alpha$ and $_\beta$ the real and imaginary components respectively.

1.3 Electric equation in the synchronous reference frame

Taking in consideration a *reference frame d–q, synchronous with the rotor*, that is rotating at the electrical rotor speed ω_{me} and with the real axis coincident to the polar rotor axis, the voltage balance can be derived applying at (1.16) the matrix transformation:

$$\begin{aligned} T_{\alpha\beta/dq} &= \begin{bmatrix} \cos\theta_{me} & \sin\theta_{me} \\ -\sin\theta_{me} & \cos\theta_{me} \end{bmatrix} \\ T_{dq/\alpha\beta} &= \begin{bmatrix} \cos\theta_{me} & -\sin\theta_{me} \\ \sin\theta_{me} & \cos\theta_{me} \end{bmatrix} \end{aligned} \tag{1.32}$$

Then, the voltage balance results:

$$\underline{u}^r = R_s\underline{i}^r + \frac{d\underline{\lambda}^r}{dt} + j\omega_{me}\underline{\lambda}^r = R_s\underline{i}^r + \underline{L}^r\frac{d\underline{i}^r}{dt} + \underline{i}^r\frac{d\underline{L}^r}{dt} + \underline{e}^r \tag{1.33}$$

where

$$\underline{u}^r = \begin{bmatrix} u_d \\ u_q \end{bmatrix} \tag{1.34}$$

$$\underline{i}^r = \begin{bmatrix} i_d \\ i_q \end{bmatrix} \tag{1.35}$$

$$\underline{e}^r = \begin{bmatrix} e_d \\ e_q \end{bmatrix} = \begin{bmatrix} -\omega_{me} L_q \\ \omega_{me} L_d i_d + \omega_{me} \Lambda_{mg} \end{bmatrix} \tag{1.36}$$

$$\underline{\lambda}^r = \begin{bmatrix} \Lambda_{mg} + \lambda_{d,i} \\ \lambda_{q,i} \end{bmatrix} \tag{1.37}$$

One can note that the flux due to the magnet has only direct components being the d–axis along the magnetic axis. The fluxes $\lambda_{d,i}$ and $\lambda_{q,i}$ are equal to:

$$\begin{aligned} \lambda_{d,i} &= L_d i_d \\ \lambda_{q,i} &= L_q i_q \end{aligned} \tag{1.38}$$

The inductance matrix $\underline{L}^r$ results equal to:

$$\underline{L}^r = \begin{bmatrix} L_d & 0 \\ 0 & L_q \end{bmatrix} = \begin{bmatrix} L_\sigma + \frac{3}{2}(L_0 - L_2) \\ L_\sigma + \frac{3}{2}(L_0 + L_2) \end{bmatrix} \tag{1.39}$$

The inductances L_d and L_q are called respectively *direct axis (d–axis) synchronous inductances* and *quadrature axis (q–axis) synchronous inductance*. Differently from the inductances in the stator reference frame voltage balance, L_d and L_q are constant and independent of the rotor position.

Finally, (1.33) can be decomposed in the direct and quadrature components:

$$\begin{aligned} u_d &= R_s i_d + L_d \frac{di_d}{dt} - \omega_{me} L_q i_q \\ u_q &= R_s i_q + L_q \frac{di_q}{dt} + \omega_{me} L_d i_d + \omega_{me} \Lambda_{mg} \end{aligned} \tag{1.40}$$

The power balance can be obtained starting from the (1.40):

$$(u_d i_d + u_q i_q) dt = R_s (i_d^2 + i_q^2) dt + L_d i_d di_d + L_q i_q di_q + \omega_{me} [\Lambda_{mg} i_q + (L_d - L_q) i_d i_q] dt \tag{1.41}$$

The last term is the mechanical power and then it is possible to derive the motor torque:

$$m = \frac{3}{2} p \Lambda_{mg} i_q + \frac{3}{2} p (L_d - L_q) i_d i_q = \frac{3}{2} p \left[\Lambda_{mg} + (L_d - L_q) i_d\right] i_q \tag{1.42}$$

The first term is the torque due to the permanent magnets, instead the second term is the reluctance torque due to the different value between the direct and quadrature axes. Finally, one can note that (1.31) is again valid exploiting (1.35) and (1.37).

The mechanical load balance is equal to:

$$m = m_L + B\omega_m + J \frac{d\omega_m}{dt} \tag{1.43}$$

where B is the viscous friction coefficient and J is the inertia of the load.

1.4 Real Behaviour of the Machine

In previous equations some simplifications are taking into account, but there are various causes that renders the machine behaviour different from that described previously. In this Section the effects due to the iron magnetic saturations are reported.

1.4.1 Iron saturation

In presence of iron saturation, the flux linkage–current relations (magnetic characteristics) for the two axes cannot be expressed through linear equations and constant inductances. They assume more complex relations, with cross effects of the d–axis current axis to the q–axis flux and viceversa (cross saturation). Neglecting, for the moment, this last phenomenon, the magnetic characteristics have to be described as follow:

$$\begin{aligned} \lambda_d(i_d) &= \Lambda_{mg} + \lambda_{d,i}(i_d) \\ \lambda_q(i_q) &= \lambda_{q,i}(i_q) \end{aligned} \tag{1.44}$$

where the PM flux linkage with the d–axis is identified with the no–load flux linkage of the same axis: $\Lambda_{mg} = \lambda_d(0)$.

In Fig.1.5 an example of magnetic characteristics is reported. In particular, Fig.1.5(a) shows the flux versus d–axis current, instead in Fig.1.5(b) the flux versus q–axis current is reported. One can note that the d-axis flux is not zero with $i_d = 0$ due to the presence of the PM. Then, the respective value is equal to Λ_{mg}. On the contrary, the q–axis flux is zero for $i_q = 0$ and, in this case, the flux vs current is symmetrical for positive and negative current values i.e. $\lambda_{q,i}(i_q) = -\lambda_{q,i}(-i_q)$.

In presence of iron saturation, the voltages balance becomes[4]:

$$\begin{aligned} u_d(t) &= R_s i_d(t) + \frac{d\lambda_d(i_d(t))}{dt} - \omega_{me}\lambda_q(i_q(t)) \\ u_q(t) &= R_s i_q(t) + \frac{d\lambda_q(i_q(t))}{dt} + \omega_{me}\lambda_d(i_d(t)) \end{aligned} \tag{1.45}$$

Expanding the derivatives it results:

$$\begin{aligned} u_d(t) &= R_s i_d(t) + \tilde{L}_d(i_d)\frac{di_d(t)}{dt} - \omega_{me}L_q(i_q)i_q(t) \\ u_q(t) &= R_s i_q(t) + \tilde{L}_q(i_q)\frac{di_q(t)}{dt} + \omega_{me}L_d(i_d)i_d(t) \end{aligned} \tag{1.46}$$

where $\tilde{L}_d(i_d)$ and $\tilde{L}_q(i_q)$ are the *differential inductances*:

$$\tilde{L}_d(i_d) = \frac{d\lambda_d(i_d)}{di_d} \tag{1.47}$$

$$\tilde{L}_q(i_q) = \frac{d\lambda_q(i_q)}{di_q} \tag{1.48}$$

$$\tag{1.49}$$

---

[4] For seek to simplicity the apex "^{r}" is omitted

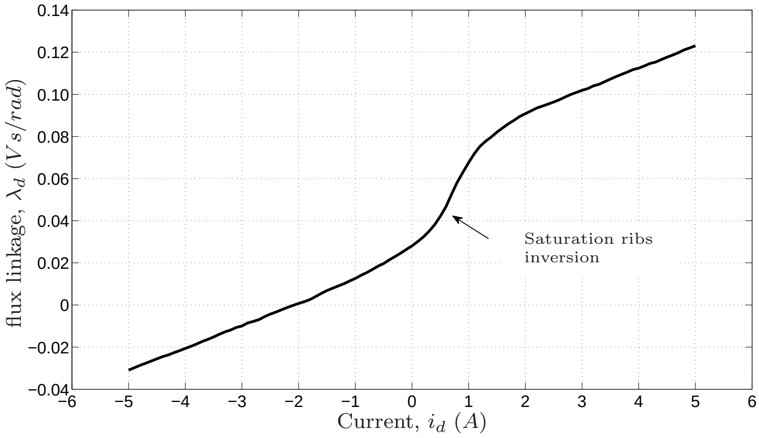

(a) Direct Flux vs. Direct Current

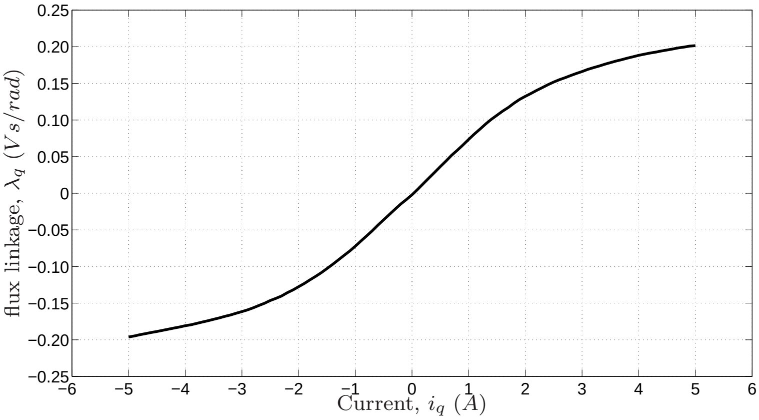

(b) Quadrature Flux vs. Quadrature Current

Figure 1.5: Example of magnet characteristics

that represent the slope of the magnetic characteristic in the point of coordinates i_d and i_q respectively. Instead, $L_d(i_d)$ and $L_q(i_q)$ are the *apparent inductances*:

$$L_d(i_d) = \frac{\lambda_d(i_d) - \Lambda_{mg}}{i_d} \tag{1.50}$$

$$L_q(i_q) = \frac{\lambda_q(i_q)}{i_q} \tag{1.51}$$

that are the slope of the straight line which connects one point of the magnetic characteristic whit the point $(0, \Lambda_{mg})$ or the plane origin respectively. As regards the torque, it can be expressed in this way:

$$m(i_d, i_q) = \frac{3}{2} p[\lambda_d(i_d) i_q - \lambda_q(i_q) i_d] \tag{1.52}$$

Using (1.50) it becomes:

$$m(i_d, i_q) = \frac{3}{2} p\{\Lambda_{mg} i_q + [L_d(i_d) - L_q(i_q)] i_d i_q\} \tag{1.53}$$

1.4.2 Cross saturation

Increasing the iron saturation level and particulary for some rotor configurations, the flux of one axis depends mainly to the respective current and secondly to the current of the other axis (cross saturation effect). Then, one has to write:

$$\begin{aligned} \lambda_d &= \lambda_d(i_d, i_q) \qquad (1.54)\\ \lambda_q &= \lambda_q(i_d, i_q) \qquad (1.55) \end{aligned}$$

Fig.1.6 shows an example of the cross–saturation effects.

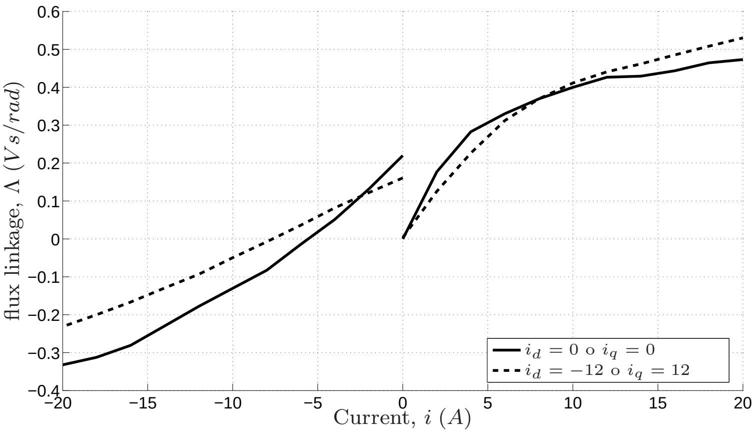

Figure 1.6: Magnetic characteristic in the presence of cross–saturation

The d–axis flux linkage is shown for negative values of the i_d in the left–hand side, with current i_q equal to zero (solid line) and positive (dashed line). In the same way, the q–axis flux is shown in the right–hand side for a positive current i_q and i_d equal to zero (solid line) and negative (dashed line).

The cross saturation is due to the saturation of the magnetic circuit portions common to the d– and q–axis. As matter of fact the saturation of one of this portion due to one current determines the variation of flux in the other axis, even if the the current of the latter remains constant. In this conditions the voltages balance result:

$$\begin{aligned} u_d(t) &= R_s id(t) + \frac{d\lambda_d(i_d(t), i_q(t))}{dt} - \omega_{me}\lambda_q(i_d(t), i_q(t)) \qquad (1.56)\\ &= R_s i_d(t) + \tilde{L}_d(i_d(t), i_q(t))\frac{di_d(t)}{dt} + \tilde{L}_{M_{dq}}(i_d, i_q)\frac{di_q(t)}{dt} - \omega_{me}\lambda_q(i_d(t), i_q(t))\\ u_q(t) &= R_s iq(t) + \frac{d\lambda_q(i_d(t), i_q(t))}{dt} + \omega_{me}\lambda_d(i_d(t), i_q(t)) \qquad (1.57)\\ &= R_s i_q(t) + \tilde{L}_q(i_d(t), i_q(t))\frac{di_q(t)}{dt} + \tilde{L}_{M_{dq}}(i_d, i_q)\frac{di_d(t)}{dt} + \omega_{me}\lambda_d(i_d(t), i_q(t)) \end{aligned}$$

where the *differential inductances* are:

$$\begin{aligned} \tilde{L}_d(i_d, i_q) &= \frac{\partial\lambda_d(i_d, i_q)}{\partial i_d} \qquad (1.58)\\ \tilde{L}_q(i_d, i_q) &= \frac{\partial\lambda_q(i_d, i_q)}{\partial i_q} \qquad (1.59) \end{aligned}$$

and the mutual differential inductances result:

$$\tilde{L}_{M_{dq}}(i_d, i_q) = \frac{\partial \lambda_d(i_d, i_q)}{\partial i_q} = \frac{\partial \lambda_q(i_d, i_q)}{\partial i_d} = \tilde{L}_{M_{qd}}(i_d, i_q) \tag{1.60}$$

in which reciprocity property of mutual inductors is applied. If the rotor has a symmetry respect both the axes, it is also valid:

$$\lambda_d(i_d, i_q) = \lambda_d(i_d, -i_q) = \lambda_d(i_d, |i_q|) \tag{1.61}$$

while it is impossible to apply the dual relation for the current i_d only if the rotor is without the magnet.

1.5 Measures on the PM synchronous motors flux linkages

Relationships as those of Fig.1.5 and 1.6 can be derived during the design or the analysis phase of the machine, exploiting the Finite Element Methods (FEM) or by means of experimental tests. In the following the steady–state operation is assumed, then all the variables are indicated with the capital letters because they are constants in this operating condition. Using a device able to feed the motor with the desired d– and q–axis current values, the characteristics $\Lambda_d(i_d, 0)$ and $\Lambda_q(0, i_q)$ can be obtained applying only the direct or the quadrature current and measuring the the quadrature U_q or direct U_d voltage respectively. To these tests the machine has to be dragged by another motor at a constant speed Ω_{me}. From the voltages U_d and U_q and using the steady–state equations the fluxes result:

$$\begin{aligned} \Lambda_d(I_d, I_q) &= \frac{U_q - R \cdot I_q}{\Omega_{me}} \\ \Lambda_q(I_d, I_q) &= -\frac{U_d - R \cdot I_d}{\Omega_{me}} \end{aligned} \tag{1.62}$$

where the derivatives are equated to zero.

One can note that these equations need the precise knowledge of the stator resistance. Aiming to getting around this trouble, it is possible to perform this measure at two speeds Ω'_{me} and Ω''_{me}, keeping the same currents. By considering the equation of the direct axis voltage at two different speed values, one obtains:

$$\begin{aligned} U'_d &= RI_d - \Lambda_q \Omega'_{me} \\ U''_d &= RI_d - \Lambda_q \Omega''_{me} \end{aligned} \tag{1.63}$$

one can derive the quadrature flux as:

$$\Lambda_q(I_d, I_q) = -\frac{U'_d - U''_d}{\Omega'_{me} - \Omega''_{me}} = -\frac{\Delta U_d}{\Delta \Omega_{me}} \tag{1.64}$$

which is not affected by the resistance.

The measures at both speeds is repeated imposing a current vector with constant d– component while the q–component is varied. For each value of I_d a different q–axis Current–Flux characteristic is obtained.

The same method is valid for deriving the direct flux characteristic. In this case the quadrature current is kept constant and the other component is varied, and results:

$$\Lambda_d(I_d, I_q) = \frac{U'_q - U''_q}{\Omega'_{me} - \Omega''_{me}} = \frac{\Delta U_q}{\Delta \Omega_{me}} \tag{1.65}$$

If the cross saturation is not interesting, these tests can be done varying only the d–axis current and keeping the quadrature one equal to zero and viceversa. In this case (1.62) results:

$$\begin{aligned} \Lambda_d(I_d, 0) &= \frac{U_q \mid_{I_q=0}}{\Omega_{me}} \\ \Lambda_q(0, I_q) &= -\frac{U_d \mid_{I_d=0}}{\Omega_{me}} \end{aligned} \tag{1.66}$$

Being one current equal to zero, there isn't voltage drop on the resistance and then only one set of measurements at one speed different from zero is enough in order to derive the fluxes.

2

Rotor configurations

2.1 Introduction

The stator of the PM synchronous motor is similar to that of an induction motor. Conversely, the rotor can assume different topologies, according to how the PM is placed in the it. The rotors (and thus the motors) are classified in three classes: Interior PM (IPM) motor, Surface–mounted PM (SPM) motor and Inset PM motor (XPM). The three machines are schematized in Fig. 2.1 where the rotor is colored in light–grey, stator in dark–grey and in black are displayed the magnets. Fig. 2.1(a) shows a four–pole and 24 slots IPM motor, whose rotor is characterized by two flux–barriers per pole. The high number of flux–barriers per pole yields a high rotor anisotropy. Both torque components (due to the PMs and to anisotropy) are high, hence the IPM motor exhibits a high torque density and it is well–suited for flux–weakening operations, up to very high speeds.

Fig. 2.1(b) shows a cross–section of a six–pole and 27 slots SPM motor. There are six PMs mounted with alternate polarity on the rotor's surface. Since the PM permeability is close to the air permeability, the rotor is isotropic.

Finally, Fig. 2.1(c) shows a four–pole and 24 slots XPM motor. Its rotor is similar to the SPM rotor, with the difference that there are an iron tooth between each couple of adjacent PMs. As in the SPM motor, the main flux is due to the PMs. The rotor teeth yield a moderate anisotropy and then a little reluctance torque.

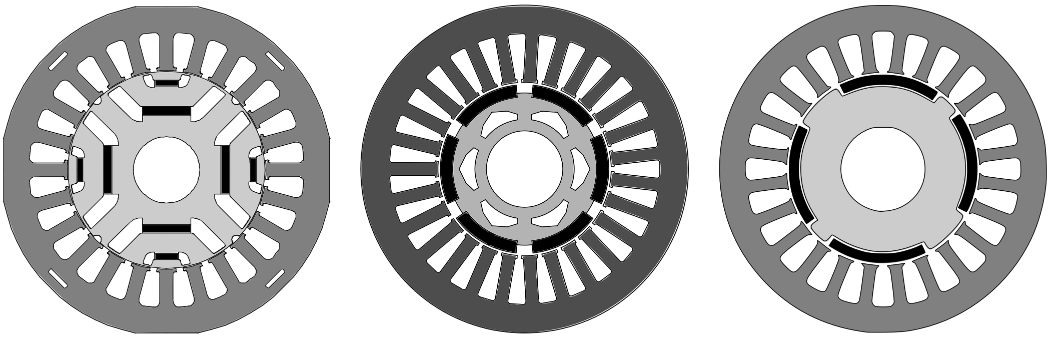

(a) IPM motor (b) SPM motor (c) XPM motor

Figure 2.1: PM rotor configurations

Hereafter, for all the machine the rotor reference frame can be represented by the d– and the q–axis. The d–axis is chosen as the PM flux axis and the q–axis leads the

d–axis of $\pi/2$ electrical radians.

In this chapter the descriptions and electrical equations of the three rotor topologies are reported. The rotor electromagnetic behaviour is studied by means of Finite Element Simulations (FEM).

2.2 IPM Motor

2.2.1 Introduction on the IPM motor

In the IPM machine the magnets are placed inside the rotor[1]. Two schematic representations of 4–pole rotor structure are reported in Fig. 2.2. Magnets are represented with grey color rectangles and the magnetization verse is indicated by the colored arrows. The magnets determine in the rotor's surface two polarities: north (N) and south (S). In Fig. 2.2 a couple of orthogonal axes in terms of electrical degree are also shown[1]: the *polar axis* (d–axis) and the *inter–polar axis* (q–axis). According to the magnetization direction of the PMs, the IPM can be distinguished in:

- *tangentially magnetized PMs*, as in Fig. 2.2(a)
- *radially magnetized PMs*, as in Fig. 2.2(b)

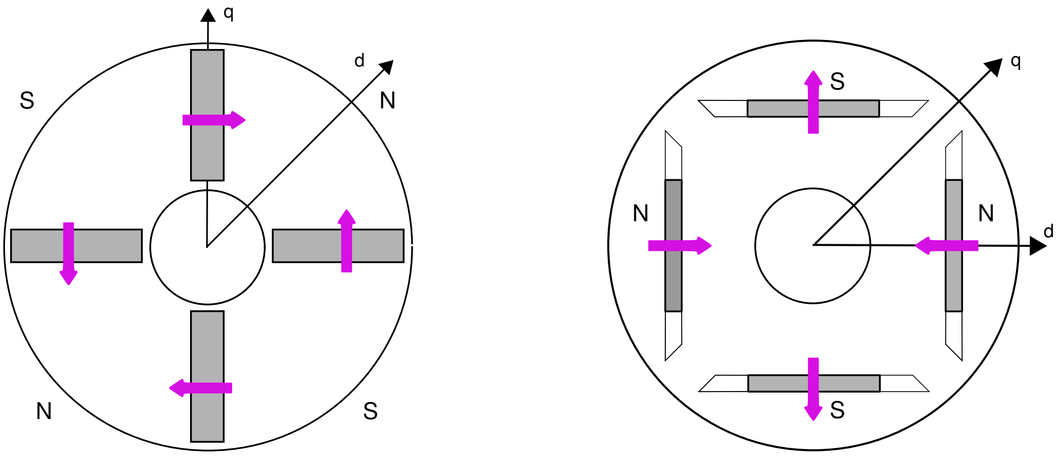

(a) Tangential magnetization

(b) Radial magnetization

Figure 2.2: Schematic representations of 4–pole IPM rotors

In this section an IPM machine of the type of Fig. 2.1(a) is taken in consideration. Its photo is reported in Fig. 2.3. This configuration is called "two barriers" because there are two flux barriers containing the magnets. In the figure one can note the air barriers.

Imposing a current along only the d-axis, the magnetic field is along the direct axis i.e. the polar axis. Then, the magnetic circuit due to the i_d current includes the

---

[1] Being the pole–pair equal to 2, the geometric angle between the d– and q–axis is equal to $\pi/4$ *rad*.

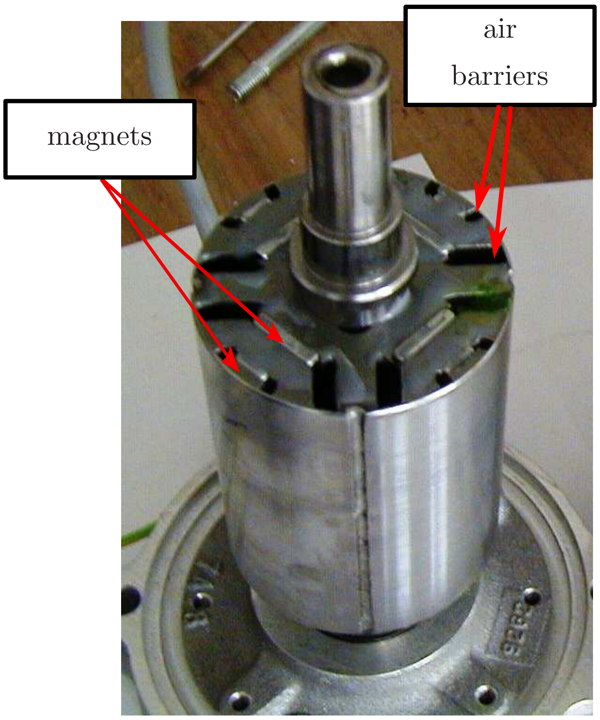

Figure 2.3: Photo of an IPM rotor

permanent magnets, according to the arrows in the Fig. 2.4(a). On the contrary, the quadrature current i_q produces a magnetic field along the q-axis. Consequently the magnetic circuit doesn't include the permanent magnets, but it follows the arrows of Fig. 2.4(b).

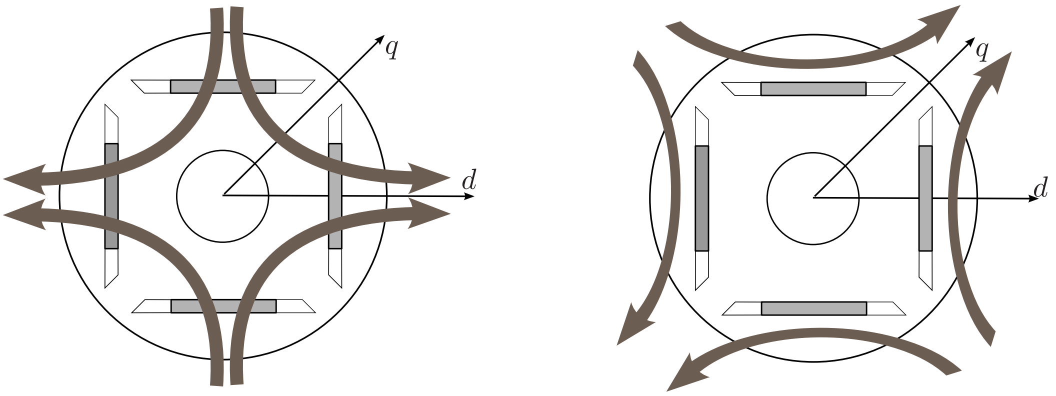

(a) d–axis magnetic flux

(b) q–axis magnetic flux

Figure 2.4: Magnetic flux path according to the direct and quadrature axes in the 4–pole IPM rotor

Using the (1.8), (1.9) and (1.39) the direct and quadrature inductances can be rewritten as follow:

$$L_d = L_\sigma + \frac{3}{2}N^2\frac{1}{\Re_d} \tag{2.1}$$

$$L_q = L_\sigma + \frac{3}{2}N^2\frac{1}{\Re_q} \tag{2.2}$$

As reported previously, the d-axis magnetic circuit includes the magnets; from the magnetic circuit point of view, are as the air. Then the equivalent air gap along the d–axis is greater than that of the q–axis, i.e. the d–axis reluctance $\Re_d$ is greater than the q-axis one $\Re_q$.

Consequently, the two inductances L_d and L_q are different due to the different respective reluctances. In particular for all the rotors of Fig. 2.2 it results $L_d < L_q$.

An important machine parameter is the *saliency ratio* ξ, that is defined as

$$\xi = \frac{L_q}{L_d} \tag{2.3}$$

This parameter gives an idea of the anisotropy degree of the machine and for the IPM machine it is greater than 1. The configuration of Fig. 2.2(b) has the particularity to allow saliency ratio up to a value of $2 \div 4$.

2.2.2 Equations in the dq reference frame

In the case of the IPM motors the voltage balance in the rotor reference frame are those reported in (1.40):

$$\begin{aligned} u_d &= R_s i_d + L_d\frac{di_d}{dt} - \omega_{me}L_q i_q \\ u_q &= R_s i_q + L_q\frac{di_q}{dt} + \omega_{me}L_d i_d + \omega_{me}\Lambda_{mg} \end{aligned} \tag{2.4}$$

and the torque is given by:

$$m = \frac{3}{2}p\Lambda_{mg}i_q + \frac{3}{2}p(L_d - L_q)i_d i_q \tag{2.5}$$

that, using (2.3), can be rewritten in:

$$m = \frac{3}{2}pL_d\left[\frac{\Lambda_{mg}}{L_d}i_q - \frac{3}{2}p(\xi - 1)i_d i_q\right] \tag{2.6}$$

The torque is given by the sum of two terms. First term is the torque due to the PM flux and it is independent of i_d and directly proportional to the quadrature current i_q. One can note that the ratio Λ_{mg}/L_d is the equivalent d–axis current that zeroes the magnet's flux. The second term is the reluctance torque due to the rotor anisotropy. It is proportional to both i_d and i_q and to the difference inductance $(L_q - L_d)$ (in other words to the saliency ratio ξ).

Finally from the (2.4), (2.5) and (1.43) the block diagram of the IPM motor is that of Fig. 2.5.

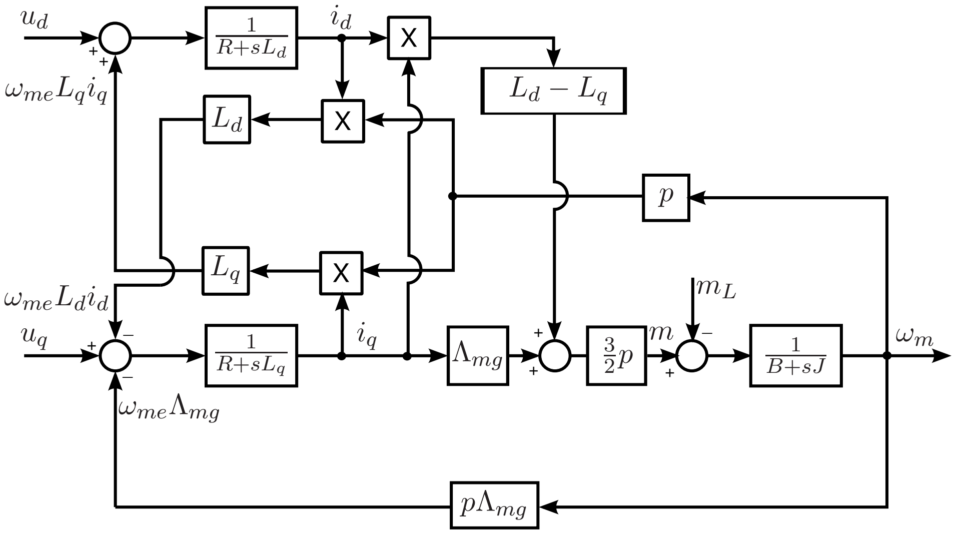

Figure 2.5: Block scheme of the IPM motor

2.2.3 FEM analysis

The machine magnetic analysis of the can be made by FEM simulations. Fig. 2.6 shows the geometry of 24 slots and 2 pole–pairs IPM motor. For convenience, it is drawn with the *d*–axis (i.e. the PM magnetization axis) along the phase *a*–axis.

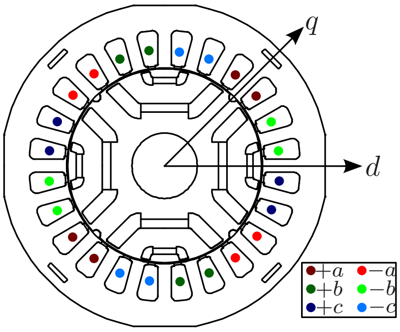

Figure 2.6: Geometry of the IPM motor

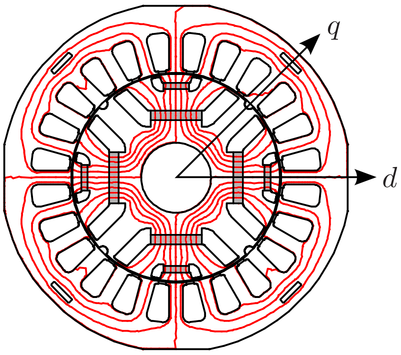

Figure 2.7: IPM motor:flux lines due to the magnets

Tab. 2.1 reports the motor geometry parameter, instead the electrical data are reported in Tab. 2.2.

First simulations have been done at no load, i.e. the *d*– and *q*–axis currents are fixed to zero. Fig. 2.7 shows the flux lines due to the PMs only. The flux is linked by each stator winding and varies with the rotor position. Phase *a* links the maximum flux that is equal to the magnet flux Λ_{mg}, being phase *a* aligned with *d*–axis.

Fig. 2.8 shows two different simulations according to the axis that's excited. In Fig. 2.8(a) a positive current imposed along only the *d*–axis produces a flux along the same *d*–axis. In order to get only the flux due to the current, the PMs de–energized in the model. A positive current is magnetizing, that is increasing the flux produced by

Table 2.1: Motor geometry

Stator inner diameter	D_i	$60\ mm$
Stator external diameter	D_e	$110\ mm$
Air gap	g	$0.35\ mm$
Stack length	L_{stk}	$40\ mm$
Slot number	Q	24
Pole number	$2p$	4

Table 2.2: Motor electric parameters

Phase to phase resistance	R_s	$9.7\ \Omega$
Nominal current	I_N	$3.9\ Arms$
Nominal torque	M_N	$2.4\ Nm$
Nominal voltage	U_N	$230\ Vrms$
Nominal speed	n	$4000\ rpm$
Power	P	$1\ kW$
Back electromotive force	EMF	$19.9\ V/krpm$

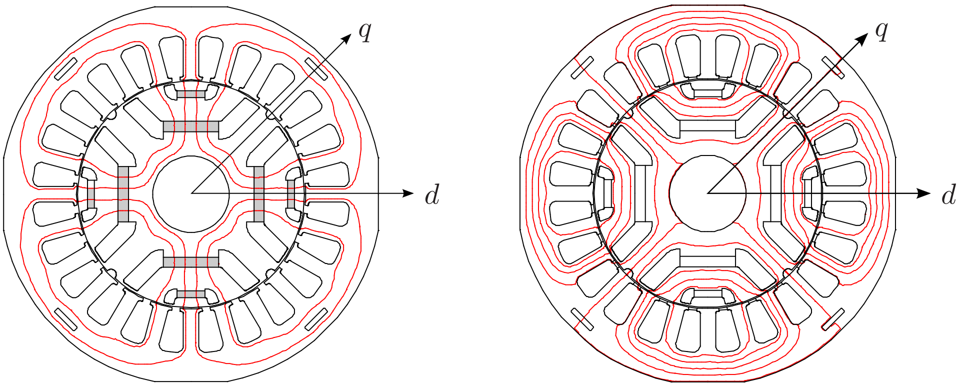

(a) Simulation with only d–axis current (b) Simulation with only q–axis current

Figure 2.8: FEM model of the IPM motor

the PM. On the contrary, negative d–axis current is demagnetizing, since it weakens the PM flux.

The flux–lines crosses the PMs, increasing the magnetic reluctance along the d–axis as described in Sec. 2.2.1. The analytical estimation of d–axis inductance L_d depends on the geometry of the rotor.

Conversely, simulation of Fig. 2.8(b) is made imposing a current only in the q–axis. In this case, the flux–lines go through the rotor without crossing the magnets. This means that the magnet does not obstruct the q–axis flux so that the q–axis inductance L_q assumes a high value. Then the d–axis inductance L_d results lower than L_q.

The flux linked from the d–axis ($\lambda_d(i_d, i_q)$) and q–axis ($\lambda_q(i_d, i_q)$) can be plotted exploiting again the FEM analysis. Flux λ_d is obtained imposing a fixed i_q current and changing the i_d. For different value of q–axis current a different flux curves are obtained. Fig. 2.9 shows the d–axis flux linkage vs. d–axis current, for five values of the current i_q. The figure points out the cross–coupling phenomena described in Sec. 1.4.2. For currents close to the nominal one, the flux increases with the increase of i_q in the right–hand quadrant and the flux decreases with the increase of i_q in the left–hand quadrant.

The flux obtained with i_d and i_q equal to zero is equivalent to the PM flux Λ_{mg}. Around d–axis current of 2–3 $Amps$, it is possibile to note the inversion of the ribs saturation. Curves given by negative value of i_q are not reported because it is valid the (1.61) for the symmetry of the rotor.

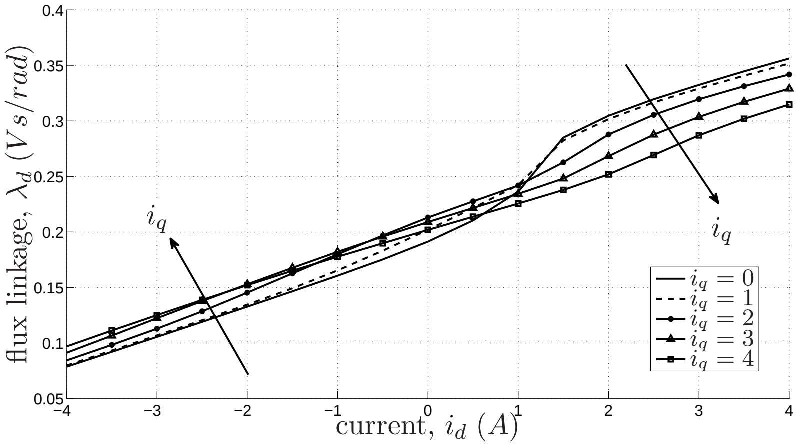

Figure 2.9: Simulated d–axis flux linkage characteristics of IPM motor

Taking the curves λ_d and λ_q (for i_q and i_d equal to zero respectively) it is possible to derive from their slope the d– and q–axis inductance values. In order to neglect the saturation effects, the inductances can be derived taking into consideration only the linear part of the curves, i.e. for small values of currents.

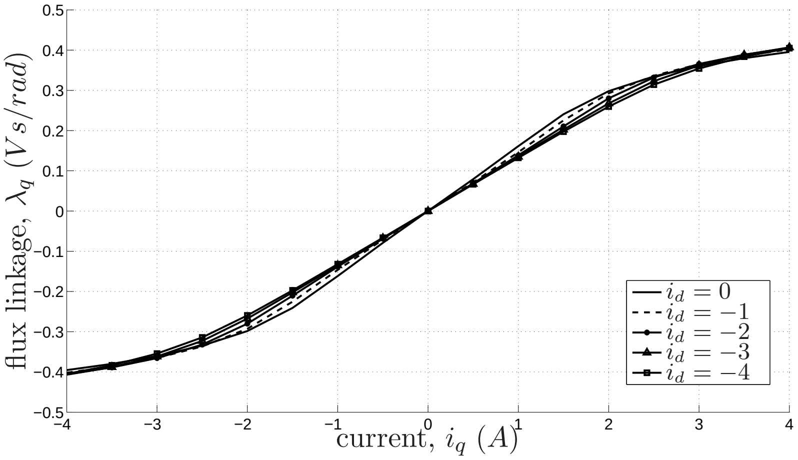

Figure 2.10: Simulated q–axis flux linkage characteristics of IPM motor

2.3 SPM Motor

In the SPM machine the magnets are mounted on the rotor surface as reported in Fig. 2.11. The magnets, that are represented with grey color rectangles, determine in the rotor surface two polarity: north (N) and south (S). The rotor has 2–pole pairs, then the d– and q–axis are displaced of $\pi/4$ (i.e. $\pi/2$ electrical degree).

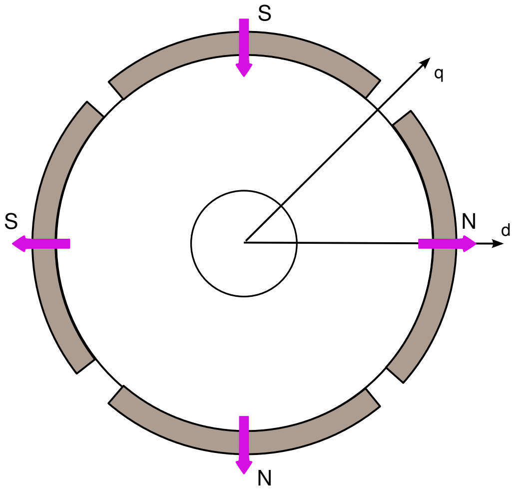

Figure 2.11: Schematic representations of 4–pole isotropic rotors

A photo of a SPM rotor is reported in Fig. 2.12. One can note that each pole is made by three PM tiles. Imposing a current along only the d-axis, the generated magnetic field is along the direct axis i.e. the polar axis. Then, the magnetic circuit due to the i_d current includes the permanent magnets, according to the arrows in the Fig. 2.13(a). Differently than the IPM case, the magnetic circuit due to the i_q includes also the permanent magnets as shown Fig. 2.13(b).

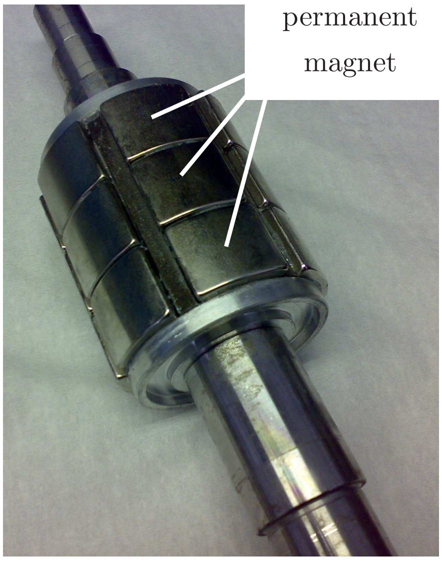

Figure 2.12: Photo of an SPM rotor

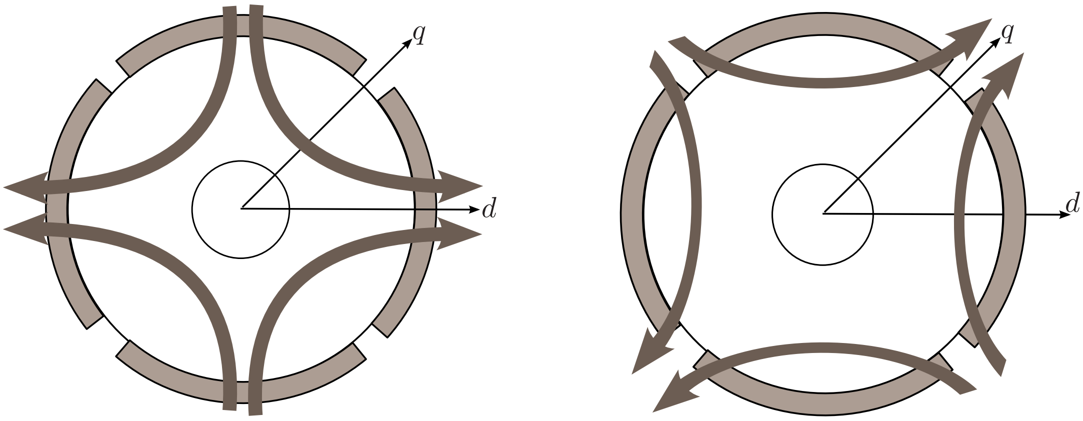

(a) d–axis magnetic flux (b) q–axis magnetic flux

Figure 2.13: Magnetic flux path according to the direct and quadrature axes in the 4–pole SPM rotor

Then the reluctance $\Re_d$ and $\Re_q$ along the d– and q–axes are equals. From (1.8), (1.9) results:

$$\Re_d = \Re_q = \Re \tag{2.7}$$

$$L_0 = N^2 \frac{1}{\Re} \tag{2.8}$$

$$L_2 = 0 \tag{2.9}$$

The sinusoidal terms in the (1.7) and (1.10) disappears, then the direct and quadrature inductances can be rewritten as follow:

$$L_d = L_\sigma + L_0 = L_\sigma + \frac{3}{2} N^2 \frac{1}{\Re} \tag{2.10}$$

$$L_q = L_\sigma + L_0 = L_\sigma + \frac{3}{2} N^2 \frac{1}{\Re} \tag{2.11}$$

$$L_d = L_q = L_s \tag{2.12}$$

One can note that the two inductances L_d and L_q are equal, this is the main peculiarity that distinguishes the isotropic motor from the anisotropic one.

2.3.1 Equations in the dq reference frame

In the case of the SPM motors, substituting (2.12) in (1.40), the voltage balance in the rotor reference frame becomes:

$$\begin{aligned} u_d &= Ri_d + L\frac{di_d}{dt} - \omega_{me} L i_q \\ u_q &= Ri_q + L\frac{di_q}{dt} + \omega_{me} L i_d + \omega_{me}\Lambda_{mg} \end{aligned} \tag{2.13}$$

and the torque is given by:

$$m = \frac{3}{2} p \Lambda_{mg} i_q \tag{2.14}$$

In the case of SPM motor the torque is due only to the PM flux and it is independent of i_d. Finally from the (2.13), (2.14) and (1.43) the block scheme of the SPM motor results that of Fig. 2.14.

2.3.2 FEM analysis

As made in the case of IPM motor, the SPM machine can be studied by means of the FEM simulations. A 3 pole–pairs SPM machine is taken into consideration, which FEM model is reported in Fig. 2.15. The main data of the motor geometry are reported in Tab. 2.3, and the electrical parameters are reported in Tab. 2.4.

Fig. 2.15 shows the geometry a 27 slots and 3 pole–pairs SPM motor. Direct axis is posed along the a–phase, while the q–axis is displaced of 90 electrical degree i.e. 30 mechanical degree.

The flux–lines due only to the PMs are shown in Fig. 2.16. Fig. 2.17(a) shows the flux plot due to the d–axis current only (i.e., without PMs). The synchronous inductance is computed by dividing the d–axis flux linkage (achieved by means of the abc–to–dq transformation) by the d–axis current.

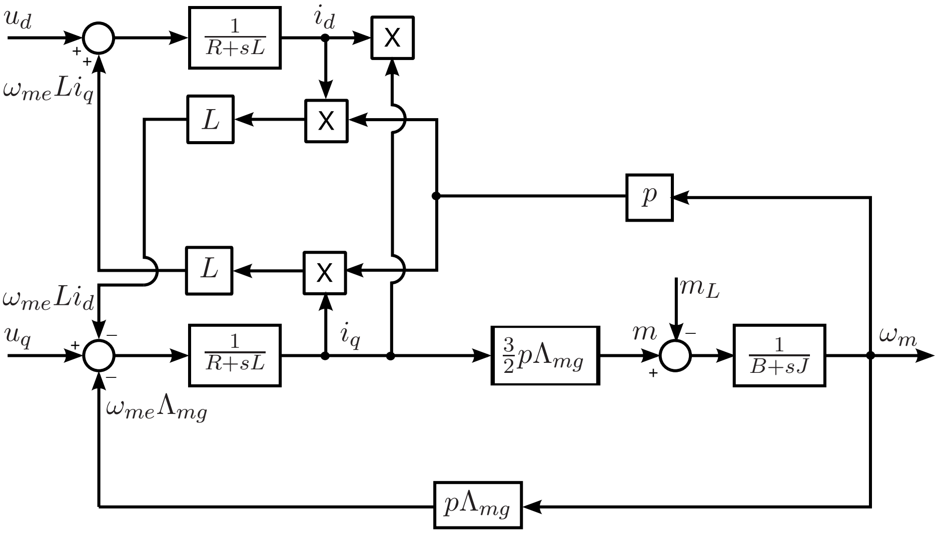

Figure 2.14: Block diagram of the SPM motor

Table 2.3: Motor geometry

Stator inner diameter	D_i	63.5 mm
Stator external diameter	D_e	120 mm
Air gap	g	0.9 mm
Stack length	L_{stk}	63 mm
Slot number	Q	27
Pole number	$2p$	6

Table 2.4: Motor electric parameters

Phase to phase resistance	R_s	1.12 Ω
Nominal current	I_N	8.51 $Arms$
Nominal torque	M_N	7.5 Nm
Nominal voltage	U_N	205 $Vrms$
Nominal speed	n	3000 rpm
Power	P	$-$ kW
Back electromotive force	EMF	60.5 $V/krpm$

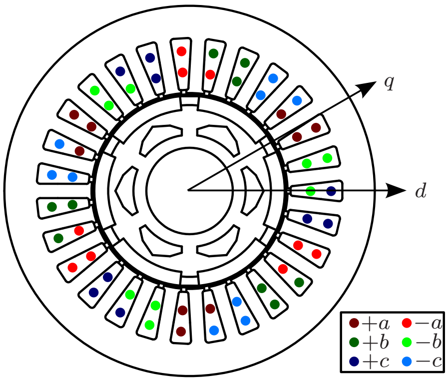

Figure 2.15: Geometry of the SPM motor

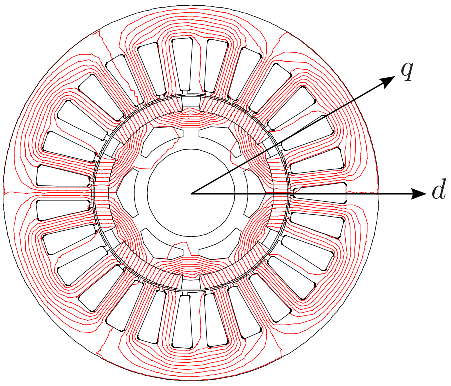

Figure 2.16: SPM motor:flux lines due to the magnets

Fig. 2.17(b) shows the flux–lines due to the q–axis current only. From the figure it is noticing that the effect of the q–axis current is to increase the flux density in half a pole, and to decrease the flux density in the other half. Being the PM permeability similar to the air permeability μ_0, in the SPM motor the q–axis inductance is practically the same of the d–axis inductance.

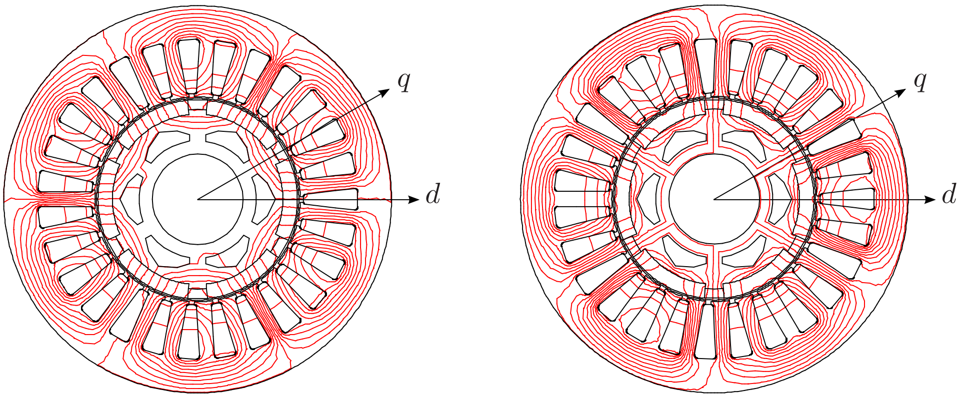

(a) Simulation with only d–axis current

(b) Simulation with only q–axis current

Figure 2.17: FEM model of the SPM motor

This fact is pointed out by the Fig. 2.18 and Fig. 2.19. In the first the d–axis flux linkages vs. the d–axis current, for different i_q values, are shown. In the second one the q–axis flux linkages vs. q–axis current, for different i_d values, are reported. Taking the curves $\lambda_d(i_d, 0)$ and $\lambda_q(0, i_q)$ into consideration, it is possible to note that both have the same slope that confirms the equality of the two axes inductances.

The saturation and cross–saturation have less effects than in the IPM motor.

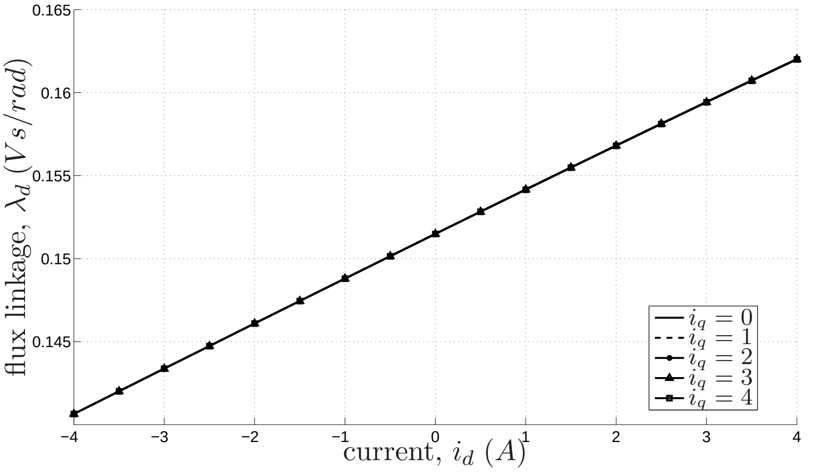

Figure 2.18: Simulated d–axis flux linkage characteristics of SPM motor

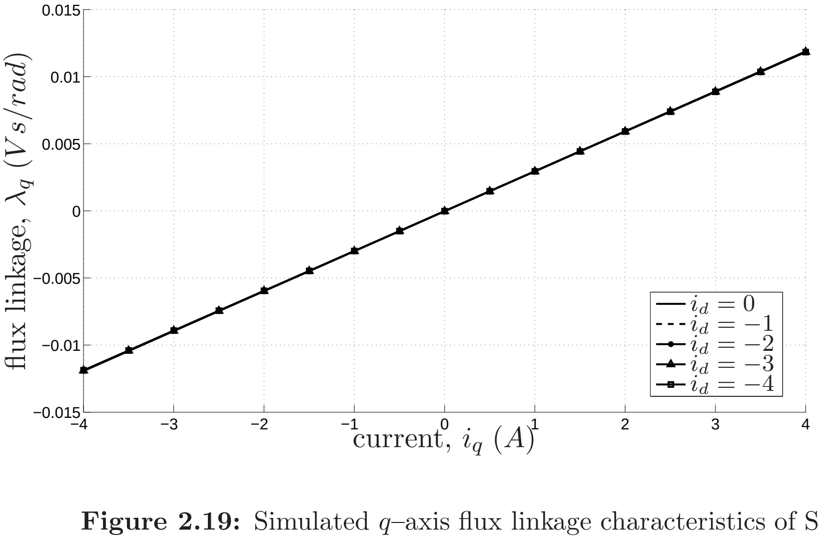

Figure 2.19: Simulated q–axis flux linkage characteristics of SPM motor

2.4 Inset Motor

In order to attain an anisotropic magnetic behaviour of the rotor, the IPM configuration is not the unique solution. In particular there are other types of machines that can present an anisotropy rotor. One of those is the inset motor[2] (here denoted as XPM motor). The XPM rotor is similar to a surface–mounted PM (SPM) rotor, but between each couple of adjacent PMs there is an iron tooth. As in the SPM motor the main flux is due to the PMs placed on the rotor surface. In addition, the rotor teeth cause a rotor saliency. However the achievable unsaturated saliency ratio is quite low (about 2 to 3) and thus the contribution to the torque is limited. The tooth width is generally not optimized in order to increase the torque, but it is more conveniently designed to minimize the torque ripple or to obtain a positive incremental saliency ratio, even at high currents.

A sketch of the XPM motor is reported in Fig. 2.1(c). It is possible to note in the rotor, colored in grey light, the iron tooth between each couple of magnets. The magnets are not posed equidistant from each other for a design choice.

A photo of the rotor is reported in Fig. 2.20. The figure highlights the presence of the iron tooth between two adjacent poles and the rotor skewing for the torque ripple reduction.

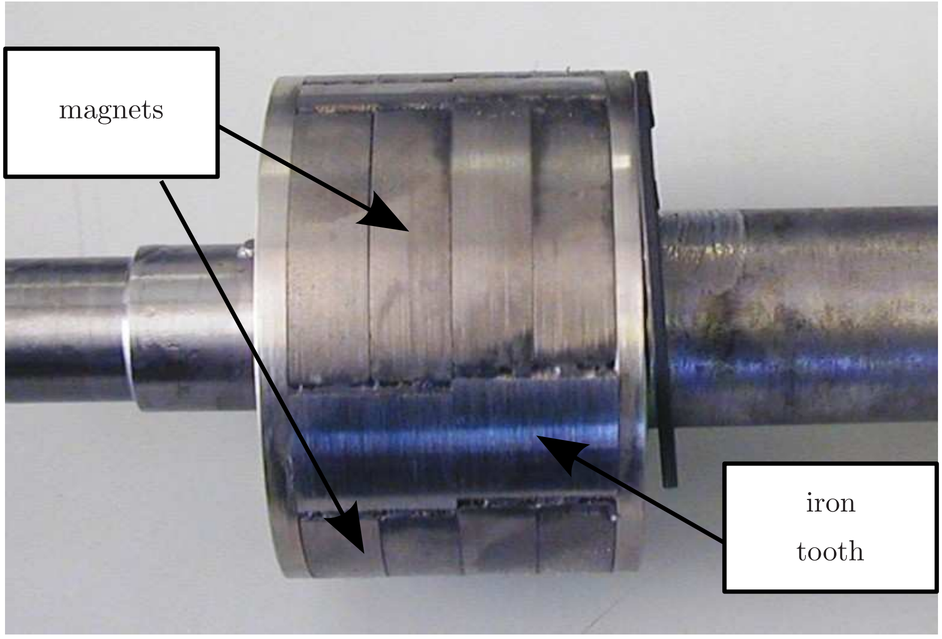

Figure 2.20: Photo of an XPM rotor

Having an anisotropic rotor behaviour, the same considerations made for the IPM motor can be applied to the XPM motor. As far as the inductances are concerned, the d–axis inductance L_d is lower than the q–axis inductance L_q. Then the (2.4) and (2.5) are stiil valid. Consequently, the motor scheme results that of Fig. 2.5.

2.4.1 FEM analysis

For the FEM analysis the two pair–poles XPM motor of Fig. 2.1(c) is taken into consideration. Tab. 2.5 reports the motor geometry parameter, instead the electrical data are reported in Tab. 2.6.

Table 2.5: Motor geometry

Stator inner diameter	D_i	66 mm
Stator external diameter	D_e	110 mm
Air gap	g	0.35 mm
Stack length	L_{stk}	40 mm
Slot number	Q	24
Pole number	$2p$	4

Table 2.6: Motor electric parameters

Phase to phase resistance	R_s	Ω
Nominal current	I_N	5 $Arms$
Nominal torque	M_N	$-$ Nm
Nominal voltage	U_N	$-$ $Vrms$
Nominal speed	n	$-$ rpm
Power	P	$-$ kW
Back electromotive force	EMF	$-$ $V/krpm$

Fig. 2.21 shows the geometry of 24 slots and 4 pole–pairs XPM motor. Direct axis is posed along the a–phase, while the q–axis is displaced of 90 electrical degree i.e. 45 mechanical degree.

Flux lines due to magnets only are reported in Fig. 2.22. A similar flux linkage is obtained imposing a current along the only d–axis, without consider the PMs effects, as pointed out in Fig. 2.23(a). Fig. 2.23(b), instead, reports the flux–lines due only to the q–axis current. One can note that the flux path are similar to that of the SPM machine (Fig. 2.17(b)), but in this case there is in addition an iron tooth which decreases the q–axis reluctance. Therefore, the inductance L_q results greater than L_d.

Finally, flux–linkage of the d–axis vs i_d and of the q–axis vs i_q are plotted in Fig. 2.24 and Fig. 2.25 respectively. Current i_d doesn't influenced very much the q–axis flux, as shown in Fig. 2.25. On the contrary the d–axis flux is influence by i_q (Fig. 2.24), in particular in the right–hand quadrant.

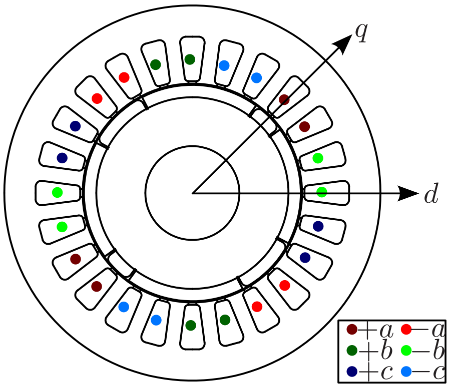

Figure 2.21: Geometry of the XPM motor

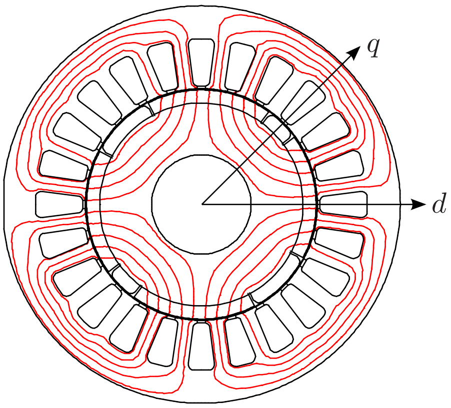

Figure 2.22: XPM motor:flux lines due to the magnets

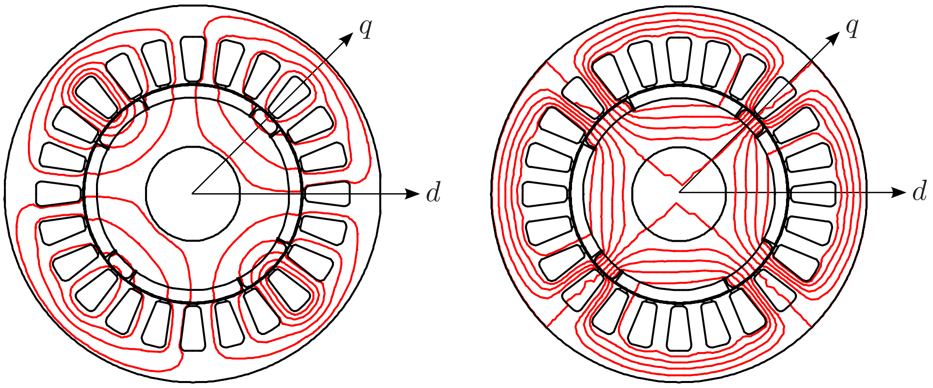

(a) Simulation with only d–axis current (b) Simulation with only q–axis current

Figure 2.23: FEM model of the XPM motor

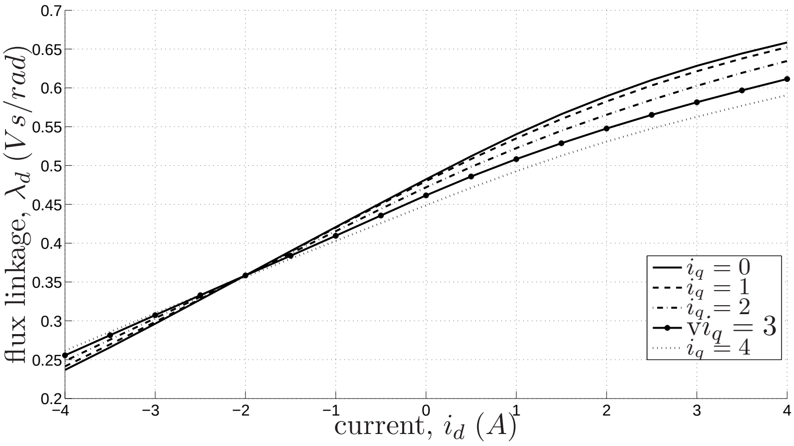

Figure 2.24: Simulated d–axis flux linkage characteristics of XPM motor

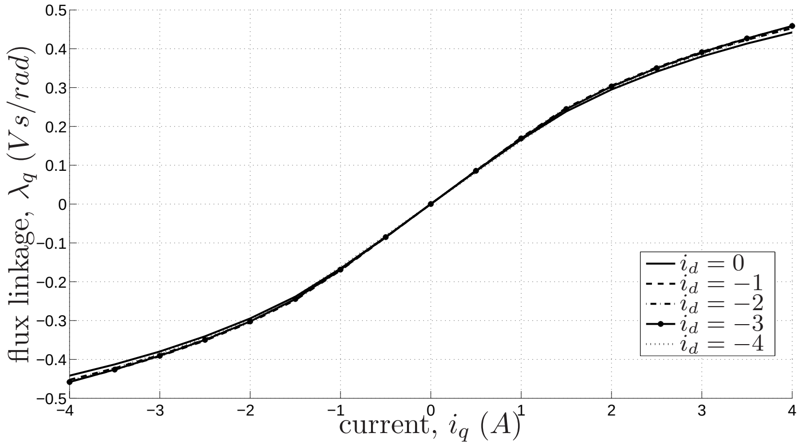

Figure 2.25: Simulated q–axis flux linkage characteristics of XPM motor

3

Sensorless Drive with PM Synchronous Machines

3.1 Sensorless Drive classification

The general scheme of a PM motor drive is shown in Fig. 3.1. The grey block represents the control system, while in the other blocks are reported: the inverter (as regard the power stage), the PM Synchronous Motor (PMSM), the currents measures and the absolute position θ_m transducers (encoder or resolver).

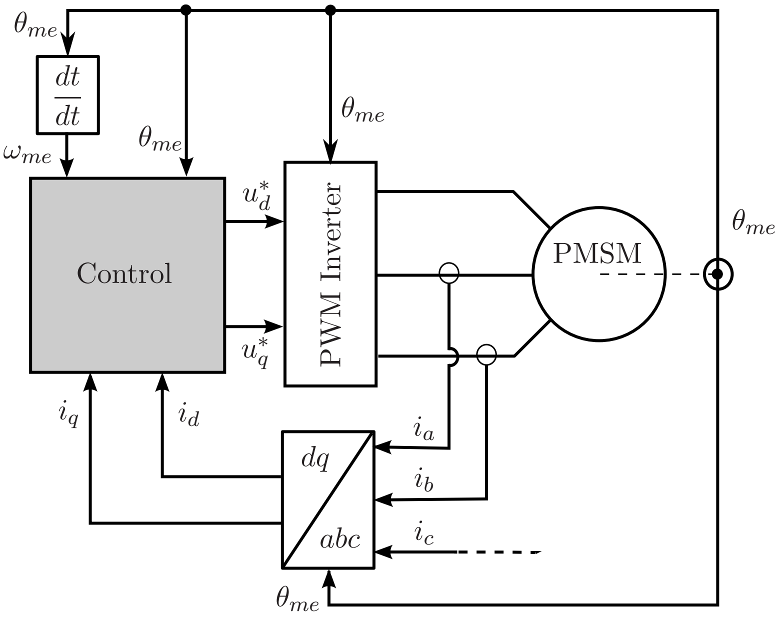

Figure 3.1: General Scheme of the PMSM drive

In order to control the machine in the rotor reference frame, the drive needs the knowledge of the electric position θ_{me} (and thus the mechanical position θ_m) for the current transformation from the stator to the rotor reference frame. Moreover, from the position derivative it is possible to obtain the mechanical speed ω_m for a possible speed control. The presence of the position transducer constitutes a drawback in terms of costs, space, maintenance and reliability.

Then, in order to avoid these disadvantages, the sensorless solution is taken into consideration. The sensorless drives allow the machine control without the use of the position transducer, estimating the rotor position (and consequently the speed) by means of particular estimation algorithms. Tab. 3.1 reports a classification of the main sensorless solutions, classified according to the rotor structure and the operating speed range.

Table 3.1: Classification of the sensorless algorithms

	Low and zero speed (Position sensorless drive)	High speed (Speed sensorless drive)
Isotropic Rotor	• In principle there aren't sensorless solutions • Possible techniques with special rotor structure (saturated rotor, ringed–pole, inset)	• Estimator based on the fundamental equations of the motor (open–loop or closed–loop estimator, observers, Kalman Filter,...)
Anisotropic Rotor	• Estimation based on the identification of the rotor anisotropy (high frequency voltage or current injection on the stator windings)	• Estimator based on the fundamental equations of the motor (open–loop or closed–loop estimator, observers, Kalman Filter,...) • Estimation based on the identification of the rotor anisotropy

On the following, two of these solutions will be illustrated. In particular the *MRAS estimator* in the high speed region and the estimation exploiting the anisotropy of the rotor in the low speed region.

3.2 MRAS Estimator

The Model Reference Adaptive Systems (MRAS) electric position estimation technique consists on calculating a motor variable $\bar{g}$, e.g. the flux vector or the back electromotive force, starting from the knowledge of the voltages and currents.

To this purpose, two different models are used: the *Reference Model* and the *Adaptive Model*. The results of the first model $\bar{g}$ is independent of the electric position θ_{me}; the results of the second model $\tilde{g}(\theta)$, instead, depends on θ_{me}. A difference between the two results highlights an erroneous value of the estimated position $\tilde{\theta}_{me}$ assumed by the adaptive model, neglecting or removing any other cause of error (e.g. measure error, parameter error, etc.). An adjustment mechanism can correct the estimation, as long as it coincides to the actual one. The estimator principle scheme is shown in Fig. 3.2.

On the following, an estimator for an isotropic motor (SPM machine) is described. The flux–linkage vector $\tilde{\lambda}_{mg}$, due to the PMs, is assumed as estimated variable $\tilde{g}$. The reference model can be described starting from the voltage balance equation in the stator reference frame:

$$\bar{u}^s = R_s\bar{i}^s + L_s\frac{d\bar{i}^s}{dt} + \frac{d\lambda^s_{mg}}{dt} \tag{3.1}$$

Measuring the currents and using the reference voltages, the flux–linkage vector can be computed by:

$$\bar{\lambda}^s_{mg} = \bar{\lambda}^s_{mg}(0) + \int_0^t (\bar{u}^s - R_s\bar{i}^s)dt - L_s\bar{i}^s \tag{3.2}$$

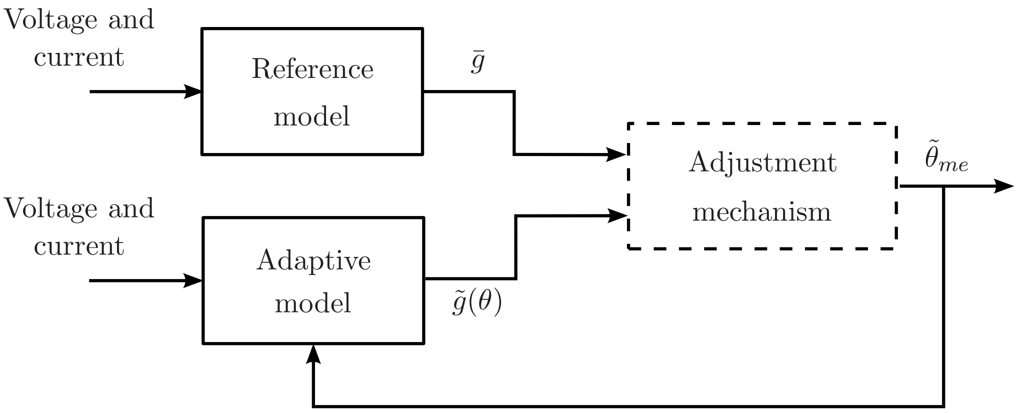

Figure 3.2: Principle scheme of the MRAS estimator

One can note that this quantity is obtained without the knowledge of the electrical position.

On the contrary, the adaptive model depends on the estimated position in this way:

$$\bar{\lambda}^s_{mg}(\tilde{\theta}_{me}) = \Lambda_{mg} e^{j\tilde{\theta}_{me}} \tag{3.3}$$

that requires no measurement.

The displacement between the two vectors (3.2) and (3.3) can be assumed as estimation error. In order to obtain this displacement, the following expression can be used:

$$\begin{aligned} \epsilon_\lambda &= Im(\bar{\lambda}^s_{mg}\check{\bar{\lambda}}^s_{mg}(\tilde{\theta}_{me}) \\ &= |\bar{\lambda}^s_{mg}||\check{\bar{\lambda}}^s_{mg}(\tilde{\theta}_{me})| \sin(\theta_{me} - \tilde{\theta}_{me}) = \\ &= -|\bar{\lambda}^s_{mg}||\check{\bar{\lambda}}^s_{mg}(\tilde{\theta}_{me})| \sin(\Delta\theta) \end{aligned} \tag{3.4}$$

where

$$\Delta\theta = \tilde{\theta}_{me} - \theta_{me} \tag{3.5}$$

The imaginary part, divided by $|\bar{\lambda}^s_{mg}||\check{\bar{\lambda}}^s_{mg}(\tilde{\theta}_{me})|$, provides the sine of the estimation error $\Delta\theta$. For $\Delta\theta$ sufficiently small, the approximation $\sin(\Delta\theta) = \Delta\theta$ is valid and then the estimation error is about $-\Delta\theta$. The adjustment mechanism brings to zero this error: this means that the estimated position coincides with the actual one. To this purpose a PI regulator is used as shown in Fig. 3.3. The regulator delivers as output the estimated speed $\tilde{\omega}_{me}$ and, by its integration, the estimated electric position.

The need of the integrator after the PI can be justified by the fact that, at steady–state operation, the speed is constant and then the position is a ramp. In order to have a steady–state null error against a ramp input, the adjustment mechanism can contain a PI regulator followed by an integrator, so as to have a system of second type. Similar solution can be developed with the back emf as estimated quantity. It will be described in Chapter 4 together to its implementation.

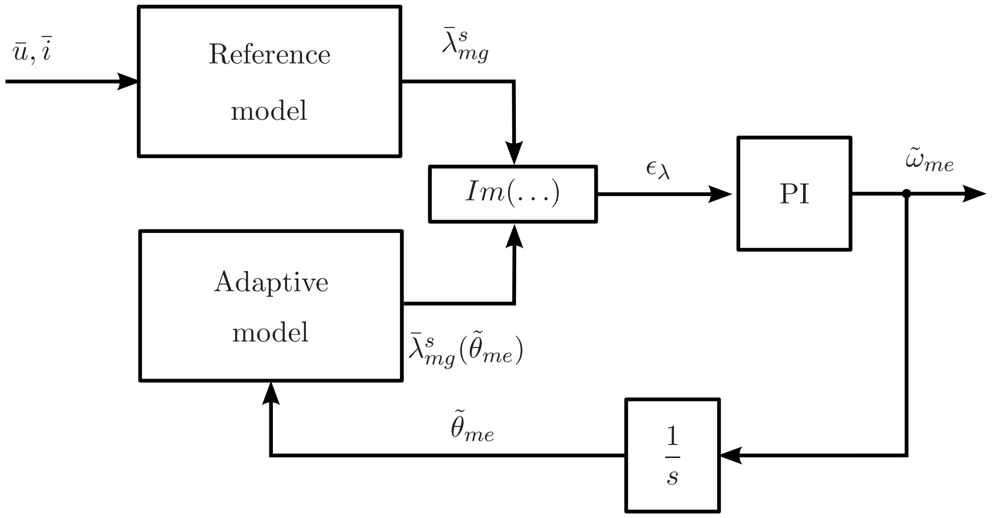

Figure 3.3: Block scheme of the MRAS estimator

3.3 Estimation with high frequency voltage injection

3.3.1 Essential of the technique

Rotor position sensorless techniques used in salient–pole PM synchronous motor drives utilize additional small value high frequency voltages to recognize the position of the anisotropic rotors also at low or zero speed.

The motor is controlled in a generic two–axis reference frame d^x, q^x, whose position θ^s_x is taken with respect to the stator. In the d^x, q^x reference frame, that rotates at the speed ω_x, the spatial vector stator equation can be written as:

$$\bar{u}^x = R\bar{i}^x + \frac{d\bar{\lambda}^x}{dt} + j\omega_x\bar{\lambda}_x \tag{3.6}$$

that is valid for both the anisotropic and the isotropic rotors.

Considering an anisotropic machine, in the rotating reference frame $d-q$ and considering small signal around a given operating point, according to Sec. 1.4.2, the flux can be expressed as follow[1]:

$$\begin{aligned}[\lambda] &= \begin{bmatrix} \lambda_d \\ \lambda_q \end{bmatrix} = \begin{bmatrix} l_d & l_M \\ l_M & l_q \end{bmatrix} \begin{bmatrix} i_d \\ i_q \end{bmatrix} + \begin{bmatrix} \lambda_{mg} \\ 0 \end{bmatrix} \\ &= \underbrace{\begin{bmatrix} l_d & 0 \\ 0 & l_q \end{bmatrix}}_{[l]} \begin{bmatrix} i_d \\ i_q \end{bmatrix} + \underbrace{\begin{bmatrix} 0 & l_m \\ l_m & 0 \end{bmatrix}}_{[l_M]} \begin{bmatrix} i_d \\ i_q \end{bmatrix} + \underbrace{\begin{bmatrix} \lambda_{mg} \\ 0 \end{bmatrix}}_{[\lambda_{mg}]}\end{aligned} \tag{3.7}$$

The flux–linkage vector can be defined in the reference system $d^x - q^x$ applying the transformation:

$$\bar{g} = \bar{g}^x e^{j(\tilde{\theta}_{me} - \theta_{me})} = \bar{g}^x e^{j\Delta\theta} \tag{3.8}$$

---

[1] Having the machine a non linear magnetic behaviour, all the variables are written in lower case denoting differential inductance values and small signal currents and fluxes.

or in other form

$$\begin{aligned}
[g] &= [T_{dq/\alpha\beta}]\,[g^x] \\
\left[T_{dq/\alpha\beta}\right] &= \begin{bmatrix} \cos\Delta\theta & -\sin\Delta\theta \\ \sin\Delta\theta & \cos\Delta\theta \end{bmatrix}
\end{aligned} \tag{3.9}$$

where the symbols are defined in Fig. 3.4.

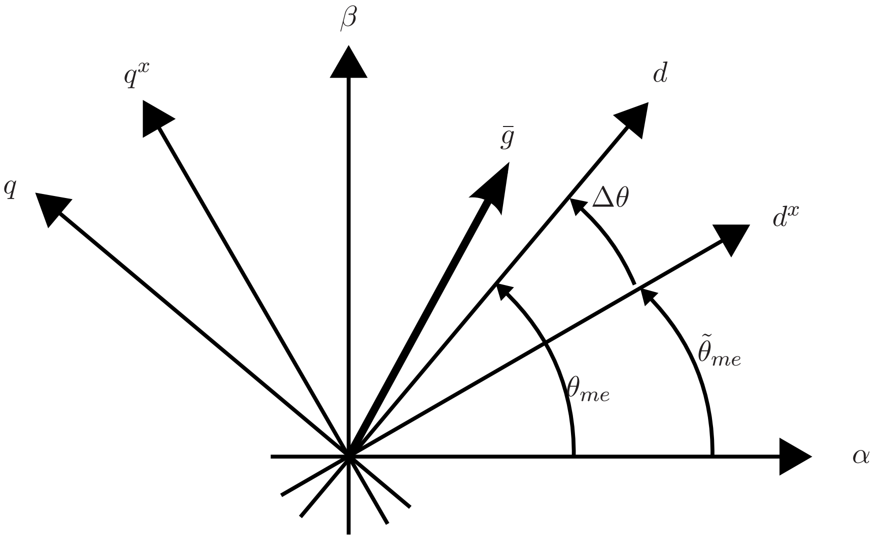

Figure 3.4: Reference systems: stationary ($\alpha-\beta$), synchronous with the rotor ($d-q$), related to the estimated position $\tilde{\theta}_{me}$ (d^x-q^x)

Applying (3.9) to (3.7), the flux–linkage in the $d^x - q^x$ reference frame results as follow:

$$[\lambda^x] = ([T^{-1}][l][T])[i^x] + ([T^{-1}][l_m][T])[i^x] + [T^{-1}][\lambda_{mg}] \tag{3.10}$$

where

$$\begin{aligned}
[l^x] &= \left[T^{-1}\right][l][T] = \begin{bmatrix} \cos\Delta\theta & \sin\Delta\theta \\ -\sin\Delta\theta & \cos\Delta\theta \end{bmatrix} \begin{bmatrix} l_d & 0 \\ 0 & l_q \end{bmatrix} \begin{bmatrix} \cos\Delta\theta & -\sin\Delta\theta \\ \sin\Delta\theta & \cos\Delta\theta \end{bmatrix} \\
&= \begin{bmatrix} l_d\cos\Delta\theta & l_q\sin\Delta\theta \\ -l_d\sin\Delta\theta & l_q\cos\Delta\theta \end{bmatrix} \begin{bmatrix} \cos\Delta\theta & -\sin\Delta\theta \\ \sin\Delta\theta & \cos\Delta\theta \end{bmatrix} \\
&= \begin{bmatrix} l_d\cos^2\Delta\theta + l_q\sin^2\Delta\theta & -l_d\cos\Delta\theta\sin\Delta\theta + l_q\sin\Delta\theta\cos\Delta\theta \\ -l_d\sin\Delta\theta\cos\Delta\theta + l_q\cos\Delta\theta\sin\Delta\theta & l_d\sin^2\Delta\theta - l_q\cos^2\Delta\theta \end{bmatrix} \\
&= \begin{bmatrix} l_\Sigma - l_\Delta\cos 2\Delta\theta & l_\Delta\sin 2\Delta\theta \\ l_\Delta\sin 2\Delta\theta & l_\Sigma - l_\Delta\cos 2\Delta\theta \end{bmatrix}
\end{aligned} \tag{3.11}$$

$$\begin{aligned}
[l_m^x] &= \left[T^{-1}\right][l_m][T] = l_m \begin{bmatrix} \cos\Delta\theta & \sin\Delta\theta \\ -\sin\Delta\theta & \cos\Delta\theta \end{bmatrix} \begin{bmatrix} 0 & 1 \\ 1 & 0 \end{bmatrix} \begin{bmatrix} \cos\Delta\theta & -\sin\Delta\theta \\ \sin\Delta\theta & \cos\Delta\theta \end{bmatrix} \\
&= l_m \begin{bmatrix} \sin\Delta\theta & \cos\Delta\theta \\ \cos\Delta\theta & -\sin\Delta\theta \end{bmatrix} \begin{bmatrix} \cos\Delta\theta & -\sin\Delta\theta \\ \sin\Delta\theta & \cos\Delta\theta \end{bmatrix} \\
&= l_m \begin{bmatrix} 2\sin\Delta\theta\cos\Delta\theta & \cos^2\Delta\theta - \sin^2\Delta\theta \\ \cos^2 2\Delta\theta - \sin^2\Delta\theta & -2\sin\Delta\theta\cos\Delta\theta \end{bmatrix} \\
&= l_m \begin{bmatrix} \sin 2\Delta\theta & \cos 2\Delta\theta \\ \cos 2\Delta\theta & -\sin 2\Delta\theta \end{bmatrix}
\end{aligned} \tag{3.12}$$

The inductance l_Σ and l_Δ are called *average inductance* and *difference inductance* respectively. They are equal to:

$$\begin{aligned}
l_\Sigma &= \frac{l_d + l_q}{2} \\
l_\Delta &= \frac{l_q - l_d}{2}
\end{aligned} \tag{3.13}$$

Substituting (3.11) and (3.12) in the (3.7) the flux–linkage matrix $[\lambda^x]$ is obtained:

$$\begin{aligned}
[\lambda^x] &= \left\{ l_\Sigma[I] + l_\Delta \begin{bmatrix} -\cos 2\Delta\theta & \sin 2\Delta\theta \\ \sin 2\Delta\theta & \cos 2\Delta\theta \end{bmatrix} \right\} [i^x] \\
&\quad + l_m \begin{bmatrix} \sin 2\Delta\theta & \cos 2\Delta\theta \\ \cos 2\Delta\theta & -\sin 2\Delta\theta \end{bmatrix} [i^x] + \begin{bmatrix} \lambda_{d,mg}^x \\ \lambda_{q,mg}^x \end{bmatrix}
\end{aligned} \tag{3.14}$$

After some manipulations, it is possible to derive the d^x– and the q^x–axis currents:

$$\begin{aligned}
i_d^x &= \frac{l_\Sigma + L_\Delta \cos 2\Delta\theta - l_m \sin 2\Delta\theta}{l_\Sigma^2 - l_\Delta^2 - l_M^2}(\lambda_d^x - \lambda_{d,mg}^x) \\
&\quad - \frac{l_\Delta \sin 2\Delta\theta + l_M \cos 2\Delta\theta}{l_\Sigma^2 - l_\Delta^2 - l_M^2}(\lambda_q^x - \lambda_{q,mg}^x)
\end{aligned} \tag{3.15}$$

$$\begin{aligned}
i_q^x &= -\frac{l_\Delta \sin 2\Delta\theta + l_M \cos 2\Delta\theta}{l_\Sigma^2 - l_\Delta^2 - l_M^2}(\lambda_d^x - \lambda_{d,mg}^x) \\
&\quad + \frac{l_\Sigma - l_\Delta \cos 2\Delta\theta + l_M \sin 2\Delta\theta}{l_\Sigma^2 - l_\Delta^2 - l_M^2}(\lambda_q^x - \lambda_{q,mg}^x)
\end{aligned} \tag{3.16}$$

The sensorless technique is based on adding at the fundamental voltages, that feed the motor, a high frequency sine wave voltages, of the type:

$$\begin{aligned}
u_{hd}^x &= U_{hd}^x \cos\omega_h t \\
u_{hq}^x &= U_{hq}^x \sin\omega_h t
\end{aligned} \tag{3.17}$$

The spatial vector of (3.17) traces in general an ellipse in the d^x, q^x plane. Using (3.6) and solving in the steady-state at the pulsation ω_h (ignoring the resistance voltage drop), the components of the stator flux $\bar{\lambda}^x$ are obtained:

$$\begin{aligned}
\lambda_{hd}^x &= \Lambda_{hd}^x \sin\omega_h t \\
\lambda_{hq}^x &= \Lambda_{hq}^x \cos\omega_h t
\end{aligned} \tag{3.18}$$

with

$$\begin{aligned}\Lambda_{hd}^{x} &= \frac{U_{hd}^{x}\omega_h - U_{hq}^{x}\omega_x}{\omega_h^2 - \omega_x^2} \\ \Lambda_{hq}^{x} &= \frac{U_{hd}^{x}\omega_x - U_{hq}^{x}\omega_h}{\omega_h^2 - \omega_x^2}\end{aligned} \tag{3.19}$$

Exploiting the (3.19) and taking into account that the the terms due to the PMs flux $\lambda_{d,mg}^{x}$ and $\lambda_{q,mg}$ are not affected by the high frequency excitation, the high frequency currents term are obtained:

$$\begin{aligned}i_{hd}^{x} &= \frac{l_\Sigma + l_\Delta \cos 2\Delta\theta - l_M \sin 2\Delta\theta}{l_\Sigma^2 - l_\Delta^2 - l_M^2}\Lambda_{hd}^{x} \sin\omega_h t \\ &\qquad - \frac{l_\Delta \sin 2\Delta\theta + l_M \cos 2\Delta\theta}{l_\Sigma^2 - l_\Delta^2 - l_M^2}\Lambda_{hq}^{x} \cos\omega_h t \\ i_{hq}^{x} &= -\frac{l_\Delta \sin 2\Delta\theta + l_M \cos 2\Delta\theta}{l_\Sigma^2 - l_\Delta^2 - l_M^2}\Lambda_{hd}^{x} \sin\omega_h t \\ &\qquad + \frac{l_\Sigma - l_\Delta \cos 2\Delta\theta + l_M \sin 2\Delta\theta}{l_\Sigma^2 - l_\Delta^2 - l_M^2}\Lambda_{hq}^{x} \cos\omega_h t\end{aligned} \tag{3.20}$$

One can note that the currents (3.20) depend on $\Delta\theta$ and thus contains information on the rotor position. In the next section two different high frequency voltage injections are studied: injection in the stator reference frame $\alpha-\beta$, injection in the rotor reference frame $d-q$[3]. According to the type of injection, different sensorless algorithms can be developed in order to estimate the electrical position.

3.4 Injection in the stator reference frame

3.4.1 High frequency currents

The high frequency voltages injection in the stator reference frame produces a rotating voltage vector[4][5], at speed ω_h, added to the normal voltage vector that feed the motor. This high frequency voltages produce a current signals dependent on the rotor position, as reported in the previous section.

The equations reported in Sec. 3.3.1 are again valid, but being in the stator reference frame the apex ^{x} is omitted and the subscripts d and q are substituted with α and β. In addition, the position θ^x ad the speed ω^x is equal to zero (then $\Delta\theta = -\theta_{me}$).

Then, the injected voltage vector components of amplitude U_h can be represented in the stationary reference frame as:

$$u_{h\alpha}(t) = U_h \cos\omega_h t \tag{3.21}$$

$$u_{h\beta}(t) = U_h \sin\omega_h t \tag{3.22}$$

According to (3.18) and (3.19) the flux–linkage components become:

$$\lambda_{h\alpha} = \frac{U_h}{\omega_h}\sin\omega_h t = \Lambda_h \sin\omega_h t \tag{3.23}$$

$$\lambda_{h\beta} = -\frac{U_h}{\omega_h}\cos\omega_h t = -\Lambda_h \cos\omega_h t \tag{3.24}$$

Starting from (3.20) and neglecting the saturation and cross-saturation effects ($l_M = 0$), the high frequency current components result:

$$\begin{aligned} i_{h\alpha} &= \frac{\Lambda_h^s}{l_d l_q}[(l_\Sigma + l_\Delta \cos 2\theta_{me}) \sin \omega_h t - (l_\Delta \sin 2\theta_{me}) \cos \omega_h t] \\ &= I_h[l_\Sigma \sin \omega_h t - l_\Delta \sin(2\theta_{me} - \omega_h t)] \qquad (3.25) \\ i_{h\beta} &= -\frac{\Lambda_h^s}{l_d l_q}[(l_\Sigma - l_\Delta \cos 2\theta_{me}) \cos \omega_h t - (l_\Delta \sin 2\theta_{me}) \sin \omega_h t] \\ &= I_h[-l_\Sigma \cos \omega_h t + l_\Delta \cos(2\theta_{me} - \omega_h t)] \qquad (3.26) \end{aligned}$$

High frequency currents contain the rotor position information. With a suitable demodulation and an adjustment scheme the estimated position can be corrected in order to extract the rotor position.

3.4.2 Demodulation and position estimation

The positive sequence voltage vector injected produces a current vector composed by a positive and negative sequences. The latter contains the rotor position information, while the first must be eliminated.

For the demodulation purpose the high frequency currents components (3.25) and (3.26) are manipulated as follow:

$$\begin{aligned} \epsilon &= i_{h\alpha} \cos(2\tilde{\theta}_{me} - \omega_h t) + i_\beta \sin(2\tilde{\theta}_{me} - \omega_h t) \\ &= I_h l_\Sigma [\sin(\omega_h t) \cos(2\tilde{\theta}_{me} - \omega_h t) - \cos(\omega_h t) \sin(2\tilde{\theta}_{me} - \omega_h t)] - \\ &\quad - I_h l_\Delta [\sin(2\theta_{me} - \omega_h t) \cos(2\tilde{\theta}_{me} - \omega_h t) - \cos(2\theta_{me} - \omega_h t) \sin(2\tilde{\theta}_{me} - \omega_h t)] \\ &= I_h l_\Sigma \sin(2\omega_h t - 2\tilde{\theta}_{me}) + I_h l_\Delta \sin(2(\tilde{\theta}_{me} - \theta_{me})) \qquad (3.27) \end{aligned}$$

Filtering (3.27) by a low pass filter (LPF), the double frequency sinusoidal term can be removed. It results:

$$\epsilon_{LPF} = I_h l_\Delta \sin(2\Delta\theta) \qquad (3.28)$$

When the estimated position is equal to the actual one ($\Delta\theta = 0$) the $\sin \Delta\theta$ is also null and the error ϵ_{LPF} is zero.

An adjustment mechanism can be introduced in order to zeroing the ϵ_{LPF}. The scheme of principle of the estimation mechanism is reported in Fig. 3.5.

A trouble of this solution is that the closed loop control forces $\Delta\theta$ to 0 by nullifying $\sin 2\Delta\theta$; therefore it converges to zero also when the angular error is equal to π and $\pm\pi/2$. The latter case is an unstable solution and then can be neglected. In the first case the estimated angle $\tilde{\theta}_{me}$ is displaced to the actual angle θ_{me} of π *rads*. This ambiguity regarding the estimated position is solved at start–up, by the injection of a sequence of positive and negative direct voltage pulses, that causes different current responses according to the sign of the PM magnetization. This is the most used solution proposed in the literature [6] – [7].

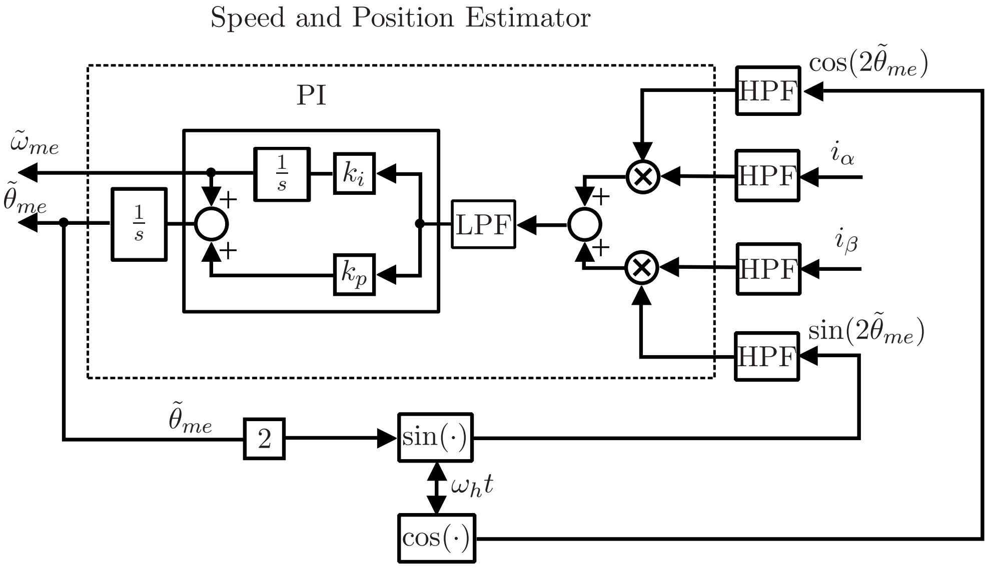

Figure 3.5: Scheme for the estimation of the speed and position, high frequency injection in the stator reference frame

3.5 Injection in the rotor reference frame

3.5.1 High frequency currents

The high frequency voltages injection in the rotor reference frame produce a pulsating or elliptic voltage vector added to the normal voltage vector that feed the motor[8]. Once again the equations reported in Sec. 3.3.1 are valid and the apex ^{x} represents the estimated reference frame according to the estimated position θ^x. The later is the estimated electrical position $\tilde{\theta}_{me}$ and then ω^x is equal to the estimated electrical speed $\tilde{\omega}_{me}$. Finally $\Delta\theta$ is the effective estimation error given by $\tilde{\theta}_{me} - \theta_{me}$.

Starting from (3.17) and in the particular case in which $U_{hq} = U_{hd}\tilde{\omega}_{me}/\omega_h$, the flux amplitudes (3.18) result in:

$$\Lambda^x_{hd} = \frac{U_{hd}}{\omega_h} \tag{3.29}$$

$$\Lambda^x_{hq} = 0 \tag{3.30}$$

which are a flux vector pulsating along the d–axis.

By solving (3.20) and imposing (3.29) and (3.30) one obtains the following high frequency current components:

$$i^x_{hd} = \frac{U_{hd}}{\omega_h}\left(\frac{l_\Sigma + l_\Delta \cos 2\Delta\theta}{l_d l_q}\right)\sin\omega_h t \tag{3.31}$$

$$i^x_{hq} = -\frac{U_{hd}}{\omega_h}\left(\frac{l_\Delta \sin 2\Delta\theta}{l_d l_q}\right)\sin\omega_h t \tag{3.32}$$

Eqs. (3.31) and (3.32) represent the steady–state components of a *pulsating vector* in the rotor reference frame, the orientation of which depends on the estimated position with respect to the actual one.

3.5.2 Position estimation

From (3.32), one notes that when the estimated position is equal to the actual one ($\Delta\theta = 0$) then $\sin 2\Delta\theta$ is also null and the high frequency quadrature component is zero as well. An adjustment mechanism can thus correct the estimated position $\tilde{\theta}_{me}$ to nullify the error $\Delta\theta$, by nullify the high frequency quadrature current component i^x_{hq} given by (3.32).

This current component is extracted by a high pass filter which has the current i^x_q (resulting from the transformation of the stator currents into the reference frame d^x, q^x) as input.

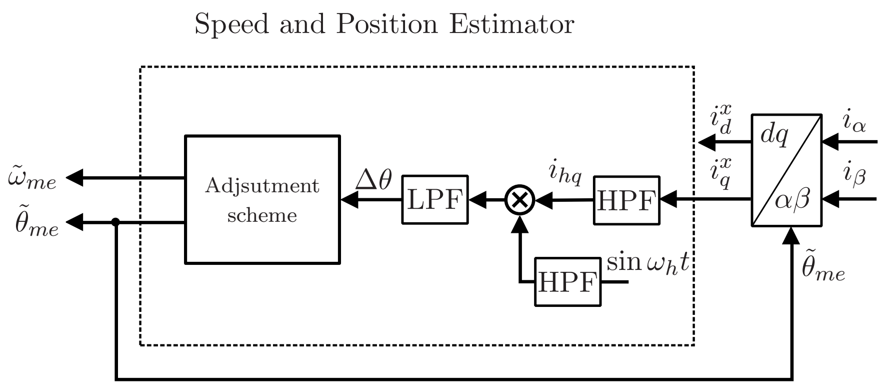

Figure 3.6: Scheme for the estimation of the speed and position

Therefore the adjustment mechanism forces to zero i^x_{hq} amplitude (extracted by a demodulation process: see later) and deliverers the estimated speed $\tilde{\omega}_{me}$ and, by integration of that, the estimated position $\tilde{\theta}_{me}$. The scheme of principle of the estimation mechanism is reported in Fig. 3.6. More details on the adjustment scheme are reported in Sec. 3.6.

A trouble of this solution is tat the closed loop control of $\Delta\theta = 0$ by nullifying $\sin 2\Delta\theta$ converges to zero also when the angular error is equal to π, i.e. the estimated angle $\tilde{\theta}_{me}$ is displaced to the actual angle θ_{me} of π rads. This ambiguity regarding the estimated position is solved at start–up, by the injection of a sequence of positive and negative direct voltage pulses, that causes different current responses according to the sign of the PM magnetization. This is the most used solution proposed in the literature [6],[7].

3.5.3 Demodulation

As reported above, the i^x_{hq} must be demodulated to extract its amplitude which contains the angular error. For the demodulation purpose,the high frequency quadrature component is manipulated in this way

$$\epsilon = i_{hq} \sin \omega_h \tag{3.33}$$

and then it results:

$$\begin{aligned}\epsilon &= -\frac{U_{hd}}{\omega_h l_d l_q}(l_\Delta \sin(2\Delta\theta))\sin(\omega_h t)\cdot\sin(\omega_h t)\\ &= -\frac{U_{hd}}{\omega_h l_d l_q}(l_\Delta \sin(2\Delta\theta))\sin^2(\omega_h t)\\ &= \underbrace{\frac{1}{2}\left(\frac{U_{hd}}{\omega_h l_d l_q} l_\Delta\right)}_{K_c}\Big(-\sin(2\Delta\theta)+\\ &\qquad +\sin(2\Delta\theta)\cos(2\omega_h t)\Big)\end{aligned} \tag{3.34}$$

If the error $\Delta\theta$ is considered small (around the steady state solution) then the previous equation can be approximated by:

$$\epsilon = -K_c\Delta\theta + K_c\Delta\theta\cos(2\omega_h t) \tag{3.35}$$

Filtering (3.35) by a low pass filter (LPF), the double frequency cosinusoidal term can be removed and the input to the adjustment scheme in Fig. 3.6 results proportional to the angular error $\Delta\theta$

$$\epsilon_{LPF} = -K_c\Delta\theta \tag{3.36}$$

In order to compensate the effect of the high pass filter applied to i_q^x, identical filter is applied for $\sin\omega_h t$ before multiplication, as shown in Fig. 3.6.

3.5.4 Cross saturation effects

Usually, for simplicity, the influence of the mutual inductance between d, q axes due to cross–saturation is neglected in sensorless rotor position control[9],[10]. However, the presence of this effect lead an error in the position estimation that can be predicted as following. Exploiting the relations in (3.20) and taking into account (3.29) and (3.30), the high frequency current components (3.31) and (3.32) become:

$$i_{hd}^x = \frac{U_{hd}}{\omega_h}\left(\frac{l_\Sigma + l_\Delta\cos 2\Delta\theta - l_M \sin 2\Delta\theta}{l_d l_q - l_M^2}\right)\sin\omega_h t \tag{3.37}$$

$$i_{hq}^x = -\frac{U_{hd}}{\omega_h}\left(\frac{l_\Delta\sin 2\Delta\theta + l_M \cos 2\Delta\theta}{l_d l_q - l_M^2}\right)\sin\omega_h t \tag{3.38}$$

By means of the scheme of Fig.3.6, the position estimation is obtained by nullify i_{hq}^x. In this case from (3.38) it results:

$$0 = l_\Delta \sin 2\Delta\theta + l_M\cos 2\Delta\theta \tag{3.39}$$

which is satisfied by

$$\Delta\theta = \frac{1}{2}\arctan\left(-\frac{l_M}{l_\Delta}\right) \tag{3.40}$$

Eq.(3.39) points out that cross–saturation causes an estimation error that depends on the mutual and difference inductances ratio. One can note that when the difference inductance change its sign, i.e. the l_d becomes larger than l_q, also the error estimation changes its sign. To be more precise, when l_Δ crosses the zero, the estimation error passes from $-\pi/2$ to $\pi/2$ *rads*. The estimation error changes sign also when l_M changes sign for given l_Δ, passing through zero.

3.6 Adjustment mechanisms for the estimator

3.6.1 PI regulator

First studied mechanism is a PI regulator which has been introduced in the Sec. 3.2. The signal to be followed is a ramp, then in order to have a null error, a system of type 2 (as the PI and the additional integrator) must be used.

Inserting a PI regulator in Fig. 3.6, the resulted scheme is shown in Fig. 3.7. The PI regulator delivers the estimated speed $\tilde{\omega}_{me}$ and, by its integration, the estimated rotor position $\tilde{\theta}_{me}$.

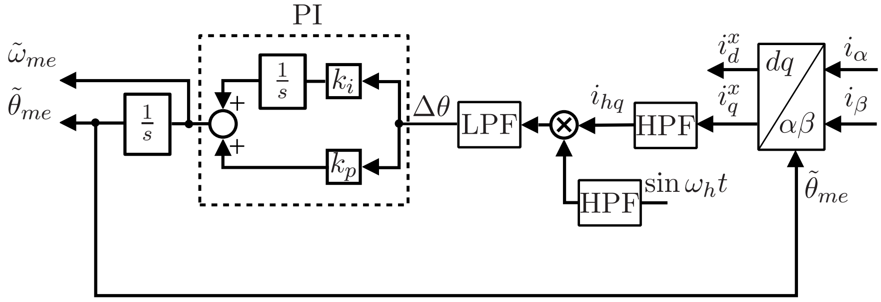

Figure 3.7: Scheme for the estimation of the speed and position with a PI regulator

3.6.2 Two states observer

The second mechanism is based on an observer[11], using a matrix $[K]$ to force the estimated values to converge on the actual ones. Taking as state matrix $[x] = [\theta_{me}\ \omega_{me}]^T$, the equations of the system can be write as:

$$\dot{\tilde{\theta}}_{me}(t) = \tilde{\omega}_{me}(t) \tag{3.41}$$

$$\dot{\tilde{\omega}}_{me}(t) = -\frac{B}{J}\tilde{\omega}_{me}(t) + \frac{1}{J}m \tag{3.42}$$

where m is the motor torque. Then the matrixes associated to the system are:

$$[x] = \begin{bmatrix} \tilde{\theta}_{me} \\ \tilde{\omega}_{me} \end{bmatrix} \tag{3.43}$$

$$
\begin{aligned}
[u] &= m && (3.44)\\
[y] &= \theta_{me} && (3.45)\\
[F] &= \begin{bmatrix} 0 & 1 \\ 0 & -\frac{B}{J} \end{bmatrix} && (3.46)\\
[G] &= \begin{bmatrix} 0 \\ \frac{1}{J} \end{bmatrix} && (3.47)\\
[H] &= [1\ 0] && (3.48)
\end{aligned}
$$

The system results completely observable because the observability matrix has rank two being[12]:

$$\mathscr{O} = \begin{bmatrix} H \\ HF \end{bmatrix} = \begin{bmatrix} 1 & 0 \\ 0 & 1 \end{bmatrix} \quad (3.49)$$

At this point the characteristic polynomial $[F]-[K][H]$ choosing the gains of the matrix $[K]$, that is of the type $[K] = [k_1\ k_2]^T$.

For the calculus the following equation is used:

$$det(s[I] - ([F] - [K][H])) = (s+\alpha_1)(s+\alpha_2) \quad (3.50)$$

where α_1 and α_2 are the eigenvalues which must be fixed. Substituting (3.46) and (3.48) in (3.50), the latter becomes:

$$det\left(\begin{bmatrix} s & 0 \\ 0 & s \end{bmatrix} - \left(\begin{bmatrix} 0 & 1 \\ 0 & -\frac{B}{J} \end{bmatrix} - \begin{bmatrix} k_1 & 0 \\ k_2 & 0 \end{bmatrix}\right)\right) = s^2 + s(\alpha_1+\alpha_2) + \alpha_1\alpha_2 \quad (3.51)$$

therefore

$$
\begin{aligned}
s^2 + s(\alpha_1+\alpha_2) + \alpha_1\alpha_2 &= det\left(\begin{bmatrix} s+k_1 & -1 \\ +k_2 & s+\frac{B}{J} \end{bmatrix}\right)\\
&= (s+k_1)\left(s+\frac{B}{J}\right) + k_2\\
&= s^2 + s(\frac{B}{J}+k_1) + (k_1\frac{B}{J}+k_2) && (3.52)
\end{aligned}
$$

The coefficients of the matrix $[K]$ can be derived from the (3.52) in this way:

$$
\begin{aligned}
\frac{B}{J} + k_1 &= \alpha_1 + \alpha_2 && (3.53)\\
k_2 + k_1\frac{B}{J} &= \alpha_1\alpha_2 && (3.54)
\end{aligned}
$$

The resulted system has the structure reported in Fig. 3.8 where the input are the electrical position and the load (derive from the knowledge of the machine's currents).

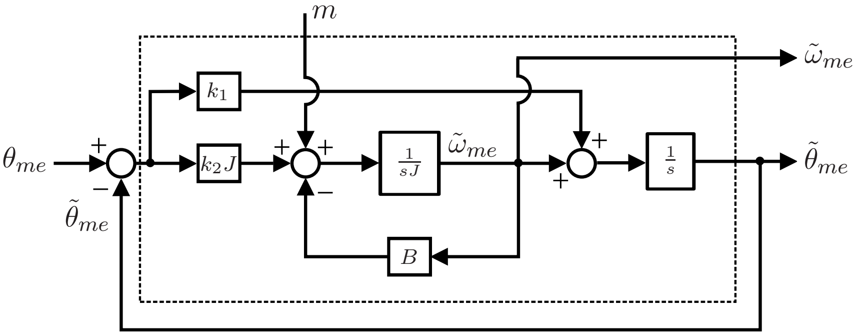

Figure 3.8: Observer at two states

The system can be written in the matrix form:

$$\begin{bmatrix} \dot{\tilde{\theta}}_{me} \\ \dot{\tilde{\omega}}_{me} \end{bmatrix} = \begin{bmatrix} -k_1 & 1 \\ -k_2 & -\dfrac{B}{J} \end{bmatrix} \begin{bmatrix} \tilde{\theta}_{me} \\ \tilde{\omega}_{me} \end{bmatrix} + \begin{bmatrix} k_1 \\ k_2 \end{bmatrix} \theta_{me} + \begin{bmatrix} 0 \\ \dfrac{1}{J} \end{bmatrix} m \tag{3.55}$$

or with the equations:

$$\dot{\tilde{\theta}}_{me} = \tilde{\omega}_{me} + k_1(\theta_{me} - \tilde{\theta}_{me}) = \tilde{\omega}_{me} - k_1\Delta\theta \tag{3.56}$$

$$\dot{\tilde{\omega}}_{me} = k_2(\theta_{me} - \tilde{\theta}_{me}) - \frac{B}{J}\tilde{\omega}_{me} + \frac{1}{J}m = -k_2\Delta\theta - \frac{B}{J}\tilde{\omega}_{me} + \frac{1}{J}m \tag{3.57}$$

One can note that the (3.56) and (3.57) depend only on the position error $\Delta\theta$ and the estimated error $\tilde{\theta}_{me}$. Then it is possible to exploit this observer in the estimation scheme based on the high frequency injection. As shown in Fig. 3.6, the position error is in input to the adjustment scheme. Therefore the observer of Fig. 3.8 can be implemented using directly the position error delivered by the demodulation. Consequently the complete scheme of the estimator algorithm is reported in Fig. 3.9, where the observer has been simplified removing the terms m and $B\tilde{\omega}_{me}$. In this way, only the dynamic behaviour are modified with respect to that of Fig. 3.8 but not the steady–state performance.

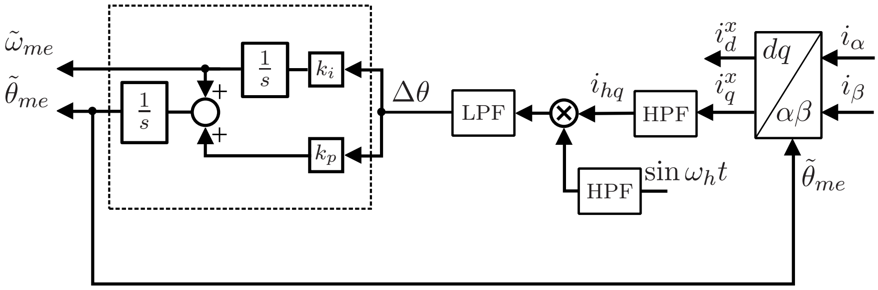

Figure 3.9: Scheme for the estimation of the speed and position with two–state observer

It is simply note as this scheme is equal to a PI control of Fig. 3.7. The difference between the two estimators stays in the estimated speed that is delivered by in the integral part in the first case.

3.6.3 Three states observer

The estimator described previously can be improved including the disturbance effects[11]. The disturbance torque m_L, that is added to the motor torque, is considered as an additional state to be estimated. Therefore, the system (3.41) can be enlarged inserting a third state that is the estimated torque load $\tilde{m}_L$:

$$\begin{aligned}
\dot{\tilde{\theta}}_{me}(t) &= \tilde{\omega}_{me}(t) \qquad &(3.58)\\
\dot{\tilde{\omega}}_{me}(t) &= -\frac{B}{J}\tilde{\omega}_{me}(t) + \frac{1}{J}m + \frac{1}{J}\tilde{m}_L \qquad &(3.59)\\
\dot{\tilde{m}}_L(t) &= 0 \qquad &(3.60)
\end{aligned}$$

where $\tilde{m}_L$ derivative is posed to be zero having no information about its dynamics. The system matrixes result:

$$[x] = \begin{bmatrix} \tilde{\theta}_{me} \\ \tilde{\omega}_{me} \\ \tilde{m}_L \end{bmatrix} \tag{3.61}$$

$$[u] = m \tag{3.62}$$

$$[y] = \theta_{me} \tag{3.63}$$

$$[F] = \begin{bmatrix} 0 & 1 & 0 \\ 0 & -\frac{B}{J} & \frac{1}{J} \\ 0 & 0 & 0 \end{bmatrix} \tag{3.64}$$

$$[G] = \begin{bmatrix} 0 \\ \frac{1}{J} \\ 0 \end{bmatrix} \tag{3.65}$$

$$[H] = \begin{bmatrix} 1 & 0 & 0 \end{bmatrix} \tag{3.66}$$

The observability matrix results:

$$\mathscr{O} = \begin{bmatrix} H \\ HF \\ HF^2 \end{bmatrix} = \begin{bmatrix} 1 & 0 & 0 \\ 0 & 1 & 0 \\ 0 & 0 & \frac{1}{J} \end{bmatrix} \tag{3.67}$$

that has rank three. Then the system is observable.

The coefficients of the matrix $[K] = [k_1\ k_2\ k_3]^T$ can be derived as following:

$$\begin{aligned}
(s+\alpha_1)(s+\alpha_2)(s+\alpha_3) &= det(s[I] - ([F] - [K][H]) \\
&= det\left(\begin{bmatrix} s+k_1 & -1 & 0 \\ k_2 & s+\dfrac{B}{J} & -\dfrac{1}{J} \\ k_3 & 0 & s \end{bmatrix}\right) \qquad (3.68) \\
&= s^3 + s^2\left(\frac{B}{J} + k_1\right) + s\left(k_2 + k_1\frac{B}{J}\right) + \frac{k_3}{J}
\end{aligned}$$

$$(3.69)$$

Making equal the coefficients of same degree, it results:

$$\frac{B}{J} + k_1 = \alpha_1 + \alpha_2 + \alpha_3 \tag{3.70}$$
$$k_2 + k_1\frac{B}{J} = \alpha_1\alpha_2 + \alpha_1\alpha_3 + \alpha_2\alpha_3 \tag{3.71}$$
$$\frac{k_3}{J} = \alpha_1\alpha_2\alpha_3 \tag{3.72}$$

Imposing the three eigenvalues, the matrix $[K]$ can be computed.

The scheme of three states observer is shown in Fig. 3.10. The input are the electrical position θ_{me} and the torque m, while the estimated states are the electrical speed $\tilde{\omega}_{me}$, the electrical position $\tilde{\theta}_{me}$ and the estimated load torque $\tilde{m}_L$.

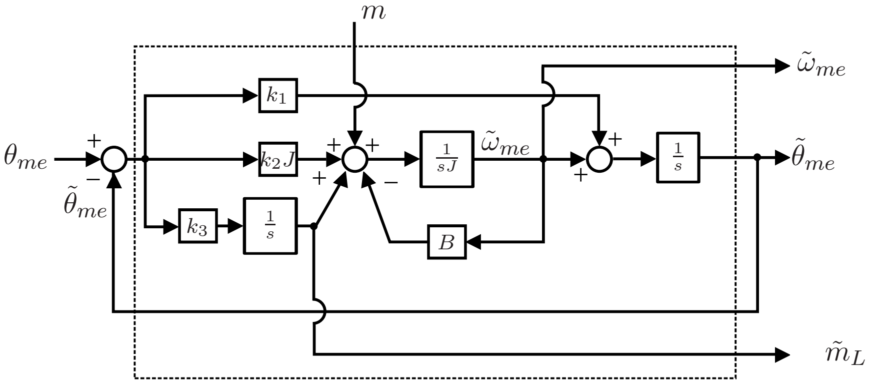

Figure 3.10: Observer at three states

Now, the equations of the observer in the matrix form can be derived:

$$\begin{bmatrix} \dot{\tilde{\theta}}_{me} \\ \dot{\tilde{\omega}}_{me} \\ \dot{\tilde{m}}_L \end{bmatrix} = \begin{bmatrix} -k_1 & 1 & 0 \\ -k_2 & -\frac{B}{J} & \frac{1}{J} \\ -k_3 & 0 & 0 \end{bmatrix} \begin{bmatrix} \tilde{\theta}_{me} \\ \tilde{\omega}_{me} \\ \tilde{m}_L \end{bmatrix} + \begin{bmatrix} k_1 \\ k_2 \\ k_3 \end{bmatrix} \theta_{me} + \begin{bmatrix} 0 \\ \frac{1}{J} \\ 0 \end{bmatrix} m \tag{3.73}$$

from which the following equations are obtained:

$$\dot{\tilde{\theta}}_{me} = k_1(\theta_{me} - \tilde{\theta}_{me}) + \tilde{\omega}_{me} = -k_1\Delta\theta + \tilde{\omega}_{me} \tag{3.74}$$
$$\dot{\tilde{\omega}}_{me} = k_2(\theta_{me} - \tilde{\theta}_{me}) - \frac{B}{J}\tilde{\omega}_{me} + \frac{1}{J}\tilde{m}_L + m \tag{3.75}$$
$$= -k_2\Delta\theta - \frac{B}{J}\tilde{\omega}_{me} + \frac{1}{J}\tilde{m}_L + m$$
$$\dot{\tilde{m}}_L = k_3(\theta_{me} - \tilde{\theta}_{me}) = -k_3\Delta\theta \tag{3.76}$$

Also in this case the system depends only by the estimated error, then it is possible to use this observer for the estimation based on the high frequency injection signal. To this purpose, the position error given by the demodulation can be used directly as input, as explained in the previous subsection. Consequently the complete scheme of the estimator algorithm is reported in Fig. 3.11. In this case the three–state observer is slightly modified, but at steady state it is equivalent to that of Fig. 3.10.

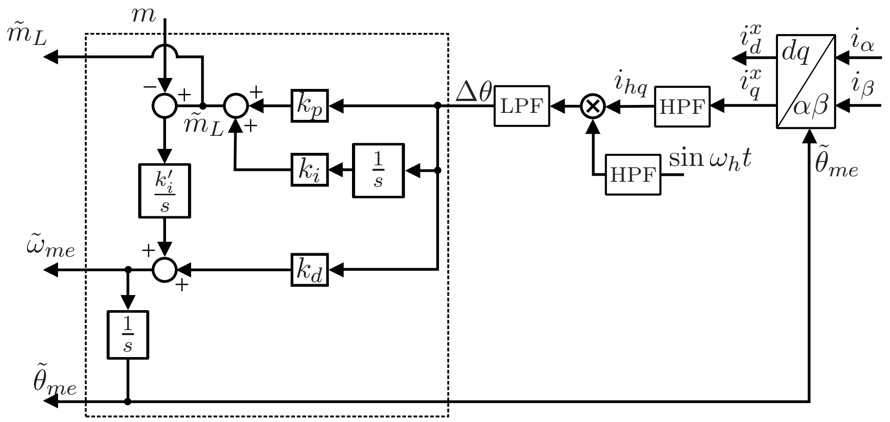

Figure 3.11: Scheme for the estimation of the speed and position with three–state observer

4

Model–based sensorless control for a hybrid catamaran application

4.1 Introduction

A HYBRID electric catamaran uses electrical power for maneuvering and propulsion in harbor and dock areas or when becalmed. The use of electrical motor reduces the fuel consumption as much as possible, with advantages in terms of smoke, smell, noise and CO_2 emission [13] –[14].

The prototype catamaran, which rendering is shown in Fig. 4.1, uses two submersed electrical motors with their shafts connected to two independent propellers. Electrical power comes from either an onboard battery pack or from a diesel-generator. When the engine is off and the catamaran is under sail, the propellers turn and they provide the recharging of the battery if necessary.

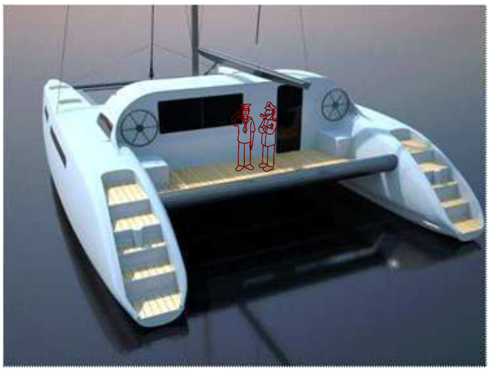

Figure 4.1: Catamaran rendering

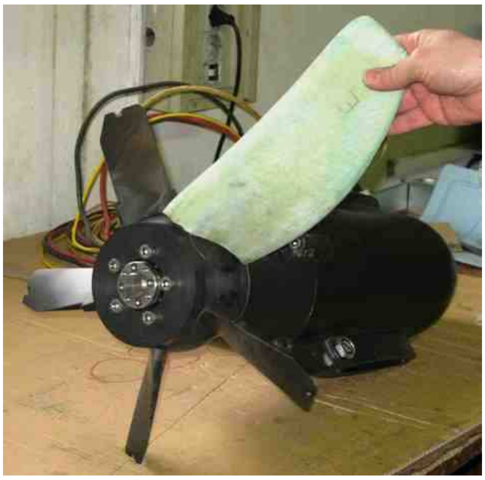

Figure 4.2: Motor bulb with propeller

In the considered hybrid catamaran, propulsion is performed by two high efficiency electric Surface-mounted Permanent Magnet (SPM) synchronous motors. These are installed inside two submersed bulbs as shown in Fig. 4.2; therefore the removal of the position transducer is required for space, reliability and maintenance reasons.

An effective and simple model-based sensorless control of the type illustrated in Sect. 3.2 has been chosen for these propulsion drives. Specifically, the proposed model-based rotor position estimator extracts the required rotor speed and position information from the back–electromotive force (bemf) vector which is reconstructed from the measured stator voltage and current vectors on the basis of the stator electric model of the motor.

The catamaran application is well suited for this sensorless algorithm, as it has limited requirement of performance at low speed, because the torque increases with the speed from a null level at standstill. There are more elaborated sensorless solutions in the state of the art [15] –[20], but that chosen here is very simple and effective and can be profitable implemented in the same microprocessor of the drive.

4.2 Bemf Sensorless Solution

Model-based rotor position estimation extracts the required information from the PM flux vector or the bemf vector, reconstructed from the measured stator voltage and current. One of the first application of this technique was proposed in [21]. Voltage references at the inverter input (instead of measuring them) and measured current are usually adopted.

As explained in Sec. 3.2 the algorithm is based on the comparison between the derivatives of two PM flux linkage vectors in the $\alpha\beta$ frame: one obtained from a reference model (that should constitute an open loop estimator) which depends only on measures (currents and voltages), the other provided by an adaptive model which depends on the angular rotor position. For this application, the bemf $\bar{e}_{\alpha\beta}$ is used in a sensorless solution in place of PM flux linkage. Fig. 4.3 points out the MRAS estimator structure. The operating principle is the same explained in Sec. 3.2. The bemf equations derived from the two models are:

$$\bar{e}_{\alpha\beta} = \frac{d\overline{\Lambda}_{mg}}{dt} = \overline{u}_{\alpha\beta} - R\bar{i}_{\alpha\beta} - L\frac{d\bar{i}_{\alpha\beta}}{dt} \tag{4.1}$$

$$\bar{e}_{\alpha\beta}^{(\tilde{\theta}_{me})} = j\tilde{\Lambda}_{mg}\tilde{\omega}_{me}e^{j\tilde{\theta}_{me}} \tag{4.2}$$

Multiplying the first vector to the complex conjugated of the second one and extracting the imaginary part of the result one obtains the error between the actual electrical position θ_{me} and the estimated electrical position $\tilde{\theta}_{me}$ as:

$$\epsilon = \mid \bar{e}_{\alpha\beta} \mid \tilde{\Lambda}_{mg}\tilde{\omega}_{me}\sin(\Delta\theta) \simeq (\tilde{\Lambda}_{mg}\tilde{\omega}_{me})^2\Delta\theta \tag{4.3}$$

where $\Delta\theta = \theta_{me} - \tilde{\theta}_{me}$, which can replace $\sin(\Delta\theta)$ for small value of position error.

The position error is used in an adaptation mechanism as shown in Fig.4.3. The $\tilde{\theta}_{me}$ is given by the integration of the estimated speed $\tilde{\omega}_{me}$ that is the output of the PI regulator that processes the error variable.

In order to reduce the speed dependence, the vector developed by the adaptive model can be an unit vector of the type:

$$\overline{g}^{(\tilde{\theta}_{me})} = je^{j\tilde{\theta}_{me}} = -\sin\tilde{\theta}_{me} + j\cos\tilde{\theta}_{me} \tag{4.4}$$

which respects the direction of the bemf $\bar{e}_{\alpha\beta}^{(\tilde{\theta}_{me})}$ removing only the speed dependence of the vector amplitude. In this case the error (4.3) becomes:

$$\epsilon = Im[\bar{e}_{\alpha\beta}\check{\overline{g}}^{(\tilde{\theta}_{me})}] = -\tilde{\omega}_{me}\tilde{\Lambda}_{mg}\sin(\Delta\theta) \simeq -\tilde{\omega}_{me}\tilde{\Lambda}_{mg}\Delta\theta \tag{4.5}$$

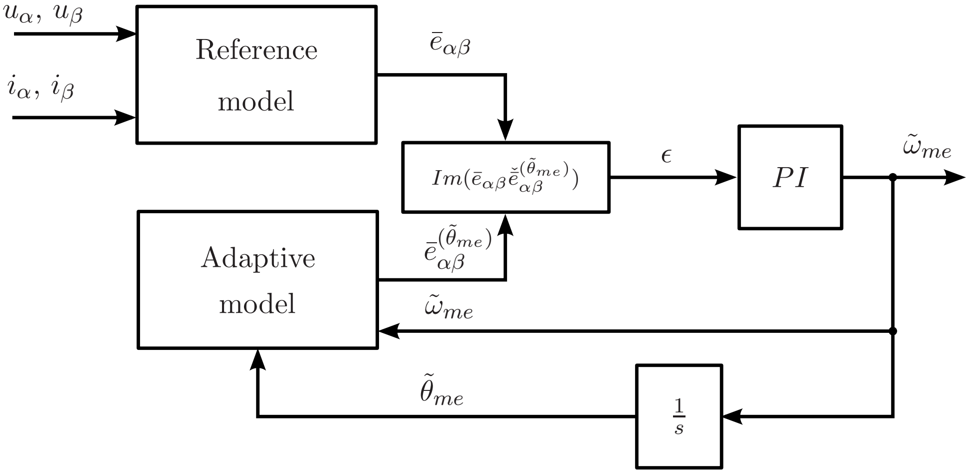

Figure 4.3: Back emf based MRAS algorithm

which is less strong dependent on speed. One can note that the error ϵ depends on the estimated speed and the sine of estimated position. The PI regulator forces ϵ to zero, but the latter is null only when the $\sin\Delta\theta$ is equal to zero i.e. when $\Delta\theta = 0 \pm 2k\pi$ with $k = 0, \pm 1, \pm 2, \ldots$[1]. So when ϵ is equal to zero, the estimated electrical position $\tilde{\theta}_{me}$ is equal to the actual one θ_{me}. The PI delivers the estimated speed $\tilde{\omega}_{me}$ and, by its integration, the estimated position $\tilde{\theta}_{me}$ that is used in the adaptive model to generate the vector $\bar{e}_{\alpha\beta}^{(\tilde{\theta}_{me})}$ or $\overline{g}^{(\tilde{\theta}_{me})}$.

The same estimated position is used also in the current vector transformation to perform the current control in the rotating d–q reference frame.

4.3 Parametric sensitivity

As reported before the control scheme forces the error ϵ to zero, so in steady–state the estimated angle $\tilde{\theta}_{me}$ is equal to the reference model one θ_{me} (open loop estimator). Then the parametric sensitivity of the estimation algorithm depends only on the parametric sensitivity of the open loop estimator.

The parametric sensitivity is defined as the ratio between the relative variation of the value of a function $\overline{f}(\overline{x}, p) = |\overline{f}|e^{j\varphi}$ and the relative variation of the parameter p considered:

$$\overline{S}^{p}_{\overline{f}}(\overline{x}, p) = \frac{\frac{d\overline{f}}{\overline{f}}}{\frac{dp}{p}} = \frac{d\overline{f}}{dp}\frac{p}{\overline{f}} = \frac{d(\ln\overline{f})}{d(\ln p)} = \frac{d(\ln|\overline{f}|)}{d(\ln p)} + j\frac{d\varphi}{d(\ln p)} \tag{4.6}$$

One can note that the sensitivity is a complex function where the real part represents the sensitivity of the module $\overline{f}$, while the imaginary part is the sensitivity of the phase. This last is defined as ratio between the normalized variation $d\varphi$ of the phase compared to a unit reference value, and the relative variation dp/p of the parameter.

---

[1] Solution for $\Delta\theta = \pi + 2k\pi$ with $k = 0, \pm 1, \pm 2, \cdot$ are non stable convergence point

The sensitivity equation can be applied to the bemf $\overline{e}_{\alpha\beta}$ expressed in a sinusoidal steady state operation. To this purpose (4.1) can be reported using the phasors as follow:

$$\overline{E} = \overline{U} - R\overline{I} - L\frac{d\overline{I}}{dt} = \overline{U} - R\overline{I} - L|\overline{I}|e^{j\theta_i}j\Omega_{me} \tag{4.7}$$

Applying (4.7) to (4.6) with reference to the resistance parameter, one obtained:

$$\overline{S}_e^R = \frac{d\bar{E}}{dR}\frac{R}{\overline{E}} = -\frac{R\overline{I}}{\overline{E}} = -\frac{R|\overline{I}|}{|\overline{E}|}e^{j\left(\theta_i - \left(\theta_{me} + \frac{\pi}{2}\right)\right)} = -\frac{R|\overline{I}|}{\Omega_{me}|\overline{\Lambda}_{mg}|} \tag{4.8}$$

that is a real number. Then the resistance error affects only the amplitude of the bemf, but not its phase (rotor position). The estimated algorithm here presented is then insensitive to resistive voltage drop (as that due to power switches) and resistive voltage drop variations (as those due to temperature). With respect the stator inductance, using the same approach applied for resistance, the sensitivity function results:

$$\overline{S}_e^L = -\frac{j\Omega_{me}L\overline{I}}{\overline{E}} = -\frac{j\Omega_{me}L|\overline{I}|}{|\overline{E}|}e^{j\left(\theta_i - \left(\theta_{me} + \frac{\pi}{2}\right)\right)} = -j\frac{L|\overline{I}|}{|\overline{\Lambda}_{mg}|} \tag{4.9}$$

that points out an independence from the speed. However this term is only imaginary so it has effect on the rotor position estimation which therefore results inductance sensitive. Fortunately the stator inductance of and SPM motor is very low and almost unaffected by the iron saturation phenomenon.

4.4 Simulation results

Some simulations have been done in order to design the control and the MRAS scheme before implementing them into the real system. The block diagram of the drive is reported in Fig.4.4. One notes that there are two control loops, for the direct and quadrature current respectively, each one with its own PI regulator. As regard the quadrature current reference, this is set according to the torque request which is the command of the skipper; instead, the direct current is imposed to zero to have a maximum torque per ampere operation mode. Alternatively, the quadrature current reference could be delivered by a speed loop, that can use the estimated speed provided by the sensorless algorithm as a feedback.

Simulations have been done in different working conditions. In Fig. 4.5, the actual and estimated electrical positions are reported at about 3800 *rpm* (63% of nominal speed) that means only 25% of the nominal power of 50 kW (which has a cubic relationship with the speed). It is possible to note the tight correspondence between the two variables. Under battery operation the power is 2 *kW* which is produced with a speed of 34% of the nominal one. Simulation results for such operating condition are in Fig. 4.6. Start–up phase and speed reversal will be discussed in the Experimental results Section.

4.5 Experimental results

Tests similar to those of the simulations have been repeated on the real system using the test-bench reported in Fig. 4.7. This is composed by the catamaran SPM motor (fed by

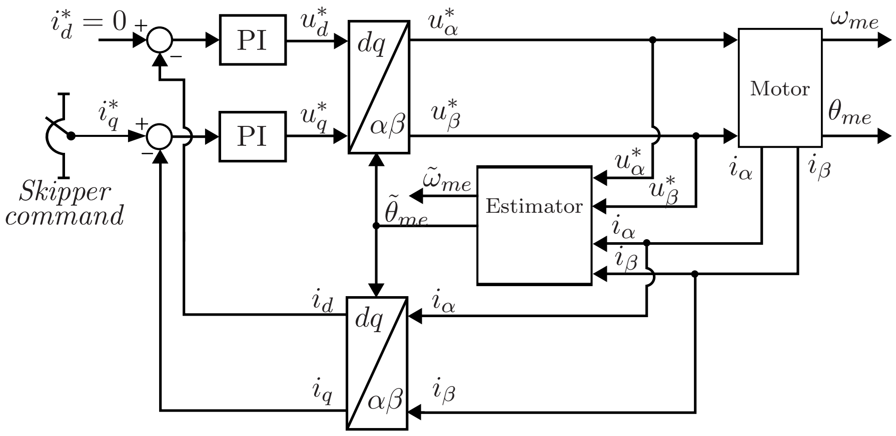

Figure 4.4: Block diagram of the drive

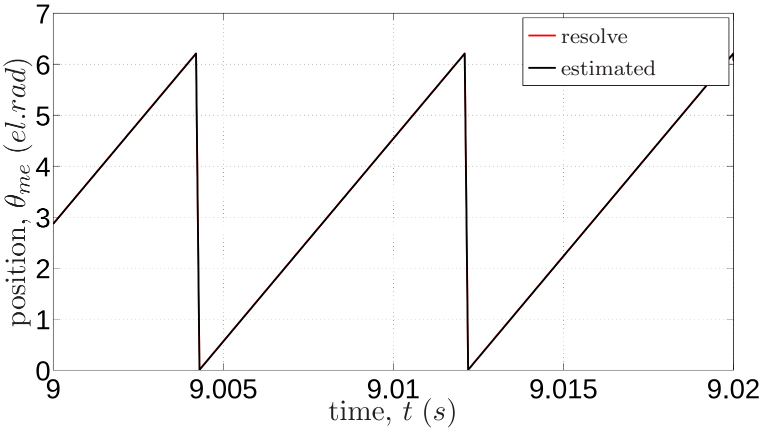

Figure 4.5: Comparison of the actual and estimated rotor position at 3800 rpm (simulation)

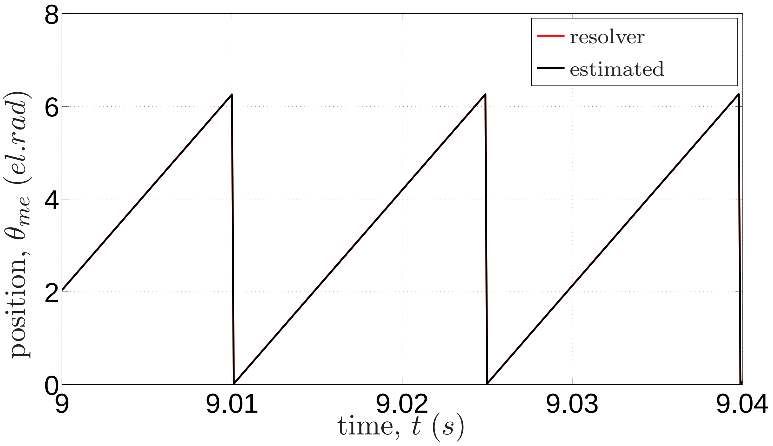

Figure 4.6: Comparison of the actual and estimated rotor position at 2000 rpm (simulation)

a PWM inverter) connected to a PM motor closed on a resistive bank, to emulate the propeller mechanical load (a quadratic relationship between power and speed instead of a cubic one is here obtained).

The results of the estimated position provided by the bemf-based MRAS algorithm, compared with the actual angular position (measured by a resolver), are shown in Fig. 4.8 at the speed of 1400 *rpm*.

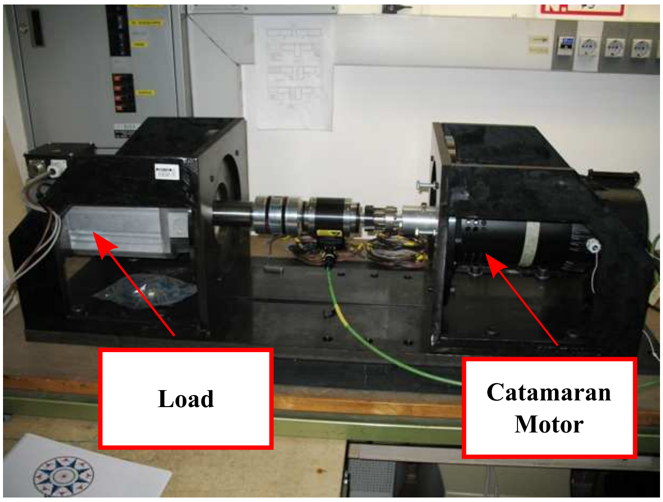

Figure 4.7: Catamaran motor test-bench

The experimental tests confirm the simulated results, showing the suitability of the sensorless algorithm to the considered application. The position error with respect to resolver measurement is about 0.13 *el.rad* and could be due to resolver inaccuracy alignment and/or voltage inaccuracy information (voltage references are used instead of measured values). However, the suspected position error does not cause any remarkable deterioration of the drive performance and torque to current operating ratio. The good performance is also confirmed by the estimated speed reported in Fig. 4.9 compared with the actual one.

In order to verify the sensitivity of the algorithm some tests have been done with three different value of resistance R and stator inductance L in the MRAS model. As reported in (4.8) and (4.9) the position error $\tilde{\theta}_{me} - \theta_{me}$ should depend on the stator inductance error but not on the resistance error. This is experimentally pointed out in the Fig. 4.10 and Fig. 4.11. Varying the stator resistance, the mean error remains around the 0.13 *el.rad*, instead varying the inductance the error changes. When the model inductance is zero ($\Delta L/L = -1$) the error is equal to 0.11 *el.rad*; instead if the inductance is four times the nominal value ($\Delta L/L = 3$) then the error is about 0.16 *el.rad*. With nominal parameters and test current level, using (4.9) the theoretical sensitivity is obtained as:

$$\overline{S}_e^L = \frac{L|\overline{I}|}{|\overline{\Lambda}_{mg}|} = \frac{1 \cdot 10^{-3} \cdot 5}{0.304} = 0.0167 \tag{4.10}$$

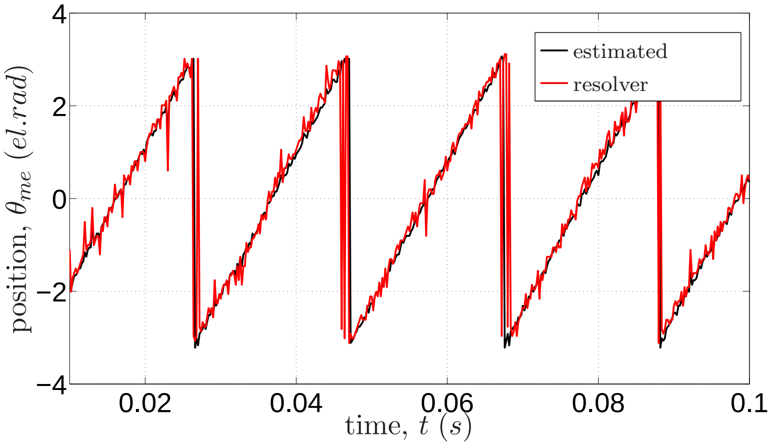

Figure 4.8: Comparison of the measured and estimated rotor position at 1450 *rpm* (experimental)

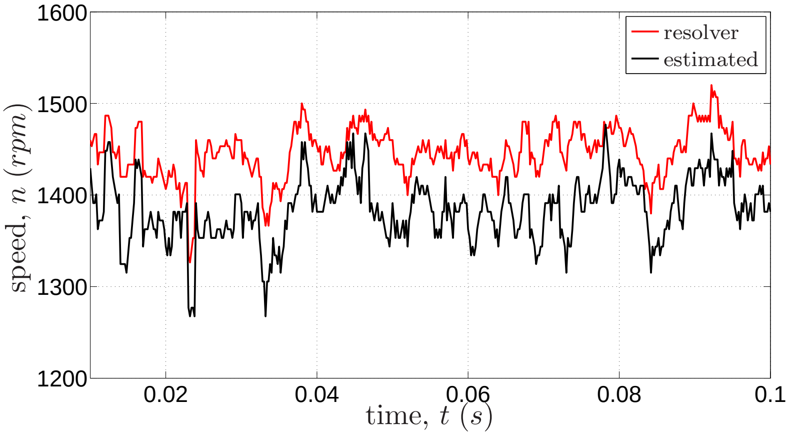

Figure 4.9: Comparison of the measured and estimated rotor speed (experimental)

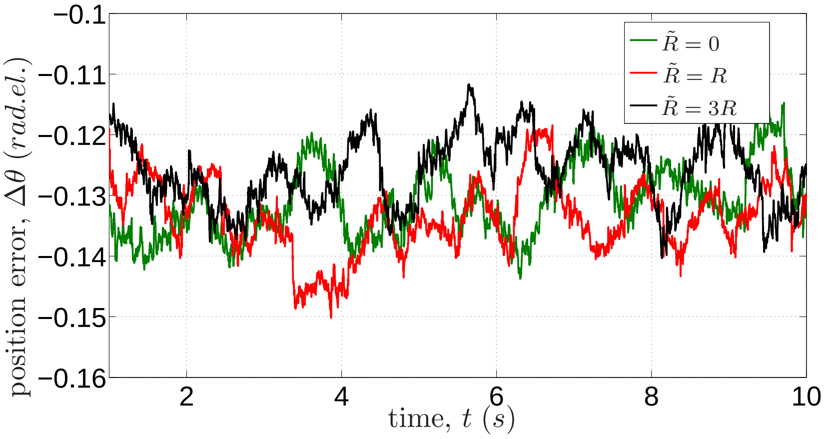

Figure 4.10: Electrical position error at different stator resistances at 1450 *rpm* (experimental)

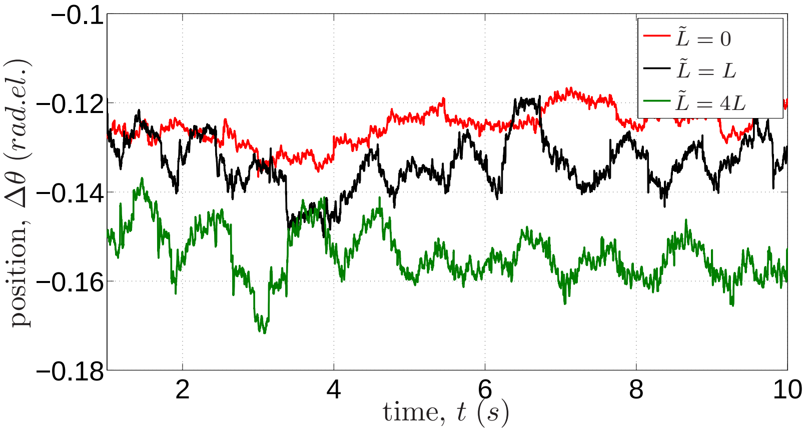

Figure 4.11: Electrical position error at different stator inductances at 1450 *rpm* (experimental)

which is very close to that derived by the experimental results, namely:

$$\overline{S}1_e^L = \frac{\Delta\theta}{\frac{\Delta L}{L}} = \frac{0.16 - 0.11}{3 - (-1)} = \frac{0.05}{4} = 0.0125 \tag{4.11}$$

Drive behaviour has been tested also by emulating a series of step changes of skipper command. Fig. 4.12 shows the corresponding quadrature current reference signal and the resulting motor speed under sensorless operation. One can realize that by increasing the current reference, the motor accelerated reaching 2000 *rpm* with a reference current of 8 *A*. One can also realize the good correspondence between the estimated speed and the actual one and the overall good performance of the drive.

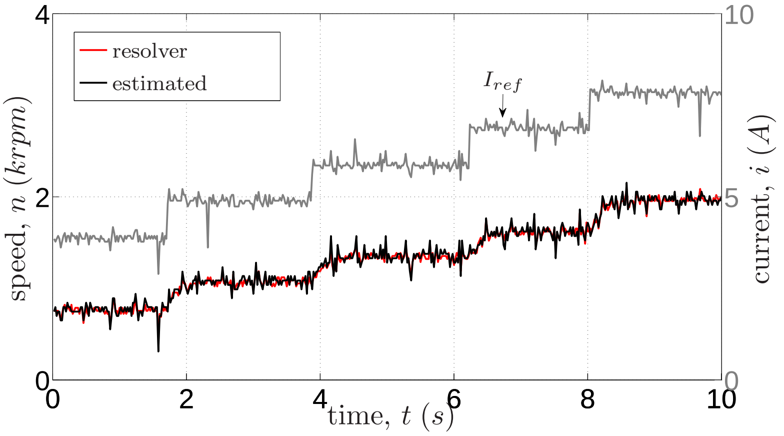

Figure 4.12: Comparison of the measured and estimated rotor speed at different current references

4.6 Peculiar requirements of the application

Peculiar drive requirements come out in a sensorless application for a catamaran system. The first problem is the start-up phase; the initial position of the rotor is unknown and the bemf vector is null, then the estimation of the position by the proposed algorithm is impossible. In fact, it is well known that the main drawback of this type of sensorless rotor estimation algorithm is its impossibility to estimate the position in the low speed range and at standstill.

Therefore, the motor has to be started imposing a rotating current vector (open–loop operation) and, when the speed reaches a threshold value above which the sensorless algorithm works properly, the estimated position is used to synchronize the currents (closed–loop operation). In addition, a dedicated procedure has been designed that allows a smooth speed reversal to be obtained, switching from open–loop and closed–loop operation according to speed and current signs and levels.

4.6.1 Detail on start–up

As reported before, the MRAS system doesn't work at zero and low speed, then a particular algorithm has to be implemented for the start–up of the machine. The motor is started up with an imposed speed ramp and the position obtained by its integration is uses in the reference frame transformation matrixes.

Therefore during the open loop start-up phase the currents i_d and i_q managed by the current control loops are not referred to the reference frame fixed with the rotor but in a generic synchronous frame, the position of which is defined by the torque level. When the speed ramp reaches the imposed final value, the estimated speed is compared with the imposed speed and if the two signals are equal, within an acceptable tolerance, it is assumed that the position is estimated correctly and the control is closed to the estimated position.

In Fig. 4.13 and 4.14 the behaviour of the estimated and measured speed and the estimation error in the start–up phase are reported. One can note that at the end of the ramp the estimated speed reaches the ramp speed (which coincides with the measured one) and the estimated position is close to the measured one. This allows the control to move to the closed loop synchronization and then the motor accelerates because the total current is imposed correctly in the quadrature axis.

If during the start–up phase the motor torque is not high enough to run the load, then the estimated speed doesn't follow the ramp (really because the motor is blocked). Measuring the error between estimated and ramp speed it is possible to launch an alarm signal anytime the measure returns an error exceeding an acceptable level. In the Fig. 4.15 it is reported the estimated speed in the case of synchronization failure; one can not that the estimated speed doesn't reach the final value of speed ramp and then an alarm is launched in the monitoring system (Fig. 4.17) and the start–up phase in stopped. The synchronization failure is verified from the no zeroing of estimation error as shown in Fig. 4.16.

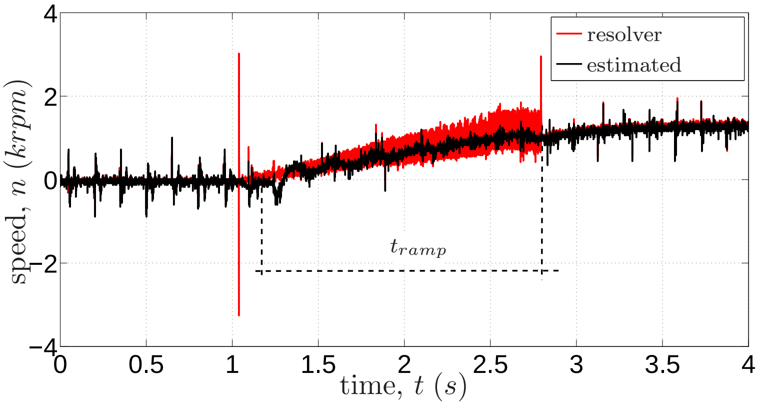

Figure 4.13: Comparison of the ramp and estimated rotor speed in the start–up phase

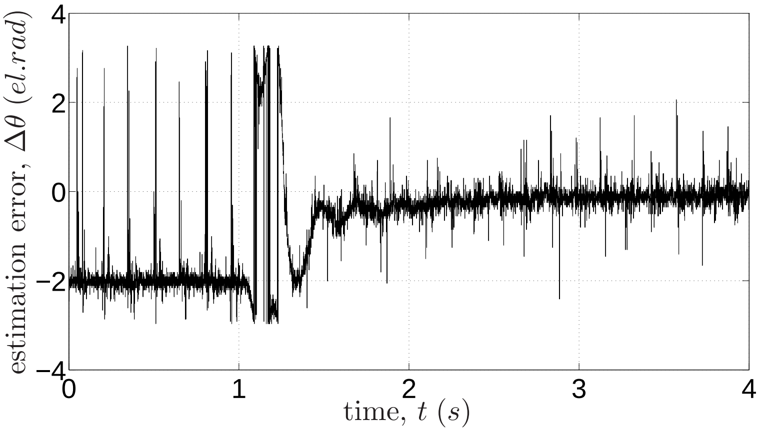

Figure 4.14: Electrical position error delivers by ramp in the start–up phase

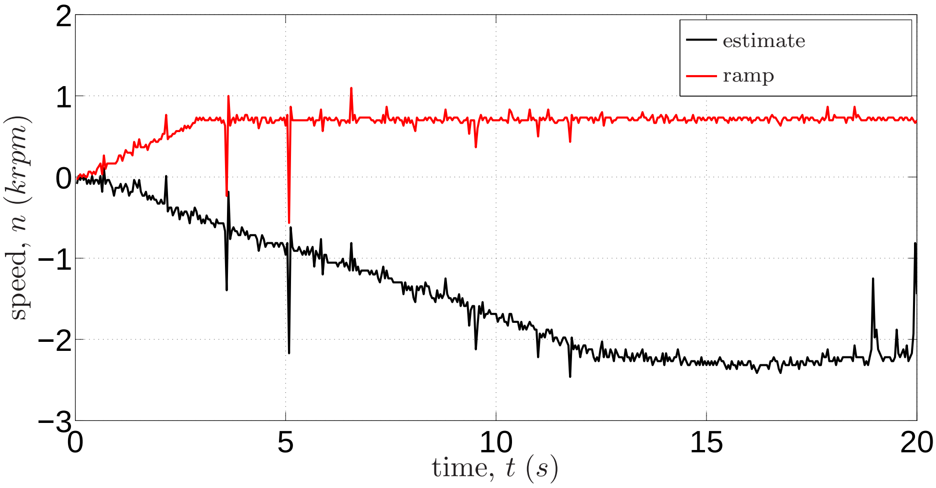

Figure 4.15: Comparison of the ramp and estimated speed in the star–up phase without synchronization

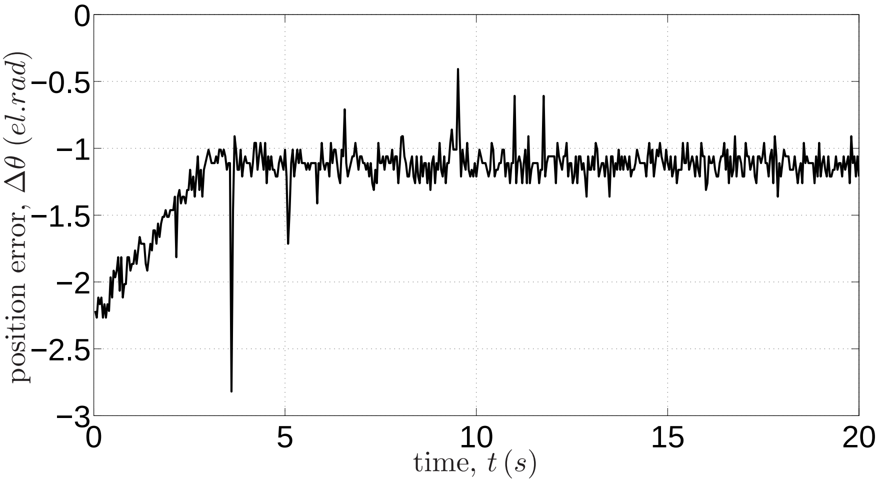

Figure 4.16: Electrical position error in the star–up phase without synchronization

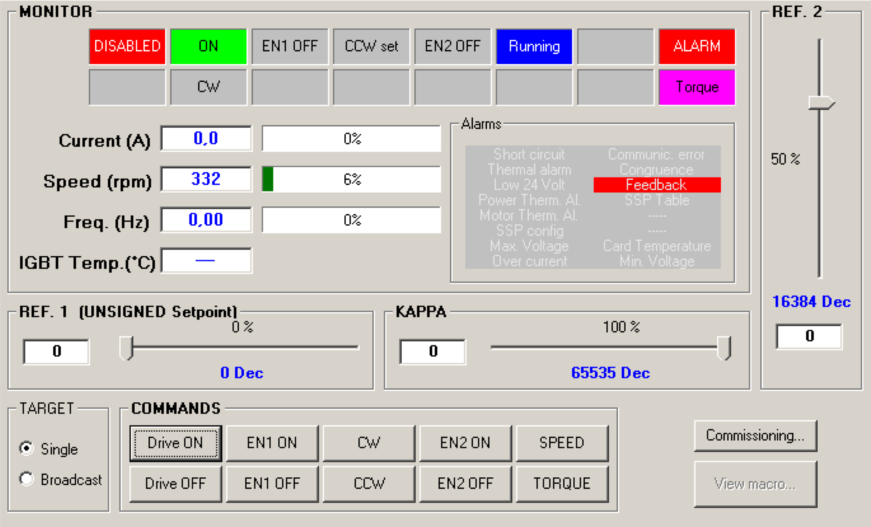

Current (A) 0,0 0%
Speed (rpm) 332 6%
Freq. (Hz) 0,00 0%
IGBT Temp.(°C) —
REF. 1 (UNSIGNED Setpoint) 0 0 % 0 Dec
KAPPA 0 100 % 65535 Dec
REF. 2 50 % 16384 Dec 0
● Single
○ Broadcast

Figure 4.17: Alarm signal in the monitoring system in the not–synchronization case

4.6.2 Details on speed reversal

The drive must have the ability to drag the propellers either in the right or in the reverse direction; then the electric motors have to rotate both in the clockwise and in the counter-clockwise direction. The control algorithm has to manage the situation of zero crossing of the speed at any speed reversal. This is obtained by moving to open loop operation when the speed falls below a threshold level, activating a start–up procedure with a ramp command speed starting from the threshold level and concluding to its opposite value.

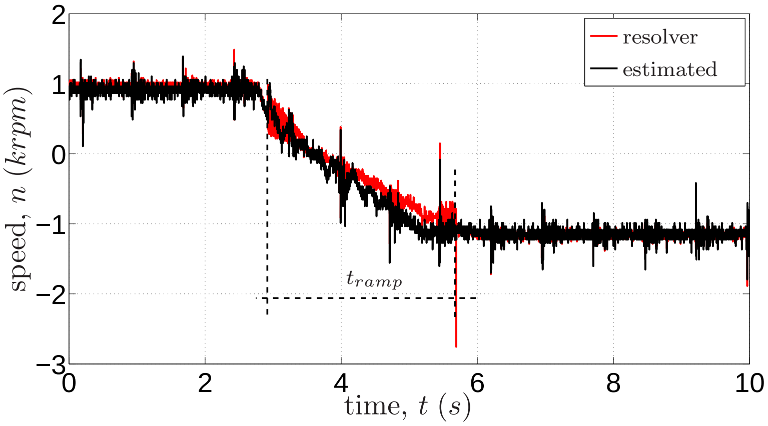

Figure 4.18: Comparison of the measured and estimated speed during a speed reversal

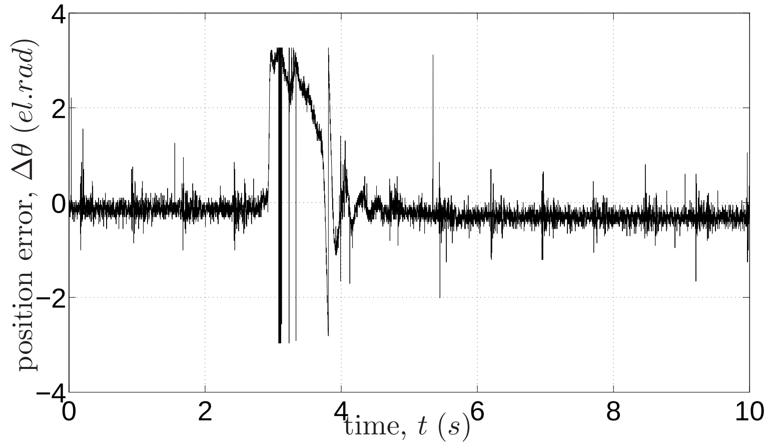

Figure 4.19: Electrical position error during a speed reversal

In Fig.4.18 it is reported the estimated speed behaviour during a speed reversal due to the changed reference quadrature current sign. Initially the reference current is positive and the motor runs with a positive speed, when the reference current becomes negative the motor decelerate and the speed decreases.

When the speed reaches an imposed minimum value Ω_{min}, the control moves from the closed loop to the open loop operation mode and a new start–up phase is started by the control. In this case the initial value of the ramp is Ω_{min} and not zero, and its slope must be negative to move the motor speed from positive to negative sign, in the way that the rotation changes the direction. After that, if the estimated speed is equal to the ramp speed, the control loop is closed again on the estimated position $\tilde{\theta}_{me}$. In Fig. 4.19 the estimation error during the speed reversal is reported. One can note that the error is not zero only during the speed reversal, i.e. when open loop control occurs.

4.7 Conclusive summary

A model–based sensorless control of a Surface–mounted permanent magnet synchronous motor drive for a hybrid catamaran has been presented. Principle and design of the rotor position estimation algorithm is at first discussed. The critical start–up mode has been deeply treated because of the MRAS limit of not working at zero and low speed. An imposed speed ramp is used to start the motor and when the sensorless estimation is converged, estimated position is used for the control loop. Proper algorithm has been developed to manage the request of propellers speed reversal.

Moreover, comparison between the analytical and experimental parametric sensitivity has been focused. A set of experimental results has been reported and they confirm the simulation results and the analytical computations.

5

High frequency injection signal sensorless based sensorless drives

5.1 Introduction

Salient–pole Permanent Magnet (SPPM) synchronous machines have become increasingly popular in recent years for a variety of emerging fields of application (as, for instance, the wide field of the more–electric–vehicles) due to their high efficiency and extended constant-power speed range. As reported in the previous chapter, the anisotropic characteristics of the rotor can be used to recognize the rotor position, also at low speed and at standstill, thus allowing any shaft sensors to be advantageously removed.

The idea of using additional voltages having frequency above the maximum motor operating frequency (thus classified as high frequency voltages) was proposed in the 90's years by [5] –[24] exploiting rotating or pulsating voltage vector. A lot of improvements to the technique was presented in the last ten years, but in spite of that it remains practicable for operation at low and null motor speed. A proposal of extending the speed range of operation was presented in [25] by using appropriate demodulation technique of the measured high frequency current and an ellipse rotating voltage vector. In this chapter the technique of ellipse rotating voltage vector injection to the stator in a guess two-axis reference frame d^x,q^x, which is then regulated to converge to the d,q reference frame oriented to the rotor polar axis, is taking into consideration. This type of injected stator voltage vector causes a current response independent on motor speed and can be thus used at any speed. Of course it requires that an inverter voltage margin be reserved to the sensorless position estimation purpose.

A crucial aspect of all the above techniques is the processing applied to the high frequency currents measured at the motor terminals. Generally speaking it requires a demodulation stage to isolate a quantity which contains information on rotor position and then the extraction of such a position. A simple demodulation process that nullify the quadrature high frequency current in the d^x,q^x reference frame is used on the following to extract the rotor position. This approach results very effective and seems well suited for an industrial application.

Sensorless oriented rotor designs have been also proposed recently, and impact of rotor geometry on sensorless rotor position detection by high frequency signal injection are here investigated [26] –[30].

On the follow the behaviour of two of the principal sensorless oriented rotor configurations (IPM and XPM machines) are experimented. The measured accuracy with that predicted by the finite element simulations carried out during the motor design are compared. Effects of iron saturation on $d-$ and $q-$ axes and cross–saturation as well are deeply investigated and discussed. As a result, additional hints to the motor design can be derived. Some parasitic effects as inverter dead-time are also considered.

5.2 Simulation and experimental results

5.2.1 Essential of high frequency voltage injection technique

Rotor position sensorless techniques used in salient-pole PM synchronous motor drives utilize additional high frequency voltages to recognize the position of the anisotropic rotors as described in Sec. 3.5.

The motor is controlled in a generic two–axis reference frame d^x, q^x, whose position θ_x^s with respect to the stator, is the estimated rotor position $\tilde{\theta}_{me}$ that has to be forced to coincide with the actual θ_{me} rotor position (that is the electrical position of the rotor polar axis).

Because of the injection of the high frequency voltage u_{hd} and u_{hq}, the high frequency current components result:

$$i_{hd}^x = \frac{U_{hd}}{\omega_h}\left(\frac{l_\Sigma + l_\Delta \cos 2\Delta\theta}{l_d l_q}\right)\sin\omega_h t \tag{5.1}$$

$$i_{hq}^x = -\frac{U_{hd}}{\omega_h}\left(\frac{l_\Delta \sin 2\Delta\theta}{l_d l_q}\right)\sin\omega_h t \tag{5.2}$$

with $l_\Sigma = (l_q + l_d)/2$, $l_\Delta = (l_q - l_d)/2$.

Eqs. (3.31) and (3.32) represent the steady–state components of a *pulsating vector* in the d^x, q^x frame, the orientation of which depends on the estimated position with respect to the actual one. With the scheme of Fig. 3.6 it is possible to obtain the estimated speed and position starting from i_{hq}, after a suitable demodulation. The sensorless drive control scheme resulting is then that of Fig. 5.1. In the upper part of the scheme it is possibile to note the injection of the high frequency voltages (reference) added to the main reference voltages that feed the motor.

The more external loop is for the speed control which is closed on the estimated speed $\tilde{\omega}_{me}$. The PI speed regulator delivers the reference signal i_q^* for the quadrature current control loop. This is compared with the current i_q^x that has not harmonics at the frequency ω_h as they are nullify by the position estimator. Finally a control loop for the direct current component i_d^x has been designed, the reference of which is provided by Maximum Torque Per Ampere (MTPA) or Flux Weakening (FW) control. The i_d^x current feedback includes a low pass filer for removing the high frequency component. Also the i_q^x current feedback can be provided of a low pass filter, even if at steady–state the high frequency componente is null. The direct and quadrature current components are derived from the stator currents using the estimated position $\tilde{\theta}_{me}$; this is used also to transform the voltage reference delivered by current PI regulators.

5.2.2 Simulated drive behaviour

To confirm the validity of the sensorless control some simulations have been done, according to the diagram scheme reported in Fig. 5.1. For the simulations the IPM

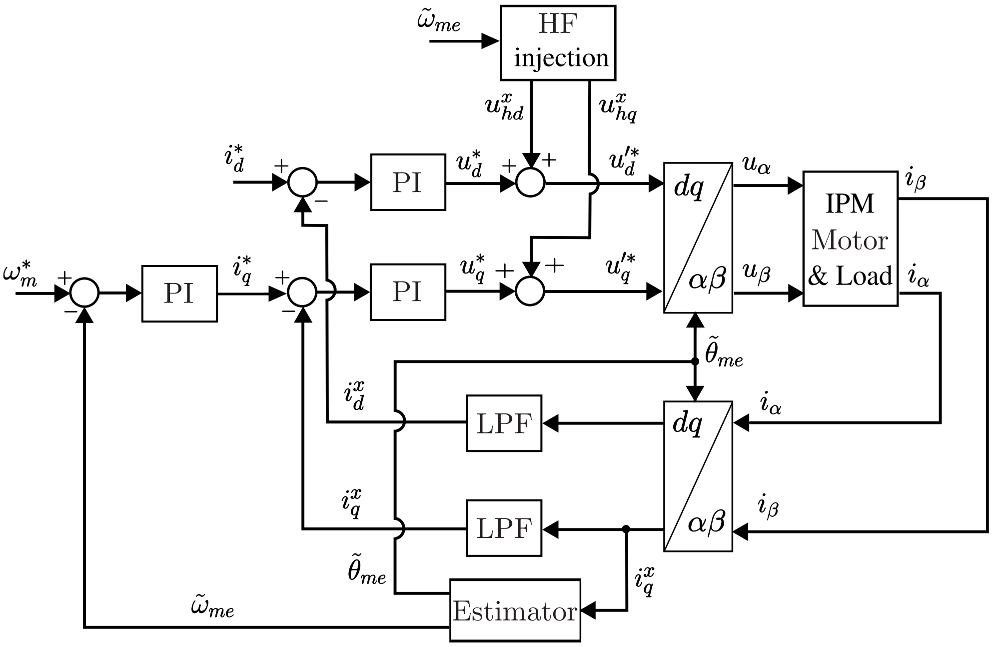

Figure 5.1: Sensorless control scheme of salient-pole PM motors with voltage injection

motor, which parameters are reported in Tab. 2.2, is taken into consideration.

For the simulations the injection pulsation of $\omega_h = 2500\ rad/s$ and a voltage $U_{hd} = 30\ V$ are used; moreover in the sensorless drive an estimated position that is displaced from the actual one of a constant angle of $\pi/3\ el.rad$ is imposed. In this way it is possible to show the effects of injection in the high frequency current components, without zeroing the q–axis component. At steady–state the mechanical speed is equal to 50 rpm and then the electrical speed ω_{me} results about 10.5 $el.rad/s$.

The two high frequency voltages injected are reported in Fig. 5.2. It is possible to note that the q–axis voltage is very smaller than the d–axis one being its amplitude given by the ratio $U_{hd}\omega_{me}/\omega_h$.

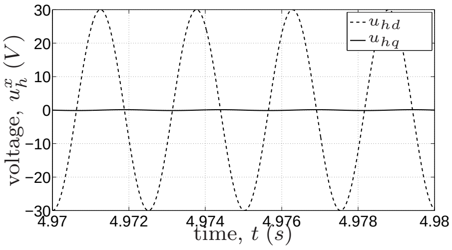

Figure 5.2: High frequency injected voltages

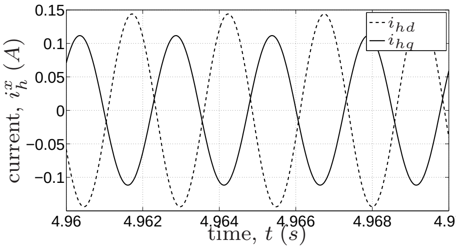

Figure 5.3: High frequency current components

As far as the currents are concerned, the high frequency components are reported in Fig. 5.3. It is possible to calculated their amplitude starting from the (5.1) and (5.2):

$$|i_{hd}^x| = \frac{30}{2500 \cdot 33e - 3 \cdot 147e - 3}(0.09 + 0.057\cos(2\pi/3) = 0.15 \quad (5.3)$$

$$|i_{hq}^x| = \frac{30}{2500 \cdot 33e - 3 \cdot 147e - 3}0.057\sin(2\pi/3) = 0.12 \quad (5.4)$$

These values are in good agrement with the simulation results reported in Fig. 5.3. Moreover, the two currents are in opposition of phase due to the minus sign in the q-axis component. The currents have of course the same period of the injected voltages, i.e. they have a pulsation of ω_h.

Multiplying the i_{hq}^x currents for $\sin\omega_h t$, error ϵ given by the (3.35) is obtained in Fig. 5.4 in dashed line. In according with the theoretical result, the signal is given by the sum of a sinusoidal wave with pulsation $2\omega_h$ and a constant offset. Finally filtering with a low pass filter, the error ϵ_{LPF} reported in (3.36) is obtained (solid line in Fig. 5.4). The error is equal to half of i_{hq}^x amplitude, in good agreement with the (3.36).

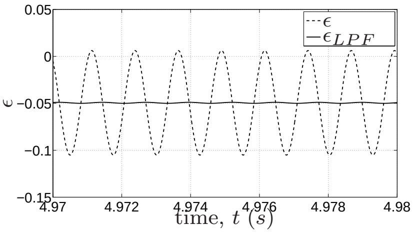

Figure 5.4: Error ϵ before and after the low pass filtering with $\Delta\theta = \pi/3$

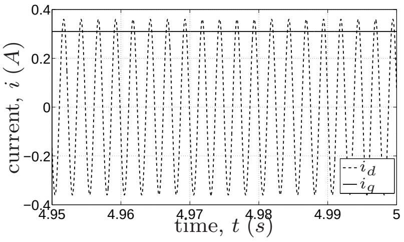

Figure 5.5: Currents i_{hd}^x and i_{hq}^x with $\Delta\theta = 0$

Second simulation has been done with the sensorless drive closed on the estimated speed and position delivered by the estimator algorithm (then with a null estimation error, i.e. $\Delta\theta = 0$). As explain in the sensorless theory, when the estimated position coincides with the actual one the q–axis current doesn't present any high frequency harmonics around the steady–state value. On the contrary the d-axis current present an harmonic at pulsation ω_h as pointed out in Fig. 5.5. The i_{hq}^x constant value is due to the q–axis current reference value imposed by the control, that is instead posed to be zero in the case of d–axis current.

An example of simulation is shown in the Fig. 5.6 where the comparison between the estimated position and the actual one is reported. One notes the good estimator performance at any speed, both at standstill and at steady–state operation. The rotor speed time behaviour and its estimation is reported in Fig. 5.7. From zero to one second, speed and currents reference are posed to be zero and only the estimator algorithm works. At one second, a reference step speed of 50 *rpm* is imposed.

One can note that the estimated position start from zero and reaches the actual one (equal to $\pi/2$) in a short time. Also when a reference speed step occurs, the estimated speed follows the real one, confirming the good behaviour of the estimation algorithm. As far as the speed is concerned, both the estimated and the actual one reaches the reference value of 50 *rpm*. In the first second there is an overshoot of 90 *rpm* of the estimated speed, but the actual one remains practically equal to zero.

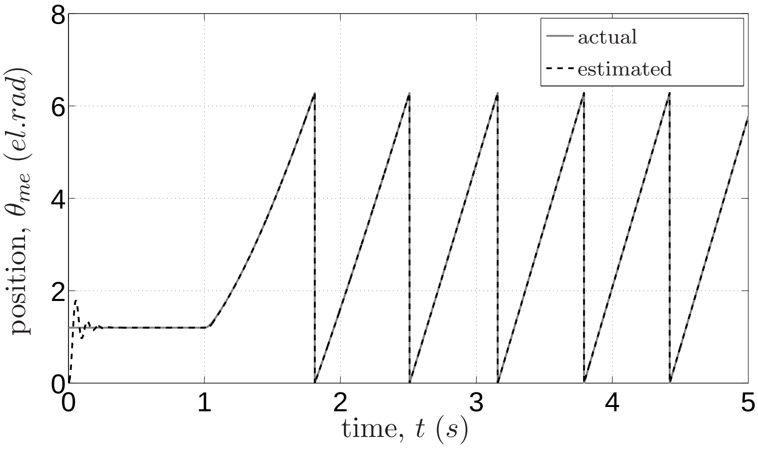

Figure 5.6: Estimated and actual position (simulation)

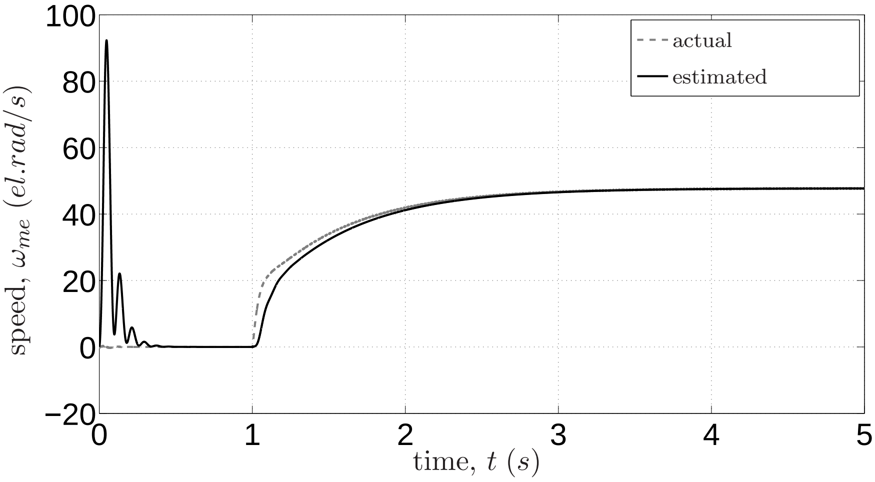

Figure 5.7: Estimated and actual speed (simulation)

5.2.3 Inverter dead time

The dead time causes an inverter voltage distortion and introduces harmonic components. To consider that, a distortion components are added to reference voltage. The real and imaginary distortion components are defined by [31]:

$$u_{\alpha,dist} = \frac{1}{3}\frac{t_d}{T_c}U_{dc}[2sgn(i_a) - sgn(i_b) - sgn(i_c)] \quad (5.5)$$

$$u_{\beta,dist} = \frac{1}{\sqrt{3}}\frac{t_d}{T_c}U_{dc}[sgn(i_b) - sgn(i_c)] \quad (5.6)$$

The effects of dead time are shows in Fig. 5.8, where the position errors with and without the dead time are represent.

One notes that with dead time the error fluctuations increase because of nonlinearity introduced on voltage, but the mean value of error does not change. Then the

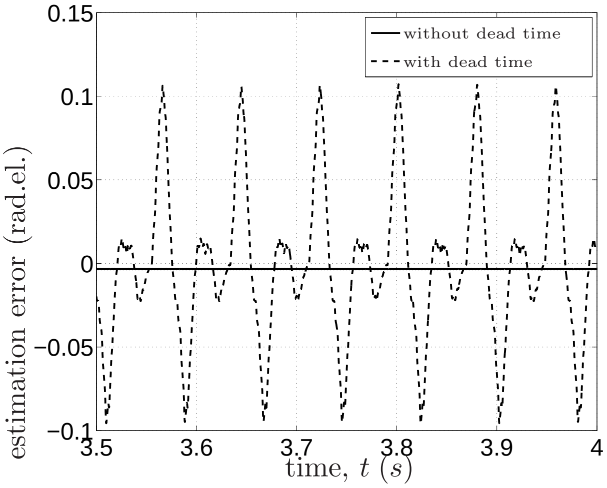

Figure 5.8: Position error trend with dead time

behaviour of the control, in simulation phase, is not dramatically influenced.

5.2.4 Measured drive behaviour

Similar tests of those in Fig .5.6 and 5.7 have been repeated in the real system, using the IPM motor with an induction motor as load. An encoder, connected to the motor, have been used to compare the estimated position with the real one. The experimental results are reported in Fig. 5.9 for the estimated and measured position and Fig. 5.10 for the speed. One can note the good correspondence between the measured and estimated quantities.

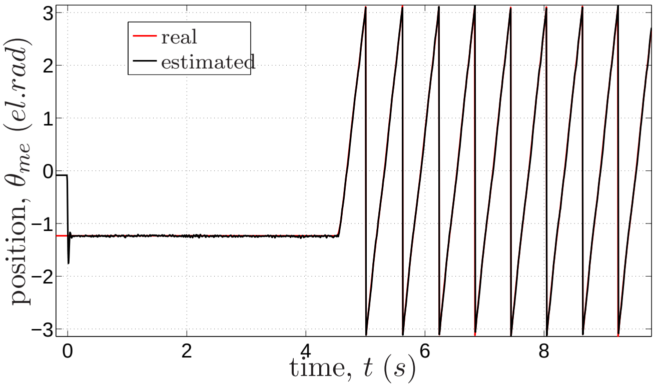

Figure 5.9: Estimated and actual position with IPM rotor (experimental)

Similar tests have been done for the XPM motor. The results are given in Fig. 5.11, 5.12, 5.13. Fig. 5.11 refers to a load torque application at zero speed. The figure shows the capability of the drive to operate properly at stand still under torque transients. Fig. 5.12, 5.13 are the time continuation of the previous figure: a step variation is

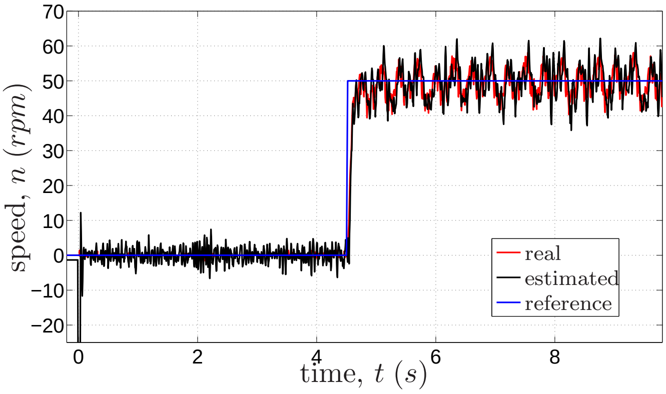

Figure 5.10: Estimated and actual speed with IPM rotor (experimental)

applied to the speed reference, causing the starting of the drive. The figures confirm the overall good performance of the drive.

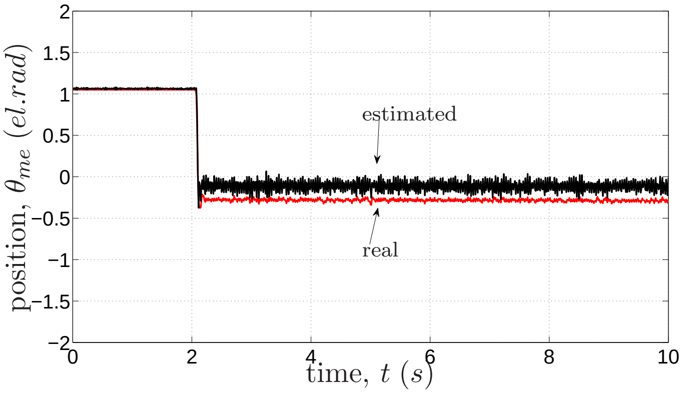

Figure 5.11: Estimated and actual position at load step with XPM rotor (experimental)

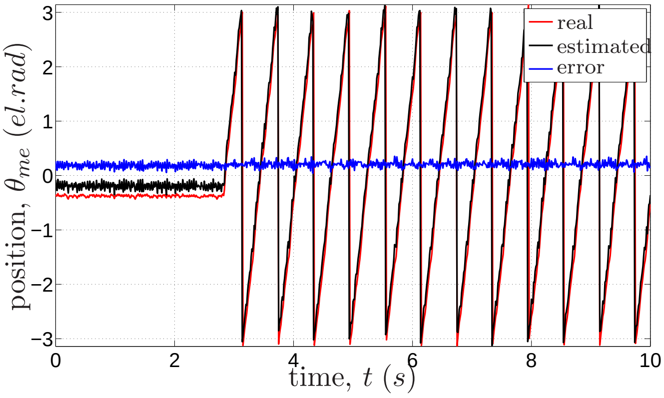

Figure 5.12: Estimated and actual position with XPM rotor at start–up (experimental)

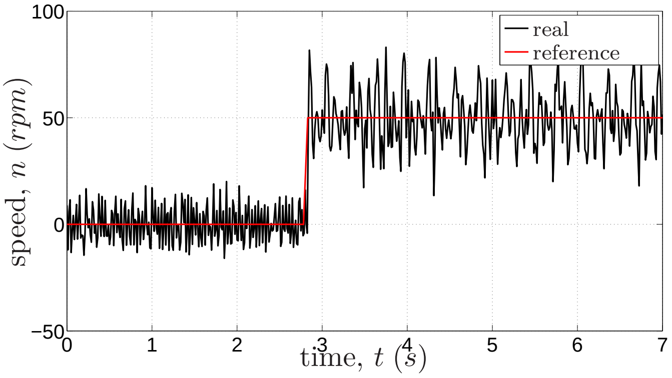

Figure 5.13: Estimated and actual speed with INSET rotor at start–up (experimental)

One can note that the estimated position presents a constant error equal to 0.2 $el.rad$. This error is due to the cross saturation between the two axes as explained in the next section.

5.3 Investigated rotor configurations

5.3.1 IPM rotor

In order to analyze and predict the motor behaviour when used into a voltage injected sensorless position detection, real flux–linkage curves have been derived and an exhaustive set of FEM Simulations have been performed.

At first let us assume that the IPM motor operates under current control at a constant speed ω_{me}. From the voltages u_d and u_q (which can be detected at the output of the d– and q– current regulators) and using the steady–state equations the fluxes result:

$$\begin{aligned} \lambda_d(i_d, i_q) &= \frac{u_q - R \cdot i_q}{\omega_{me}} \\ \lambda_q(i_d, i_q) &= -\frac{u_d - R \cdot i_d}{\omega_{me}} \end{aligned}$$

One can note that these equations need the precise knowledge of the stator resistance. Aiming to getting around this trouble, it is possible to perform this measure at two speeds ω'_{me} and ω''_{me}, keeping the same currents. By considering the equation of the direct axis voltage at two different speed values, one obtains:

$$\begin{aligned} u'_d = Ri_d - \lambda_q \omega'_{me} \\ u''_d = Ri_d - \lambda_q \omega''_{me} \end{aligned} \tag{5.7}$$

and one can derive the quadrature flux as:

$$\lambda_q(i_d, i_q) = -\frac{u'_d - u''_d}{\omega'_{me} - \omega''_{me}} = -\frac{\Delta u_d}{\Delta \omega_{me}} \tag{5.8}$$

which is not affected by the resistance.

The measures at both the speeds have been repeated imposing a current vector with

constant d– component while the q–component is varied. For each value of i_d a different q–axis Current–Flux characteristic is obtained.
The same method is valid for deriving the direct flux characteristic. In this case the quadrature current is kept constant and the other component is varied, and it results:

$$\lambda_d(i_d, i_q) = \frac{u'_q - u''_q}{\omega'_{me} - \omega''_{me}} = \frac{\Delta u_q}{\Delta \omega_{me}}$$

In Fig. 5.14 the measured flux linkage versus current characteristics are reported.

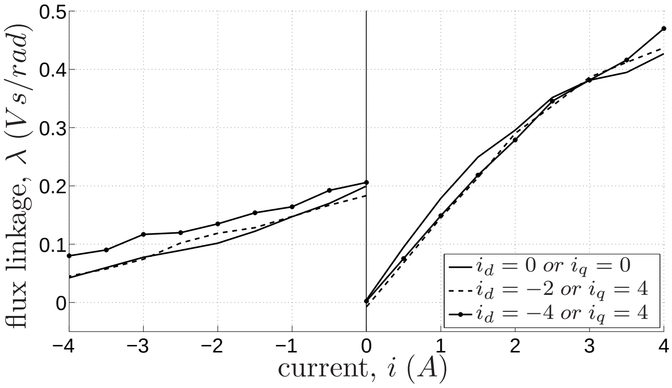

Figure 5.14: Measured fluxes–linkage characteristics of IPM rotor

The figures show the $d - axis$ flux linkage vs. $d - axis$ current, for different $q - axis$ currents in the left–hand quadrant. Instead in the right–hand quadrant the $q - axis$ flux linkage vs. $q - axis$ current for different $d - axis$ currents is reported. One can note the good correspondence between the measured and the simulated results reported in Sec. 2.2.3. The effect of the saturation along the $q - axis$ is evident, when the $q - axis$ current assumes a high value. During these operating conditions, the difference inductance l_Δ decreases rapidly toward zero and may become even negative.

This situation is pointed out by Fig. 5.15 where the two–axis differential inductances are reported. The $d - axis$ inductance is drawn by solid line, while the $q - axis$ inductance is drawn by dashed line.

The curve drawn in bold line defines the locus in the d, q plane where the difference inductance l_Δ is zero i.e. l_d is equal to l_q. For the sensorless control the feasible operating region lies below the bold curve so as to have $l_\Delta > 0$. Above that locus, i.e. when $l_\Delta < 0$, the estimation technique confuses the d-axis with the q-axis and an estimated position error of $\pm\pi/2\ el.rads.$ occurs.

As reported in (3.40) the estimated error depends also on the mutual inductance l_M; then the two–axis mutual inductance is derived from FE analysis results in order to predict the influence of cross–saturation in the position estimation.

The mutual differential inductance is reported in the i_d, i_q plane in Fig. 5.16, where the curve in bold defines the locus in which l_M is equal to zero. Exploiting the results reported in Fig. 5.15 and Fig. 5.16, it is possible to predict the estimation error $\Delta\theta$ due to cross–saturation by (3.40). The result is reported in Tab. 5.1 for some current values. The grey area refers to the experimented current ranges. A fixed $\pm\pi/2$ error has to be added for the current values above the curve $l_\Delta = 0$ as explained above.

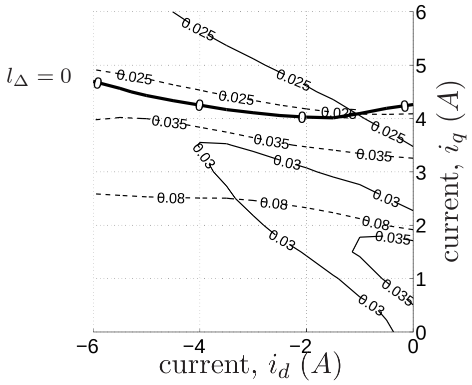

Figure 5.15: Constant direct (solid line) and quadrature (dashed line) differential inductance loci of the IPM rotor

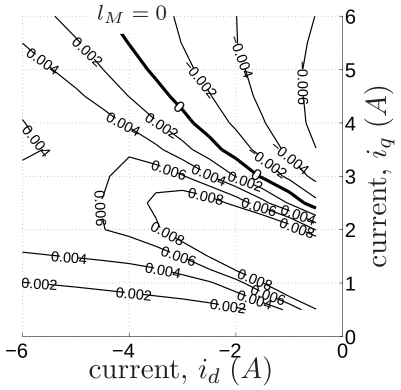

Figure 5.16: Constant mutual differential inductance loci of the IPM rotor

Table 5.1: Cross-saturation position error prediction vs. current vector of IPM rotor

$\boldsymbol{i_d}$ $\boldsymbol{i_q}$	**-6**	**-5**	**-4**	**-3**	**-2**	**-1**
6	**0.28**	**0.11**	-0.06	-0.22	-0.37	-0.49
5	**0.61**	**0.43**	**0.13**	-0.22	-0.44	-0.57
4	-0.38	-0.51	-0.63	-0.47	**0.76**	**0.76**
3	-0.14	-0.15	-0.22	-0.26	-0.12	**0.19**
2	-0.07	-0.07	-0.08	-0.12	-0.18	-0.17
1	-0.02	-0.02	-0.02	-0.03	-0.04	-0.09

The sign of the position error depends on the signs of l_Δ and l_M as results from (3.40). This is clearly pointed out in Fig. 5.17.

It is worth also to noticing that the operating point locus of the IPM motor is along the Maximum Torque Per Amps (MTPA) curves which approximately crosses diagonally the second quadrant of the d, q current plane, starting from the plane origin. Therefore MTPA curve is very near to the $l_M = 0$ locus for the IPM motor here considered, as reported in Fig. 5.17. As a consequence it will exhibits a limited position

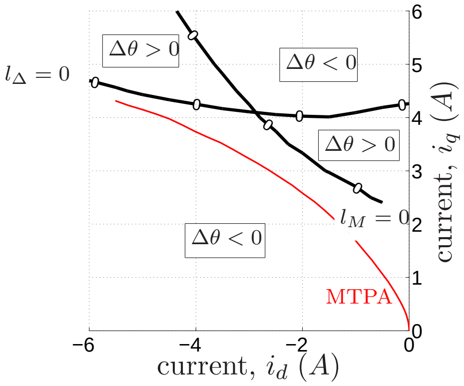

Figure 5.17: Sign of error $\Delta\theta$ in the $d-q$ plane and MTPA curve in the IPM motor

estimation error if used under MTPA operating condition, apart from at maximum torque where the operating point falls in the proximity of the critical $l_\Delta = 0$ curve.

In order to verify the simulation results, some measurements of position error have been done in the feasible area of application of the sensorless technique, by the drive reported in Fig. 5.1. The tests have been carried out with a speed reference posed to zero. The torque load has been increased in order to increase the q–axis currents. Finally, the d–axis reference current is varied from 0 to -4 in order to varying the working point of the machine.

In Tab. 5.2 the estimation errors at three different injection frequencies are reported. One can realizes that the frequency of the injected signal affects the estimation accuracy. This is due to the fact that the high frequency self and mutual inductances differ from the differential inductances computed by the stationary flux–current characteristics as done for Fig. 5.15 and Fig. 5.16. A closer behaviour between predicted and measured results occurs by increasing the frequency.

5.3.2 XPM rotor

By FE simulations applied to the geometry of Fig. 2.1(c), the flux linkage vs. current characteristics, and then the direct l_d and quadrature l_q incremental inductance and the mutual inductance l_M are derived. In Fig. 5.18 the measured flux linkage versus current characteristics are reported.

The figures show the $d-axis$ flux linkage vs. $d-axis$ current, for different $q-axis$ currents in the left–hand quadrant. Instead, in the right–hand quadrant, the $q-axis$ flux linkage vs. $q-axis$ current is reported, for different $d-axis$ currents. One can note the good correspondence between the measured results and the simulated ones reported in Sec. 2.4.1

Small signal behaviour is pointed out by Fig. 5.19 where the two–axis differential inductances are reported. The $d-axis$ inductance is drawn by solid line, while the $q-axis$ inductance is drawn by dashed line.

The curve drawn in bold line defines the locus in the d, q plane where the difference inductance l_Δ is zero i.e. l_d is equal to l_q. Also in this case of course, the feasible operating region for the sensorless control lies below the bold curve so as to have $l_\Delta > 0$. Above that locus, i.e. when $l_\Delta < 0$, an estimated position error of $\pm\pi/2$

Table 5.2: Measured position error vs. current vector of IPM rotor

(a) $\omega_h = 1675.5\ rad/s$

i_d i_q	**-4**	**-3**	**-2**	**-1**	**0**
4	-0.125	-0.125	-0.15	-0.125	**0.125**
3	-0.15	-0.15	-0.09	-0.04	**0.06**
2	-0.125	-0.1	-0.1	-0.125	-0.02
1	-0.07	-0.035	-0.04	-0.05	-0.15
0	-0.02	0	0	0	0

(b) $\omega_h = 2513.3\ rad/s$

i_d i_q	**-4**	**-3**	**-2**	**-1**	**0**
4	-0.6	-0.6	-0.6	-0.5	**0.75**
3	-0.4	-0.45	-0.4	-0.4	**0.25**
2	-0.3	-0.35	-0.3	-0.2	-0.01
1	-0.15	-0.15	-0.15	-0.15	-0.1
0	0	0	0	0	0

(c) $\omega_h = 5026\ rad/s$

i_d i_q	**-4**	**-3**	**-2**	**-1**	**0**
4	-0.4	-0.4	-0.3	**0**	**0.45**
3	-0.3	-0.3	-0.25	-0.15	**0.15**
2	-0.2	-0.22	-0.2	-0.17	-0.02
1	-0.1	-0.1	-0.08	-0.08	-0.03
0	0	0	0	0	0

electrical rads occurs. The considered XPM motor is less affected by this phenomenon as the $l_\Delta = 0$ curves can be reached only under heavy overcurrent conditions.

As reported in (3.40) the estimated error depend also on the mutual inductance l_M, then the two–axis mutual inductance is derived by FE analysis in order to verify the influence of cross–saturation in the position estimation. The mutual differential inductance is reported in the i_d, i_q plane in Fig. 5.20, where the curve in bold defines the locus in which l_M is equal to zero. In this case the sign of the position errore is pointed out in Fig. 5.21.

By applying (3.40), the estimated error of the XPM motor is predicted from the FE analysis results, and is reported in Tab. 5.3.

It is worth to noticing that the behaviour of the XPM motor is different from that of the IPM motor. In particular the MTPA curve of the XPM motor coincides with the q–axis (neglecting reluctance torque contribution) which is far from the $l_M = 0$ locus as shown in Fig. 5.21, causing a higher position estimation error due to cross-saturation than that of the IPM motor.

To verify the simulated position error, the same tests done to the IPM machine have been repeated for the XPM motor. The measured position estimation errors,

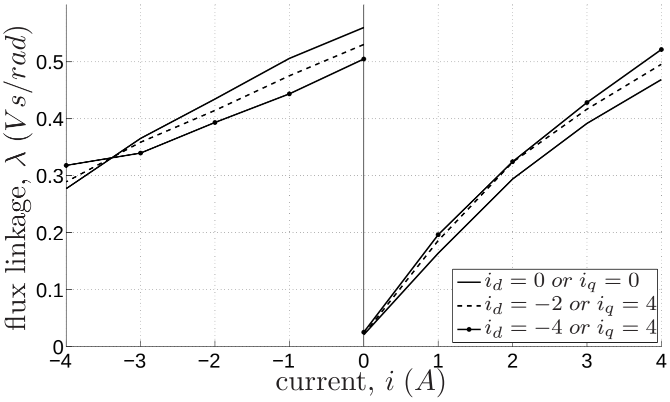

Figure 5.18: Measured fluxes–linkage characteristics of XPM rotor

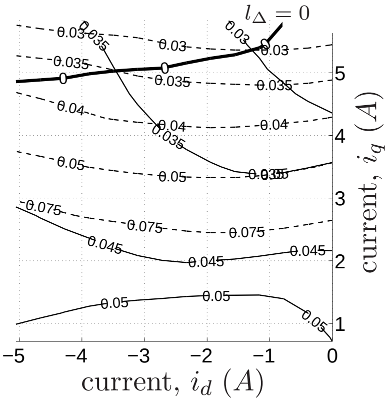

Figure 5.19: Constant direct (solid line) and quadrature (dashed line) differential inductance of XPM rotor

for three different injection frequency, are reported in Tab. 5.4. Experimental results reproduce the predicted ones quite well especially at the higher frequencies. Then with the knowing of the estimation error it is possible to compensate it with opportune technique[32].

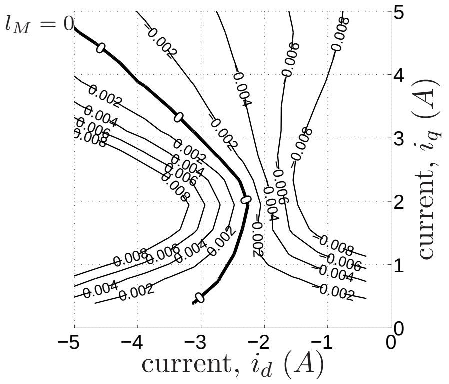

Figure 5.20: Constant mutual differential inductance of XPM rotor

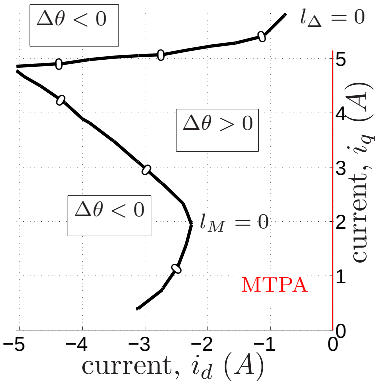

Figure 5.21: Sign of error $\Delta\theta$ in the $d - q$ plane and MTPA curve in the XPM motor

Table 5.3: Cross–saturation position error prediction vs. current vector of XPM rotor

i_q \ i_d	**-5.05**	**-4.28**	**-3.5**	**-2.7**	**-1.94**	**-1.17**	**-0.39**
5.05	**0.41**	**0.65**	**0.61**	**0.59**	**0.59**	**0.60**	**0.60**
4.28	-0.18	**0.03**	**0.26**	**0.39**	**0.45**	**0.49**	**0.54**
3.50	-0.19	-0.11	**0.00**	**0.15**	**0.27**	**0.37**	**0.44**
2.72	-0.21	-0.16	-0.09	**0.00**	**0.13**	**0.25**	**0.35**
1.94	-0.21	-0.18	-0.13	-0.05	**0.04**	**0.13**	**0.21**
1.17	-0.13	-0.09	-0.05	-0.01	**0.02**	**0.05**	**0.08**
0.39	-0.02	-0.01	0.00	**0.00**	**0.00**	**0.00**	**0.01**

Table 5.4: Measured position error vs. current vector of XPM rotor

(a) $\omega_h = 1675.5\ rad/s$

i_d i_q	**-4**	**-3**	**-2**	**-1**	**0**
4	-0.035	**0.05**	**0.07**	**0.1**	**0.1**
3	-0.01	-0.01	**0.1**	**0.15**	**0.125**
2	-0.06	**0.015**	**0.12**	**0.1**	**0.12**
1	-0.04	-0.01	**0.01**	**0.045**	**0.1**
0	-0.03	**0**	**0**	**0**	**0**

(b) $\omega_h = 2513.3\ rad/s$

i_d i_q	**-4**	**-3**	**-2**	**-1**	**0**
4	**0.1**	**0.09**	**0.2**	**0.25**	**0.3**
3	**0.05**	**0.075**	**0.15**	**0.2**	**0.25**
2	**0**	**0.02**	**0.075**	**0.15**	**0.2**
1	-0.02	**0.04**	**0.15**	**0.08**	**0.1**
0	**0.03**	**0.02**	**0**	**0**	**0**

(c) $\omega_h = 5026\ rad/s$

i_d i_q	**-4**	**-3**	**-2**	**-1**	**0**
4	**0.15**	**0.15**	**0.25**	**0.3**	**0.3**
3	**0.075**	**0.1**	**0.2**	**0.25**	**0.25**
2	-0.025	**0.05**	**0.12**	**0.15**	**0.2**
1	-0.05	**0**	**0.05**	**0.1**	**0.125**
0	**0.05**	**0**	**0**	**0**	**0.05**

6

A new configuration Ringed–Pole SPM motor for sensorless drive

6.1 Inductance measurement for different SPM rotor configurations.

As pointed out in the previous Chapter, the sensorless position control has been largely adopted with Interior Permanent Magnet (IPM) synchronous machines thanks to their anisotropic rotor that makes simpler the rotor position estimation [33] –[35]. However, from an industrial point of view, this increases the manufacturing difficulties and costs. In addition torque control is more difficult as both permanent magnet and reluctance components of torque have to be properly produced and balanced.

Differently, the Surface–mounted Permanent Magnet (SPM) synchronous machine, is preferred for its low cost and simple construction. In added its control is also easier. Unlikely, the sensorless control of SPM motors remains an unsolved issue because it exhibits an isotropic rotor configuration. Then, the SPM machine needs a position sensor for the torque control at low or zero speed, since the back electromotive force is not perceptible for sensorless purposes. As demonstrated in the Sec. 2.4, modifying the rotor in the inset configuration there is the possibility to give an anisotropic characteristic also in the SPM machine.

Another possible solution is the rotor position estimation based on the saturation due to the PM flux as explained in [18]. Practically, the saturation due to the PM flux makes anisotropic the machine at the high frequency.

In order to verify that this assertion is valid, a set of measures has been performed to estimate the d– and the q–axis inductances at both low and high frequencies.

6.1.1 Measurement schemes

The stator inductance can be measured as describe in the following. Phases b and c are supplied by means of a sinusoidal voltage at an imposed frequency, while phase a is maintained open. The impedance (modulus) is computed as the ratio between the voltage amplitude and the current amplitude. Fig. 6.1 and Fig. 6.2 show the measurement schemes with the rotor in the two different positions. The chosen supply connection generates a field orthogonal to the axis of phase a.

In the test shown of Fig. 6.1, a sinusoidal voltage is imposed between phase b and c. Since the magnetic field is along the q–axis, the quadrature axis impedance is measured. Also during the test of Fig. 6.2 a sinusoidal voltage is imposed between phase b and

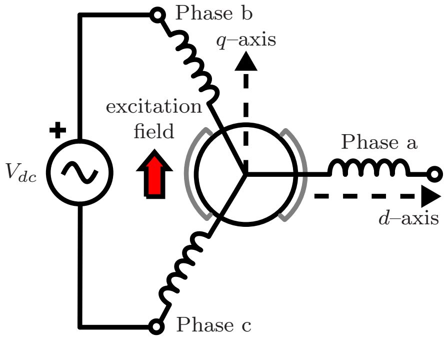

Figure 6.1: High frequency impedance measurement scheme, only q–axis current is supplied

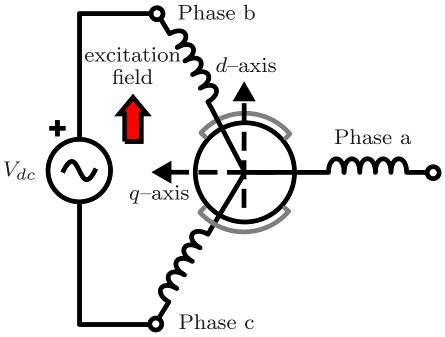

Figure 6.2: High frequency impedance measurement scheme, only d–axis current is supplied

c. However, in this case, the magnetic field is along the d–axis, and the direct axis impedance can be measured. Same tests can be made with the rotor in a generic position.

6.1.2 Test results

Using the measurement scheme reported previously, some tests have been carried out for different SPM machines. First tested motor is reported in Fig. 6.3. The main parameters of the motor, instead, are reported in Tab. 6.1.

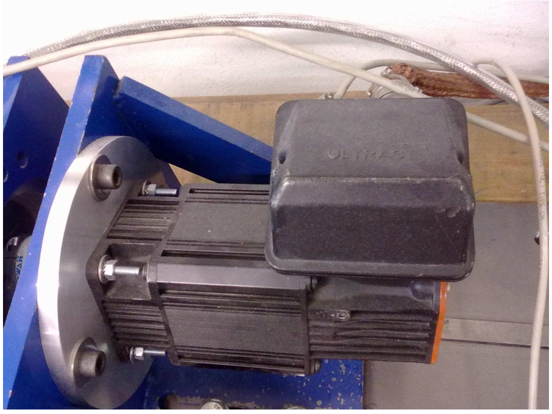

Figure 6.3: Photo of Ultract SPM machine

First test have been done imposing a sinusoidal voltage of 5 $Vrms$ between phase b and c, with the phase a open, at frequency of $f_h = 50\ Hz$. The voltage and the measured phase current are reported in Fig. 6.4(a) (with the measurement scheme of Fig. 6.2) and in Fig. 6.4(b) (with the measurement scheme of Fig. 6.1).

One can note that in the two cases the currents are practically equal, it means that the d–axis impedance is equal to the q–axis one. In both the cases the module of the stator impedance results:

$$|Z| = |R_{ff} + j2\pi f_h L_s| = \frac{U_{pk-pk}}{I_{pk-pk}} \tag{6.1}$$

Table 6.1: Electrical Parameter Ultract SPM machine

Sigla	Valore	Unità
N_{max}	4200	rpm
T_n	2.8	Nm
T_p	14.6	Nm
I_n	3.1	$Arms$
$2p$	8	
R_{ff}	3	Ω

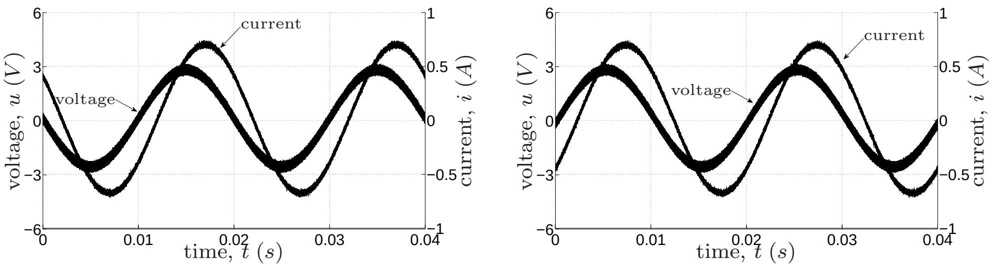

(a) Flux along d-axis

(b) Flux along q–axis

Figure 6.4: Ultract motor, tests at 50 kHz

and the phase–to–phase inductance can be computed by the knowledge of the phase to phase resistance:

$$L_s = \frac{\sqrt{|Z|^2 - R_{ff}^2}}{2\pi f_h} \tag{6.2}$$

The subscript pk–pk indicates the peak to peak values that are used in place of the peak ones in order to neglected possible offset. In another way, it is possible to apply a Fourier analysis on the signal of Fig. 6.4 and take the peak value of the first harmonic, i.e. the harmonic at the frequency of 50 Hz.

In the case of Fig. 6.4(a) it results:

$$\begin{aligned} |Z| &= \frac{5.66}{1.38} = 4.11 && (6.3)\\ L_s &= \frac{\sqrt{4.11^2 - 3^2}}{2\pi 50} = 9\ mH && (6.4)\\ L_d &= \frac{L_s}{2} = \frac{9}{2} = 4.5\ mH && (6.5) \end{aligned}$$

Instead, in the case of Fig. 6.4(b) results:

$$\begin{aligned} |Z| &= \frac{5.66}{1.37} = 4.13 && (6.6)\\ L_s &= \frac{\sqrt{4.13^2 - 3^2}}{2\pi 50} = 9.04\ mH && (6.7)\\ L_q &= \frac{L_s}{2} = \frac{9.04}{2} = 4.57\ mH && (6.8) \end{aligned}$$

Then, the saliency is obtained from the ratio L_q/L_d that is equal to 1.01.

The second test has been done at 1 kHz with a sinusoidal voltage of 20 V. The experimental results are reported in Fig. 6.5(a) for the d–axis and in Fig. 6.5(b) as regard the q–axis.

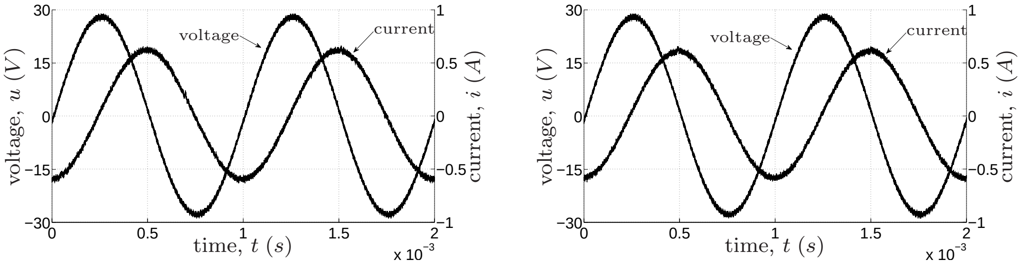

(a) Flux along d-axis

(b) Flux along q–axis

Figure 6.5: Ultract motor, tests at 1 kHz

Using the (6.1) and (6.2), the two axes inductances results:

$$\begin{aligned}
L_d &= \frac{1}{2}\frac{\sqrt{\left(\frac{U_{pk--pk}}{I_{pk--pk}}\right)^2 - R_{ff}^2}}{2\pi f_h} = \frac{1}{2}\frac{\sqrt{\left(\frac{56.56}{1.23}\right)^2 - 3^2}}{2\pi 1000} = 3.65\ mH \\
L_q &= \frac{1}{2}\frac{\sqrt{\left(\frac{56.56}{1.22}\right)^2 - 3^2}}{2\pi 1000} = 3.7\ mH \\
\xi &= \frac{L_q}{L_d} = \frac{3.7}{3.65} = 1.02
\end{aligned}$$

The tests confirms that the machine has an isotropic behaviour at all frequencies, consequently is not possible applied the sensorless technique based on the high frequency injection signal.

Another tested motor has an external rotor with two pole–pair and a stator resistance of 18 Ω. The motor hasn't a name then hereafter it is called "Motor 3" Also for this machine a tests at 50 Hz and 1 kHz have been carried out in order to derive the d– and q–axis inductances. Fig. 6.6(a) and 6.6(b) show the results for the d– and q–axis respectively, in the case of 50 Hz injected voltage.

Using (6.1) and (6.2) the d– and q–axis inductance at 50 Hz can be derived. From 6.6(a) it results:

$$|Z| = \frac{5.5}{0.28} = 19.643 \tag{6.9}$$

$$L_s = \frac{\sqrt{19.643^{-}18^2}}{2\pi 50} = 25\ mH \tag{6.10}$$

$$L_d = \frac{L_s}{2} = \frac{9}{2} = 12.5\ mH \tag{6.11}$$

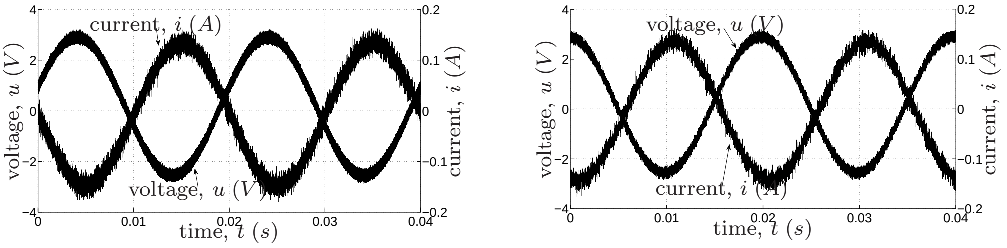

(a) Flux along d-axis

(b) Flux along q–axis

Figure 6.6: Motor 3, tests at 50 Hz

$$
\begin{aligned}
|Z| &= \frac{5.6}{0.285} = 19.65 && (6.12)\\
L_s &= \frac{\sqrt{19.65^2 - 18^2}}{2\pi 50} = mH && (6.13)\\
L_q &= \frac{L_s}{2} = \frac{9.04}{2} = 25.1\ mH && (6.14)
\end{aligned}
$$

Then, the saliency is obtained from the ratio L_q/L_d that is practical 1.

As far as tests at 1 kHz is concerned, the results are shown in Fig. 6.7. Fig. 6.7(a) is relative to d–axis and the inductance can be derived in this way:

$$
\begin{aligned}
|Z| &= \frac{28.2}{0.295} = 95.6 && (6.15)\\
L_s &= \frac{\sqrt{95.6^2 - 18^2}}{2\pi 1000} = 14.9\ mH && (6.16)\\
L_d &= \frac{L_s}{2} = \frac{14.9}{2} = 7.45\ mH && (6.17)
\end{aligned}
$$

Instead Fig. 6.7(b) reports the result for the q–axis:

$$
\begin{aligned}
|Z| &= \frac{28.22}{0.23} = 122.7 && (6.18)\\
L_s &= \frac{\sqrt{19.65^2 - 18^2}}{2\pi 50} = 19.3\ mH && (6.19)\\
L_q &= \frac{L_s}{2} = \frac{9.04}{2} = 9.7\ mH && (6.20)
\end{aligned}
$$

Then at high frequency this motor presents an anisotropic behaviour being the saliency equal to $\xi = 1.3$.

Similar experiments have been done for other different commercial SPM motors, the results are reassumed in Tab. 6.2.

For each motor are reported the poles number, the d– and q–axis inductances and the relatively saliency. The tests have been done at two different frequencies (except for the last machine in the Table): 50 Hz and 1 kHz.

The obtained results highlight that most part of the machines have an isotropic behaviour (the respectively values are in bold). The other motors, instead, present

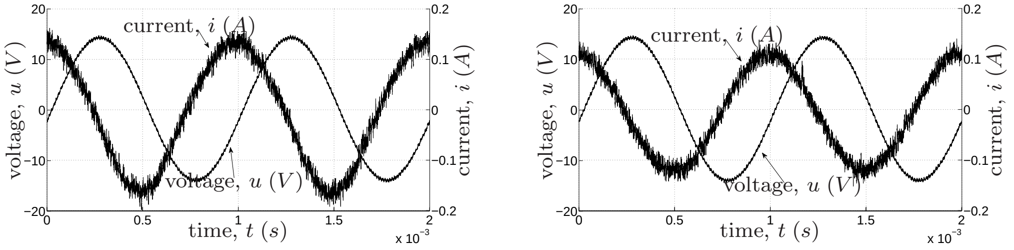

(a) Flux along d-axis (b) Flux along q–axis

Figure 6.7: Motor 3, tests at 1 kHz

Table 6.2: Saliency measurement for differently SPM rotor configurations

		f = 50 Hz			**f = 1 kHz**		
Motore	**2p**	**L_d (mH)**	**L_q (mH)**	**ξ**	**L_d (mH)**	**L_q (mH)**	**ξ**
Magnetic SPM BLQ43M36	**4**	9.94	12.8	1.29	**12.3**	**12.3**	**1**
Ultract	8	**4.51**	**4.56**	**1.01**	**3.64**	**3.71**	**1.02**
Wheel		**0.251**	**0.252**	**1.01**			
Lift	24	32	43.1	1.35	24.6	36.6	1.49
Motor 1	8	**15.1**	**15.1**	**1**	**7.08**	**7.29**	**1.03**
Motor 2	6	**7.2**	**7.1**	**1**	**6.49**	**6.58**	**1.01**
Motor 3	4	**12.5**	**12.5**	**1**	7.45	9.7	1.3
Motor 5	18	8.83	11.1	1.26	1.11	1.36	1.22
Motor 6	16	3.74	4.21	1.12	**1.09**	**1.09**	**1**
SPM Sec.2.3	6	**3.8**	**4**	**1.05**	2.75	3.18	1.15
		f = 100 Hz					
Fan	8	**3.6**	**3.6**	**1**			

an anisotropic behaviour at high frequency and, in some cases, also at low frequency. Consequently, the sensorless method based on the high frequency injection can not works properly with all the SPM motor.

A possible solution to modify the rotor configuration, in order to create an anisotropic behaviour at the high frequency, will be proposed in the next sections.

6.2 New SPM Motor Proposal

In order to perform the sensorless rotor position detection of an SPM motor, the key idea is to create a high frequency rotor anisotropy. For this purpose, a rotor cage is mounted so as to get different electromagnetic behaviours along the direct and quadrature axis. This cage is realized by providing each pole of a short circuited ring around the PM tiles as shown in Fig. 6.8.

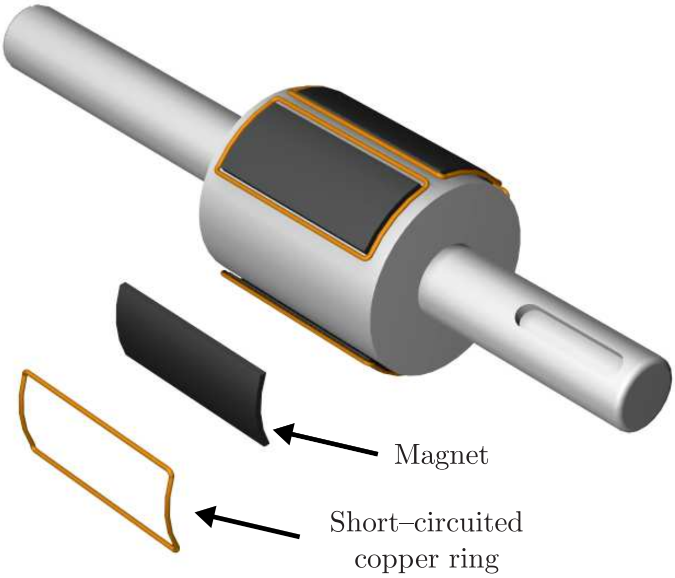

Figure 6.8: Scheme of the short–circuited ring around the magnet of an SPM motor

Some simulations by using the Finite Elements Method (FEM) have been carried out in absence of magnetic saturation. A sketch of the motor with the rotor in two different positions with respect to the supplied windings are reported in Fig. 6.9 and Fig. 6.10.

In the simulations, only two phases are supplied (phase b and phase c) by 1 kHz ac currents, so that the flux results in the direction orthogonal to the axis of the phase a. The two circles beside each rotor pole are the cross sections of the ring that is wound around the respective pole.

In Fig. 6.9 the rotor polar axis is aligned with the axis of the phase a, so that the current results along the quadrature axis only. The flux lines do not link the pole ring, therefore no current is induced.

In Fig. 6.10 the rotor is rotated of 90 electrical degrees so that the PM axis results orthogonal to the axis of the phase a. Therefore, the flux results along the direct axis. In this case, the flux due to the stator current lines links the ring, so a current is induced

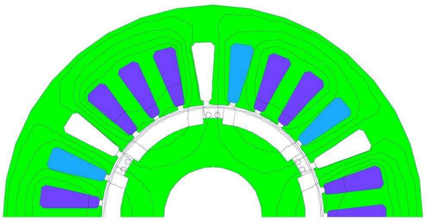

Figure 6.9: FEM analysis: quadrature axis current only

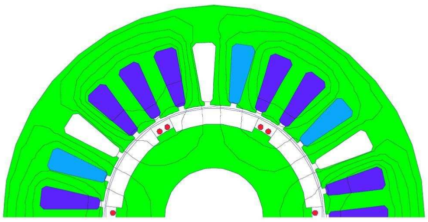

Figure 6.10: FEM analysis: direct axis current only

in the ring itself. The background color, in Fig. 6.10, highlights the high current density induced in the ring.

6.3 Electrical Circuit and Frequency Analysis

6.3.1 Equivalent Electrical Circuit

The schematic representation of the motor, in the synchronous $d - q$ reference frame, is reported in Fig. 6.11. The ring is represented by an inductance L_r because it can be considered as an additional rotor coil from the electrical point of view. In addition, the mutual inductance L_M between the ring and the d–axis stator winding is pointed out.

The SPM motor is an isotropic machine and then the direct and quadrature stator inductances are both equal to L_s. To describe completely the machine the stator resistance R_s, the coil resistance R_r and the ring current i_r are taken into account.

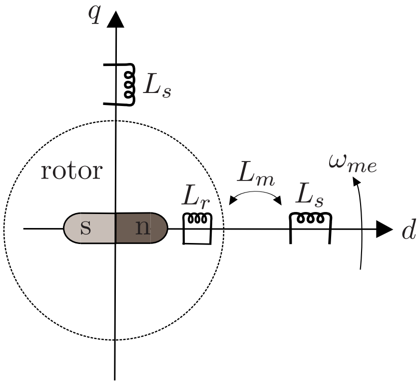

Figure 6.11: Schematic representation of the motor in the $d - q$ reference frame

Assuming a linear behaviour of the magnetic circuit (an acceptable assumption with SPM machine), the direct and quadrature flux linkages can be expressed as follows:

$$\lambda_d = L_s i_d + \mathbf{L_M i_r} + \Lambda_{mg} \tag{6.21}$$
$$\lambda_q = L_s i_q \tag{6.22}$$

The bold term represents the additional contribution in the direct flux due to the ring, given by the product between the mutual inductance L_M and the current flowing in the ring. The presence of the ring does not affect the quadrature flux linkage, which remains equal to that of a conventional SPM motor.

Using (6.21) and (6.22), the voltage equations result in:

$$\begin{aligned} u_d &= R_s i_d + L_s \frac{di_d}{dt} + \mathbf{L_M \frac{di_r}{dt}} - \omega_{me} L_s i_q \qquad (6.23) \\ u_q &= R_s i_q + L_s \frac{di_q}{dt} + \omega_{me}(L_s i_d + \mathbf{L_M i_r} + \Lambda_{mg}) \\ \mathbf{u_r = 0} &= \mathbf{R_r i_r + L_r \frac{di_r}{dt} + L_M \frac{di_d}{dt}} \qquad (6.24) \end{aligned}$$

where R_r is the total resistance of the six ring series and L_r is the ring inductance. Terms due to the ring are again written in bold. The first two equations report the direct and quadrature axis voltages balance. The third one reports the ring voltage that is posed to be zero because the ring is short circuited.

6.3.2 High frequency analysis

In the proposed machine, the rotor anisotropy is a function of the frequency. In order to derive an analytical model, all speed–dependent voltage terms are ignored in (6.23) and (6.24), because the rotor speed is assumed to be zero. Injecting a stator voltages of the type

$$\begin{aligned} u_{hd} &= U_d \cos \omega_h t \qquad (6.25) \\ u_{hq} &= U_q \sin \omega_h t \qquad (6.26) \end{aligned}$$

and neglecting the stator resistive voltage drop, the (6.23)–(6.24) become:

$$\begin{aligned} u_d &= L_s \frac{di_d}{dt} + L_M \frac{di_r}{dt} \qquad (6.27) \\ u_q &= L_s \frac{di_q}{dt} \qquad (6.28) \\ 0 &= R_r i_r + L_r \frac{di_r}{dt} + L_M \frac{di_d}{dt} \qquad (6.29) \end{aligned}$$

From these equations the equivalent circuits of direct and quadrature axis result those drawn in Fig. 6.12(a) and 6.12(b), respectively.

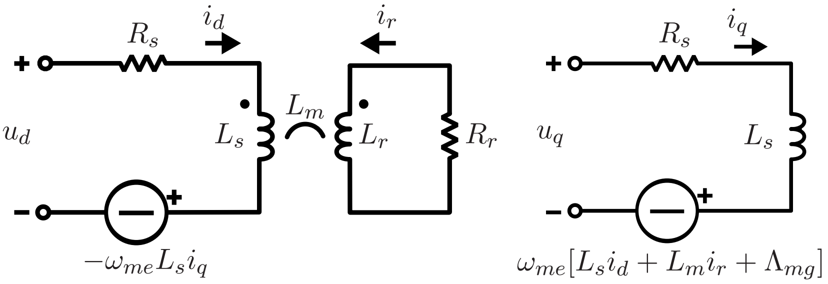

(a) d–axis (b) q–axis

Figure 6.12: Equivalent circuits in the $d - q$ reference frame.

Eqs. (6.27)–(6.29) can be computed at steady state ac operation at angular frequency ω_h.

$$\begin{aligned} \bar{U}_d(j\omega_h) &= j\omega_h L_s \bar{I}_d(j\omega_h) + j\omega_h L_M \bar{I}_r(j\omega_h) && (6.30)\\ \bar{U}_q(j\omega_h) &= j\omega_h L_s \bar{I}_q(j\omega_h) && (6.31)\\ 0 &= R_r \bar{I}_r(j\omega_h) + j\omega_h L_r \bar{I}_r(j\omega_h) + j\omega_h L_M \bar{I}_d(j\omega_h) && (6.32) \end{aligned}$$

As far as the q–axis impedance is concerned, it is easily computable starting from (6.31):

$$\dot{Z}_q(\omega_h) = \frac{\overline{U}_q(\omega_h)}{\overline{I}_q(\omega_h)} = j\omega_h L_s \tag{6.33}$$

As regard the d–axis impedance, instead, it is given by the ratio between $\bar{U}_d(\omega_h)$ and $\bar{I}_d(\omega_h)$. The (6.32) can be rearranged as follow:

$$\bar{I}_r(\omega_h) = -\frac{j\omega_h L_M \bar{I}_d}{R_r + j\omega_h L_r} \tag{6.34}$$

Substituting (6.34) in (6.30) results:

$$\begin{aligned} \bar{U}_d(\omega_h) &= j\omega_h L_s \bar{I}_d(\omega_h) + \frac{\omega_h^2 L_M^2 \bar{I}_d(\omega_h)}{R_r + j\omega_h L_r} && (6.35)\\ &= j\omega_h L_s \bar{I}_d(\omega_h)\left[1 + \frac{\omega_h^2 L_M^2}{j\omega_h L_s (R_r + j\omega_h L_r)}\right] && (6.36)\\ &= j\omega_h L_s \bar{I}_d(\omega_h) \frac{R_r + j\omega_h L_r - j\omega_h \dfrac{L_M^2}{L_s}}{R_r + j\omega_h L_r} && (6.37) \end{aligned}$$

Then, the d–axis impedance can be expressed as:

$$\dot{Z}_d(\omega_h) = \frac{\overline{U}_d(\omega_h)}{\overline{I}_d(\omega_h)} = \frac{j\omega_h L_s}{\dot{\xi}(\omega_h)} \tag{6.38}$$

where

$$\dot{\xi}(\omega_h) = \frac{\dot{Z}_q(\omega_h)}{\dot{Z}_d(\omega_h)} = \frac{R_r + j\omega_h L_r}{R_r + j\omega_h L_{rt}} \tag{6.39}$$

is the high frequency saliency and

$$L_{rt} = L_r - \frac{L_M^2}{L_s} \tag{6.40}$$

is the rotor transient inductance.

One can note that the q–axis inductance is constant and equal to the stator inductance L_s. On the contrary, the d–axis equivalent inductance is a function of the frequency, given by the ratio between L_s and the saliency $\dot{\xi}(\omega_h)$.

The amplitude and the phase of $\dot{\xi}(\omega_h)$ versus ω_h are reported in Fig. 6.13. At low frequency, the amplitude of $\dot{\xi}(\omega_h)$ is equal to 1 and then the d–axis inductance is equal to L_s from (6.38), that is equal to the q–axis inductance. At high frequency

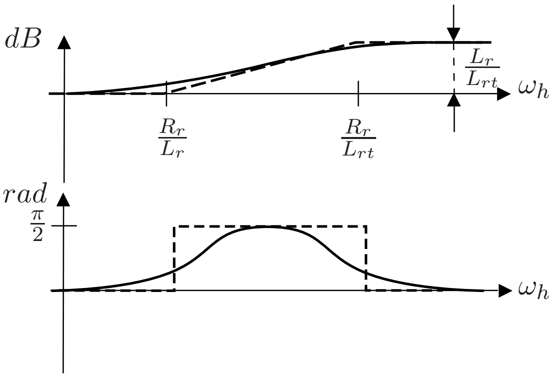

Figure 6.13: Frequency response of the saliency $\dot{\xi}(\omega_h)$

$(\omega_h > R_r/L_r)$, the $\dot{\xi}(\omega_h)$ amplitude increases. The maximum ratio between the q–axis inductance and the d-axis inductance is:

$$\frac{L_r}{L_{rt}} = \left(1 - \frac{L_M^2}{L_r L_s}\right)^{-1} = (1 - k^2)^{-1} \tag{6.41}$$

where k is the coupling coefficient between stator and rotor d–axis coils. It results that a high coupling coefficient is required to obtain high frequency rotor anisotropy.

Thus, the rotor exhibits an electromagnetic anisotropy due to the ringed–pole structure, which can be detected by means of a position sensorless identification technique based on rotor anisotropy.

6.4 Experimental results

From the analysis above, the effective possibility to realize a rotor anisotropy has been envisaged. A machine prototype has been realized for laboratory verifications.

To this purpose, the rotor of a conventional six–pole SPM machine has been modified. A short circuited copper ring has been placed around each pole in order to modify the d–axis flux linkage dynamic model. A scheme of the machine pole arrangement is reported in Fig. 6.8.

Fig. 6.14 shows the rotor prototype, characterized by the ringed–poles.

Figure 6.14: SPM rotor with ringed–poles

6.4.1 Low and high frequency impedance measurements

In order to obtain the low frequency (or dc) inductance, the method described in Sec. 1.5 has been taken into consideration. Tests have been carried out dragging the machine at two speeds 300 rpm and 600 rpm. The resulting flux characteristics are shown in Fig. 6.15. In the left half plane are reported the d–axis flux linkage and in the right half plane the q-axis flux linkage. Same experiment has been done for the machine without the ring and the results are reported in the Fig. 6.16. Once again, the d– and the q–axis flux linkage are shown in the left and right half plane respectively.

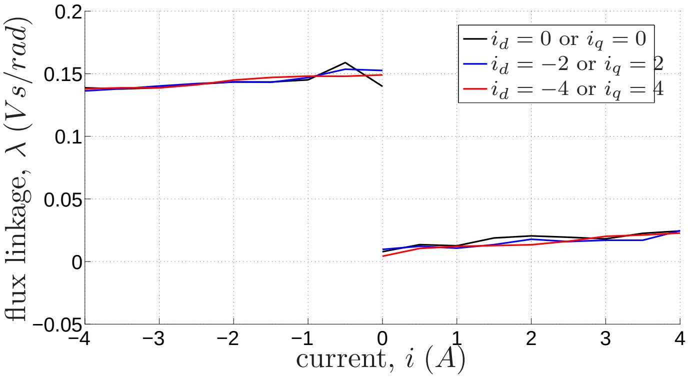

Figure 6.15: Measured d– and q–axis current–flux characteristics of the ringed–pole motor: $\lambda_d(i_d, i_q)$ on the left half plane, $\lambda_q(i_d, i_q)$ on the right half plane

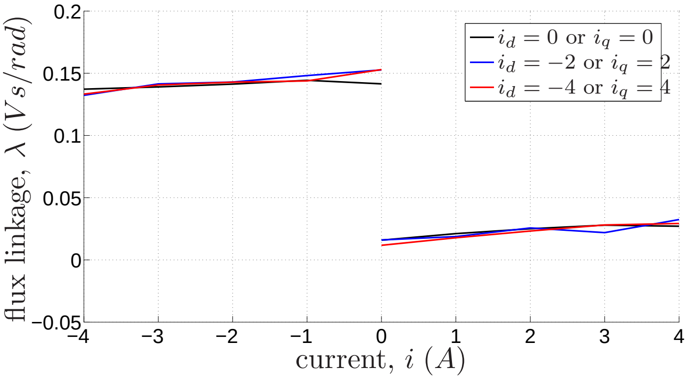

Figure 6.16: Measured d– and q–axis current–flux characteristics of the motor without the ring: $\lambda_d(i_d, i_q)$ on the left half plane, $\lambda_q(i_d, i_q)$ on the right half plane

One can note the good agrement between the flux characteristics of the two machine. For both the cases it is possible compute a d–axis inductance equal to about 3.8 mH and q–axis inductance of about $4\,mH$.Cosequently, the resulted saliency is equal to 1.02. This result confirm the fact that the ring doesn't affect the electromagnetic behaviour in the low frequency region. Moreover, experimental results are in good agreement with the simulated ones shown in Fig. 2.18 and 2.19 in the Sec. 2.3.2. The simulation results validates the experimental tests.

In order to obtain the high frequency inductance, the tests described in the Sec. 6.1.1

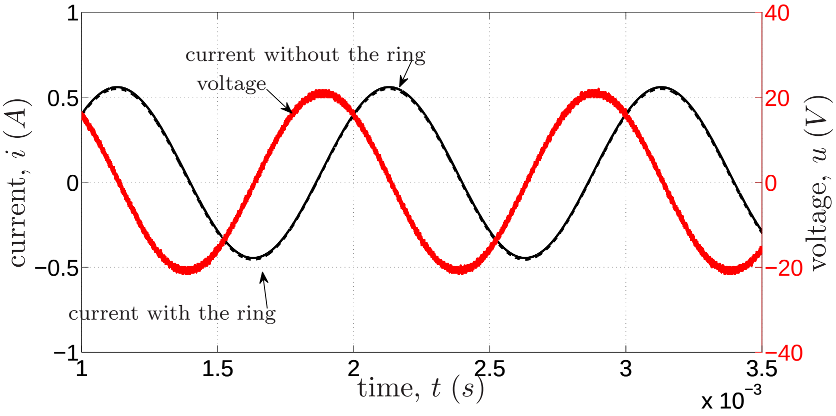

Figure 6.17: Supplied stator voltage and stator current response, test with rotor aligned as Fig. 6.1

have been repeated to measure the motor impedance at different rotor position. Phases b and c are supplied by means of a sinusoidal voltage at frequency of 1 kHz and peak value of 20 V, while phase a is maintained open. The measures have been made both the prototype machine and the motor without the ring.

The measured current and voltage are reported in Fig. 6.17 and 6.18. First figure reports the case where only q–axis is excited (measurement scheme of Fig. 6.1). The measured currents result to be the same, for both the prototype rotor and the standard rotor. Since the currents in the two cases have the same amplitude; it means that the two q–axis inductances are equal.

In the case of Fig. 6.18 the magnetic field is along the d–axis, and the direct axis impedance can be measured (measurement scheme of Fig. 6.2). It is worth noticing that the amplitudes of the currents are different. Adopting the ringed–pole rotor the current is higher, as expected, for a given voltage.

In addition, the q–axis current results higher than the d–axis current, Fig. 6.18, verifying that the d–axis inductance is lower than the q–axis one.

Similar tests have been carried out for different positions of the rotor, moving it by steps of 15 electrical degrees. The results are plotted in Fig. 6.19. The dashed and the solid lines refer to the motor without and with the ring, respectively. The inductance of the two phases is derived by the ratio between the voltage and the current (the peak to peak values are used to cancel dc offset), for each electrical rotor position θ_{me} (according to the procedure illustrate in Sec. 6.1.2).

Electrical position equal to 0 electrical degrees identifies the situation where the direct axis is aligned with the stator excitation flux. Electrical position equal to 90 $el.deg.$ means that the quadrature axis is aligned with the stator flux. The d– and q–axis inductance are half of the measured inductance obtained by the scheme of Fig. 6.1 and Fig. 6.2 respectively.

The machine without ring (dashed line) exhibits a little difference between L_q and L_d. The saliency ratio is 1.1. This ratio increases to 1.4 in the prototype machine, where the pole ring exalts the high frequency electrical anisotropy of the rotor. The small rotor magnetic isotropy at dc and low frequency has been verified in [36], and the

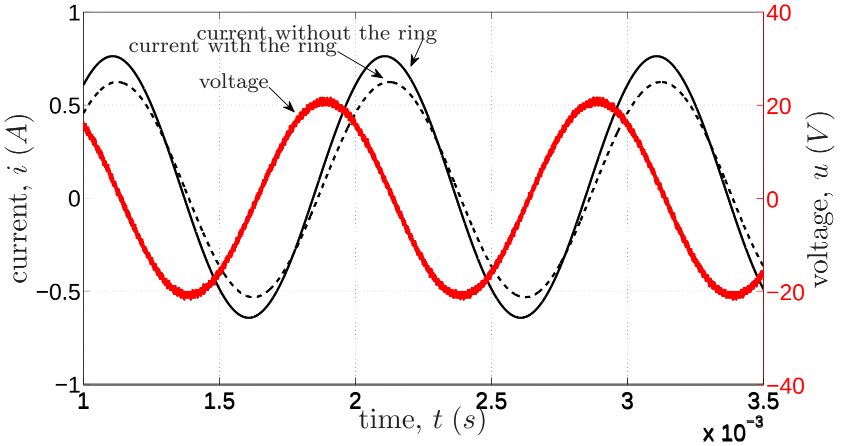

Figure 6.18: Supplied stator voltage and stator current response, test with rotor aligned as Fig. 6.2

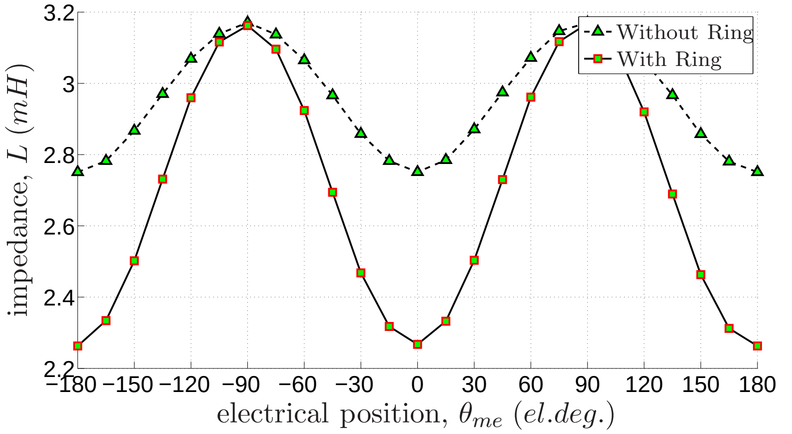

Figure 6.19: Two phases inductance versus electrical rotor position θ_{me}

L_d and L_q inductances result to be 3.8 mH and 4 mH respectively.

6.4.2 Calculation of the ring resistance

As regard the ring resistance, it is possible to derive its value exploiting the knowledge of the geometrical parameter. The resistance R of a conductor wire is given by:

$$R = \rho \frac{l}{S} \tag{6.42}$$

where ρ is the electrical resistivity measured in $\Omega \cdot m$, l is the wire length in m and finally S is the section area in mm^2.

The ring is long 60 mm and width 30 mm, then the total length of the wire is 180 mm. Moreover, the wire radius is 0.6 mm and the section results $S = \pi r^2 = 1.13\ mm^2$. Finally, being a copper wire an electrical resistivity of 0.0175 $\Omega \cdot mm^2/m$ can be taken in consideration. Using the (6.42), the resistance of one R_{ring} results:

$$R_{ring} = 0.0175 \frac{0.18}{1.13} = 2.8\ (m\Omega) \tag{6.43}$$

This value refers to one ring, therefore the total resistance of the rotor cage is equal to:

$$R_r = 6 \cdot R_{ring} = 6 \cdot 2.8 = 16.8\ (m\Omega) \tag{6.44}$$

6.4.3 Measures of the ring current

As aforementioned, the cage is mounted along the direct axis and then an induced current flows in the ring only when this is linked to time varying d–axis flux, as show in the flux plot of Fig. 6.10. On the contrary, if the flux does not link the ring, no current is induced in it, as shown in Fig. 6.9.

Some tests have been carried out in order to measure the ring current as a function of the rotor position. To this purpose the ring has been extended, brought out the motor frame and closed by a loop. The current of the ring is measured by a probe inserted in this loop.

The response of the current when only 1 kHz ac q–axis current is supplied (scheme of Fig. 6.1) is reported in Fig. 6.20. The supply voltage, the stator current and the ring current are reported. It is worth noticing that the ring current is practically zero, while stator current is orthogonal to the voltage.

In the other case, when only 1 kHz ac d–axis current is supplied (scheme of Fig. 6.2), the peak amplitude of the ring current reaches 3.7 A as shown in the Fig. 6.21. This current has a phase displacement of about 60 electrical degrees with respect to the opposite of the stator current due to the ring resistance. However, this current waveform displacement does not affect the sensorless rotor position detection if the latter is based on zeroing the ring current.

It has been also verified that the peak ring current varies from zero to the maximum value of 3.7 A as shown in Fig.6.22 while the excitation field moves from the $q-$ to the d–axis.

Further tests have been carried out in order to quantified the dynamic effect of the ring placed in the rotor. To this purpose, a voltage step is imposed along the d–axis and the current response is measured. The results of this test are reported in Fig. 6.23.

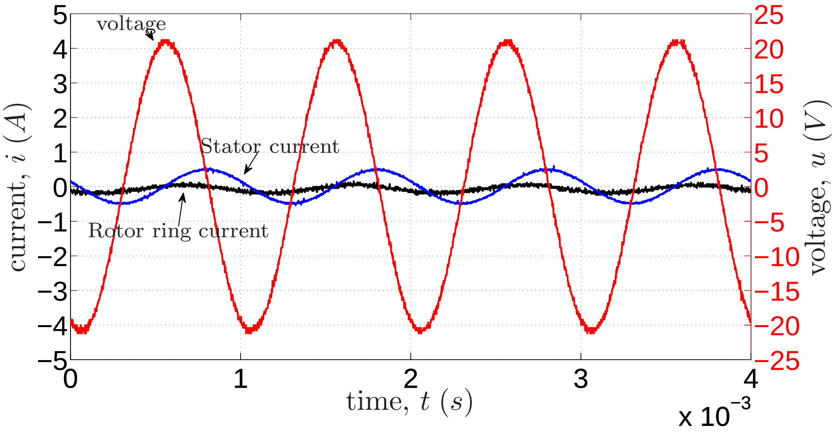

Figure 6.20: Stator voltage and current together with the current ring, with the rotor aligned as in Fig. 6.1

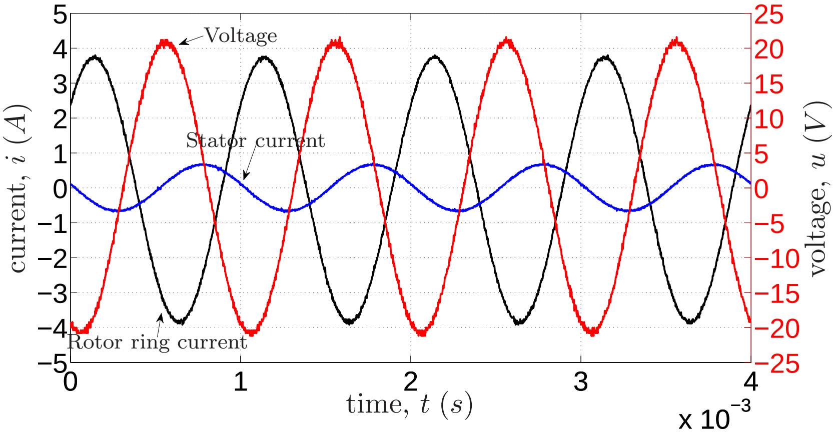

Figure 6.21: Stator voltage and current together with the current ring, with the rotor aligned as in Fig. 6.2

One can note that the presence of the rotor ring has a slight effect on the d–axis current dynamic, proving that the coupling coefficient of the structure under test is not high. In spite of that, there is not requirement for any addition decoupling for the cage.

6.5 Finite elements analysis

Some time harmonic FEM simulations have been carried out in order to derive the electric parameters of the motor and to have a good model for future analysis and control. In order to realize the prototype machine, the SPM rotor structure describe in the Sec.2.3 is taken into account. In it, the space between a couple of poles is large enough to allow the placing of the ring around each pole. Then, the main data of the motor geometry are reported in Table 2.3, and the electric parameters are reported in Table 2.4.

First simulations have been carried out without the rings, in order to derive the

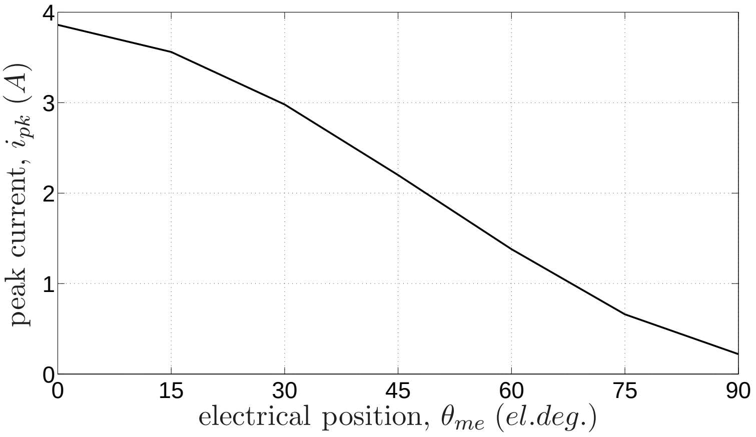

Figure 6.22: Peak value of the current ring vs the electrical position

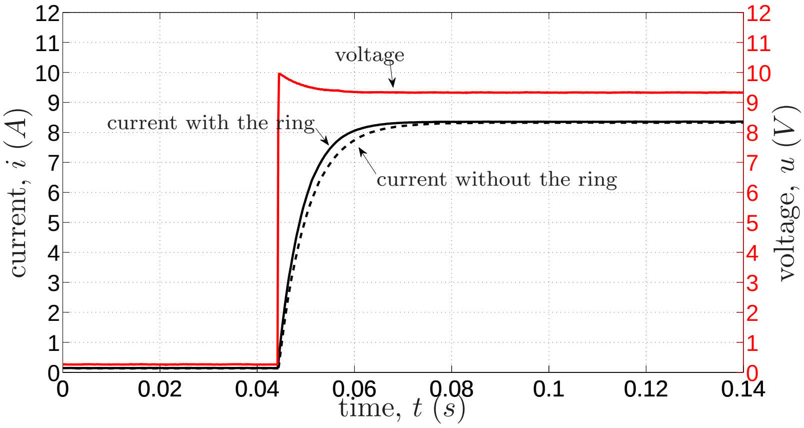

Figure 6.23: Stator current response after application of a stator step

stator inductance. To this purpose the simulation have been done at the frequency of 1 kHz. AC direct axis current of $I_d = 1\ A$ has been imposed, then the simulation configuration is equivalent to that of Fig. 6.2 used for the tests. Considering to feed an equivalent winding formed by phases b and c, the flux linkage results in:

$$\Lambda_s = \Lambda_{bc} = 4.65\ mVs \tag{6.45}$$

Dividing the flux linkage by the phase current I_s, that is equal to 0.866 A ($I_s = I_d\sqrt{3}/2$), the stator inductance L_s is obtained:

$$L_s = \frac{\Lambda_s}{I_s} = \frac{4.65}{0.866} = 5.37\ mH \tag{6.46}$$

that divide by two delivered the d–axis inductance

$$L_d = \frac{L_s}{2} = \frac{5.37}{2} = 2.68\ mH \tag{6.47}$$

This value is in good agreement with the experimental tests of Fig. 6.19, to be more precise this value is the double of the d–axis inductance because it refers to two windings. The same result can be derived in other two ways: from the d–axis flux linkage and from the energy. From the FEM simulations it is possible to calculate the flux linkage of to the d–axis that results equal to $\Lambda_d = 2.68\ mVs$, imposing a d–axis current of 1 A. The d–axis inductance is given by:

$$L_d = \frac{\Lambda_d}{I_d} = \frac{2.68}{1} = 2.68\ (mH) \tag{6.48}$$

In the other way, the magnetic energy W_m can be equalize to:

$$W_m = \frac{3}{2}\left[\frac{1}{2}L_d\left(\frac{I_d}{\sqrt{2}}\right)^2\right] \tag{6.49}$$

Being from the simulation $W_m = 0.9983\ mJ$ consequently the inductance results:

$$L_d = \frac{2}{3}\left[\frac{4W_m}{I_d^2}\right] = \frac{2}{3}\left[\frac{4 \cdot 0.9983e-3}{1^2}\right] = 2.66\ mH \tag{6.50}$$

The values obtained in the three cases result practically the same.

After verify the good correspondence between the FEM model and the motor, the rings are inserted in the FEM model. Repeating the previous simulation with the rings, the current in the ring results 10.6 Arms (15 A peak). The power losses P_{l_r} in the 6 rings result equal to 1.88 Watts (a total power loss of 2.54 Watts is computed including the permanent magnets). This confirms the prediction of the losses in the rings from the rotor resistance obtained by the (6.44), as:

$$P_{l_r} = \cdot R_r \cdot I_r^2 = 1.887\ W \tag{6.51}$$

The values obtained in the two ways is practically equal, then the value of the ring resistance, estimated by its geometry, is reasonable.

Using the model with the ring, it is possible to derive the stator inductance variation against the electrical position θ_{me}. Fig. 6.24 shows the simulation results (solid line) and the values obtained by the experimental tests (as reported also in Fig. 6.19). The good agreement between the FEM results and the actual tests confirms the accuracy of the motor model.

By calculating the stator inductance for different frequency, imposing the rotor both aligned and orthogonal to the phase a, the saliency behaviour against the frequency can be computed. It is shown in Fig.6.25. It is worth noticing the good agreement with the theoretical behaviour give in Fig. 6.13.

For all the tests, a frequency of 1 kHz has been used. From Fig.6.25 it appears that a proper saliency (about 1.2) is achieved according to a frequency equal to 400 Hz. This is a typical value of the injected signal frequency in sensorless control of PM machines.

In order to estimate the ring inductance, a simulation has been done imposing a current of 1 A in each rings at frequency of 1 kHz. No stator current is imposed. The flux linkage of the rings (the six rings are considered as to be series connected) is equal to 2.73 μVs. The rings inductance L_r is obtained dividing the flux linkage by the ring current, as:

$$L_r = \frac{\Lambda_r}{I_r} = 2.73\ \mu H \tag{6.52}$$

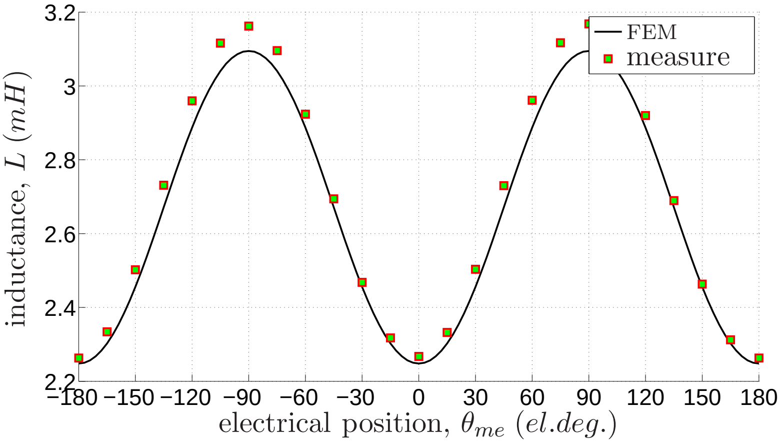

Figure 6.24: Stator inductance against position

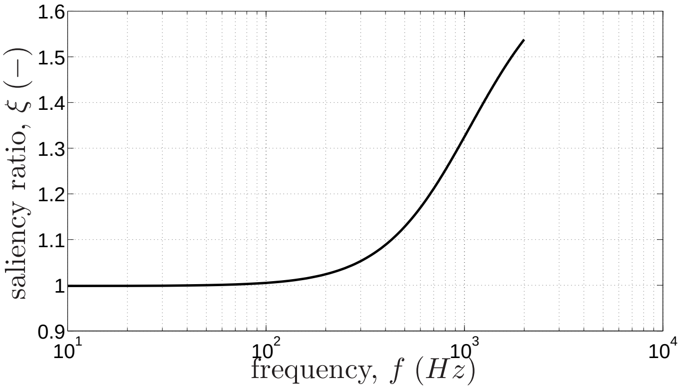

Figure 6.25: Saliency against frequency

From the same simulation, it is also possible to estimate the mutual inductance L_M between the stator and rotor windings. As a matter of fact, L_M is given by the flux linkage Λ_s of the equivalent stator winding *b*–*c* divided by the rotor current, as:

$$L_M = \frac{\Lambda_s}{I_r} = 73.7\ \mu H \tag{6.53}$$

6.5.1 Effects of the PM conductivity

In the previous sections, the FEM simulations has been focused in the analysis of the ring effects. However, being the PMs conductive, there is also a slight effect on the rotor anisotropy just due to that conductivity.

In the following FEM analysis, the effect of the ring is separated from the effect of the PMs, by comparing three simulations: the first carried out with only the effect of the ring (magnet conductivity $\sigma_{PMs} = 0$ and iron conductivity $\sigma_{Fe} = 0$), the second with the effect of both the ring and the magnets ($\sigma_{PMs} = 0.69\ MS/m$ and $\sigma_{Fe} = 0$) and the last with only the effect of the PMs ($\sigma_{Fe} = 0$), i.e. without the ring.

The rotor iron conductivity (σ_{Fe}) is always neglected in the simulations, because it has been verified its negligible contribution, since the rotor iron is laminated. The frequency range spans from 10 Hz to 10000 Hz.

FEM simulations have been carried out with current in both d and q axis; in the former case the flux is linked with the ring, in the latter one the flux does not involve the ring. Saliency ξ is obtained from the ratio λ_q/λ_d performed for each frequency.

Fig. 6.26 shows the d–axis flux linkage versus the frequency when the rotor is aligned with the axis of the phase a. The effect of the ring is evident at least up to 3000 Hz (solid blue line). The d–axis flux decrease from about 2.8 Vs to about 1.8 Vs. At frequencies greater than 6000 Hz the effect of the ring is constant. Both introducing the PMs conductivity and removing the ring (black circle–marked line) the parasitic currents in the PMs decrease the d–axis flux. The prototype machine presents both the effects, ring and PMs conductivity, and the d–axis flux goes down to the 1.7 Vs (dashed red–line).

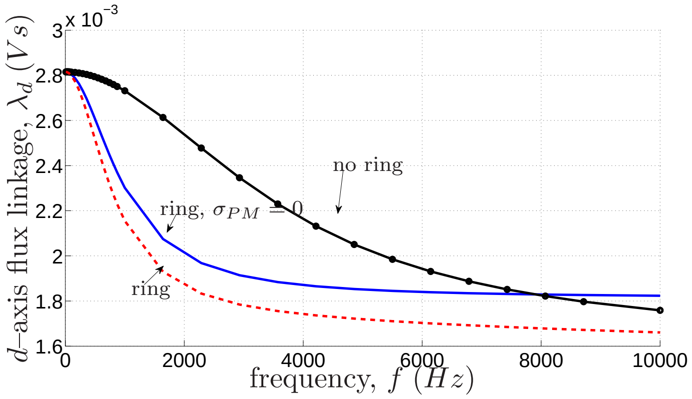

Figure 6.26: d–axis flux versus frequency (high frequency current on d–axis) - distributed winding

Fig. 6.27 shows the flux on q–axis versus the frequency when the rotor is orthogonal to the axis of the phase a. In this case the effect of the ring is negligible (solid blue line), since it has no effect on q–axis flux as explained above. The effect of the PMs yields an effect on the q–flux like in the d–axis case. The PMs conductivity causes the slight anisotropic behaviour highlighted in Fig. 6.28 in black circle–marked line.

Fig. 6.28 shows the saliency versus the frequency. At first, a small saliency of about 1.07 can be noticed at low frequencies. It is due to the slight rotor anisotropy of the rotor iron, since the PMs are separated by a small iron tooth (see Fig. 2.1(b)).

If only the ring is considered, the saliency spans from 1.07 to about 1.65; at the frequency of 1000 Hz an appreciable saliency variation is found, magnified if also the PMs are considered (see red dashed line). The effect of the PM conductivity increases the saliency (up to about 20000 Hz).

If the ring is removed, PMs yield a saliency variation, but it appears at higher frequencies. Since the frequency of interest is lower than 1000 Hz, no saliency variation due to only PMs is achieved.

Fig. 6.29 shows the phase inductance versus the rotor electric angle, achieved for a frequency of 1000 Hz. This figure reassumes the behavior of the motor; the anisotropy

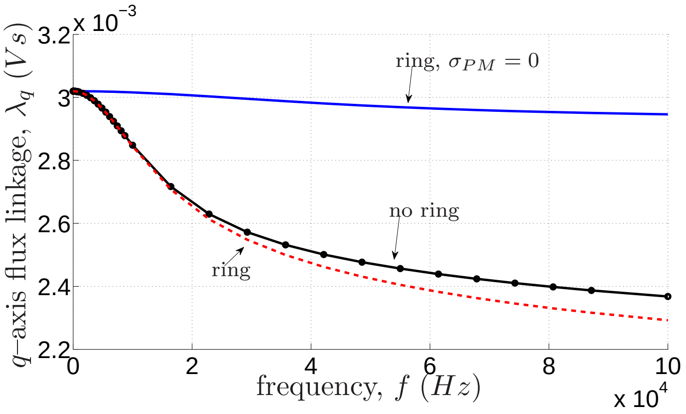

Figure 6.27: q–axis flux versus frequency (high frequency current on q–axis) - distributed winding

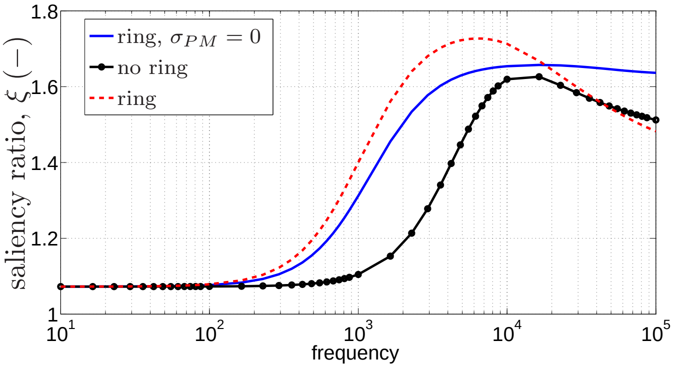

Figure 6.28: Saliency versus frequency - distributed winding

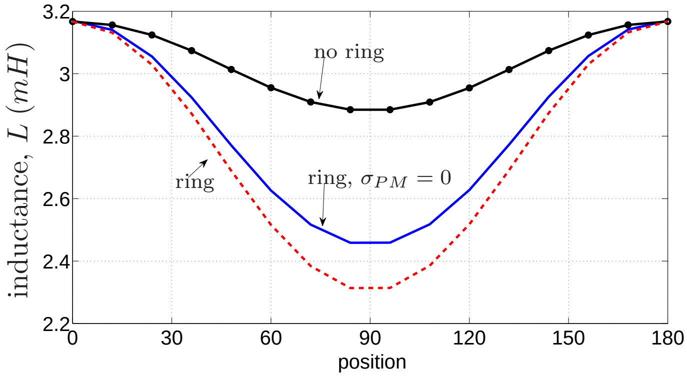

Figure 6.29: Inductance versus rotor electric angle - distributed winding

obtained by injecting a high frequency signal is significant only if a ring is present around the pole, and the effect of the PMs conductivity is beneficial to increase the saliency.

6.5.2 Concentrated winding

In order to analyze the goodness of the ring solution in all situations, the previous stator with a distributed windings is changed with a concentrated windings one. The motor, with 9–slots 6–poles (number of slots per pole per phase $q = 0.5$), is sketched in Fig. 6.30. Since the slot pitch $y_q \simeq 1$, the motor has a concentrated winding with non–overlapped coils.

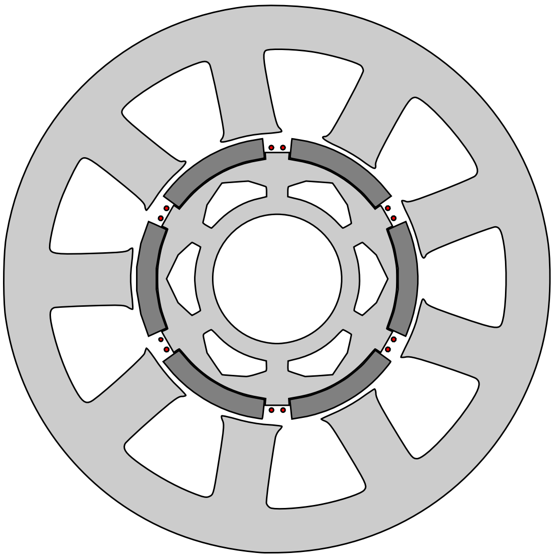

Figure 6.30: 9–slot 6–pole motor (concentrated winding)

Figs. 6.31 and 6.32 show d– and q–axis flux linkages versus frequency. Fig. 6.33 shows the saliency versus frequency and Fig. 6.34 the inductance versus rotor electric angle at 1000 Hz.

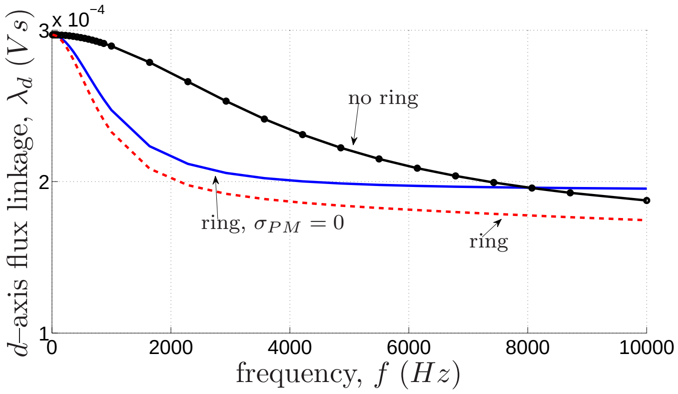

Figure 6.31: d–axis flux versus frequency (high frequency current on d–axis) – concentrated winding

The results are similar to those obtained for the previous motor. Thus also this motor is suited for position detection using high frequency signal injection.

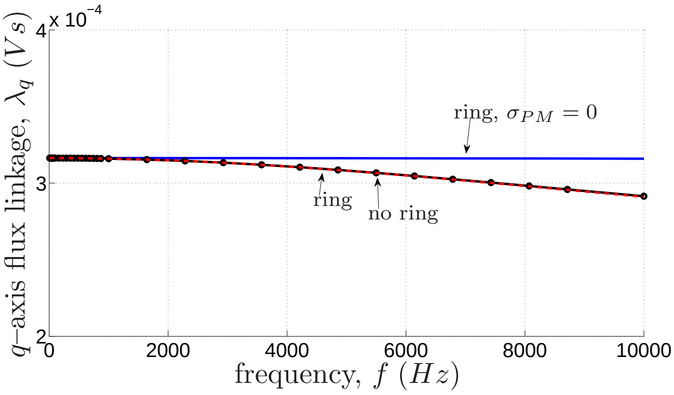

Figure 6.32: q–axis flux versus frequency (high frequency current on q–axis) – concentrated winding

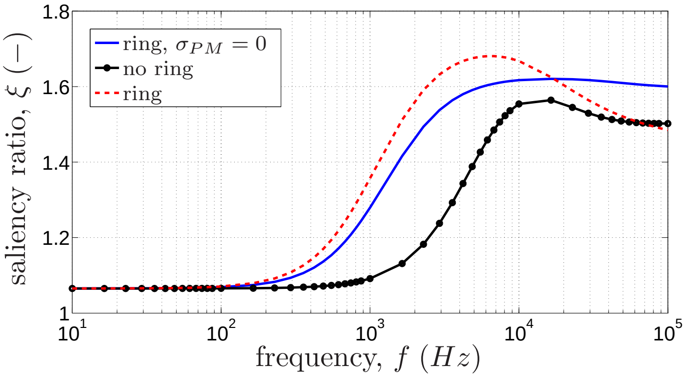

Figure 6.33: Saliency versus frequency – concentrated winding

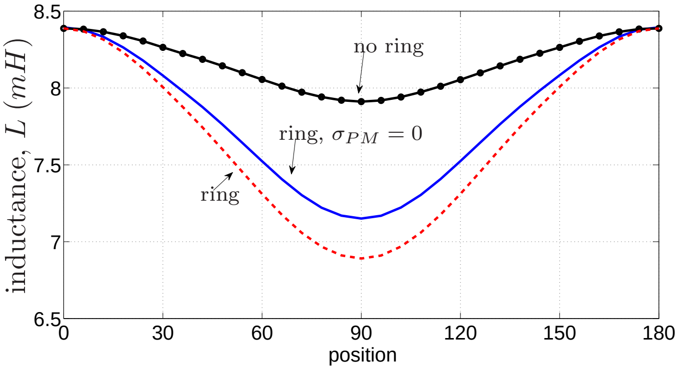

Figure 6.34: Inductance versus rotor electric angle – concentrated winding

6.6 Conclusive summary

In order to allow a rotor position sensorless detection, a short–circuited ring has been wound around each pole of an SPM motor. Adopting a sensorless technique based on an injection of a high–frequency signal, the *d*–axis high frequency inductance lower than the *q*–axis inductance can be exploited. This allows the detection of the rotor position of the SPM motor (which has an isotropic rotor) to be achieved also at null speed.

The effect of the short–circuited ring has been investigated for different excitation frequency. Then, the two–axis model of the motor is proposed and verified by means of both FEM simulations and measurements.

Several tests have been carried out on a prototype rotor modified by introducing the ring in a standard sample. By means of the ring, the saliency ratio becomes about 1.4 at 1 kHz. In addition, the current in the ring remains to a limited value, causing negligible losses in the rotor.

The various tests carried out yield to limited losses in the rotor rings. A slight increase of the losses is expected due to the space MMF harmonics and switching phenomenon under nominal operating condition. [However, such an increase is limited, since the mutual coupling is low.

7

Sensorless drive with the Ringed–pole machine

7.1 Simulation results

A new Ringed–pole rotor configuration has been analyzed and simulated by means of FEM analysis in the previous Chapter. The tests effectuated demonstrates the effective machine anisotropy at high frequency. Then, some simulations by means of *Simulink* Matlab toolbox and experimental tests have been done in order to verify the effectively electrical position estimation using the high frequency injection technique.

From the point of view of the control the main characteristic of the ringed–pole machine is the high frequency anisotropic behaviour that it presents despite of its SPM configuration. Then it can replace a salient pole anisotropic machine, as an interior permanent magnet motor, in a high frequency signal injection sensorless control. To investigate the validity of the novel idea, some simulations have been done at first, implementing the scheme of Fig. 7.1(a).

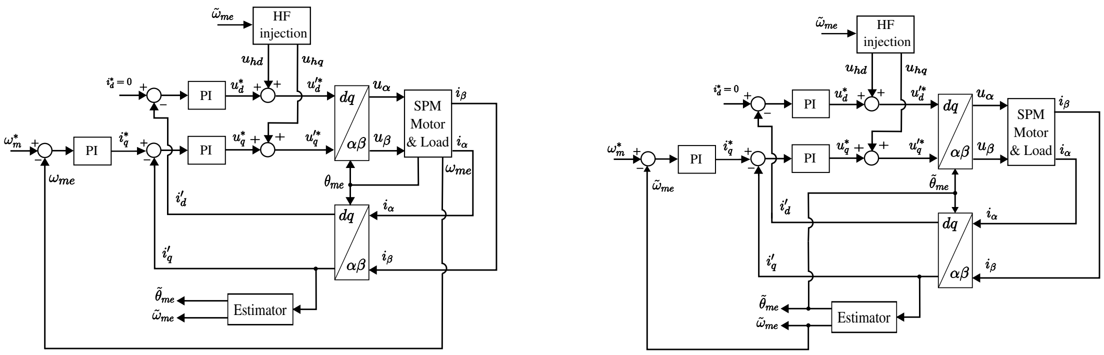

(a) Off–line rotor speed and position estimation.

(b) On–line rotor speed and position estimation.

Figure 7.1: Control scheme of SPM motor with injection voltage.

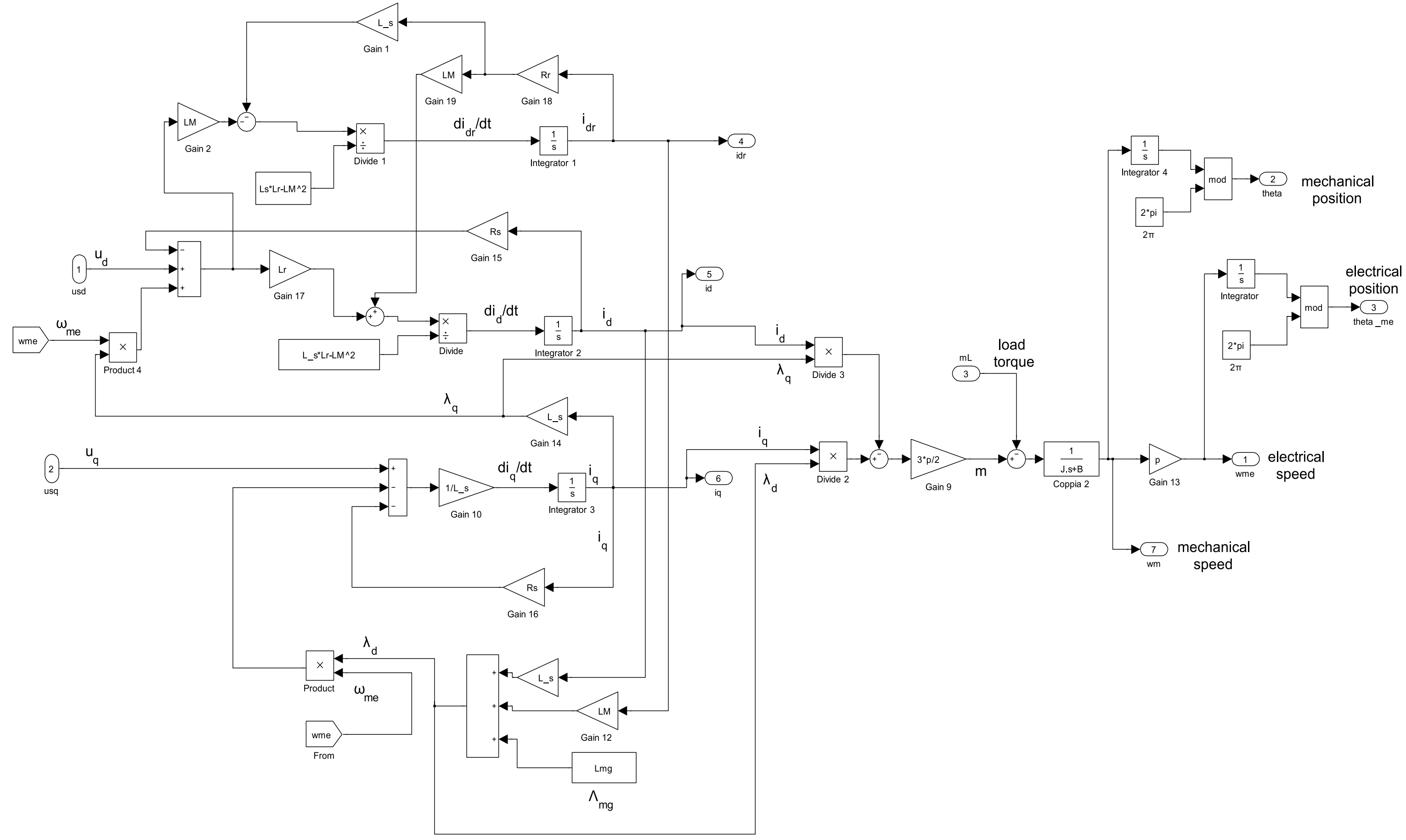

Figure 7.2: Simulation scheme of the ringed–pole machine

The simulation motor model can be derived from the three motor equations (6.23) and (6.24), written in the state space form:

$$
\begin{aligned}
\frac{di_d}{dt} &= \frac{L_r(u_d + \omega_{me} L_s i_q - R_s i_d) + L_M R_r i_r}{L_s L_r - L_M^2} \\
\frac{di_q}{dt} &= \frac{u_q - \omega_{me}(L_s i_d + L_M i_r + \Lambda_{mg}) - R_s i_q}{L} \\
\frac{di_r}{dt} &= \frac{-L \cdot R_r \cdot i_r - L_M \cdot (u_d + \omega_{me} \cdot L \cdot i_q - R_s i_d)}{L \cdot L_r - L_M^2}
\end{aligned}
\tag{7.1}
$$

which are added to the torque and mechanical equations and implemented inside the block called *SPM Motor & Load* in Fig. 7.1.The block contains also $\alpha\beta/dq$ input voltage transformation and $dq/\alpha\beta$ output current transformation, commanded by the actual rotor position. Simulation scheme of the ringed–pole motor is reported in Fig. 7.2.

As in [25] the motor is fed by the fundamental voltages provided by the current control in addition to the high frequency voltage signals (6.25) and (6.26) with:

$$U_{hq} = \frac{\omega_{me}}{\omega_h} U_{hd}. \tag{7.2}$$

The SPM machine is controlled to have a Maximum Torque Per Ampere (MTPA) operation, then two current loops are implemented for the direct and the quadrature currents. According to the MTPA control, the direct current is maintained to zero and the quadrature current reference is given by the external speed loop regulator.

In the lowest block of the scheme of Fig. 7.1, the off–line position estimator is implemented. The estimation algorithm is one of those described in Sec. 3.5, but any other method can be used [34]. Hereunder, both two and three states observed estimators are taken into consideration.

7.1.1 Observer with two states

The estimator scheme implemented is that of Fig. 3.9. All simulations have been carried out imposing a speed step reference of 50 rpm (1.5% of the nominal speed). The reference is command after one second of operation at standstill.

Some results are shown in Fig. 7.3 and 7.4. In the first second on time, during the standstill operation, both the current references are forced to zero disabling the speed control. During such a time no current is imposed to the motor and only the estimator works. After this second a reference step of 50 rpm (about 1.5% of the nominal speed) is imposed. During standstill operation the rotor position estimator of Fig. 3.9 adjust its estimated position (with initial value equal to zero) to converge to the actual one (fixed to a casual initial position equal to about 60 $el.degs$ in the simulations) as highlighted in Fig. 7.4. Consequently the estimated speed has an initial pulse and then return to zero, Fig. 7.3. This overshoot doesn't affect the actual speed dynamic because the estimator is working *off–line*.

At the application of the speed reference step the motor reaches quickly the speed reference. A PI speed controller with appropriate anti–windup features has been designed. It's also worth noting that the estimated speed exhibits a delay with respect to the actual one that can be modeled by a first order lag with time constant of about 20–30 ms depending on the injected signal frequency that determines the gain and thus the bandwidth of the closed loop estimator of Fig. 3.9. In general from Figs. 7.3 and 7.4 one can observe the good performance of the estimator both at zero and non zero speed.

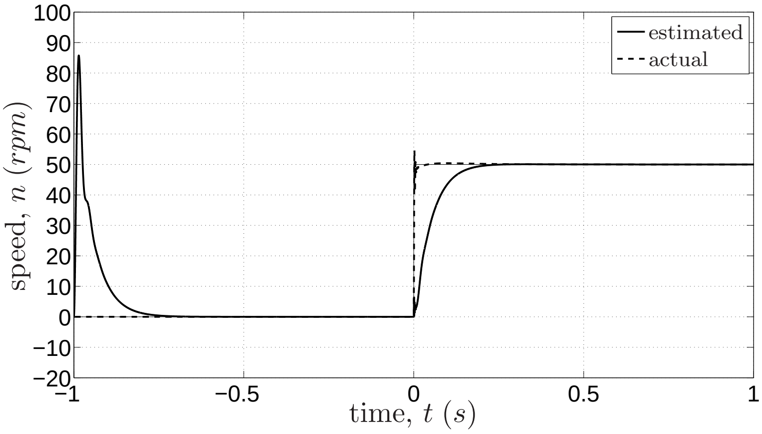

Figure 7.3: Estimated and actual speed with off–line estimation and two states observer (simulation)

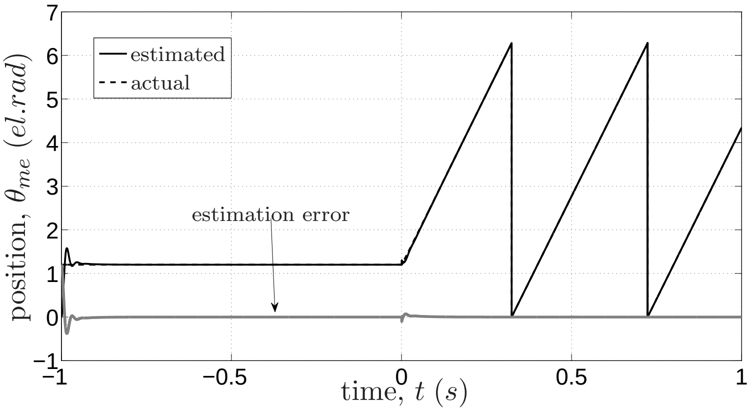

Figure 7.4: Estimated and actual position with off–line estimation and two states observer (simulation)

Second simulation is carried out using the *on–line estimation* configuration as shown in Fig. 7.1(b). Therefore, estimated speed $\tilde{\omega}_{me}$ and position $\tilde{\theta}_{me}$ are exploited in the control loops . As in the previous test, a speed reference step of 50 rpm is imposed after one second of standstill operation.

The estimator responses are illustrated in Figs. 7.5 and 7.6. Fig. 7.5 shows that the speed response present an overshoot and the the speed loop control is slower than that reported in Fig. 7.3. This occurs because the bandwidth of the speed loop control must be decreased to maintain the system stability having a lowest phase margin due

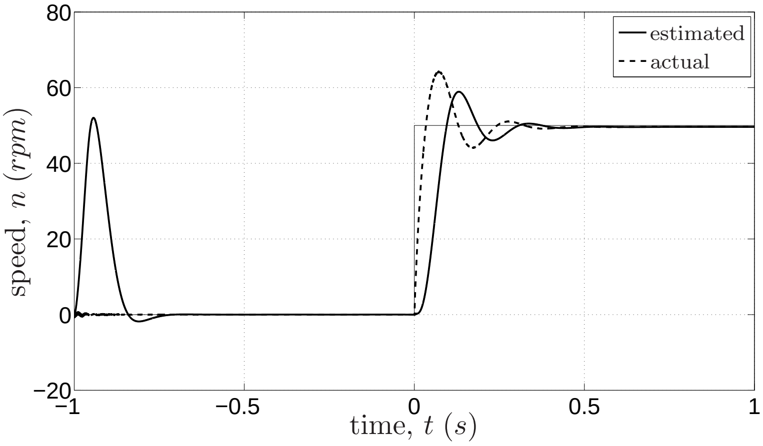

Figure 7.5: Estimated and actual speed with on–line estimation and two states observer (simulation)

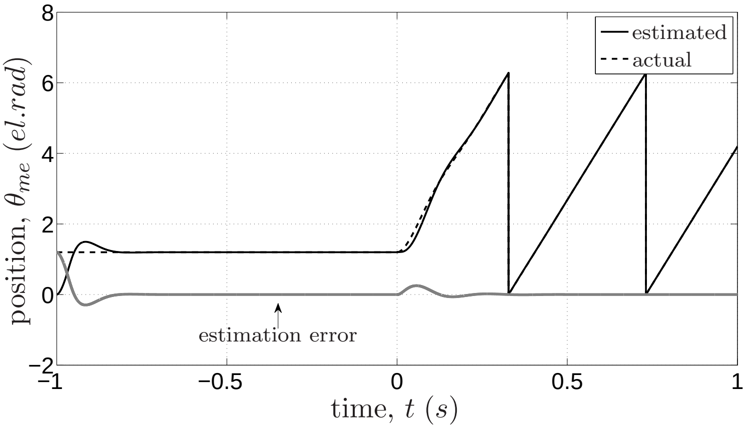

Figure 7.6: Estimated and actual position with on–line estimation and two states observer (simulation)

to the presence of the estimator. In this case the actual speed reaches the reference in about 0.4 s.

Fig. 7.6 reports the rotor position response. Estimated and actual position and estimation error are shown. One can note that the estimation error goes to zero in about 0.2 s in the standstill operation. When the speed reference step occurs, the estimated follows the the actual one (with a initial briefly transitory) obtaining a steady–state null estimation error.

7.1.2 Estimator with three states observed

The estimator scheme implemented is that of Fig. 3.10. All simulations have been carried out imposing a speed reference step of 50 rpm (1.5% of the nominal speed). The reference is command after one second of operation at stand still.

First simulation has been done with the estimator that works off–line, in order to design the regulators parameters and the estimator coefficients. In other words, in Fig. 7.1 the actual electrical speed θ_{me} is used in the transformation from $\alpha\beta$ to dq and viceversa. Moreover, the actual speed is used as feedback in the speed loop.

Estimated speed $\tilde{\omega}_{me}$ and the actual one are reported in Fig. 7.7. Instead in Fig. 7.8 the estimated electrical angle $\tilde{\theta}_{me}$ and the actual one θ_{me} (which has a random initial value different from zero) are reported. One can notice the good performance of the estimator both at standstill and non zero speed.

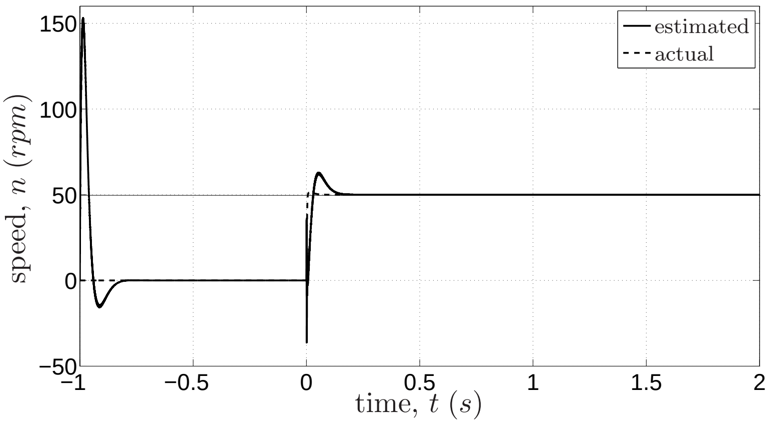

Figure 7.7: Estimated and actual speed with off–line estimation (simulation) and two states observer

After verifying that the estimator works properly off–line, the next step is the use of the estimates in the reference transformation blocks and in the speed loop (*on–line estimation*) as shown Fig. 7.1(b). In this case the estimator slows down the speed loop dynamic, then the PI speed regulator parameters have to be changed to maintain the closed–loop stability. As in the previous test, a speed step of 50 rpm is imposed at $t = 1s$. In Fig. 7.9 one can note that the speed response is slower than that reported in Fig. 7.7, but there is a good agrement between the estimated position and the actual one as reported in Fig. 7.10.

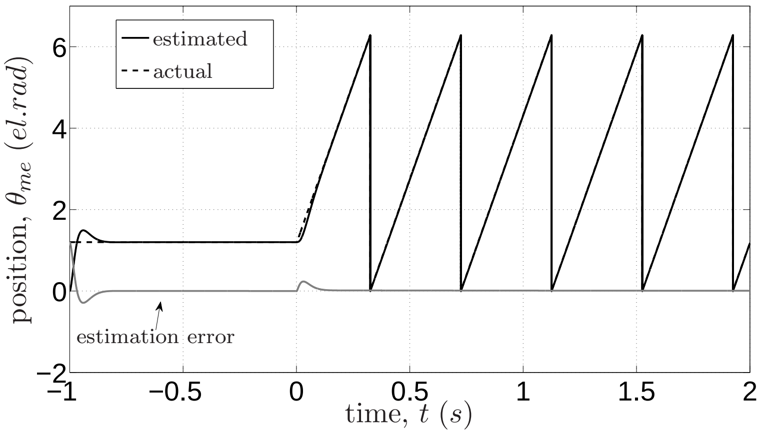

Figure 7.8: Estimated and actual position with off–line estimation (simulation) and two states observer

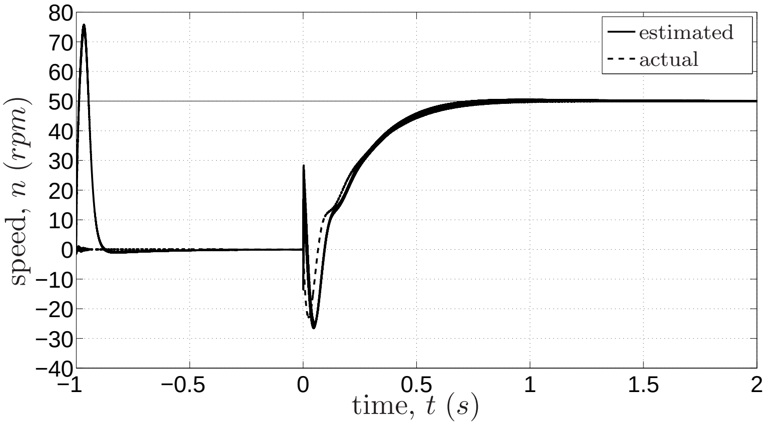

Figure 7.9: Estimated and actual speed with on–line estimation (simulation) and two states observer

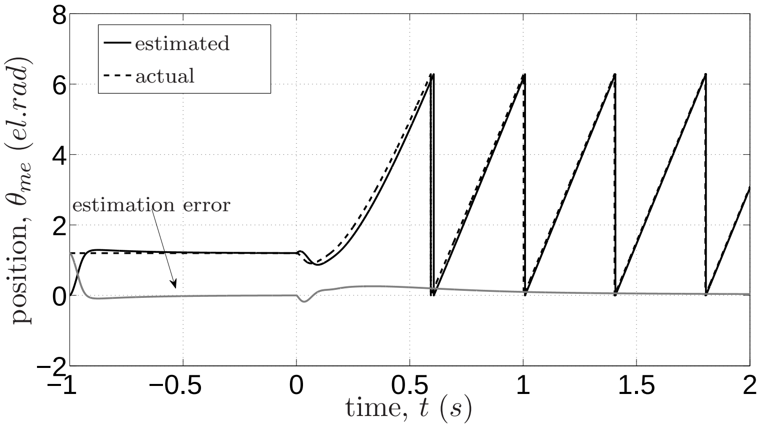

Figure 7.10: Estimated and actual position with on–line estimation (simulation) and two states observer

7.2 Experimental results

The same tests simulated in Sec. 7.1 have been carried out in the actual system, using the test bench reported in Fig. 7.11. The prototype ringed-pole SPM motor is shown on the left side while the dragging/loading induction motor is shown on the right side. An encoder, connected to the motor, allows to compare the estimated position to the actual one.

As in the simulation, the first tests have been carried out with the estimator working off–line (Fig. 7.1(a)). After having verified that the estimator works properly, the second tests have been done with the estimator working on–line (according to Fig. 7.1(b)).

The tests have been carried out using the two estimators type as in the simulation phase.

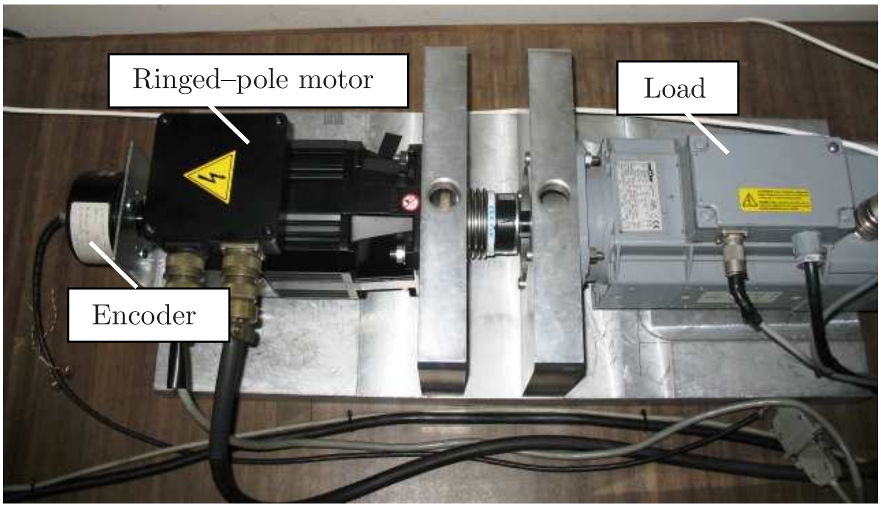

Figure 7.11: Test bench for ringed–pole SPM motor

7.2.1 Test with two–state estimator

First experimental results are shown in Fig. 7.12 and Fig. 7.13, obtained with the estimator that works off–line as in Fig. 7.1(a). In Fig. 7.12 the estimated and measured speed are reported.

At the instant time $-1\ s$, the estimator is enabled and the estimated position reaches the actual one. Both initial value in the motor and in the estimator are set casually. One can note that at standstill there is a little estimation error due to the cross-saturation effect or the not exactly alignment of the encoder. In this phase the estimated speed have an initial overshoot of 20 rpm, then coming back to zero as shown in Fig. 7.12.

When it is imposed the speed reference step, the actual speed reaches quickly the reference value, instead the estimated speed reaches the actual one in about 1 s. Adjusting the estimator parameters it is possible to obtain a faster response of the estimation speed.

When the estimated speed $\tilde{\omega}_{me}$ is closed in the speed loop and the estimated position is used for the transformation from the $\alpha - \beta$ to $d - q$ reference frame and viceversa

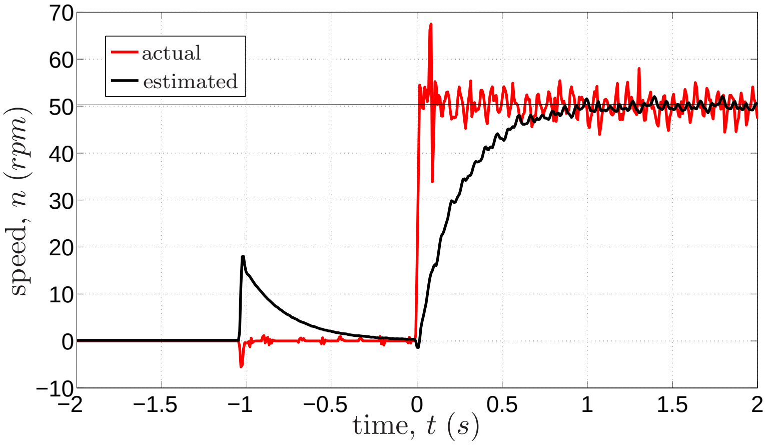

Figure 7.12: Estimated and actual speed with off–line estimation and two states observer (experimental)

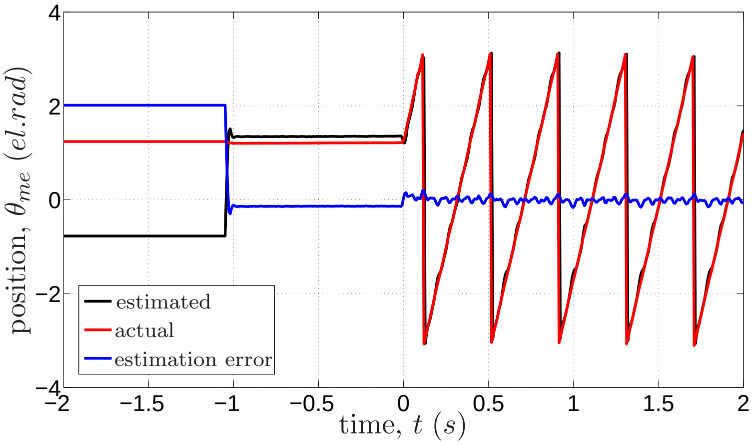

Figure 7.13: Estimated and actual position with off–line estimation and two states observer (experimental)

(Fig. 7.1(b)), the bandwidth of the speed loop has to be reduced, otherwise excessive oscillations occur. The bandwidth of quadrature current loop has been extended as much as possible, limited only by the system stability in order to reduce the torque and speed oscillations. The reduction of the speed loop bandwidth brings a slowly actual speed response, as point out in Fig. 7.14. The motor speed approaches the reference value in about 4 s. Again, adjusting the control parameters an improvement of the system could be obtained.

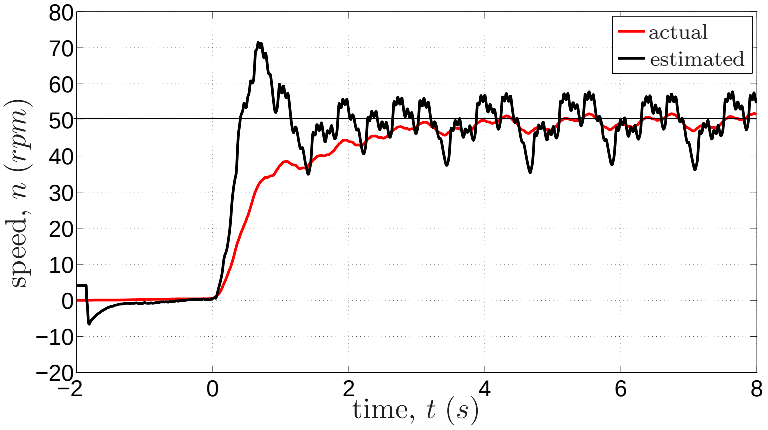

Figure 7.14: Estimated and actual speed with on–line estimation and two states observer (experimental test)

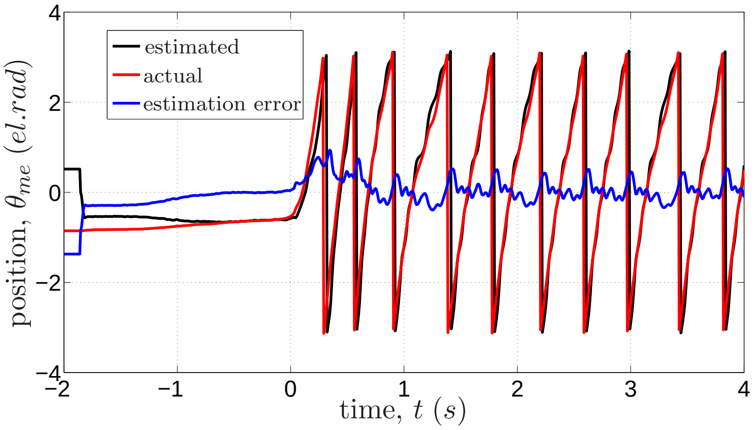

Figure 7.15: Estimated and actual position with on–line estimation and two states observer (experimental test)

As regard the estimated position, Fig. 7.15 shows that when the estimation is activated at the instant time of about -2 s, $\tilde{\theta}_{me}$ reaches the actual position. Differently from the simulations in the standstill operation the current controls are not excludes and then a slightly movement of the rotor occurs.

Finally, one can note a steady–state oscillation at angular frequency both in the estimated speed and in the actual one, which can be recognized in Fig. 7.14. This is caused by inverter non linearities and spatial harmonics in the motor. This oscillation is also recognized in the behaviour of the estimated and actual position of the rotor as reported in Fig. 7.15. In spite of such oscillation, satisfactory performance of the sensorless control is achieved.

7.2.2 Test with three–state estimator

As in the simulation, the first tests have been carried out with the estimator working off–line (Fig. 7.1(a)). The experimental results are shown in Fig. 7.16 for the estimated and measured speed and Fig. 7.17 for the estimated and measured position. Initial position are set casually both in the motor and in the estimator.

The estimated speed and, consequently, the estimated position have an oscillation around the steady–state value due to slotting effects and mechanical irregularities. However it has to be taken into account that the steady–state speed is only $1,5\%$ of the rated value and then the speed oscillations are of very limited amplitude.

One can note the good correspondence between the measured and estimated quantities, a part from the speed during initial transients, required for the convergence of the estimated position to the actual one.

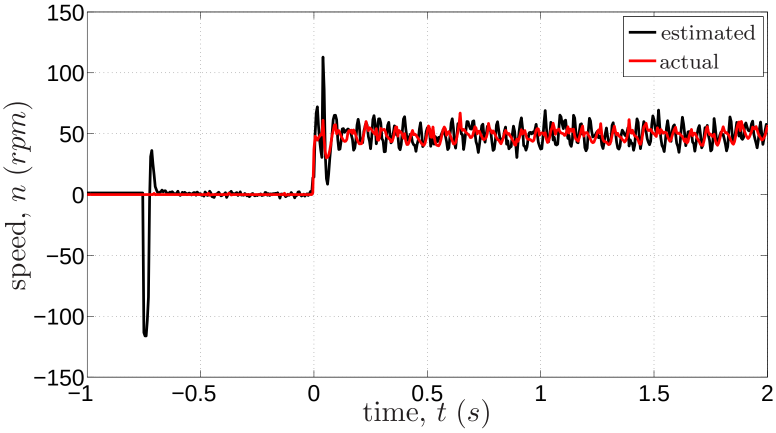

Figure 7.16: Estimated and actual speed with off–line estimation and three states observer (experimental)

When the estimated speed $\tilde{\omega}_{me}$ is closed in the speed loop and the estimated position is used for the transformation from the $\alpha - \beta$ to $d - q$ reference frame and viceversa the bandwidth of the speed loop has to be reduced, otherwise excessive oscillations occur. As written above, the bandwidth of quadrature current loop has been extended as much as possible, limited only by the system stability in order to reduce the torque and speed oscillations.

Fig. 7.18 shows the response of the estimated speed in comparison to the actual one after a speed reference step of 50 rpm. The actual speed has a large overshoot at the startup and a steady–state oscillation at angular frequency $6\omega_{me}$, which can be recognized in Fig. 7.18, as in the case of Fig. 7.14.

This oscillation is also recognized in the behaviour of the estimated and actual position of the rotor as reported in Fig. 7.19. In spite of such oscillation, satisfactory

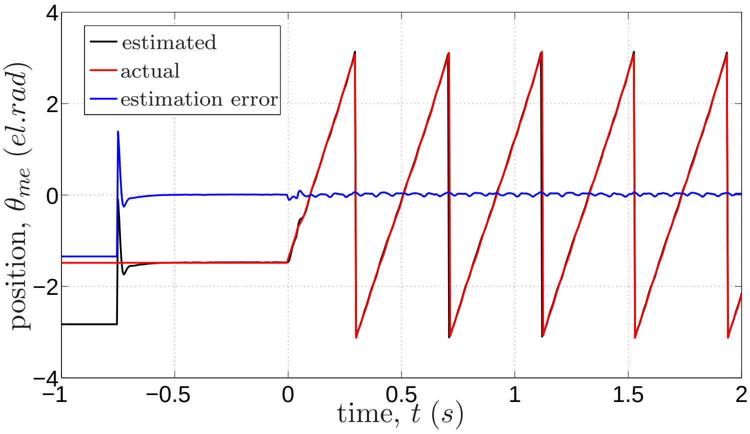

Figure 7.17: Estimated and actual position with off–line estimation and three states observer (experimental)

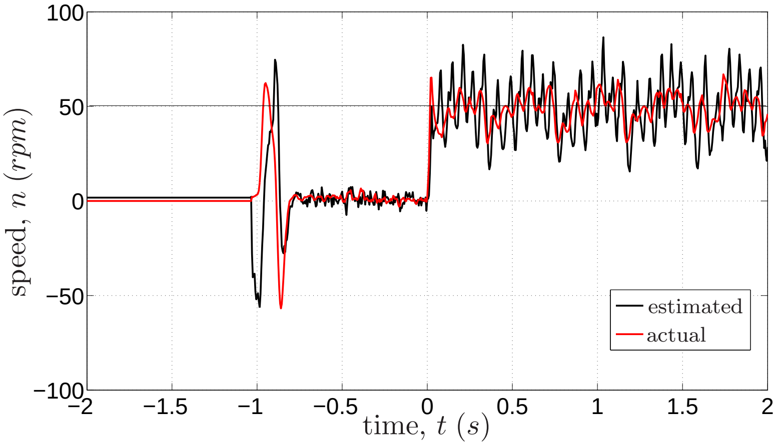

Figure 7.18: Estimated and actual speed with on–line estimation and three states observer (experimental test)

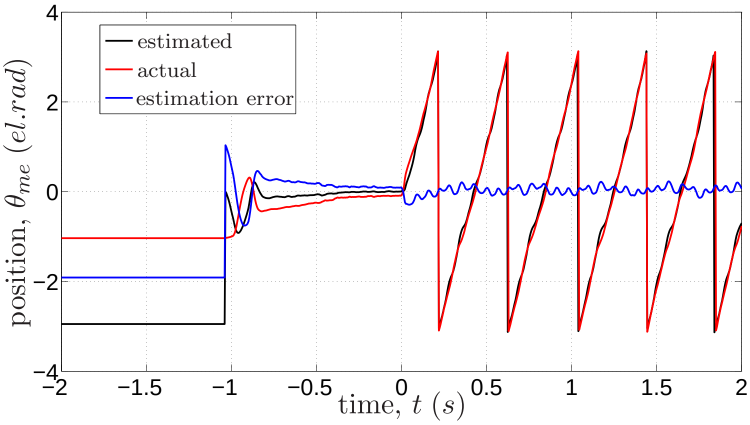

Figure 7.19: Estimated and actual position with on–line estimation and three states observer (experimental test)

performance of the sensorless control is achieved.

Fig. 7.20 shows the response of the estimated and actual rotor position after a load torque step application, under on–line estimation. When the torque step occurs, the drive maintains the control of the motor thanks to the good estimation of the position. Even if the bandwidth of the speed loop is reduced, the response of the actual speed is again fast. Fig. 7.21 shows the reference and actual q–axis current, highlighting the time instant in which the load torque is applied. The current rises from zero to roughly 30% of the nominal current. The initial overshoot is due to the choice of keeping high the proportional and integral gains of the q–axis current regulator. This is necessary to increase the speed loop dynamic and to improve the performance of the estimation loop.

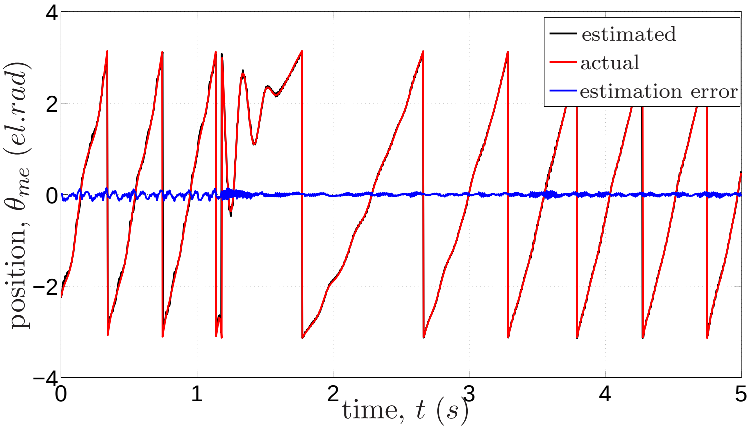

Figure 7.20: Response of estimated and actual rotor position to a load torque step with on–line estimation (experimental test)

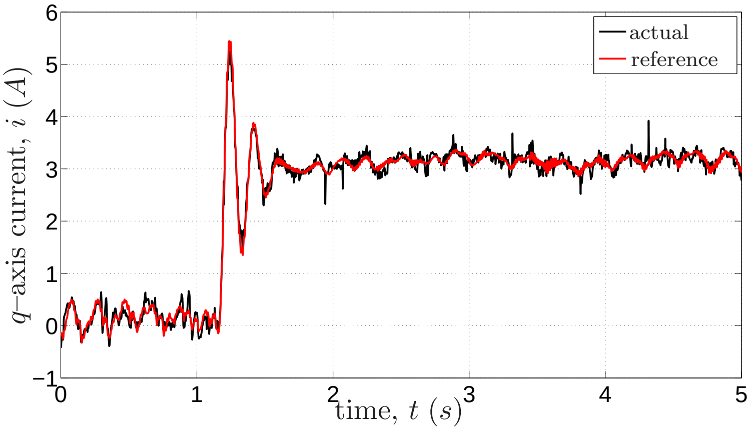

Figure 7.21: Response of q–axis current to a load torque step with on–line estimation (experimental test)

8

Rotor position estimation in IPM motor drives based on PWM harmonics excitation

8.1 Introduction

Extracting the rotor position information using high frequency injected voltages is a sensorless technique for IPM motor drives largely investigated and described in Sec. 3.3 and in Chapter 7. It consists of the addition of high frequency sine wave voltages to the fundamental voltages that feed the machine. The injection can be implemented in the stator (α–β) reference frame [22], [37][33], or in the rotor (d–q) reference frame [18], [25][35].

The Space Vector Pulse Width Modulation (PWM) adopted by the power inverters causes an intrinsic high frequency injection. Therefore, this chapter studies the potentials offered by the PWM effects in the stator current in estimating the rotor position, then developing an innovative technique for the sensorless rotor position detection. In the case of three–phase motors, the reference voltages that feed the machine are three sinusoidal displaced of 120° degree.

Really due to the PWM modulation the voltages applied to motor terminal are given by a harmonic series. According to the reference voltage vector $\bar{U}^*$ a couple of spatial vectors are applied (plus the two null vectors). In Fig. 8.1 are reported the six spatial vectors form $\bar{U}_1$ to $\bar{U}_6$ and the two null vectors $\bar{U}_0$ and $\bar{U}_7$. The Fig. 8.1 reports the case wherein the reference vector voltage is in the first sector. In order to obtain the vector $\bar{U}^*$, three phase voltages shown in Fig. 8.2 are generated with a modulation of the type single edge.

The application sequence of the spatial vector are show in Fig. 8.3. First the null vector $\bar{U}_7$ is applied for time $T_0/2$. After, the two vectors $\bar{U}_2$ and $\bar{U}_1$ are generated for time T_2 and T_1 respectively. Finally, the other null vector $\bar{U}_0$ is given for $T_0/2$.

One can hypothesized an alternative representation of the application sequence as shown in Fig. 8.4. Starting from the reference voltage vector $\bar{U}^*$, the vector $\bar{U}'$ is added in order to obtain the null vector $\bar{U}_7$. After that vector $\bar{U}''$ and $\bar{U}'''$ are added to $\bar{U}^*$ to derive vectors $\bar{U}_2$ and $\bar{U}_1$ respectively. Finally again vector $\bar{U}'$ is imposed to given the null vector $\bar{U}_0$. From the sequence of Fig. 8.4 it is possible to deduce that a rotating voltage (with variable amplitude) is added to the voltage reference, so as occurs in the estimation method based on the high frequency voltage injection.

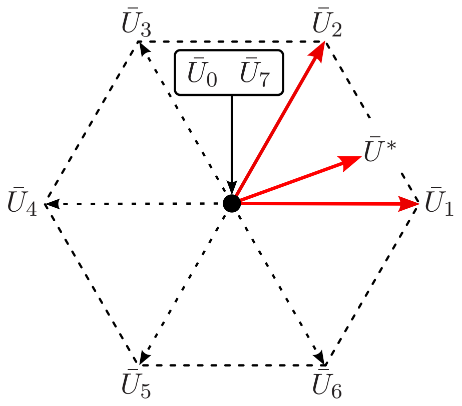

Figure 8.1: Spatial vectors used in the PWM modulation

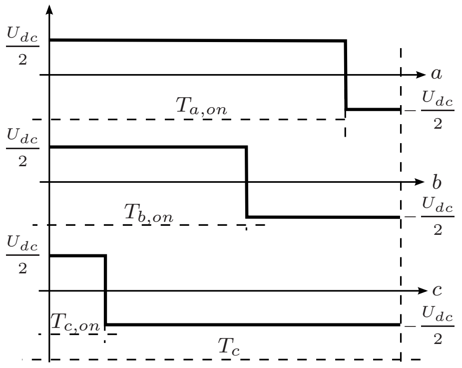

Figure 8.2: Single edge PWM in the case with $\bar{U}^*$ in the first sector

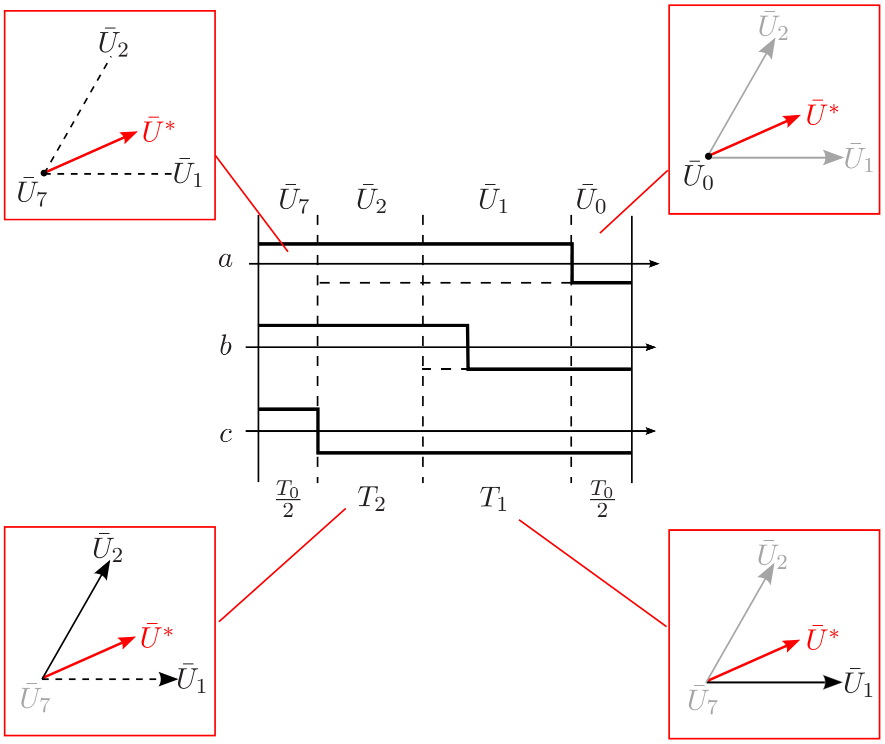

Figure 8.3: Application sequence of the spatial vectors

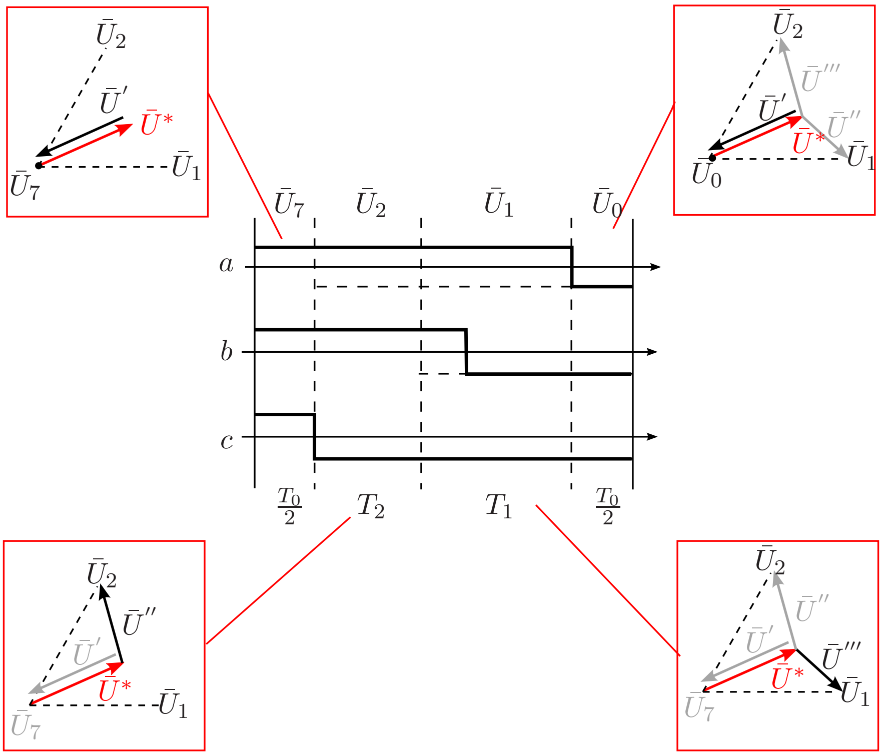

Figure 8.4: An alternative representation of the application sequence of the spatial vectors

8.2 Analytic expressions of the spectrum signals with PWM modulation

In the case of three–phase motors, the reference voltages that feed the machine are of the type:

$$\begin{aligned} u_a^*(t) &= |u|\cos(\theta_u) \\ u_b^*(t) &= |u|\cos\left(\theta_u - \frac{2\pi}{3}\right) \\ u_c^*(t) &= |u|\cos\left(\theta_u + \frac{2\pi}{3}\right) \end{aligned} \tag{8.1}$$

where, given the voltage vector $\bar{u}$, $|u|$ and θ_u are the module and the phase respectively. Angle $\theta_u = \theta_u(t)$ is the sum of the electrical rotor position θ_{me} and the phase θ_u^r of the voltage vector in the $d-q$ reference frame. In the case of a sensorless drive the electrical rotor position must be substituted with the estimated electrical position $\tilde{\theta}_{me}$.

Because of inverter presence, the actual voltages applied to the motor result from the PWM modulation. In the case of the single edge PWM modulation, the three–phase voltages inside a switching period $T_c = 1/f_c$ (where f_c is the PWM frequency) are those reported in Fig. 8.2. Each voltage u (referred to the mid–point of the DC supply) is equal to $U_{dc}/2$ during T_{on} and equal to $-U_{dc}/2$ during T_{off}, where U_{dc} is the DC bus voltage.

Applying the complex form Fourier series, it is possible to express the voltage harmonic component u_c at switching frequency f_c of each phase voltage. It results:

$$\begin{aligned} u_c(t) &= \dot{u}^+ e^{i\omega_c t} + \dot{u}^- e^{-i\omega_c t} && (8.2) \\ \text{with} \quad & \dot{u}^+ \text{ and } \dot{u}^- \in \mathbf{C} \text{ and } \dot{u}^- = conjug(\dot{u}^+) && (8.3) \end{aligned}$$

where $\omega_c = 2\pi f_c = \dfrac{2\pi}{T_c}$.

Starting from the voltage $u_a(t)$, the Fourier coefficient, $\dot{u}^+_{a_c}$ results:

$$\dot{u}^+_{a_c} = \frac{1}{T_c}\int_0^{T_c} u_a(t) e^{-i\omega_c t} \tag{8.4}$$

By function $u_a(t)$ real, the following equality:

$$\dot{u}^-_{a_c} = \dot{u}^{+^*}_{a_c} \tag{8.5}$$

is also valid. In Appendix. A the complete mathematical study carried out in order to derive the voltage harmonics expression for the three–pase voltages and the transformation in the $\alpha\beta$ reference frame is reported. From App. A.1 and taking into account the sensorless drive, the following three–phases voltages are obtained:

$$\begin{aligned} u_{a_c} = A_0 \sin(\omega_c t) &+ \sum_{n=1}^{+\infty}(-1)^n \frac{A_{2n-1}}{2}\cos\left(\omega_c t + (2n-1)(\tilde{\theta}_{me} + \theta^r_u)\right) \\ &+ \sum_{n=1}^{+\infty}(-1)^n \frac{A_{2n-1}}{2}\cos\left(\omega_c t - (2n-1)(\tilde{\theta}_{me} + \theta^r_u)\right) \\ &+ \sum_{n=1}^{+\infty}(-1)^n \frac{A_{2n}}{2}\sin\left(\omega_c t + 2n(\tilde{\theta}_{me} + \theta^r_u)\right) \\ &+ \sum_{n=1}^{+\infty}(-1)^n \frac{A_{2n}}{2}\sin\left(\omega_c t - 2n(\tilde{\theta}_{me} + \theta^r_u)\right) \end{aligned} \tag{8.6}$$

$$\begin{aligned} u_{b_c} = A_0 \sin(\omega_c t) &+ \sum_{n=1}^{+\infty}(-1)^n \frac{A_{2n-1}}{2}\cos\left(\omega_c t + (2n-1)\left((\tilde{\theta}_{me} + \theta^r_u) - \frac{2\pi}{3}\right)\right) \\ &+ \sum_{n=1}^{+\infty}(-1)^n \frac{A_{2n-1}}{2}\cos\left(\omega_c t - (2n-1)\left((\tilde{\theta}_{me} + \theta^r_u) - \frac{2\pi}{3}\right)\right) \\ &+ \sum_{n=1}^{+\infty}(-1)^n \frac{A_{2n}}{2}\sin\left(\omega_c t + 2n\left((\tilde{\theta}_{me} + \theta^r_u) - \frac{2\pi}{3}\right)\right) \\ &+ \sum_{n=1}^{+\infty}(-1)^n \frac{A_{2n}}{2}\sin\left(\omega_c t - 2n\left((\tilde{\theta}_{me} + \theta^r_u) - \frac{2\pi}{3}\right)\right) \end{aligned} \tag{8.7}$$

$$
\begin{aligned}
u_{c_c} = A_0 \sin(\omega_c t) &+ \sum_{n=1}^{+\infty}(-1)^n \frac{A_{2n-1}}{2} \cos\left(\omega_c t + (2n-1)\left((\tilde{\theta}_{me} + \theta_u^r) - \frac{2\pi}{3}\right)\right) \\
&+ \sum_{n=1}^{+\infty}(-1)^n \frac{A_{2n-1}}{2} \cos\left(\omega_c t + (2n-1)\left((\tilde{\theta}_{me} + \theta_u^r) + \frac{2\pi}{3}\right)\right) \\
&+ \sum_{n=1}^{+\infty}(-1)^n \frac{A_{2n}}{2} \sin\left(\omega_c t + 2n\left((\tilde{\theta}_{me} + \theta_u^r) + \frac{2\pi}{3}\right)\right) \\
&+ \sum_{n=1}^{+\infty}(-1)^n \frac{A_{2n}}{2} \sin\left(\omega_c t - 2n\left((\tilde{\theta}_{me} + \theta_u^r) + \frac{2\pi}{3}\right)\right)
\end{aligned} \tag{8.8}
$$

where A_0, A_{2n-1} and A_{2n} are reported in (A.19). One can note that the three–phases voltages spectrum have a principle harmonics at switching frequency and a series of other harmonics at frequency symmetrical respect to the first. At steady–state $\tilde{\theta}_{me}$can be written as $\tilde{\omega}_{me}t$, while θ_u^r is constant. Then the voltage spectrum has a harmonics at frequency $f_c \pm k f_{me}$ with $k \in \mathbb{I}$ and f_{me} is the fundamental frequency given by $\tilde{\omega}_{me}/2\pi$.

Applying the transformation matrix $T_{abc,\alpha\beta}$ at the (8.6), (8.7) and (8.8) the $\alpha\beta$ reference frame is obtained (see App. A.2):

$$
\begin{aligned}
u_{\alpha_c} = &\frac{2}{3}\sum_{n=1}^{+\infty}(-1)^n \frac{A_{2n-1}}{2} \cos\left(\omega_c t + (2n-1)(\tilde{\omega}_{me}t + \theta_u^r)\right)\left(1 - \cos\left((2n-1)\frac{2\pi}{3}\right)\right) \\
&+ \frac{2}{3}\sum_{n=1}^{+\infty}(-1)^n \frac{A_{2n-1}}{2} \cos\left(\omega_c t - (2n-1)(\tilde{\omega}_{me}t + \theta_u^r)\right)\left(1 - \cos\left((2n-1)\frac{2\pi}{3}\right)\right) \\
&+ \frac{2}{3}\sum_{n=1}^{+\infty}(-1)^n \frac{A_{2n}}{2} \sin\left(\omega_c t + 2n(\tilde{\omega}_{me}t + \theta_u^r)\right)\left(1 - \cos\left(2n\frac{2\pi}{3}\right)\right) \\
&+ \frac{2}{3}\sum_{n=1}^{+\infty}(-1)^n \frac{A_{2n}}{2} \sin\left(\omega_c t - 2n(\tilde{\omega}_{me}t + \theta_u^r)\right)\left(1 - \cos\left(2n\frac{2\pi}{3}\right)\right)
\end{aligned} \tag{8.9}
$$

$$
\begin{aligned}
u_{\beta_c} = &\frac{2}{\sqrt{3}}\sum_{n=1}^{+\infty}(-1)^n \frac{A_{2n-1}}{2} \sin\left(\omega_c t + (2n-1)(\tilde{\omega}_{me}t + \theta_u^r)\right) \sin\left((2n-1)\frac{2\pi}{3}\right) \\
&- \frac{2}{\sqrt{3}}\sum_{n=1}^{+\infty}(-1)^n \frac{A_{2n-1}}{2} \sin\left(\omega_c t - (2n-1)(\tilde{\omega}_{me}t + \theta_u^r)\right) \sin\left((2n-1)\frac{2\pi}{3}\right) \\
&- \frac{2}{\sqrt{3}}\sum_{n=1}^{+\infty}(-1)^n \frac{A_{2n}}{2} \cos\left(\omega_c t + (2n(\tilde{\theta}_{me} + \theta_u^r))\right) \sin\left(2n\frac{2\pi}{3}\right) \\
&+ \frac{2}{\sqrt{3}}\sum_{n=1}^{+\infty}(-1)^n \frac{A_{2n}}{2} \cos\left(\omega_c t - (2n(\tilde{\theta}_{me} + \theta_u^r))\right) \sin\left(2n\frac{2\pi}{3}\right)
\end{aligned} \tag{8.10}
$$

One can note that u_{α_c} and u_{β_c} are given by a series of harmonics centered around the switching frequency, then with frequency $f_c \pm f_{me}$. In App. A is also demonstrated that the harmonics at frequency $f_c \pm 3k f_{me}$ with $k \in \mathbb{I}$ are null. In other words there are not harmonics at frequency f_c plus or minus the third harmonics (respect to the electric frequency) and its multiplies.

Finally, the harmonics amplitude decrease as the frequency differs from f_c. Then from all the terms it is possible taking into consideration those at frequency $f_c \pm f_{me}$:

$$\begin{aligned} u_{\alpha_c} &= -\frac{A_1}{2}\cos(\omega_c t + \tilde{\theta}_{me} + \theta_u^r) - \frac{A_1}{2}\cos(\omega_c t - \tilde{\theta}_{me} - \theta_u^r) \\ &= -U\cos(\omega_c t + \tilde{\theta}_{me} + \theta_u^r) - U\cos(-\omega_c t + \tilde{\theta}_{me} + \theta_u^r) \\ u_{\beta_c} &= -\frac{A_1}{2}\sin(\omega_c t + \tilde{\theta}_{me} + \theta_u^r) + \frac{A_1}{2}\sin(\omega_c t - \tilde{\theta}_{me} - \theta_u^r) \\ &= -U\sin(\omega_c t + \tilde{\theta}_{me} + \theta_u^r) - U\sin(-\omega_c t + \tilde{\theta}_{me} + \theta_u^r) \end{aligned} \tag{8.11}$$

From (8.11) one can note that the high frequency voltage vector is given by two rotating vectors at speed $\omega_c + \omega_{me}$ and $-\omega_c + \omega_{me}$. Then the voltage vector can be split in this way:

$$\bar{u}^s_{\alpha\beta_c} = \underbrace{\bar{u}^s_{\omega_c^+}}_{anti-clockwise} + \underbrace{\bar{u}^s_{\omega_c^-}}_{clockwise} \tag{8.12}$$

8.3 Stator currents analysis at switching frequency

To calculate the high frequency currents, it is possible to study separately the effects due to the two voltage vectors $\bar{u}^s_{\omega_c^-}$ and $\bar{u}^s_{\omega_c^+}$, using similar procedures to those described in Secs. 3.3.1 and 3.4.1. As reported in App. A.3 the high frequency currents due to the voltages (8.11) are the following:

$$\begin{aligned} i_{\alpha_c} = &-I_0^+\sin(\omega_c t + \tilde{\theta}_{me}(t) + \theta_u^r) - I_1^+\sin(\omega_c t + \tilde{\theta}_{me}(t) - 2\theta_{me}(t) + \theta_u^r) - \\ &- I_0^-\sin(\omega_c t - \tilde{\theta}_{me}(t) - \theta_u^r) - I_1^-\sin(\omega_c t - \tilde{\theta}_{me}(t) + 2\theta_{me}(t) - \theta_u^r) \end{aligned} \tag{8.13}$$

$$\begin{aligned} i_{\beta_c} = &\ I_0^+\cos(\omega_c t + \tilde{\theta}_{me}(t) + \theta_u^r) - I_1^+\cos(\omega_c t + \tilde{\theta}_{me}(t) - 2\theta_{me}(t) + \theta_u^r) - \\ &- I_0^-\cos(\omega_c t - \tilde{\theta}_{me}(t) - \theta_u^r) + I_1^-\cos(\omega_c t - \tilde{\theta}_{me}(t) + 2\theta_{me}(t) - \theta_u^r) \end{aligned} \tag{8.14}$$

with

$$\begin{aligned} I_0^+ &= \frac{l_\Sigma}{l_d l_q}\frac{U}{\omega_c + \tilde{\omega}_{me}} \\ I_1^+ &= \frac{l_\Delta}{l_d l_q}\frac{U}{\omega_c + \tilde{\omega}_{me}} \\ I_0^- &= \frac{l_\Sigma}{l_d l_q}\frac{U}{\omega_c - \tilde{\omega}_{me}} \\ I_1^- &= \frac{l_\Delta}{l_d l_q}\frac{U}{\omega_c - \tilde{\omega}_{me}} \end{aligned} \tag{8.15}$$

where l_d and l_q are the d– and q–axis inductances respectively, $\tilde{\omega}_{me}$ is the estimated speed and

$$\begin{aligned} l_\Sigma &= \frac{l_q + l_d}{2} \\ l_\Delta &= \frac{l_q - l_d}{2} \end{aligned}$$

One can note that the current vector is given by a sum of two direct sequences[1]

$$\begin{aligned}
&I_0^+[-\sin(\omega_c t + \tilde{\theta}_{me}(t) + \theta_u^r) + j\cos(\omega_c t + \tilde{\theta}_{me}(t) + \theta_u^r)] \\
&I_1^-[-\sin(\omega_c t - \tilde{\theta}_{me}(t) + 2\theta_{me}(t) - \theta_u^r) + j\cos(\omega_c t - \tilde{\theta}_{me}(t) + 2\theta_{me}(t) - \theta_u^r)]
\end{aligned}$$

and two inverse sequences

$$\begin{aligned}
&I_1^+[-\sin(\omega_c t - \tilde{\theta}_{me}(t) - \theta_u^r) - j\cos(\omega_c t - \tilde{\theta}_{me}(t) - \theta_u^r)] \\
&I_0^-[-\sin(\omega_c t + \tilde{\theta}_{me} - 2\theta_{me}(t) + \theta_u^r) - j\cos(\omega_c t + \tilde{\theta}_{me} - 2\theta_{me}(t) + \theta_u^r)]
\end{aligned}$$

8.4 Simulation model

Some simulations have been done in order to validate the analytical study presented previously by means of *Simulink® toolbox of Matlab®*. To this purpose the simulation model in Fig. 8.5 has been realized, in which it is possibile to highlight three main parts: the motor, the control and the inverter.

In the first block, the IPM motor model in the *d*–*q* reference frame has implemented, as reported in Fig. 8.6. Moreover, the block accepts the voltages in the α–β reference frame thanks to the transformation matrix from *abc* to $\alpha\beta$ and from $\alpha\beta$ to *dq* that are incorporated in the IPM motor block (not illustrated). In the second block, the speed, direct and quadrature current control loops are implemented as reported in Fig. 8.7. The speed control supplies the quadrature current reference, while the direct current reference can be fixed according to the drive operating point. The reference frame transformation (from measured $i_\alpha - i_\beta$ to $i_d - i_q$ for the current and from $u_d^* - u_q^*$ to $u_\alpha^* - u_\beta^*$ for the voltages) are performed using the estimated position $\tilde{\theta}_{me}$. The currents used as feedbacks are measured at the switching frequency f_c. Finally, in the last block the single–edge PWM modulation is realized as shown in Fig. 8.8. The algorithm is implemented in an *Embedded MATLAB function*. The modulated voltages are delivered at output of the block, on the basis of the reference voltages $u_\alpha^*(t)$ and $u_\beta^*(t)$, given by the current controls.

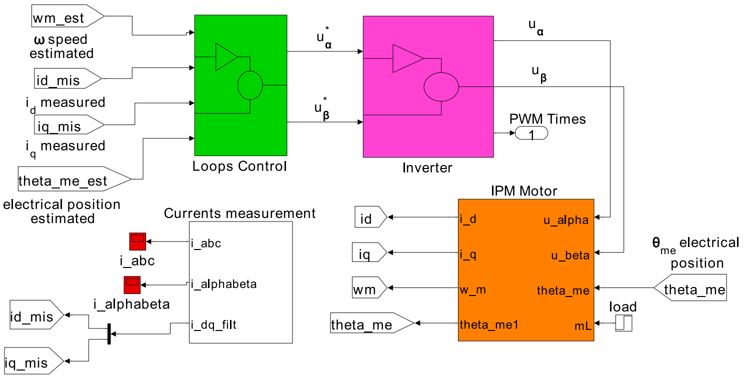

Figure 8.5: Simulink model of the system

---

[1] $\sin\theta + j\cos\theta = j(\cos\theta - j\sin\theta) \Rightarrow$ Inverse sequence
$\sin\theta - j\cos\theta = -j(\cos\theta + j\sin\theta) \Rightarrow$ Direct sequence

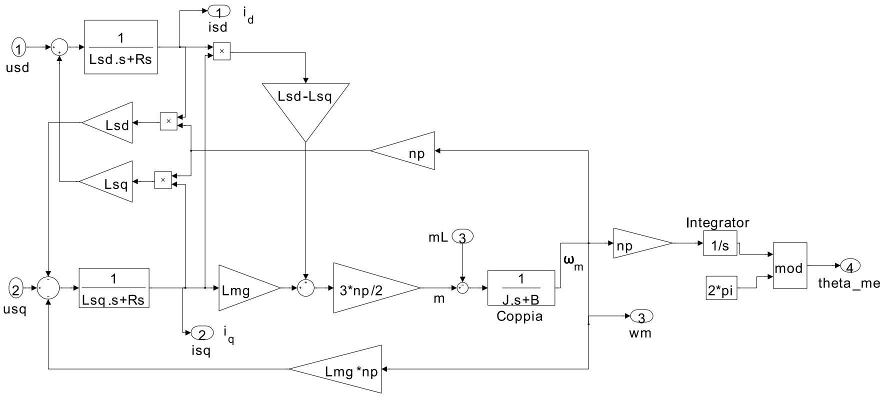

Figure 8.6: IPM motor model

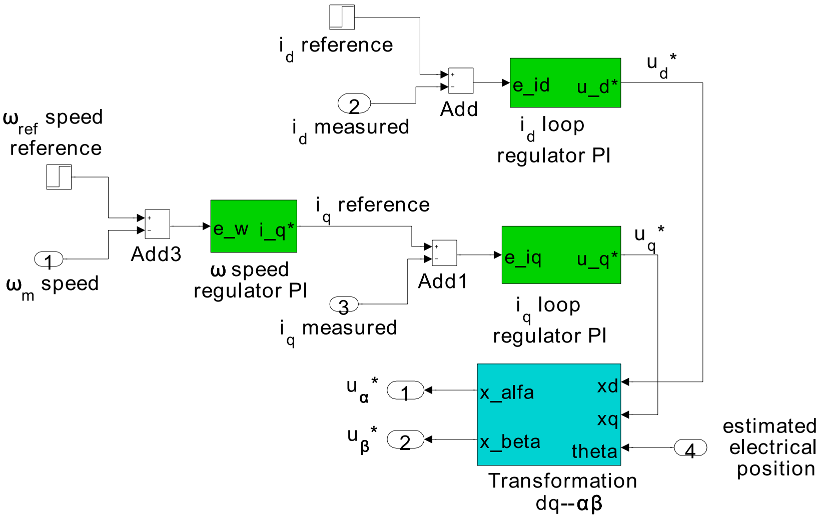

Figure 8.7: Loops control model

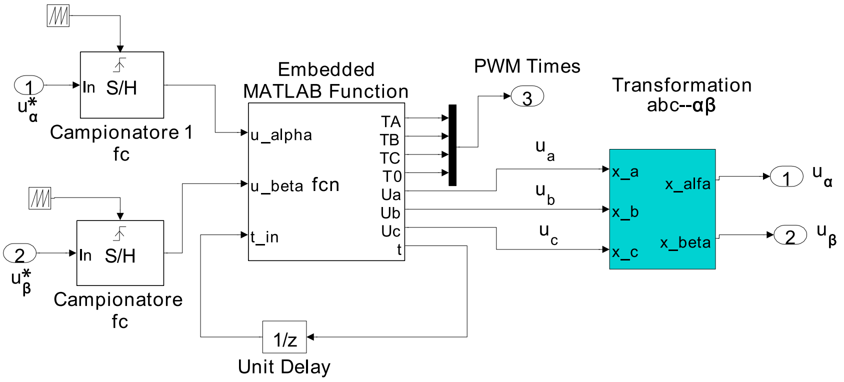

Figure 8.8: Inverter model

Simulations have been carried out taking into account a reference voltage vector of amplitude 100 V. The 4–pole motor is dragged at about 3000 rpm and then the fundamental frequency f_{me} is equal to 100 $el.period/s$. The PWM period is equal to 100 μs and then the carrier frequency f_c is 10 kHz. The DC bus is 500 V and then the leg voltages are $\pm U_{DC}/2 = \pm 250\ [V]$. The modulated voltages are compared with the reference voltages at the input to the PWM blocks of Fig. 8.8. Voltage u_α^* is compared with the voltage $u_{\alpha_{LP}}$ given by the PWM modulation, after a low pass filtering. Similar comparison is made for u_β. Fig. 8.9 shows the simulation results.

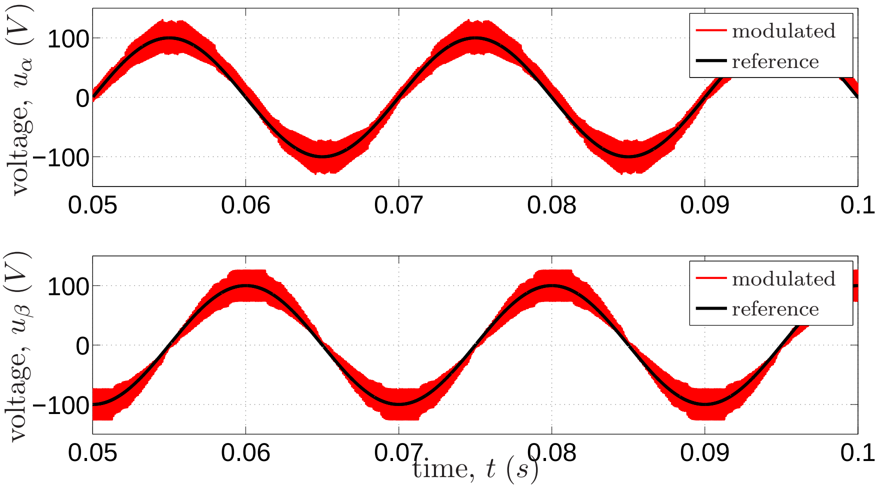

Figure 8.9: PWM voltage motor fed after a low pass filter

One can note the good correspondence between the two signals, then the motor is fed with a voltages which fundamental components are equal to the reference ones. The voltage u_{a0} of the phase a is delivered by the PWM function and its frequency spectrum is reported in Fig. 8.10.

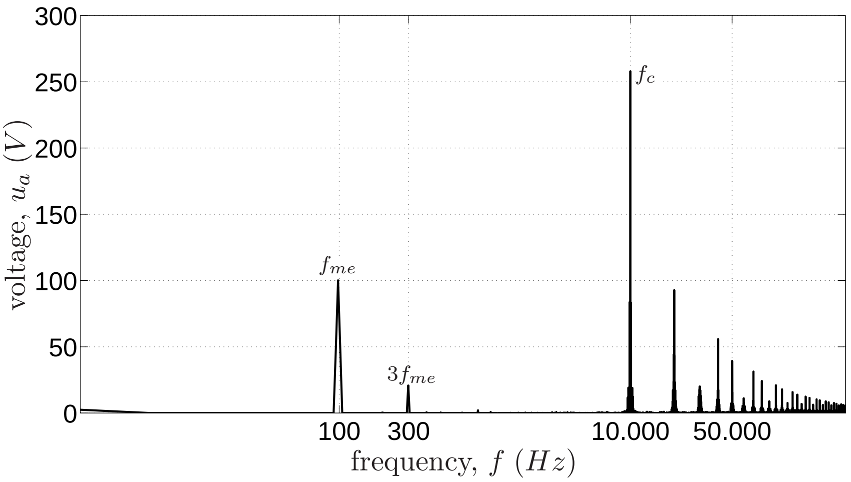

Figure 8.10: FFT spectrum of phase a voltage u_a

The spectrum of phase a is also composed to harmonics cluster around to fundamental frequency f_{me} and around to frequencies multiplies of f_c. All three–phase voltages harmonic components at frequencies kf_c can be derived in similar way carried out in App. A.

At low frequency the highest harmonics are the first and the third respect to the fundamental frequency as shown in Fig. 8.10. Instead, around the switching frequency, the harmonic at f_c is the highest (that is also the highest in the frequency spectrum) and it is comparable to the maximum inverter–leg voltage of 250 V. The other harmonics are at frequency $f_c + kf_{me}$. Their amplitude decreases with the distance respect to the harmonic at frequency f_c, as shown in Fig. 8.11.

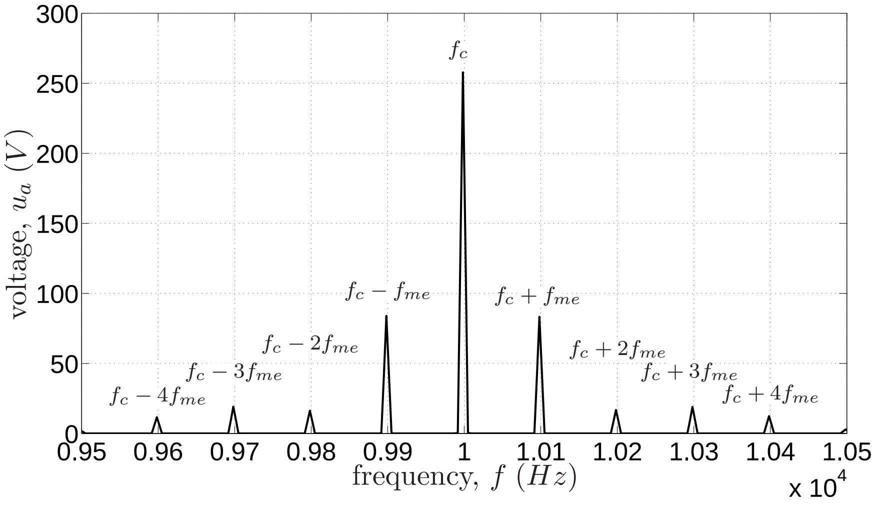

Figure 8.11: FFT spectrum of phase a voltage u_a, zoom around the carrier frequency f_c

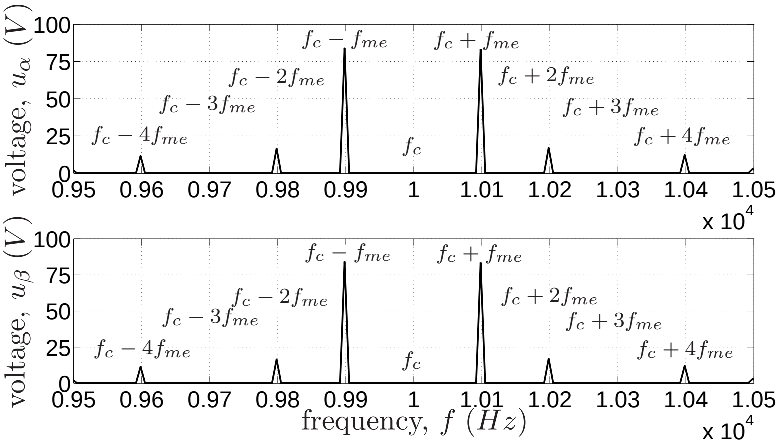

Figure 8.12: FFT spectrum of voltage u_α and u_β, zoom around the carrier frequency f_c

The same behaviour can be recognized for the harmonic components around to the frequency multiple of the swicthing one. Their amplitude decreases quickly with the increase of the frequency. Same considerations can be done for the voltages u_b and u_c, as demonstrate in (8.7) and (8.8).

The voltages u_α and u_β are obtained from these three voltages using the matrix transformation $[T_{abc/\alpha\beta}]$. The result reported in Sec. 8.2 shows that the harmonics at frequency $f_c + 3kf_{me}$ with $k \in \mathbf{Z}$ are equal to zero. This is confirmed by the Fig. 8.12 where the frequency spectrum, around f_c, of u_α (on the top) and u_β (on the bottom) are reported. One can note that there are not harmonics at frequency f_c and $f_c \pm 3f_{me}$.

Some simulations have been done in order to verify the high frequency currents i_{α_c} and i_{β_c} given by (8.13) and (8.14). To this purpose the motors current, filtered with a pass band filter centered around the switching frequency, are compared with currents given by (8.13) and (8.14). The electrical position $\theta_{me}(t)$ is that of the motor, the phase θ_u^r is calculated from the knowledge of the reference voltage u_d^* and u_q^*. Finally the voltage U is estimated by a FFT analysis. Simulation results are reported in Fig. 8.13 and Fig. 8.14.

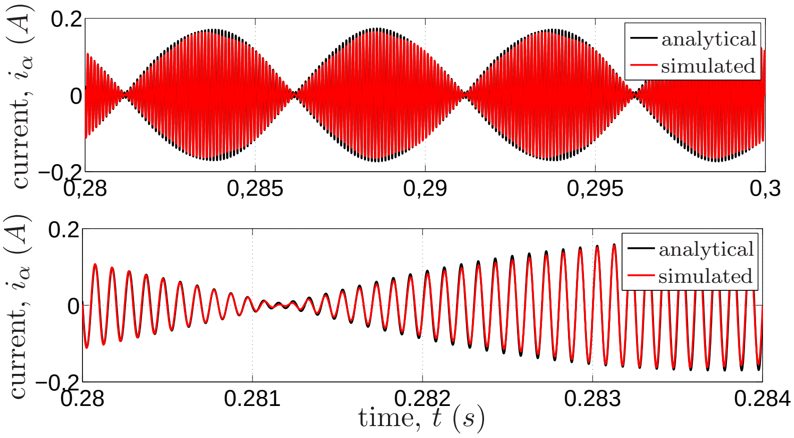

Figure 8.13: Real and reconstructed current i_α harmonics around the carrier frequency

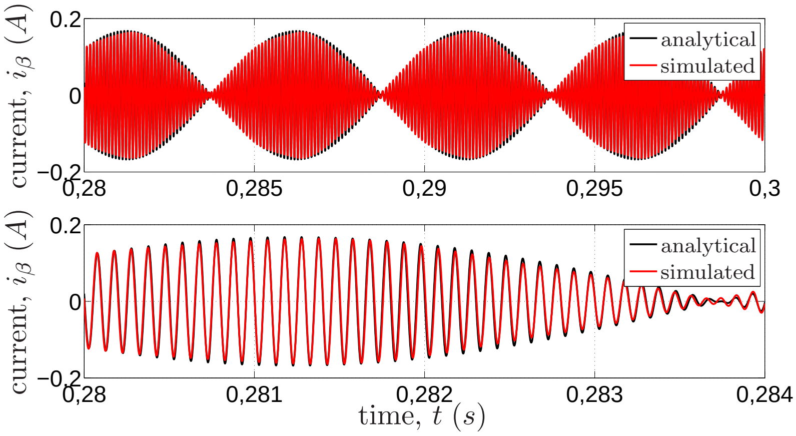

Figure 8.14: Real and reconstructed current i_β harmonics around the carrier frequency

Practically, the current i_α has frequency f_c (as shown in the bottom part of Fig. 8.13) and amplitude modulated by $\sin(\omega_{me}t)$ (as shown in the top part of Fig. 8.13). The difference between the actual current and the reconstructed one is due to the other harmonics that are not taken into consideration in the mathematic analysis reported in Sec.8.3. Same considerations can be done for the current i_β as reported in Fig. 8.14.

8.5 Position estimation

The estimated electric position can be delivered in a similar way used in [38]. The high frequency stator current (8.13) and (8.14) are manipulated as follows:

$$\begin{aligned}\epsilon &= i_{\alpha_c}\cos(\omega_c t-\tilde{\theta}_{me}-\theta_u^r)-i_{\beta_c}\sin(\omega_c t-\tilde{\theta}_{me}-\theta_u^r)\\ &= -I_0^+\sin(2\omega_c t)-I_1^+\sin(2(\tilde{\theta}_{me}+\theta_u^r-\theta_{me}))-\\ &\quad -I_1^-\sin(2\omega_c t-2(\tilde{\theta}_{me}+\theta_u^r-\theta_{me}))\end{aligned} \tag{8.16}$$

where $\tilde{\theta}_{me}$ is the estimated position, θ_{me} is the rotor electrical position and θ_u^r is the voltage vector phase in the $d-q$ reference frame. Filtering (8.16) by a low pass filter, the term at frequency $2\omega_c$ is removed and it results:

$$\epsilon_{LPF}=-I_1^+\sin(2(\tilde{\theta}_{me}+\theta_u^r-\theta_{me})) \tag{8.17}$$

Finally, imposing $\tilde{\theta}'_{me}=\tilde{\theta}_{me}+\theta_u^r$, it is possible to define a new estimated angle. Then the (8.17) becomes:

$$\epsilon'_{LPF}=-I_1^+\sin(2\Delta\theta) \tag{8.18}$$

where $\Delta\theta=\tilde{\theta}'_{me}-\theta_{me}$. The $\sin(2\Delta\theta_{me})$ is equal to zero when also $\Delta\theta_{me}$ is zero, that is when $\tilde{\theta}'_{me}$ is equal to the electrical position θ_{me}. An adjustment mechanism can thus correct the estimated position $\tilde{\theta}'_{me}$ to nullify the error $\Delta\theta_{me}$. To this purpose, the estimator scheme of Fig. 8.15 is used.

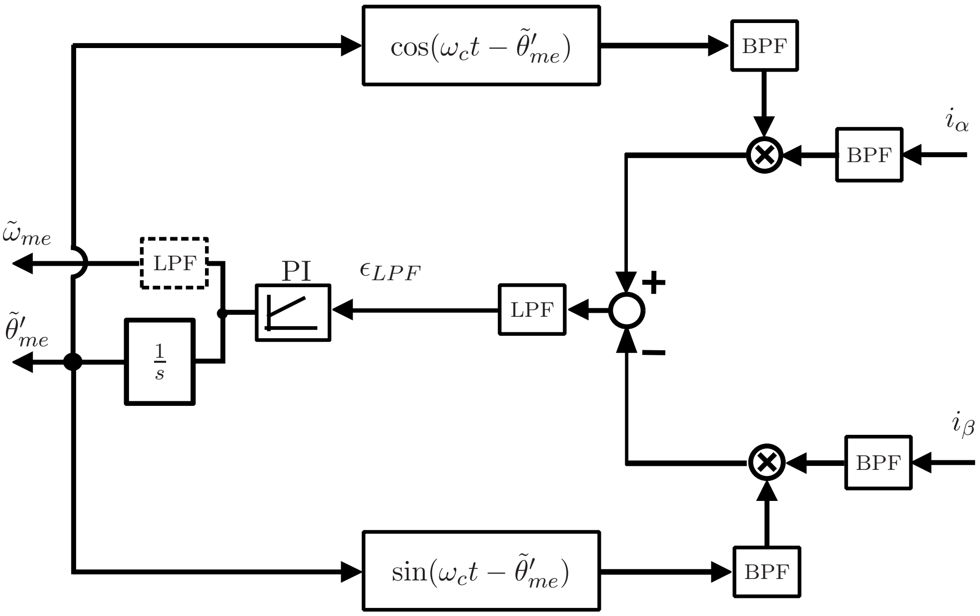

Figure 8.15: Speed and position estimator scheme

A PI regulator is used to nullify ϵ_{LPF} and to deliver the estimated speed and, by its integration, the estimated position. At standstill, since the voltage vector is null also its high frequency components are equal to zero[2] and then, the position information couldn't be extracted. With an opportune arrangement of the PWM modulation, it is possible getting around this trouble.

The high frequency stator currents i_{α_c} and i_{β_c} are given by filtering the stator currents i_α and i_β with a pass band filter. In order to confirm the estimation algorithm a simulation has been done, using the scheme reported in Fig. 8.5. The motor is dragged at speed 50 $[rad/s]$ and the i_d and i_q reference currents are imposed. The transformation from the stator reference frame to the rotor reference frame and viceversa are performed using the estimated position. The estimated electric position and the actual one are reported in Fig. 8.16. One can note the good correspondence between the two signal after the initial transient. In Fig. 8.17, instead shows the estimated and the actual speed. After an initial transitory, the estimation reaches the real speed in 0.1 s. At steady–state $\tilde{\omega}_{me}$ presents an oscillation, that is also visible in the estimated position.

Simulations confirms the possibility to estimate the rotor position from the high frequency stator currents due to the PWM modulation.

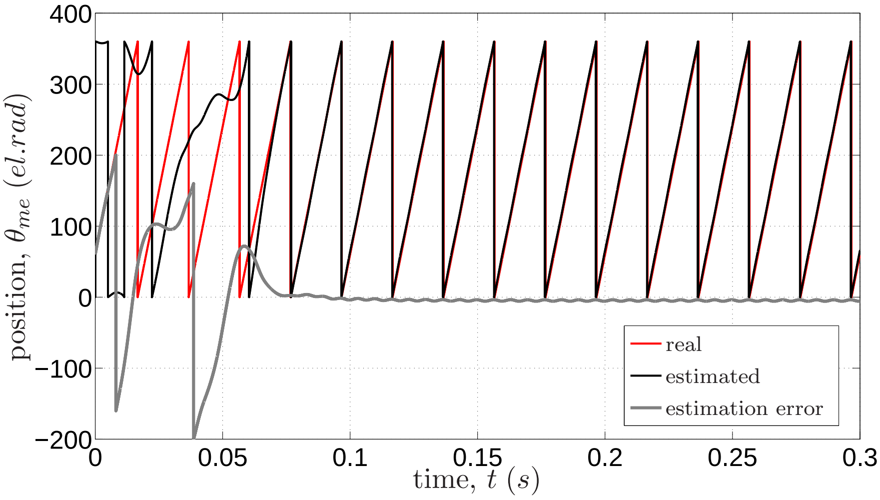

Figure 8.16: Estimated position and actual one (simulation)

---

[2] Taking for example the phase a, being $|u| = 0$ then u_a^* is null and $T_{a,on}$ is equal to $T_c/2$. Substituting the latter in (A.10) one can note that u_{a_c} is nullify

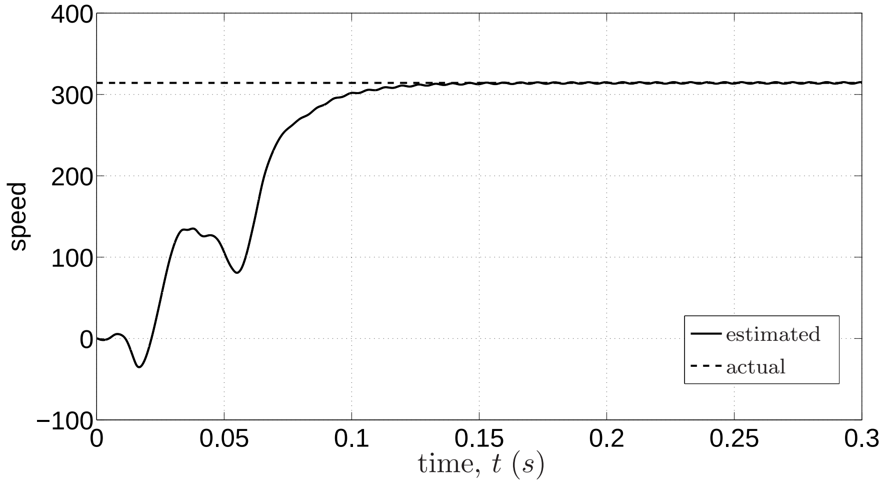

Figure 8.17: Estimated speed and actual one (simulation)

A

Analytic expressions of the spectrum signals with PWM modulation

A.1 Study in the abc reference frame

In the case of three–phase motors, the reference voltages that feed the machine are of the type:

$$\begin{aligned} u_a^*(t) &= |u|\cos(\theta_u) \\ u_b^*(t) &= |u|\cos\left(\theta_u - \frac{2\pi}{3}\right) \\ u_c^*(t) &= |u|\cos\left(\theta_u + \frac{2\pi}{3}\right) \end{aligned} \tag{A.1}$$

Where, given the voltage vector $\bar{u}$, $|u|$ and θ_u are the module and the phase respectively.

A cause of the presence of the inverter, the actual voltages applied to the motor result from the PWM modulation. In the case of the single edge PWM modulation the three–phase voltages value are:

$$\begin{aligned} u_a(t) &= \begin{cases} \frac{U_{dc}}{2} & 0 \leq t \leq T_{a,on} \\ -\frac{U_{dc}}{2} & T_{a,on} \leq t \leq T_c \end{cases} \\ u_b(t) &= \begin{cases} \frac{U_{dc}}{2} & 0 \leq t \leq T_{b,on} \\ -\frac{U_{dc}}{2} & T_{b,on} \leq t \leq T_c \end{cases} \\ u_c(t) &= \begin{cases} \frac{U_{dc}}{2} & 0 \leq t \leq T_{c,on} \\ -\frac{U_{dc}}{2} & T_{c,on} \leq t \leq T_c \end{cases} \end{aligned} \tag{A.2}$$

Applying the complex form Fourier series, it is possible to express the voltage harmonic component $u_{_c}$ at switching frequency f_c of each phase voltage. It results:

$$u_{_c}(t) = \dot{u}^+ e^{i\omega_c t} + \dot{u}^- e^{-i\omega_c t} \tag{A.3}$$

$$\text{with} \quad \dot{u}^+ \text{ and } \dot{u}^- \in \mathbf{C} \text{ and } \dot{u}^- = conjug(\dot{u}^+) \tag{A.4}$$

where $\omega_c = 2\pi f_c = \dfrac{2\pi}{T_c}$.

Starting from the voltage $u_a(t)$, the Fourier coefficient, $\dot{u}_{a_c}^+$ results:

$$\dot{u}_{a_c}^+ = \frac{1}{T_c}\int_0^{T_c} u_a(t)e^{-i\omega_c t} \tag{A.5}$$

According to (A.2), integral in (A.5) can be split up into two parts as following[1]:

$$\begin{aligned}
\dot{u}_{a_c}^{+} &= \frac{1}{T_c}\left[\int_0^{T_{a,on}} \frac{U_{dc}}{2} e^{-i\omega_c t} dt + \int_{T_{a,on}}^{T_c} -\frac{U_{dc}}{2} e^{-i\omega_c t} dt\right] && \text{(A.6)}\\
&= \frac{1}{T_c}\frac{U_{dc}}{2}\left[-\frac{1}{i\omega_c} e^{-i\omega_c t}\Big|_0^{T_{a,on}} - (-\frac{1}{i\omega_c}) e^{-i\omega_c t}\Big|_{T_{a,on}}^{T_c}\right] \\
&= \frac{1}{T_c}\frac{U_{dc}}{2}\frac{i}{\omega_c}\left[e^{-i\omega_c T_{a,on}} - 1 - e^{-i2\pi} + e^{-i\omega_c T_{a,on}}\right] \\
&= \frac{iU_{dc}}{4\pi}\left[2e^{-i\omega_c T_{a,on}} - 2\right] = \frac{iU_{dc}}{2\pi}\left[e^{-i\omega_c T_{a,on}} - 1\right] && \text{(A.7)}
\end{aligned}$$

The function $u_a(t)$ is real, then it is possible to derive quickly the expression of $\dot{u}^-$ from (A.7):

$$\dot{u}_{a_c}^{-} = \dot{u}_{a_c}^{+*\,[2]} = -\frac{iU_{dc}}{2\pi}\left[e^{i\omega_c T_{a,on}} - 1\right] \tag{A.8}$$

Substituting (A.5) and (A.8) in the (A.3) results:

$$\begin{aligned}
u_{a_c} &= i\frac{U_{dc}}{2\pi}\left[e^{-i\omega_c T_{a,on}} - 1\right](\cos(\omega_c t) + i\sin(\omega_c t)) && \text{(A.9)}\\
&\qquad - i\frac{U_{dc}}{2\pi}\left[e^{i\omega_c T_{a,on}} - 1\right](\cos(\omega_c t) - i\sin(\omega_c t)) \\
&= i\frac{U_{dc}}{2\pi}\cos(\omega_c t)\left[e^{-i\omega_c T_{a,on}} - 1 - e^{i\omega_c T_{a,on}} + 1\right] \\
&\qquad + i\frac{U_{dc}}{2\pi}(i\sin(\omega_c t))\left[e^{-i\omega_c T_{a,on}} - 1 + e^{i\omega_c T_{a,on}} - 1\right] \\
&= i\frac{U_{dc}}{2\pi}\cos(\omega_c t)\left[e^{-i\omega_c T_{a,on}} - e^{i\omega_c T_{a,on}}\right] - \frac{U_{dc}}{2\pi}\sin(\omega_c t)\left[e^{-i\omega_c T_{a,on}} + e^{i\omega_c T_{a,on}} - 2\right] \\
&= \frac{U_{dc}}{\pi}\cos(\omega_c t)\left[\frac{e^{i\omega_c T_{a,on}} - e^{-i\omega_c T_{a,on}}}{2i}\right] \\
&\qquad - \frac{U_{dc}}{\pi}\sin(\omega_c t)\left[\frac{e^{-i\omega_c T_{a,on}} + e^{i\omega_c T_{a,on}}}{2}\right] - \frac{U_{dc}}{\pi}\sin(\omega_c t) \\
&= \frac{U_{dc}}{\pi}\cos(\omega_c t)\sin(\omega_c T_{a,on}) - \frac{U_{dc}}{\pi}\sin(\omega_c t)\cos(\omega_c T_{a,on}) - \frac{U_{dc}}{\pi}\sin(\omega_c t) && \text{(A.10)}
\end{aligned}$$

In the case of the phase a voltage, the time T_{on} is equal to:

$$T_{a,on} = \frac{T_c}{U_{dc}}u_\alpha + \frac{T_c}{2} = \frac{T_c}{U_{dc}}|u|\cos\theta_u + \frac{T_c}{2} \tag{A.11}$$

Then using this expression in the (A.10) results:

$$\begin{aligned}
u_{a_c} &= \frac{U_{dc}}{\pi}\cos(\omega_c t)\sin\left(\omega_c\left(\frac{T_c|u|}{U_{dc}}\cos\theta_u + \frac{T_c}{2}\right)\right) - \\
&\quad - \frac{U_{dc}}{\pi}\sin(\omega_c t)\cos\left(\omega_c\left(\frac{T_c|u|}{U_{dc}}\cos\theta_u + \frac{T_c}{2}\right)\right) - \frac{U_{dc}}{\pi}\sin(\omega_c t) && \text{(A.12)}
\end{aligned}$$

---

[1] $\omega_c T_c = \frac{2\pi}{T_c}T_c = 2\pi$, then $e^{-i\omega_c T_c} = e^{-i2\pi} = 1$

[2] Simbolysm x^* indicates the complex conjugate of x

For seek of simplicity, the sine and cosine of $\omega_c T_{a,on}$ are calculated separately.

$$\begin{aligned}
\sin(\omega_c T_{a,on}) &= \sin\left(\omega_c \frac{T_c|u|}{U_{dc}}\cos\theta_u + \frac{\omega_c T_c}{2}\right) \\
&= \sin\left(2\pi\frac{|u|}{U_{dc}}\cos\theta_u + \pi\right) \\
&= -\sin\left(2\pi\frac{|u|}{U_{dc}}\cos\theta_u\right) \qquad \text{(A.13)}
\end{aligned}$$

which can be expressed, using the Jacobi-Anger expansions[3], in this way:

$$\sin\left(2\pi\frac{|u|}{U_{dc}}\cos\theta_u\right) = -2\sum_{n=1}^{+\infty}(-1)^n J_{2n-1}\left(\frac{2\pi|u|}{U_{dc}}\right)\cos((2n-1)\theta_u) \qquad \text{(A.14)}$$

Finally

$$\sin(\omega_c T_{a,on}) = 2\sum_{n=1}^{+\infty}(-1)^n J_{2n-1}\left(\frac{2\pi|u|}{U_{dc}}\right)\cos((2n-1)\theta_u) \qquad \text{(A.15)}$$

In the same way:

$$\begin{aligned}
\cos(\omega_c T_{a,on}) &= \cos\left(\omega_c \frac{T_c|u|}{U_{dc} + \omega_c \dfrac{T_c}{2}}\cos\theta_u\right) \\
&= -\cos\left(\frac{2\pi|u|}{U_{dc}}\cos\theta_u\right) \\
&= -J_0\left(\frac{2\pi|u|}{U_{dc}}\right) - 2\sum_{n=1}^{+\infty}(-1)^n J_{2n}\left(\frac{2\pi|u}{U_{dc}}\right)\cos(2n\theta_u) \qquad \text{(A.16)}
\end{aligned}$$

Substituting (A.15) and (A.16) in (A.12), the voltage harmonic of phase a at switching

---

[3] the Jacobi–Anger expansion (or Jacobi–Anger identity) is an expansion of exponentials of trigonometric functions in the basis of their harmonics:

$$\begin{aligned}
\cos(z\cos\theta) &= J_0(z) + 2\sum_{n=1}^{\infty}(-1)^n J_{2n}(z)\cos(2n\theta) \\
\sin(z\cos\theta) &= -2\sum_{n=1}^{\infty}(-1)^n J_{2n-1}(z)\cos[(2n-1)\theta] \\
\cos(z\sin\theta) &= J_0(z) + 2\sum_{n=1}^{\infty} J_{2n}(z)\cos(2n\theta) \\
\sin(z\sin\theta) &= 2\sum_{n=1}^{\infty} J_{2n-1}(z)\sin[(2n-1)\theta]
\end{aligned}$$

where $J_n(z)$ is the n–th Bessel function.

frequency is equal to:

$$\begin{aligned} u_{a_c} &= \frac{U_{dc}}{\pi}\cos(\omega_c t)\left[2\sum_{n=1}^{+\infty}(-1)^n J_{2n-1}\left(\frac{2\pi|u|}{U_{dc}}\right)\cos\Big((2n-1)\theta_u\Big)\right] \\ &\quad + \frac{U_{dc}}{\pi}\sin(\omega_c t)\left[J_0\left(\frac{2\pi|u|}{U_{dc}}\right) + 2\sum_{n=1}^{+\infty}(-1)^n J_{2n}\left(\frac{2\pi|u|}{U_{dc}}\right)\cos\Big(2n\theta_u\Big)\right] \\ &\quad - \frac{U_{dc}}{2\pi}\sin(\omega_c t) \end{aligned} \tag{A.17}$$

that can be written in the compact form:

$$u_{a_c} = A_0\sin(\omega_c t) + \sum_{n=1}^{+\infty}(-1)^n A_{2n-1}\cos\Big((2n-1)\theta_u\Big)\cos(\omega_c t) - \sum_{n=1}^{+\infty}A_{2n}\cos\Big(2n\theta_u\Big)\sin(\omega_c t) \tag{A.18}$$

with

$$\begin{aligned} A_0 &= \frac{U_{dc}}{\pi}\left[J_0\left(\frac{2\pi|u|}{U_{dc}}\right) - \frac{1}{2}\right] \\ A_{2n-1} &= 2\frac{U_{dc}}{\pi}J_{2n-1}\left(\frac{2\pi|u|}{U_{dc}}\right) \\ A_{2n} &= 2\frac{U_{dc}}{\pi}J_{2n}\left(\frac{2\pi|u|}{U_{dc}}\right) \end{aligned} \tag{A.19}$$

In the case of phase b the time $T_{b,on}$ is equal to:

$$\begin{aligned} T_{b,on} &= -\frac{1}{2}\frac{T_c}{U_{dc}}u_\alpha + \frac{\sqrt{3}}{2}\frac{T_c}{U_{dc}}u_\beta + \frac{T_c}{2} \\ &= \frac{T_c}{U_{dc}}|u|\cos\theta_u\cos\left(\frac{2\pi}{3}\right) + \frac{T_c}{U_{dc}}|u|\sin\theta_u\sin\left(\frac{2\pi}{3}\right) + \frac{T_c}{2} \\ &= \frac{T_c}{U_{dc}}|u|\cos\left(\theta_u - \frac{2\pi}{3}\right) + \frac{T_c}{2} \end{aligned} \tag{A.20}$$

One can note that the previously passage made for voltage u_a can be repeat for voltage u_b, substituting θ_u with $\theta_u - 2\pi/3$.
Then, voltage u_b results:

$$\begin{aligned} u_{b_c} = A_0\sin(\omega_c t) &+ \sum_{n=1}^{+\infty}(-1)^n A_{2n-1}\cos(\omega_c t)\cos\left((2n-1)\left(\theta_u - \frac{2\pi}{3}\right)\right) \\ &+ \sum_{n=1}^{+\infty}(-1)^n A_{2n}\sin(\omega_c t)\cos\left(2n\left(\theta_u - \frac{2\pi}{3}\right)\right) \end{aligned} \tag{A.21}$$

Instead, in the case of phase c the time $T_{c,on}$ is equal to:

$$\begin{aligned} T_{c,on} &= -\frac{1}{2}\frac{T_c}{U_{dc}}u_\alpha - \frac{\sqrt{3}}{2}\frac{T_c}{U_{dc}}u_\beta + \frac{T_c}{2} \\ &= \frac{T_c}{U_{dc}}|u|\cos\theta_u\cos\left(\frac{4\pi}{3}\right) + \frac{T_c}{U_{dc}}|u|\sin\theta_u\sin\left(\frac{4\pi}{3}\right) + \frac{T_c}{2} \\ &= \frac{T_c}{U_{dc}}|u|\cos\left(\theta_u + \frac{2\pi}{3}\right) + \frac{T_c}{2} \end{aligned} \tag{A.22}$$

Eq. (A.22) can be substitute in (A.10). Substituting θ_u with $\theta_u + 2\pi/3$, the voltage u_c becomes:

$$\begin{aligned} u_{c_c} = A_0 \sin(\omega_c t) &+ \sum_{n=1}^{+\infty} (-1)^n A_{2n-1} \cos(\omega_c t) \cos\left((2n-1)\left(\theta_u + \frac{2\pi}{3}\right)\right) \\ &+ \sum_{n=1}^{+\infty} (-1)^n A_{2n} \sin(\omega_c t) \cos\left(2n\left(\theta_u + \frac{2\pi}{3}\right)\right). \end{aligned} \tag{A.23}$$

Eqs. (A.18), (A.21) and (A.23) can be rewritten as following:

$$\begin{aligned} u_{a_c} = {} & A_0 \sin(\omega_c t) + \sum_{n=1}^{+\infty} (-1)^n \frac{A_{2n-1}}{2} \cos\left(\omega_c t + (2n-1)\theta_u\right) \\ & + \sum_{n=1}^{+\infty} (-1)^n \frac{A_{2n-1}}{2} \cos\left(\omega_c t - (2n-1)\theta_u\right) \\ & + \sum_{n=1}^{+\infty} (-1)^n \frac{A_{2n}}{2} \sin\left(\omega_c t + 2n\theta_u\right) \\ & + \sum_{n=1}^{+\infty} (-1)^n \frac{A_{2n}}{2} \sin\left(\omega_c t - 2n\theta_u\right) \end{aligned} \tag{A.24}$$

$$\begin{aligned} u_{b_c} = {} & A_0 \sin(\omega_c t) + \sum_{n=1}^{+\infty} (-1)^n \frac{A_{2n-1}}{2} \cos\left(\omega_c t + (2n-1)\left(\theta_u - \frac{2\pi}{3}\right)\right) \\ & + \sum_{n=1}^{+\infty} (-1)^n \frac{A_{2n-1}}{2} \cos\left(\omega_c t - (2n-1)\left(\theta_u + \frac{2\pi}{3}\right)\right) \\ & + \sum_{n=1}^{+\infty} (-1)^n \frac{A_{2n}}{2} \sin\left(\omega_c t + 2n\left(\theta_u - \frac{2\pi}{3}\right)\right) \\ & + \sum_{n=1}^{+\infty} (-1)^n \frac{A_{2n}}{2} \sin\left(\omega_c t - 2n\left(\theta_u - \frac{2\pi}{3}\right)\right) \end{aligned} \tag{A.25}$$

$$\begin{aligned} u_{c_c} = {} & A_0 \sin(\omega_c t) + \sum_{n=1}^{+\infty} (-1)^n \frac{A_{2n-1}}{2} \cos\left(\omega_c t + (2n-1)\left(\theta_u \frac{2\pi}{3}\right)\right) \\ & + \sum_{n=1}^{+\infty} (-1)^n \frac{A_{2n-1}}{2} \cos\left(\omega_c t + (2n-1)\left(\theta_u + \frac{2\pi}{3}\right)\right) \\ & + \sum_{n=1}^{+\infty} (-1)^n \frac{A_{2n}}{2} \sin\left(\omega_c t + 2n\left(\theta_u + \frac{2\pi}{3}\right)\right) \\ & + \sum_{n=1}^{+\infty} (-1)^n \frac{A_{2n}}{2} \sin\left(\omega_c t - 2n\left(\theta_u + \frac{2\pi}{3}\right)\right) \end{aligned} \tag{A.26}$$

A.2 Study in the $\alpha\beta$ reference frame

Applying the transformation matrix $T_{abc,\alpha\beta}$ at the (A.18), (A.21) and (A.23), the $\alpha\beta$ reference frame is obtained. To simplify the study the single voltage can be splitting in three terms:

$$u_{x_c} = u_{x_0} + u_{x_{2n-1}} + u_{x_{2n}} \tag{A.27}$$

For example for phase a is valid the following equality:

$$\begin{aligned}
u_{a_0} &= A_0 \sin(\omega_c t) && \text{(A.28)}\\
u_{a_{2n-1}} &= \sum_{n=1}^{+\infty} (-1)^n A_{2n-1} \cos\Big((2n-1)\theta_u\Big)\cos(\omega_c t) \\
u_{a_{2n}} &= \sum_{n=1}^{+\infty} (-1)^n A_{2n} \cos\Big(2n\theta_u\Big)\sin(\omega_c t) && \text{(A.29)}
\end{aligned}$$

Consequently also the voltages in the $\alpha\beta$ reference frame can be expressed with three terms. The first is obtained in this way:

$$\begin{aligned}
u_{\alpha_0} &= \frac{2}{3}\Big(u_{a_0} - \frac{u_{b_0}}{2} - \frac{u_{c_0}}{2}\Big) && \text{(A.30)}\\
&= \frac{2}{3} A_0 sin\omega_c t \left(1 - \frac{1}{2} - \frac{1}{2}\right) = 0 && \text{(A.31)}
\end{aligned}$$

Second term instead results in:

$$\begin{aligned}
u_{\alpha_{2n-1}} &= \frac{2}{3}\sum_{n=1}^{+\infty} (-1)^n A_{2n-1} \cos(\omega_c t)\Big[\cos\Big((2n-1)\theta_u\Big) \\
&\qquad - \frac{1}{2}\cos\left((2n-1)\theta_u - \frac{2\pi}{3}\right) \\
&\qquad\qquad - \frac{1}{2}\cos\left((2n-1)\theta_u + \frac{2\pi}{3}\right)\Big] \\
&= \frac{2}{3}\sum_{n=1}^{+\infty} (-1)^n A_{2n-1} \cos(\omega_c t)\Big[\cos\Big((2n-1)\theta_u\Big) \\
&\qquad - \cos\Big((2n-1)\theta_u\Big)\cos\left((2n-1)\frac{2\pi}{3}\right)\Big] \\
&= \frac{2}{3}\sum_{n=1}^{+\infty} (-1)^n A_{2n-1} \cos(\omega_c t)\cos\Big((2n-1)\theta_u\Big)\left(1 - \cos\left((2n-1)\frac{2\pi}{3}\right)\right)
\end{aligned} \tag{A.32}$$

Finally the third term is:

$$
\begin{align}
u_{\alpha_{2n}} &= \frac{2}{3}\sum_{n=1}^{+\infty}(-1)^n A_{2n}\sin(\omega_c t)\Bigg[\cos\Big(2n\theta_u\Big)-\frac{1}{2}\cos\Bigg(2n\left(\theta_u-\frac{2\pi}{3}\right)\Bigg) \tag{A.33}\\
&\qquad -\frac{1}{2}\cos\Bigg(2n\left(\theta_u+\frac{2\pi}{3}\right)\Bigg)\Bigg] \nonumber\\
&= \frac{2}{3}\sum_{n=1}^{+\infty}(-1)^n A_{2n}\sin(\omega_c t)\left(\cos\Big(2n\theta_u\Big)-\cos\Big(2n\theta_u\Big)\cos\left(2n\frac{2\pi}{3}\right)\right) \nonumber\\
&= \frac{2}{3}\sum_{n=1}^{+\infty}(-1)^n A_{2n}\sin(\omega_c t)\cos\Big(2n\theta_u\Big)\left(1-\cos\left(2n\frac{2\pi}{3}\right)\right) \tag{A.34}
\end{align}
$$

The same arrangements can be carried out in order to derive voltage u_β. It results:

$$
\begin{align}
u_{\beta_0} &= \frac{1}{\sqrt{3}}\left(u_{b_0}-u_{c_0}\right) \nonumber\\
&= \frac{1}{\sqrt{3}}A_0 sin\omega_c t\left(1-1\right)=0 \tag{A.35}
\end{align}
$$

$$
\begin{align}
u_{\beta_{2n-1}} &= \frac{1}{\sqrt{3}}\sum_{n=1}^{+\infty}(-1)^n A_{2n-1}\cos(\omega_c t)\Bigg[\cos\Bigg((2n-1)\left(\theta_u-\frac{2\pi}{3}\right)\Bigg) \nonumber\\
&\qquad -\cos\Bigg((2n-1)\left(\theta_u+\frac{2\pi}{3}\right)\Bigg)\Bigg] \nonumber\\
&= \frac{2}{\sqrt{3}}\sum_{n=1}^{+\infty}(-1)^n A_{2n-1}\cos(\omega_c t)\sin((2n-1)\theta_u)\sin\left((2n-1)\frac{2\pi}{3}\right) \tag{A.36}
\end{align}
$$

$$
\begin{align}
u_{\beta_{2n}} &= \frac{1}{\sqrt{3}}\sum_{n=1}^{+\infty}(-1)^n A_{2n}\sin(\omega_c t)\Bigg[\cos\Bigg(2n\left(\theta_u+\frac{2\pi}{3}\right)\Bigg) \nonumber\\
&\qquad -\cos\Bigg(2n\left(\theta_u+\frac{2\pi}{3}\right)\Bigg)\sin(\omega_c t)\Bigg] \nonumber\\
&= -\frac{2}{\sqrt{3}}\sum_{n=1}^{+\infty}(-1)^n A_{2n}\sin(\omega_c t)\sin(2n\theta_u)\sin\left(2n\frac{2\pi}{3}\right) \tag{A.37}
\end{align}
$$

Reassuming, the voltages u_{α_c} and u_{β_c} are given from the sum of (A.30), (A.32) and (A.34) for the first and (A.35), (A.36) and (A.37) for the latter:

$$
\begin{align}
u_{\alpha_c} &= \frac{2}{3}\sum_{n=1}^{+\infty}(-1)^n A_{2n-1}\cos(\omega_c t)\cos\Big((2n-1)\theta_u\Big)\left(1-\cos\left((2n-1)\frac{2\pi}{3}\right)\right) \nonumber\\
&\qquad +\frac{2}{3}\sum_{n=1}^{+\infty}(-1)^n A_{2n}\sin(\omega_c t)\cos\Big(2n\theta_u\Big)\left(1-\cos\left(2n\frac{2\pi}{3}\right)\right) \tag{A.38}
\end{align}
$$

$$\begin{aligned}u_{\beta_c} &= \frac{2}{\sqrt{3}}\sum_{n=1}^{+\infty}(-1)^n A_{2n-1}\cos(\omega_c t)\sin((2n-1)\theta_u)\sin\left((2n-1)\frac{2\pi}{3}\right)\\ &\qquad\qquad + \frac{2}{\sqrt{3}}\sum_{n=1}^{+\infty} A_{2n}\Big(\sin(2n\theta_u)\sin\left(2n\frac{2\pi}{3}\right)\Big)\sin(\omega_c t)\end{aligned}\tag{A.39}$$

In the case of sensorless control the phase θ_u is given by the sum of the estimated position $\tilde{\theta}_{me}$ and the phase θ_u^r. Substituting this equality in (A.38) and (A.39) it results:

$$\begin{aligned}u_{\alpha_c} &= \frac{2}{3}\sum_{n=1}^{+\infty}(-1)^n A_{2n-1}\cos(\omega_c t)\cos\left((2n-1)(\tilde{\theta}_{me}+\theta_u^r)\right)\left(1-\cos\left((2n-1)\frac{2\pi}{3}\right)\right)\\ &\qquad + \frac{2}{3}\sum_{n=1}^{+\infty}(-1)^n A_{2n}\sin(\omega_c t)\cos\left(2n(\tilde{\theta}_{me}+\theta_u^r)\right)\left(1-\cos\left(2n\frac{2\pi}{3}\right)\right)\end{aligned}\tag{A.40}$$

$$\begin{aligned}u_{\beta_c} &= \frac{2}{\sqrt{3}}\sum_{n=1}^{+\infty}(-1)^n A_{2n-1}\cos(\omega_c t)\sin((2n-1)(\tilde{\theta}_{me}+\theta_u^r))\sin\left((2n-1)\frac{2\pi}{3}\right)\\ &\qquad + \frac{2}{\sqrt{3}}\sum_{n=1}^{+\infty}(-1)^n A_{2n}\sin(\omega_c t)\sin(2n(\tilde{\theta}_{me}+\theta_u^r))\sin\left(2n\frac{2\pi}{3}\right)\end{aligned}\tag{A.41}$$

In the steady–state operation the equality $\tilde{\theta}_{me} = \tilde{\omega}_{me}t$, while θ_u^r can be considerate constant. Moreover, $\tilde{\omega}_{me}$ is equal the electrical speed ω_{me}. Then one can arranged (A.42) and (A.43) in this way:

$$\begin{aligned}u_{\alpha_c} &= \frac{2}{3}\sum_{n=1}^{+\infty}(-1)^n \frac{A_{2n-1}}{2}\cos\left(\omega_c t+(2n-1)(\tilde{\omega}_{me}t+\theta_u^r)\right)\left(1-\cos\left((2n-1)\frac{2\pi}{3}\right)\right)\\ &\quad + \frac{2}{3}\sum_{n=1}^{+\infty}(-1)^n \frac{A_{2n-1}}{2}\cos\left(\omega_c t-(2n-1)(\tilde{\omega}_{me}t+\theta_u^r)\right)\left(1-\cos\left((2n-1)\frac{2\pi}{3}\right)\right)\\ &\quad + \frac{2}{3}\sum_{n=1}^{+\infty}(-1)^n \frac{A_{2n}}{2}\sin\left(\omega_c t+2n(\tilde{\omega}_{me}t+\theta_u^r)\right)\left(1-\cos\left(2n\frac{2\pi}{3}\right)\right)\\ &\quad + \frac{2}{3}\sum_{n=1}^{+\infty}\frac{A_{2n}}{2}\sin\left(\omega_c t-2n(\tilde{\omega}_{me}t+\theta_u^r)\right)\left(1-\cos\left(2n\frac{2\pi}{3}\right)\right)\end{aligned}\tag{A.42}$$

$$\begin{aligned}
u_{\beta_c} = & \frac{2}{\sqrt{3}}\sum_{n=1}^{+\infty}(-1)^n\frac{A_{2n-1}}{2}\sin\left(\omega_c t+(2n-1)(\tilde{\omega}_{me}t+\theta_u^r)\right)\sin\left((2n-1)\frac{2\pi}{3}\right) \\
& -\frac{2}{\sqrt{3}}\sum_{n=1}^{+\infty}(-1)^n\frac{A_{2n-1}}{2}\sin\left(\omega_c t-(2n-1)(\tilde{\omega}_{me}t+\theta_u^r)\right)\sin\left((2n-1)\frac{2\pi}{3}\right) \\
& -\frac{2}{\sqrt{3}}\sum_{n=1}^{+\infty}(-1)^n\frac{A_{2n}}{2}\cos\left(\omega_c t+(2n(\tilde{\theta}_{me}+\theta_u^r))\right)\sin\left(2n\frac{2\pi}{3}\right) \\
& +\frac{2}{\sqrt{3}}\sum_{n=1}^{+\infty}(-1)^n\frac{A_{2n}}{2}\cos\left(\omega_c t-(2n(\tilde{\theta}_{me}+\theta_u^r))\right)\sin\left(2n\frac{2\pi}{3}\right)
\end{aligned} \tag{A.43}$$

One can note that u_{α_c} and u_{β_c} are given by a series of harmonics centered around the switching frequency, then with frequency $f_c \pm f_{me}$. It is noticed that one harmonic is null in the case where:

$$\begin{aligned}
1-\cos\left((2n-1)\frac{2\pi}{3}\right) &= 0 \\
\sin\left(2n\frac{2\pi}{3}\right) &= 0 \\
1-\cos\left(2n\frac{2\pi}{3}\right) &= 0 \\
\sin\left((2n-1)\frac{2\pi}{3}\right) &= 0
\end{aligned}$$

This occurs when:

$$\begin{aligned}
(2n-1)\frac{2\pi}{3} &= 2k\pi \quad \text{with} \quad k \in \mathbb{I} \\
2n-1 &= 3k\pi
\end{aligned}$$

or

$$\begin{aligned}
2n\frac{2\pi}{3} &= 2k\pi \quad \text{with} \quad k \in \mathbb{I} \\
n &= \frac{3}{2}k \\
&= 3k' \quad \text{with k'even}
\end{aligned} \tag{A.44}$$

In both the cases the null harmonics are those that have a frequency of $f_c \pm 3f_{me}$, i.e. switching frequency ± the third harmonics and its multiplies.

A.3 Stator currents analysis at switching frequency

From all the terms of the (A.42) and (A.43) it is possible taking into consideration those at frequency $f_c \pm f_{me}$:

$$\begin{aligned} u_{\alpha_c} &= -\frac{A_1}{2}\cos(\omega_c t + \tilde{\theta}_{me} + \theta_u^r) - \frac{A_1}{2}\cos(\omega_c t - \tilde{\theta}_{me} - \theta_u^r) \\ &= -U\cos(\omega_c t + \tilde{\theta}_{me} + \theta_u^r) - U\cos(-\omega_c t + \tilde{\theta}_{me} + \theta_u^r) \\ u_{\beta_c} &= -\frac{A_1}{2}\sin(\omega_c t + \tilde{\theta}_{me} + \theta_u^r) + \frac{A_1}{2}\sin(\omega_c t - \tilde{\theta}_{me} - \theta_u^r) \\ &= -U\sin(\omega_c t + \tilde{\theta}_{me} + \theta_u^r) - U\sin(-\omega_c t + \tilde{\theta}_{me} + \theta_u^r) \end{aligned} \tag{A.45}$$

From (A.45) one can note that the high frequency voltage vector is given by two rotating vectors at speed $\omega_c + \omega_{me}$ and $-\omega_c + \omega_{me}$. Then the voltage vector can be split in this way:

$$\bar{u}^s_{\alpha\beta_c} = \underbrace{\bar{u}^s_{\omega_c^+}}_{anti-clockwise} + \underbrace{\bar{u}^s_{\omega_c^-}}_{clockwise} \tag{A.46}$$

To calculate the high frequency currents, it is possible to study separately the effects due to the two voltage vectors $\bar{u}^s_{\omega_c^-}$ and $\bar{u}^s_{\omega_c^+}$, using similar procedures to those described in Secs. 3.3.1 and 3.4.1.

Taking the first vector $\bar{u}^s_{\omega_c^+}$ and splitting in the two components α and β:

$$\begin{aligned} u_{\alpha_c^+} &= -U\cos(\omega_c t + \tilde{\theta}_{me} + \theta_u^r) \\ u_{\beta_c^+} &= -U\sin(\omega_c t + \tilde{\theta}_{me} + \theta_u^r) \end{aligned} \tag{A.47}$$

the following flux linkage are derived (neglecting the resistance voltage drop):

$$\lambda_{\alpha_c^+} = -\frac{U}{\omega_c + \tilde{\omega}_{me}}\sin(\omega_c t + \tilde{\theta}_{me} + \theta_u^r) = -\Lambda^+\sin(\omega_c t + \tilde{\theta}_{me} + \theta_u^r) \tag{A.48}$$

$$\lambda_{\beta_c^+} = \frac{U}{\omega_c + \tilde{\omega}_{me}}\cos(\omega_c t + \tilde{\theta}_{me} + \theta_u^r) = \Lambda^+\cos(\omega_c t + \tilde{\theta}_{me} + \theta_u^r) \tag{A.49}$$

where the apex ^{s} is neglecting, the apex $^+$ indicates the positive sequence and the subscript $_c$ indicates that is a harmonics at switching frequency. In general the following expressions for the current are valid (Sec.3.3.1):

$$\begin{aligned} i_{\alpha_c} &= \frac{l_\Sigma + l_\Delta\cos 2\Delta\theta}{l_\Sigma^2 - l_\Delta^2}\lambda_{\alpha_c} - \frac{l_\Delta\sin 2\Delta\theta}{l_\Sigma^2 - l_\Delta^2}\lambda_{\beta_c} \\ i_{\beta_c} &= \frac{l_\Sigma - l_\Delta\cos 2\Delta\theta}{l_\Sigma^2 - l_\Delta^2}\lambda_{\beta_c} - \frac{l_\Delta\sin 2\Delta\theta}{l_\Sigma^2 - l_\Delta^2}\lambda_{\alpha_c} \end{aligned} \tag{A.50}$$

Then substituting the (A.48) in (A.50) and imposing $\Delta\theta = -\theta_{me}$ (the stationary reference frame is taken into consideration) from the (A.48), the current components given by the positive sequence voltage result:

$$\begin{aligned}
i_{\alpha_c^+} &= -\frac{\Lambda^+}{l_d l_q}(l_\Sigma + l_\Delta \cos 2\theta_{me}) \sin(\omega_c t + \tilde{\theta}_{me} + \theta_u^r) \\
&\qquad + \frac{\Lambda^+}{l_d l_q}(l_\Delta \sin 2\theta_{me}) \cos(\omega_c t - \tilde{\theta}_{me} - \theta_u^r) \\
&= -\frac{\Lambda^+}{l_d l_q} l_\Sigma \sin(\omega_c t + \tilde{\theta}_{me} + \theta_u^r) - \frac{\Lambda^+}{l_d l_q} l_\Delta (\cos 2\theta_{me} \sin(\omega_c t + \tilde{\theta}_{me} + \theta_u^r) \\
&\qquad - \sin 2\theta_{me} \cos(\omega_c t + \tilde{\theta}_{me} + \theta_u^r)) \\
&= -\frac{\Lambda^+}{l_d l_q} l_\Sigma \sin(\omega_c t + \tilde{\theta}_{me} + \theta_u^r) - \frac{\Lambda^+}{l_d l_q} l_\Delta \sin(\omega_c t + \tilde{\theta}_{me} - 2\theta_{me} + \theta_u^r) \quad (A.51)
\end{aligned}$$

$$\begin{aligned}
i_{\beta_c^+} &= \frac{\Lambda^+}{l_d l_q}(l_\Sigma - l_\Delta \cos 2\theta_{me}) \cos(\omega_c t + \tilde{\theta}_{me} + \theta_u^r) \\
&\qquad - \frac{\Lambda^+}{l_d l_q}(l_\Delta \sin 2\theta_{me}) \sin(\omega_c t - \tilde{\theta}_{me} - \theta_u^r) \\
&= \frac{\Lambda^+}{l_d l_q} l_\Sigma \cos(\omega_c t + \tilde{\theta}_{me} + \theta_u^r) - \frac{\Lambda^+}{l_d l_q} l_\Delta (\cos 2\theta_{me} \sin(\omega_c t + \tilde{\theta}_{me} + \theta_u^r) \\
&\qquad + \sin 2\theta_{me} \cos(\omega_c t + \tilde{\theta}_{me} + \theta_u^r)) \\
&= \frac{\Lambda^+}{l_d l_q} l_\Sigma \cos(\omega_c t + \tilde{\theta}_{me} + \theta_u^r) - \frac{\Lambda^+}{l_d l_q} l_\Delta \cos(\omega_c t + \tilde{\theta}_{me} - 2\theta_{me} + \theta_u^r) \quad (A.52)
\end{aligned}$$

As far as the anti-clockwise rotating voltage vector is concerned, its components are:

$$\begin{aligned}
u_{\alpha_c^-} &= -U \cos(\omega_c t - \tilde{\theta}_{me} - \theta_u^r) \qquad (A.53) \\
u_{\beta_c^-} &= U \sin(\omega_c t - \tilde{\theta}_{me} - \theta_u^r)
\end{aligned}$$

from which the flux–linkage components can be derived:

$$\begin{aligned}
\lambda_{\alpha_c^-} &= -\frac{U}{\omega_c - \tilde{\omega}_{me}} \sin(\omega_c t - \tilde{\theta}_{me} - \theta_u^r) = -\Lambda^- \sin(\omega_c t - \tilde{\theta}_{me} - \theta_u^r) \quad (A.54) \\
\lambda_{\beta_c^-} &= -\frac{U}{\omega_c - \tilde{\omega}_{me}} \cos(\omega_c t - \tilde{\theta}_{me} - \theta_u^r) = -\Lambda^- \cos(\omega_c t - \tilde{\theta}_{me} - \theta_u^r) \quad (A.55)
\end{aligned}$$

Substituting (A.54) in (A.50) the current components obtained by the negative sequence voltage result:

$$\begin{aligned}
i_{\alpha_c^-} &= -\frac{\Lambda^-}{l_d l_q}(l_\Sigma + l_\Delta \cos 2\theta_{me}) \sin(\omega_c t - \tilde{\theta}_{me} - \theta_u^r) \\
&\qquad - \frac{\Lambda^-}{l_d l_q}(l_\Delta \sin 2\theta_{me}) \cos(\omega_c t - \tilde{\theta}_{me} - \theta_u^r) \\
&= -\frac{\Lambda^-}{l_d l_q} l_\Sigma \sin(\omega_c t - \tilde{\theta}_{me} - \theta_u^r) - \frac{\Lambda^-}{l_d l_q} l_\Delta (\cos 2\theta_{me} \sin(\omega_c t - \tilde{\theta}_{me} - \theta_u^r) \\
&\qquad + \sin 2\theta_{me} \cos(\omega_c t - \tilde{\theta}_{me} - \theta_u^r)) \\
&= -\frac{\Lambda^-}{l_d l_q} l_\Sigma \sin(\omega_c t - \tilde{\theta}_{me} - \theta_u^r) - \frac{\Lambda^-}{l_d l_q} l_\Delta \sin(\omega_c t - \tilde{\theta}_{me} + 2\theta_{me} - \theta_u^r) \quad (A.56)
\end{aligned}$$

$$\begin{aligned}
i_{\beta_c^-} &= -\frac{\Lambda^-}{l_d l_q}(l_\Sigma - l_\Delta \cos 2\theta_{me}) \cos(\omega_c t - \tilde{\theta}_{me} - \theta_u^r) \\
&\qquad - \frac{\Lambda^-}{l_d l_q}(l_\Delta \sin 2\theta_{me}) \sin(\omega_c t - \tilde{\theta}_{me} - \theta_u^r) \\
&= -\frac{\Lambda^-}{l_d l_q} l_\Sigma \cos(\omega_c t - \tilde{\theta}_{me} - \theta_u^r) + \frac{\Lambda^-}{l_d l_q} l_\Delta (\cos 2\theta_{me} \sin(\omega_c t - \tilde{\theta}_{me} - \theta_u^r) \\
&\qquad - \sin 2\theta_{me} \cos(\omega_c t - \tilde{\theta}_{me} - \theta_u^r)) \\
&= -\frac{\Lambda^-}{l_d l_q} l_\Sigma \cos(\omega_c t - \tilde{\theta}_{me} - \theta_u^r) + \frac{\Lambda^-}{l_d l_q} l_\Delta \cos(\omega_c t - \tilde{\theta}_{me} + 2\theta_{me} - \theta_u^r) \quad (A.57)
\end{aligned}$$

Adding (A.51) to the (A.56) and (A.52) to the (A.57), the total current vector components are obtained:

$$\begin{aligned}
i_{\alpha_c} &= -I_0^+ \sin(\omega_c t + \tilde{\theta}_{me}(t) + \theta_u^r) - I_1^+ \sin(\omega_c t + \tilde{\theta}_{me} - 2\theta_{me}(t) + \theta_u^r) - \\
&\quad - I_0^- \sin(\omega_c t - \tilde{\theta}_{me}(t) - \theta_u^r) - I_1^- \sin(\omega_c t - \tilde{\theta}_{me}(t) + 2\theta_{me}(t) - \theta_u^r)
\end{aligned} \quad (A.58)$$

$$\begin{aligned}
i_{\beta_c} &= I_0^+ \cos(\omega_c t + \tilde{\theta}_{me}(t) + \theta_u^r) - I_1^+ \cos(\omega_c t + \tilde{\theta}_{me} - 2\theta_{me}(t) + \theta_u^r) - \\
&\quad - I_0^- \cos(\omega_c t - \tilde{\theta}_{me}(t) - \theta_u^r) + I_1^- \cos(\omega_c t - \tilde{\theta}_{me} + 2\theta_{me}(t) - \theta_u^r)
\end{aligned} \quad (A.59)$$

with

$$\begin{aligned}
I_0^+ &= \frac{l_\Sigma}{l_d l_q} \frac{U^+}{\omega_c + \tilde{\omega}_{me}} \\
I_1^+ &= \frac{l_\Delta}{l_d l_q} \frac{U^+}{\omega_c + \tilde{\omega}_{me}} \\
I_0^- &= \frac{l_\Sigma}{l_d l_q} \frac{U^-}{\omega_c - \tilde{\omega}_{me}} \\
I_1^- &= \frac{l_\Delta}{l_d l_q} \frac{U^-}{\omega_c - \tilde{\omega}_{me}}
\end{aligned} \quad (A.60)$$

where l_d and l_q are the d– and q–axis inductances respectively, $\tilde{\omega}_{me}$ is the estimated speed and

$$\begin{aligned}
l_\Sigma &= \frac{l_q + l_d}{2} \\
l_\Delta &= \frac{l_q - l_d}{2}
\end{aligned}$$

List of Symbols

Roman Symbols

$T_{dq/\alpha\beta}$	matrix transformation from the rotor to the stator reference frame	
B	motor viscous friction coeffcient	$Nms/rad.$
$\bar{e}$	back–electromotive force vector	
f_c	switching frequency	Hz
f_{me}	fundamental frequency	
$i_\alpha,\ i_\beta$	real part, imaginary part of the current vector in the stator reference frame	A
$i_a,\ i_b,\ i_c$	phase a, b, c current	A
$i_{\alpha_c},\ i_{\beta_c}$	real, imaginary part of the current component at switching frequency	A
$i_d,\ i_q$	d–axis, q–axis component of the current vector in the rotor reference frame	A
$i_{hd},\ i_{hq}$	d–axis, q–axis high frequency current	
i_r	current ring	A
J	motor inertia	kgm^2
$L_{aa},\ L_{bb},\ L_{cc}$	phase a, b, c self–inductances	H
$\lambda_\alpha,\ \lambda_\beta$	real part, imaginary part of the flux–linkage vector in the stator reference frame	$Vs/rad.$
$\lambda_{hd}, \lambda_{hq}$	d–axis, q–axis high frequency flux linkage	
$l_d,\ l_q$	d–axis, q–axis inductance at small signals	H
l_Δ	difference inductance	H
$L_d,\ L_q$	d–axis, q–axis inductance	H
l_M	mutual inductance between d– q–axis at small signal	H
$L_{ab},\ L_{bc},\ L_{ac}$	mutual inductance	H
L_{rt}	transient inductance	H
L_s	stator inductance	H
l_Σ	average inductance	H
m	motor torque	Nm
m_L	load torque	Nm
n	mechanical speed	rpm

p	pole–pair	–
$\Re_d$	d–axis reluctance	H^{-1}
$\Re_q$	q–axis reluctance	H^{-1}
R_r	resistance of all ring series	Ω
R_{ring}	resistance of a single ring	Ω
R_s	stator resistance	Ω
$T_{\alpha\beta/abc}$	matrix transformation from the stator to the three–phase reference frame	
$T_{\alpha\beta/dq}$	matrix transformation from the stator to the rotor reference frame	
$T_{abc/\alpha\beta}$	matrix transformation from the three–phase to the stator reference frame	
$u_\alpha,\ u_\beta$	real part, imaginary part of the voltage vector in the stator reference frame	V
$u_a,\ u_b,\ u_c$	phase a, b, c voltage	V
$u_{a_c},\ u_{b_c},\ u_{c_c}$	phase a, b, c voltage component at switching frequency	V
$u_{\alpha_c},\ u_{\beta_c}$	real, imaginary part of the voltage spatial vector in the stator reference frame	V
$u_d,\ u_q$	d–axis, q–axis component of the voltage vector in the rotor reference frame	V
$u_{hd},\ u_{hq}$	d–axis, q–axis high frequency injected voltage	
u_r	voltage ring	V
$\dot{Z}$	impedance	

Greek Symbols

$\Delta\theta$	estimation error $\tilde{\theta}_{me} - \theta_{me}$	$el.rad.$
$\lambda_a,\ \lambda_b,\ \lambda_c$	phase a, b, c flux linkage	$Vs/rad.$
$\bar{\lambda}_{mg}$	PM flux linkage vector	
Λ_{mg}	maximum flux linkage of each phase due to the PM	$Vs/rad.$
$\bar{\lambda}$	flux linkage spatial vector	
ω_{me}	electrical rotor speed	$el.rad./s$
ω_c	switching pulsation $2\pi f_c$	rad/s
θ_m	mechanical position	$rad.$
$\tilde{\theta}_{me}$	estimated electrical rotor position	$el.rad.$
θ_{me}	electrical rotor position	$el.rad.$

θ_u^r	phase of the voltage spatial vector in the rotor reference frame	
ω_m	mechanical speed	$rad./s$
$\tilde{\omega}_{me}$	estimated electrical rotor speed	
ω_h	injection pulsation	$rad./s$
ξ	saliency ratio L_q/L_d	–

Superscripts

r	rotor reference frame
s	stator reference frame
x	general reference frame

Subscripts

α, β	real and immaginary part in the stator reference frame
$d,\ q$	direct, quadrature component in the rotor reference frame

Other Symbols

$\breve{\bar{g}}$	complex conjugated of spatial vector $\bar{g}$
$\bar{g}$	spatial vector
G	constant quantities, i.e. at steady–state
$\underline{g}$	matrix
$\dot{g}$	$\frac{dg}{dt}$
$\tilde{g}$	estimated value
$\bar{G}$	phasor representation of vector $\bar{g}$
g^*	reference value

Acronyms

FEM	finite element method
HPF	high pass filter
IPM	interior permanent magnet
LPF	low pass filter
PM	permanent magnet
SPM	surface mounted permanent magnet
XPM	inset rotor configuration

Bibliography

[1] T.M. Jahns. *Design, Analysis, and Control of Interior PM Synchronous Machines*, chapter *IPM machine electrical analysis and performance*, pages 2.1–2.22. IEEE IAS Tutorial Course notes, IAS Annual Meeting, CLEUP, Seattle, October 3, 2005. (info@cleup.it).

[2] N. Bianchi, S. Bolognani, Ji-Hoon Jang, and Seung-Ki Sul. Advantages of Inset PM Machines for Zero-speed Sensorless Position Detection. *IEEE Transactions on Industry Applications*, 44(4):1190–1198, July/August 2008.

[3] Y.S. Jeong, R.D. Lorenz, T.M. Jahns, and S.K. Sul. Initial rotor position estimation of an IPM synchronous machine using carrier–frequency injection methods. *IEEE Trans. on Industry Applications*, IA–40(1):38–45, Jan/Feb 2005.

[4] P.B. Schmidt, M.L. Gasperi, G. Ray, and A.H. Wijenayake. Initial rotor angle detection of a nonsalient pole permanent magnet synchronous machine. In *Industry Applications Conference, 1997. Thirty-Second IAS Annual Meeting, IAS '97., Conference Record of the 1997 IEEE*, volume 1, pages 459 –463 vol.1, October 1997.

[5] P. L. Jansen and R. D. Lorenz. Transducerless position and velocity estimation in induction and salient AC machines. *IEEE Transactions on Industry Applications*, 31(2):240–247, March/April 1995.

[6] T. Aihara, A. Toba, T. Yanase, A. Mashimo, and K. Endo. Sensorless torque control of salient-pole synchronous motor at zero-speed operation. *Power Electronics, IEEE Transactions on*, 14(1):202–208, Jan 1999.

[7] J. Holtz. Initial rotor polarity detection and sensorless control of pm synchronous machines. *Industry Applications Conference, 2006. 41st IAS Annual Meeting. Conference Record of the 2006 IEEE*, 4:2040–2047, Oct. 2006.

[8] S. Shinnaka. "New "mirror-phase vector control" for sensorless drive of permanent-magnet synchronous motor with pole saliency". *IEEE Transactions on Industry Applications.*, 40(2):599–606, March-April 2004.

[9] J. Ha, K. Ide, T. Sawa, and S.K. Sul. Sensorless rotor position estimation of an interior permanent–magnet motor from initial states. *IEEE Trans. Industry Applications*, IA–39(3):761–767, May 2003.

[10] Ji-Hoon Jang, Seung-Ki Sul, Jung-Ik Ha, K. Ide, and M. Sawamura. Sensorless drive of smpm motor by high frequency signal injection. In *Applied Power Electronics Conference and Exposition, 2002. APEC 2002. Seventeenth Annual IEEE*, volume 1, pages 279 –285 vol.1, 2002.

[11] R.D. Lorenz and K. Van Patten. High resolution velocity estimation for all digital, ac servo drives. *IEEE Trans. on Industry Applications*, 27(4):701–705, July/Aug 1991.

[12] A. Emani-Naeini G. F. Franklin, J. D. Powell. *Feedback Control of Dynamic System.* Pearson Education, fourth edition, 2002.

[13] S. Gay, M. Ehsani, Y. Gao, and A. Emani. Modern electric, hybrid electric and fuel cell vehicle. In *CRC Press*, 2005.

[14] C.C. Chan and K.T. Chau. Modern electric vehicle technology. In *Oxford University Press*, 2001.

[15] N. Matsui. Sensorless pm brushlerss dc motor drives. *IEEE Transaction of Industrial Electronics*, Vol. 43 n.2:300–308, 1996.

[16] M. Linke, R. Kennel, and J. Holtz. Sensorless position control of permanent magnet synchronous machines without limitation at zero speed. In *IECON 02 [Industrial Electronics Society, IEEE 2002 28th Annual Conference of the]*, volume 1, pages 674 – 679 vol.1, 5-8 2002.

[17] M. Linke, R. Kennel, and J. Holtz. Sensorless speed and position control of synchronous machines using alternating carrier injection. In *Proc. of International Electric Machines and Drives Conference (IEMDC'03)*, pages 1211–1217, Madison, WI, 2–4 June 2003.

[18] Ji-Hoon Jang, Seung-Ki Sul, Jung-Ik Ha, K. Ide, and M. Sawamura. "Sensorless drive of surface-mounted permanent-magnet motor by high-frequency signal injection based on magnetic saliency". *IEEE Transactions on Industry Applications*, 39(4):1031–1039, July/August 2003.

[19] P. Vas. *Sensorless Vector and Direct Torque Control.* Oxford University Pubblications, 1992.

[20] L. Harnefors and H.-P. Nee. A general algorithm for speed and position estimation of ac motors. *Industrial Electronics, IEEE Transactions on*, 47(1):77–83, Feb 2000.

[21] R. Wu and G.R. Slemon. A permanent magnet motor drive without a shaft sensor. *Industry Applications, IEEE Transactions on*, 27(5):1005–1011, Sep/Oct 1991.

[22] M. J. Corley and R. D. Lorenz. Rotor position and velocity estimation for a salient-pole permanent magnet synchronous machine at standstill and high speeds. *IEEE Transactions on Industry Applications*, 34(4):784–789, July/August 1998.

[23] A. Consoli, G. Scarcella, and A. Testa. Industry application of zero-speed sensorless control techniques for PM synchronous motors. *IEEE Transactions on Industry Applications*, 37(2):513–521, March/April 2001.

[24] Ji-Hoon Jang, Seung-Ki Sul, Jung-Ik Ha, K. Ide, and M. Sawamura. Sensorless drive of SMPM motor by high frequency signal injection. In *Applied Power Electronics Conference and Exposition, 2002. APEC 2002. Seventeenth Annual IEEE*, volume 1, pages 279–285, Dallas, TX, March 10–14, 2002.

[25] S. Shinnaka. "A new speed-varying ellipse voltage injection method for sensorless drive of permanent-magnet synchronous motors with pole saliency–new pll method using high-frequency current component multiplied signal". *IEEE Transactions on Industry Applications.*, 44(3):777–788, May-june 2008.

[26] N. Bianchi and S. Bolognani. Sensorless-oriented-design of pm motors. *Industry Applications Conference, 2007. 42nd IAS Annual Meeting. Conference Record of the 2007 IEEE*, pages 668–675, Sept. 2007.

[27] N. Bianchi, S. Bolognani, Ji-Hoon Jang, and Seung-Ki Sul. Comparison of PM Motor Structures and Sensorless Control Techniques for Zero-speed Rotor Position Detection. *IEEE Transactions on Power Electronics*, 22(6):2466–2475, November 2007.

[28] N. Bianchi and S. Bolognani. Influence of Rotor Geometry of an IPM Motor on Sensorless Control Feasibility. *IEEE Transactions on Industry Applications*, 43(1):87–96, January/February 2007.

[29] A. Vagati, M. Pastorelli, F. Scapino, and G. Franceschini. Impact of cross saturation in synchronous reluctance motors of the transverse-laminated type. *IEEE Transactions on Industry Applications*, 36(4):1039–1046, July/August 2000.

[30] Y. Li, Z. Q. Zhu, D. Howe, C. M. Bingham, and D. Stone. Improved Rotor Position Estimation by Signal Injection in Brushless AC Motors, Accounting for Cross-coupling Magnetic Saturation. In *Industry Applications Conference, 2007. 42nd IAS Annual Meeting. Conference Record of the 2007 IEEE*, pages 2357–2364, New Orleans, LA, September 23–27, 2007.

[31] S. Bolognani and M. Zigliotto. Self-commissioning compensation of inverter non-idealities for sensorless AC drives applications. In *Power Electronics, Machines and Drives, 2002. International Conference on (Conf. Publ. No. 487)*, pages 30–37, June 4–7, 2002.

[32] D.Howe Z.Q.Zhu, Y.Li and C.M.Bingham. Compensation for rotor position estimation error due to cross coupling magnetic saturation in signal injection based sensorless control of pm brushless ac motors. In *electrical machines and drives conference (IEMDC)*, 2007.

[33] Hyunbae Kim and R.D. Lorenz. "Carrier signal injection based sensorless control methods for ipm synchronous machine drives". *Conference Record of the 2004 IEEE, 39th IAS Annual Meeting.*, pages p:977–984 vol.2, Oct. 2004.

[34] S. Bolognani, S. Calligaro, R. Petrella, and M. Tursini. "Sensorless control of IPM motors in the low-speed range and at stand-still by HF-injection and DFT processing". In *IEEE International Electric Machines and Drives Conference, 2009. IEMDC '09.*, pages 1557–1564, Miami, FL, USA, May 3–6, 2009.

[35] Nicola Bianchi, Silverio Bolognani, and Adriano Faggion. "Predicted and measured errors in estimating rotor position by signal injection for salient-pole PM synchronous motors". In *IEEE International Electric Machines and Drives Conference, 2009. IEMDC '09.*, pages 1565–1572, Miami, FL, USA, May 3–6, 2009.

[36] S. Bolognani, N. Bianchi, and A. Faggion. "Ringed–pole Permanent Magnet Synchronous Motor for Position Sensorless Drives". In *Energy Conversion Congress and Exposition, 2009. ECCE '09. IEEE International*, San José, CA, USA, September 20–24, 2009.

[37] Hyunbae Kim, Kum-Kang Huh, R. D. Lorenz, and T. M. Jahns. A novel method for initial rotor position estimation for IPM synchronous machine drives. *IEEE Transactions on Industry Applications*, 40(5):1369–1378, September/October 2004.

[38] Limei Wang and R.D. Lorenz. "Rotor position estimation for permanent magnet synchronous motor using saliency-tracking self-sensing method". *Industry Applications Conference, 2000. Conference Record of the 2000 IEEE*, 1:445–450 vol.1, 2000.

Acknowledgments

Firstly, I would like to express my deepest gratitude to Prof. Silverio Bolognani, for always being an enthusiastic supervisor throughout my doctoral period. I am also indebted to Prof. Nicola Bianchi, Prof. Mauro Zigliotto and Prof. Roberto Petrella for their help and their good company in these three years.

I am very grateful to the members of past and actual EDlab. I would especially like to thank Emanuele, Massimo and Luca for their friendship.

I would lile to thank my friend Andrea, Gianluca and Davide for your lasting friendship.

I am immensely grateful to my family for their support and encouragement. I would really thank them for believing me and for allowing me to continue the study.

Lastly, but definitely not the least, I like to express my greatest love to Enrica for the good times we had together and to encourage me in the difficult moments.

Padova, 31 January 2011 Adriano Faggion

This Thesis is written in LaTeX.
An electronic version is available at: *http://paduaresearch.cab.unipd.it*